CUKUROVA UNIVERSITY
INSTITUTE OF NATURAL AND APPLIED SCIENCES

PhD THESIS

Estimation of Actual Evapotranspiration Using Remote Sensing Techniques and Energy Balance Models in the Lower Seyhan Plain of the Eastern Mediterranean Region of Türkiye

OMAR ALSENJAR

Agricultural Structures and Irrigation Department

February, 2025

CUKUROVA UNIVERSITY
INSTITUTE OF NATURAL AND APPLIED SCIENCES

PhD THESIS APPROVAL

Estimation of Actual Evapotranspiration Using Remote Sensing Techniques and Energy Balance Models in the Lower Seyhan Plain of the Eastern Mediterranean Region of Türkiye

Omar ALSENJAR

Agricultural Structures and Irrigation Department

This Doctorate Thesis was evaluated by the following Jury Members on 10/02/2025 and was approved by unanimity / ~~majority~~ of votes.

Jury : Prof. Dr. Mahmut ÇETİN (Advisor) ……………………

: Prof. Dr. Fatih TOPALOĞLU ……………………

: Prof. Dr. Recep YURTAL ……………………

: Prof. Dr. Ahmet İRVEM ……………………

: Assoc. Prof. Dr. Hakan AKSU ……………………

This Thesis was written in the Department of Agricultural Structures and Irrigation, Institute of Natural and Applied Sciences.

Thesis Number:

Prof. Dr. Sadık DİNÇER
Director
Institute of Natural and Applied Sciences

This study was financially supported by CU Scientific Research Projects Unit (BAP).
Project No: FDK-2022-14907

CONTENTS

ABSTRACT I
ÖZ II
EXTENDED SUMMARY III
GENİŞLETİLMİŞ ÖZET IX
ACKNOWLEDGEMENTS XV
LIST OF TABLES XVII
LIST OF FIGURES XIX
SYMBOLS AND ABBREVIATIONS XXVI
1. INTRODUCTION 1
2. PRELIMINARY WORK 9
3. MATERIALS AND METHODS 23
3.1. Study Area 23
3.2 Datasets 25
3.2.1. Meteorological data 26
3.2.2. Ground truth data of crops 27
3.2.3. Remotely sensed data 32
3.2.4. Digital elevation model (DEM) 36
3.2.5. Standard crop coefficient K_c 37
3.3. Methods 39
3.3.1. Crop type processing 39
3.3.2. Reference evapotranspiration (ET_o) calculation 42
3.3.3. Crop evapotranspiration (ET_c) estimation 43
3.3.4. NDVI calculation 43
3.3.5. Mapping EvapoTranspiration at high Resolution and with Internalized Calibration (*METRIC*) model and EEFlux-METRIC 44
3.3.6. Surface Energy Balance Algorithm for Land (*SEBAL*) model and GeeSEBAL 49
3.3.7. $K_{c\text{-}NDVI}$ method 53
3.3.8. Estimation of evaporation over lagoons in the LSP using the METRIC and Kohler-Nordenson-Fox models 54
3.3.9. Statistical comparisons 55
4. RESULTS AND DISCUSSION 57
4.1. Reference evapotranspiration (ET_o) and precipitation 57
4.2. Crop type classification and plant distribution mapping 59
4.3. Estimation of ET_a by the standard METRIC and EEFlux METRIC and comparison with ET_o by the FAO-PM approach 68

4.4. Estimation of ET_a by the standard SEBAL and GeeSEBAL and comparison with ET_o by the FAO- PM approach 85
4.5. Comparison of ET_a by the SEB models with the ET_c method 95
4.5.1. Comparison of ET_a by the SEB models with ET_c method over the AID for monthly and yearly time scales 95
4.5.2. Comparison of ET_a by the METRIC and SEBAL models with ET_c method for some crops at satellite image acquisition dates 99
4.6. ET_a estimation by the $K_{c\text{-}NDVI}$ model for some crops 114
4.7. Temporal variations in daily ET_a using the METRIC, SEBAL, $K_{c\text{-}NDVI}$, and ET_c methods for some crops at satellite image acquisition dates 119
4.8. Performance statistics of linear regression model for actual evapotranspiration by the ET_c and SEB models for some crop types 125
4.9. Evaporation estimation by the METRIC model over lagoons of the LSP 136
4.10. Assessing the relationship between leaf area index (LAI) and NDVI by the METRIC model for some crop types over the AID 140
5. CONCLUSIONS AND RECOMMENDATIONS 153
5.1. Conclusions to cropping pattern 153
5.2. Conclusions on ET_a estimations by the SEB models, $K_{c\text{-}NDVI}$ and the “two-step” approach 154
5.3. Evaluation and recommendations for ET_a estimation tools 154
5.4. Conclusions on ET_a estimation for various crops and evaporation from saline lagoons using the METRIC method at satellite image acquisition dates 156
REFERENCES 159
CURRICULUM VITAE 169

CUKUROVA UNIVERSITY
INSTITUTE OF NATURAL AND APPLIED SCIENCES

PhD THESIS

Estimation of Actual Evapotranspiration Using Remote Sensing Techniques and Energy Balance Models in the Lower Seyhan Plain of the Eastern Mediterranean Region of Türkiye

OMAR ALSENJAR

Advisor: Prof. Dr. Mahmut ÇETİN

Department of Agricultural Structures and Irrigation

ABSTRACT

This study provides a comprehensive analysis of estimating actual evapotranspiration (ET_a) using surface energy balance (SEB) models in the Lower Seyhan Plain (LSP) in Türkiye, encompassing both non-stressed areas (Akarsu Irrigation District, i.e., AID) and stressed areas near saline lagoons of the LSP. It evaluates the applicability of SEB models (METRIC, SEBAL, EEFlux-METRIC, and GeeSEBAL) and the $K_{c\text{-}NDVI}$ method for computing ET_a over a large irrigation scheme in four consecutive water years (2020, 2021, 2022, and 2023). Landsat data, data sets obtained from field campaigns, in-situ climatic observations from local meteorological stations within the study area, and global meteorological data were utilized to estimate ET_a by SEB models and the $K_{c\text{-}NDVI}$ method. In this study, the results of the crop classification in the AID and the ground truth data acquired from the stressed areas were used to estimate ET_a using SEB models, to evaluate the accuracy of EEFlux-METRIC and GeeSEBAL, and to investigate the relationship between NDVI and LAI for selected crops. The R-METRIC model and LandMOD ET Mapper toolbox in MATLAB facilitated robust ET_a estimation. Furthermore, spatio-temporal variations for different crop types were shown on a large scale. SEB models were validated against the ET_o-FAO model and ET_c method, focusing on metrics such as R^2, RMSE, MAE, and agreement index (d) to assess model performance. The findings demonstrate strong agreement between ET_a estimates from SEB models and ET_o-FAO, ET_c methods, with the METRIC model showing slightly better performance than the SEBAL algorithm. The $K_{c\text{-}NDVI}$ method demonstrated a stronger correlation with the ET_c method during the mid-growth stages of crops, with a Pearson correlation coefficient (r) ranging from 0.67 to 0.99 and RMSE values between 1.30 mm day^{-1} and 0.21 mm day^{-1}, compared to the initial and harvesting stages in the AID throughout the water years 2020-2023. The proposed equations ($ET_{a\text{-}METRIC}$-ET_o, $ET_{a\text{-}EEFlux}$-ET_o, $ET_{a\text{-}SEBAL}$-ET_o, $K_{c\text{-}NDVI}$, LAI-NDVI) have the potential to apply and generalize to different crop types in semi-arid regions worldwide.

Keywords: Evapotranspiration, Remote sensing (RS), Surface energy balance models, Artificial neural network (ANN), Lower Seyhan Plain (LSP).

ÇUKUROVA ÜNİVERSİTESİ
FEN BİLİMLERİ ENSTİTÜSÜ

DOKTORA TEZİ

Uzaktan Algılama Teknikleri ve Enerji Dengesi Modelleri Kullanılarak Gerçek Evapotranspirasyon Tahmini : Aşağı Seyhan Ovası'nda Bir Uygulama

---

OMAR ALSENJAR

Danışman: Prof. Dr. Mahmut ÇETİN

Tarımsal Yapılar ve Sulama Anabilim Dalı

ÖZ

Bu çalışma, Türkiyee'nin *Aşağı Seyhan Ovası*'nda (ASO) yüzey enerji dengesi (SEB) modellerini kullanarak gerçek buharlaşma-terleme (ET_a) tahminine yönelik kapsamlı bir analiz sunmakta, hem stres altında olmayan alanları (Akarsu Sulama Bölgesi, yani ASB) hem de ASO'daki tuzlu lagünler yakınındaki stres altındaki alanları kapsamaktadır. SEB modellerinin (METRIC, SEBAL, EEFlux-METRIC ve GeeSEBAL) ve $K_{c\text{-}NDVI}$ yönteminin dört ardışık su yılı (2020, 2021, 2022 ve 2023) süresince büyük bir sulama şebekesi üzerinde gerçek evapotranspirasyonu (ET_a) hesaplamadaki uygulanabilirliği değerlendirilmektedir. SEB modelleri ve $K_{c\text{-}NDVI}$ yöntemiyle ET_a'yı tahmin etmek için Landsat verileri, arazi çalışmalarıyla elde edilen veri setleri, çalışma alanındaki yerel meteoroloji istasyonlarından alınan yerinde iklim gözlemleri ve küresel meteorolojik veriler kullanılmıştır. Bu çalışmada, ASB'deki bitki sınıflandırma sonuçları ve stresli alanlardan elde edilen yer gözlem verileri, SEB modelleri kullanılarak ET_a'yı tahmin etmek, EEFlux-METRIC ve GeeSEBAL'in doğruluğunu değerlendirmek ve seçilen bitkiler için NDVI ile LAI arasındaki ilişkiyi incelemek amacıyla kullanılmıştır. R-METRIC modeli ve MATLAB'deki LandMOD ET Mapper araç kutusu, ET_a tahminini kolaylaştırmıştır. Ayrıca, farklı bitki türleri için mekansal ve zamansal değişiklikler büyük ölçekte gösterilmiştir. SEB modellerinin model performansını değerlendirmek amacıyla ET_o-FAO modeli ve ET_c yöntemi ile karşılaştırılarak R^2, RMSE, MAE ve uyum indeksi (d) gibi metrikleri kullanılarak doğrulanma yapılmıştır. Bulgular, SEB modellerinden elde edilen ET_a tahminleri ile ET_o-FAO ve ET_c yöntemleri arasında güçlü bir uyum olduğunu göstermiştir. Ayrıca, METRIC modelinin, SEBAL algoritmasından daha iyi performans gösterdiği saptanmıştır. $K_{c\text{-}NDVI}$ yöntemi, 2020-2023 su yıllarını kapsayan dönemde ASB'deki bitkilerin başlangıç ve hasat dönemlerine kıyasla, orta büyüme evrelerinde ET_c yöntemi ile daha güçlü bir korelasyon göstermiştir. Pearson korelasyon katsayısı (r) 0.67 ile 0.99 arasında değişirken, RMSE değerleri 1.30 mm gün^{-1} ile 0.21 mm gün^{-1} arasında gerçekleşmiştir. Önerilen denklemler ($ET_{a\text{-}METRIC}$-ET_o, $ET_{a\text{-}EEFlux}$-ET_o, $ET_{a\text{-}SEBAL}$-ET_o, $K_{c\text{-}NDVI}$, LAI-NDVI) dünya genelindeki yarı kurak bölgelerde farklı bitki türlerine uygulanma ve genelleştirilme potansiyeline sahiptir.

Anahtar Kelimeler: Buharlaşma-terleme, Uzaktan algılama (UA), Yüzey enerjisi denge (SEB) modelleri, Yapay sinir ağı (YSA), Aşağı Seyhan Ovası (ASO).

EXTENDED SUMMARY

In recent decades, the availability of freshwater resources has been increasingly limited due to the growing demands of agricultural practices and the impacts of climate change in semi-arid regions of the world. Türkiye, as a Mediterranean country, has experienced a reduction in water resources, particularly in the Lower Seyhan Plain (LSP) (Cetin et al., 2020). Given the importance of the LSP as a highly productive agricultural area in Türkiye, where a variety of crops, including citrus, saplings, wheat, and both first and second crops of corn, cotton, soybeans, and peanuts are cultivated, precise ET_a estimation is crucial for optimal field-scale irrigation water management. Remote sensing (RS) techniques offer the capability to estimate actual evapotranspiration (ET_a) with high spatial and temporal resolution across extensive irrigation areas. This study utilizes RS-based actual evapotranspiration models to compute ET_a for crops using Landsat images coupled with in-situ climatic data, as well as global datasets at large irrigation schemes. Also, this study encompasses both non-stressed areas (9,495 ha in the Akarsu District Irrigation, known as AID) and stressed areas (53,000 ha) near saline lagoons in the LSP of Türkiye during the 2020-2023 water years.

Over the past few decades, several models have been utilized to compute ETa using RS data, with surface energy balance (SEB) models particularly prominent. SEB models can show spatial and temporal variations of the crop-based ET_a values across extensive regions, offering a significant advantage over point-scale measurements like those obtained from lysimeters and eddy covariance systems.

In this research, SEB models utilizing RS techniques were used for ET_a estimation, including the Surface Energy Balance Algorithm for Land (SEBAL) developed by Bastiaanssen et al. (1998a), and Mapping Evapotranspiration at High Resolution with Internalized Calibration (METRIC) introduced by Allen et al. (2007a), among others. The study applied standard METRIC and SEBAL models to estimate ET_a based on local climatic data coupled with RS data over the two regions of the LSP of Türkiye for the water years of 2020-2023. The EEFlux-METRIC and GeeSEBAL platforms were also utilized to estimate ET_a in the study area for the water years 2020, 2021, 2022, and 2023. These platforms leverage Landsat data stored in the cloud through the Google Earth Engine environment. Additionally, global datasets such as CFSV2 with a spatial resolution of 4 km × 4 km and ERA5 with a spatial resolution of 9 km × 9 km were integrated into that platform for estimating ET_a.

These SEB models require extensive input data, such as climatic and RS data, and necessitate expert users proficient in handling RS techniques for ET_a estimations. Therefore, an alternative approach was employed, which involves using the relationship between the Normalized Difference Vegetation Index (NDVI) and standard crop coefficient (K_c) as outlined by TAGEM-(General Directorate of Agricultural Research and Policies) –DSI, i.e., State Hydraulic Works (2017). This method generates a modified K_c, multiplied by the reference evapotranspiration (ET_o), to estimate

ET_a, utilizing the established $K_{c\text{-}NDVI}$ relationship. ET_a was assessed by comparing the $K_{c\text{-}NDVI}$ approach with SEB models (METRIC and SEBAL), and these were evaluated against reference evapotranspiration (ET_o) and ET_c methods for various crop types at the time of satellite overpass. Additionally, the research compared ET_a estimates using the METRIC model for crops such as wheat, citrus, and both first and second-crop types of cotton, corn, soybean, and peanut in non-stressed areas (AID) and stressed areas near saline lagoons of the LSP. The relationship between the Leaf Area Index (LAI) and NDVI was also assessed using the METRIC model to determine crop health status for different crops in the AID at the time of the satellite overpass.

Crop classification was conducted using the Artificial Neural Network (ANN) model through supervised classification in the Environment for Visualizing Images (ENVI) software. This classification process utilized ground truth data combined with high-resolution remote sensing (RS) data for crops in the AID of the LSP from 2020 to 2023. Similarly, ground truth data on cultivated crops were used to classify the crop types located near the saline lagoons of the Lower Seyhan Plain (LSP) during the study period. This approach significantly enhanced the interpretation of ET_a results obtained from SEB models, ET_c, and $K_{c\text{-}NDVI}$ methods in the study area. The performance of the METRIC model, standard SEBAL models, EEFlux, and GeeSEBAL platforms was evaluated in non-stressed areas. At the same time, METRIC and EEFlux were specifically assessed in stressed areas during satellite overpasses. Moreover, the METRIC model was applied to examine the differences in ET_a estimation for various crops between the non-stressed and stressed areas of the LSP. Additionally, the evaporation of saline lakes was estimated using the METRIC model when the satellite passed over the study area. Evaluation metrics—including Root Mean Square Error (RMSE), Mean Absolute Error (MAE), Coefficient of Determination (R^2), and Willmott's Index of Agreement (d)—were performed to evaluate actual evapotranspiration (ET_a) estimated by SEB models and the $K_{c\text{-}NDVI}$ method against ET_c estimated by the "two-step" procedure for some crops such as corn, cotton, soybean, peanut and over the AID. These metrics were used to compare the performance of models like METRIC, SEBAL, and $K_{c\text{-}NDVI}$ methods against the ET_c method, serving as the reference.

Classified crop maps were produced based on field visit data combined with RS data, utilizing the ANN approach and achieving high overall accuracy in the AID for the years 2020-2023. For example, in 2021, certain crops such as lettuce, potato, sesame-II, palm, and watermelon achieved 100% estimation accuracy, while onion and wheat exceeded 90%. Crops like citrus, first and second crops of cotton, soybean, peanut, and corn achieved over 77% accuracy, except for fruits, where discrepancies occurred due to shape similarities or coverage features with citrus orchards. Moreover, this misclassification likely arises because deciduous fruit trees, such as apples, pomegranates, and peaches, and very young citrus saplings often share similar land characteristics, such as bare soil, during the winter months. The ANN model under supervised classification proved to be a robust tool for high-accuracy crop-type classification in the AID throughout the water years 2020-2023. Conversely, ground truth data collected through field observations of each crop were used to identify the types of crops grown in stressed regions of the LSP and to estimate their actual evapotranspiration (ET_a). This data also offered additional validation of stress factors such as salinity, alkalinity, and rising groundwater levels throughout the stressed areas of the LSP, significantly enhancing the overall value of the research.

The study demonstrated a strong correlation between actual evapotranspiration estimates obtained using the METRIC model and the ET_o by the FAO-PM model during satellite overpasses in both non-stressed (NSA) and stressed areas (SA) of the Lower Seyhan Plain. Evaluation metrics, such as correlation coefficients and RMSE, indicated a consistent agreement between the METRIC and SEBAL models relative to the ET_c method in NSA (AID) over the period from 2020 to 2023. Differences in annual ET_a estimates between the METRIC, SEBAL models, and the ET_c method were attributed to the latter's use of reference K_c values based on normal crop conditions, whereas RS-based models capture actual field conditions. The EEFlux-METRIC and GeeSEBAL models showed limitations in correcting scan line errors, particularly in Landsat 7 data, unlike standard models that address these errors beforehand. ET_a values from EEFlux-METRIC and GeeSEBAL models can serve as reliable ET_a references, particularly when local climatic data is lacking.

This study estimated actual evapotranspiration (ET_a) using the METRIC model implemented through two distinct tools. The first tool, the LandMOD ET Mapper toolbox in MATLAB, supports all types of Landsat satellites (7, 8, and 9) as well as moderate-resolution imaging spectroradiometer (MODIS) data. The second tool, the R-METRIC model, available within the water package of the R programming language, is designed specifically for Landsat 7 and 8 data. Specific dates were selected for analysis to compare the ET_a results obtained from these tools, including September 9, 2021 (Day of Year, i.e., DOY 190) and October 21, 2021 (DOY 294). The results from both tools were nearly identical. However, variations were negligible between the LandMOD ET Mapper and R-METRIC model results, likely due to differences in climatic data requirements and the types of Landsat data utilized by each model. The R-METRIC model typically uses data from a single weather station, averaging climatic parameters from a network or subdividing the area to estimate ET_a for each sub-area before merging the results. However, this study did not apply the latter method, finding it unnecessary. Instead, the LandMOD ET mapper in MATLAB incorporated multiple weather stations using interpolation methods for variables like solar radiation, temperature, wind speed, and relative humidity. Although the ET_a estimates from the R-METRIC model and the LandMOD ET mapper were similar, the LandMOD process is more time-intensive, especially during data preparation and interpolation using techniques like Inverse Distance Weighting (IDW). The LandMOD ET mapper is user-friendly, allowing one-click ET_a estimation using METRIC and SEBAL models. In contrast, R-METRIC only supports METRIC but offers more detailed control over inputs and outputs, with visibility into each processing step and additional results, such as NDVI, LAI, albedo, and various heat fluxes. While the LandMOD ET mapper lacks step-by-step transparency, it generates combined K_c maps for METRIC and SEBAL models and supports Landsat and MODIS data. One significant advantage of LandMOD ET in MATLAB is its compatibility with a broader range of data sources, including Landsat 9 and UAVs, whereas R-METRIC is limited to Landsat 7 and 8 data. This difference, particularly in handling Landsat 9 data, is crucial to the research. Despite their differences, both tools effectively estimate ET_a using the METRIC model for the Lower Seyhan Plain and other global regions.

The METRIC model demonstrated its capability to estimate ET_a for mixed intercropping. It remains a common practice in citrus plantations in the LSP, such as combinations involving saplings with watermelon and saplings with cabbage, offering valuable insights. This model provided valuable insights by demonstrating that mixed intercropping had higher ET_a values than orchards consisting solely of saplings during the same period. Furthermore, the METRIC model estimated evaporation (E) from saline lagoons and ET_a from pasture areas and agricultural fields adjacent to lagoons during satellite overpasses, uncovering significant spatiotemporal variations. Determination of these changes is challenging to capture comprehensively using traditional methods on a large scale.

In this study, ET_a estimated by the METRIC and SEBAL (via Python, i.e., PySEBAL) models were compared to ET_a measurements from a lysimeter for the second crop type, soybean (soybean-II), at a 0.12-hectare field located in the Research Fields of the Agricultural Structures and Irrigation Department at Cukurova University in 2009. For DOY 197 (July 16, 2009), the ET_a values estimated by the METRIC model were 2.53 mm day^{-1}, and for DOY 213 (August 1, 2009), they were 2.81 mm day^{-1}. In contrast, lysimeter measurements for these dates showed ET_a values of 2.9 mm day^{-1} and 2.5 mm day^{-1}, respectively. Similarly, Sawadogo et al. (2020) reported PySEBAL-derived ET_a values of 2.3 mm day^{-1} and 3.1 mm day^{-1} for the same pixel on the corresponding dates. Thus, the ET_a outcomes for soybean-II using the METRIC model exhibited superior performance compared to those derived from the PySEBAL model when validated against lysimeter measurements. The ET_a estimates from SEB models were compared with those derived using a "two-step" ET_c method through a simple linear regression model. To assess the performance of the SEB models and the $K_{c\text{-}NDVI}$ approach, key metrics such as RMSE, MAE, R^2, and the Willmott index of agreement (d) were calculated. These indicators were used to evaluate the accuracy of METRIC, SEBAL, and $K_{c\text{-}NDVI}$, with the ET_c method as the reference. Statistical analysis of ET_a demonstrated robust agreement among the METRIC, SEBAL, and $K_{c\text{-}NDVI}$ methods with ET_c across various crops, encompassing wheat, citrus, and first and second crops of cotton, corn, soybean, and peanut. The $K_{c\text{-}NDVI}$ method demonstrated a stronger correlation with the ET_c method during the mid-growth stages, with a Pearson correlation coefficient (r) ranging from 0.67 to 0.99 and RMSE values between 1.30 mm day^{-1} and 0.21 mm day^{-1}, compared to the initial and harvesting stages. Furthermore, the suggested $K_{c\text{-}NDVI}$ equations, formulated based on the relationship between reference K_c and NDVI for specific crops, can be universally applied by researchers and stakeholders. This provides an adapted method for estimating ET_a that differs from the ET_c method. It is a promising methodology and suitable for use in this region and analogous Mediterranean regions worldwide.

A key finding of this thesis is the development of a regional ET_a estimation model based on the METRIC approach, specifically applied to a citrus plantation in Cotlu village within the AID. The Cotlu field was chosen due to its proximity to the Cotlu meteorological station. It was analyzed to assess how well the ET_a estimates for citrus in this field represent ET_a across all citrus crops in the AID. Linear regression analysis and key metrics such as r, RMSE, MAE, and d were employed. The highest accuracy was found when comparing $ET_{a\text{-}METRIC}$ for citrus near Cotlu with the mean $ET_{a\text{-}METRIC}$ for citrus in the AID under non-stressed conditions, showing a strong correlation (r = 0.91), low error (RMSE = 0.54 mm day^{-1}, MAE = 0.40 mm day^{-1}), and excellent agreement (d = 0.95). The proposed equation ($ET_{a\text{-}METRIC\text{-}AID} = 0.8615 \times ET_{a\text{-}METRIC\text{-}Cotlu} + 0.2662$) can be used to estimate ET_a for all citrus crops in the AID once ET_a for the Cotlu field is determined using METRIC. This method provides a reliable approach for calculating citrus ET_a across the Lower Seyhan Plain under varying conditions. Statistical evaluations were also performed to compare ET_a values estimated by the METRIC model between non-stressed ($ET_{a\text{-}METRIC\text{-}NSA}$) and stressed areas ($ET_{a\text{-}METRIC\text{-}SA}$) for specific crops in the Lower Seyhan Plain (LSP) during satellite overpasses in the 2020 and 2023 growing seasons. In the LSP of Türkiye, the METRIC model has proven highly reliable for estimating ET_a across various conditions, including non-stressed areas in the AID and stressed regions near the eastern Mediterranean coast. Saplings achieved the lowest RMSE (0.61 mm day^{-1}) and MAE (0.47 mm day^{-1}) among the crops, indicating precise ET_a estimates in the AID and stressed areas. Cotton-I displayed the highest R^2 (0.96) and Pearson correlation coefficient (r = 0.98), indicating very accurate ET_a estimates despite slightly higher RMSE (1.10 mm day^{-1}) and MAE (0.98 mm day^{-1}) values compared to other crops. Wheat, citrus, and corn also showed strong correlations between non-stressed and stressed area estimates, with low error values, reinforcing the model's accuracy for these crops. However, soybean-II had a lower correlation (r = 0.81) and R^2 (0.65) between $ET_{a\text{-}METRIC\text{-}NS}$ and $ET_{a\text{-}METRIC\text{-}S}$ areas, though it still achieved a relatively low RMSE (0.72 mm day^{-1}) among soybean varieties, indicating acceptable precision. Variations in model performance are attributed to crop type, irrigation methods, and local climate. Overall, the METRIC model's capacity to estimate ET_a accurately plays a crucial role in optimizing water resource management in water-scarce regions like the LSP. Additionally, this study explored the relationship between the average Leaf Area Index (LAI) and the average Normalized Difference Vegetation Index (NDVI) for selected crops during satellite overpasses within the Akarsu Irrigation District (AID). The findings revealed that the NDVI–LAI relationship follows an exponential (growth) model, fitting average NDVI (denoted as independent variable) with average LAI (denoted as a dependent variable) for specific crops (first and second crops of corn, cotton, soybean, peanut as well as wheat) across the AID. The resulting equations from this relationship can be widely utilized to assess vegetation cover, estimate production, and calculate LAI without needing the METRIC model, which requires more inputs and specialized expertise. By identifying NDVI and applying the proposed equations, LAI can be easily estimated for a variety of plant types over large-scale irrigation areas, even under different vegetation cover conditions.

The application of remote sensing (RS)--based ET_a models and the $K_{c\text{-}NDVI}$ approach showed strong agreement with ET_o from the FAO-PM and ET_c methods throughout the study area. For large-scale regions, RS-based models like METRIC and SEBAL effectively estimated ET_a for different crops across various growth stages, providing high spatial resolution in the flat terrain of semi-arid environments. The ET_a maps generated by the RS-based ET_a models (METRIC and SEBAL) can serve as valuable input for a better understanding of agricultural hydrology processes and for managing water resources at the catchment scale. Additionally, it can be concluded that the METRIC and SEBAL algorithms are highly suitable tools for assessing actual evapotranspiration, with results that can inform agricultural planning and water management in arid and semi-arid regions worldwide.

GENİŞLETİLMİŞ ÖZET

Son yıllarda, dünya üzerindeki yarı kurak bölgelerde tarımsal uygulamalardaki artan talepler ve iklim değişikliğinin etkileri nedeniyle tatlı su kaynaklarının mevcudiyeti giderek sınırlı hale gelmiştir. Türkiye, bir Akdeniz ülkesi olarak, özellikle Aşağı Seyhan Ovası'nda (ASO) su kaynaklarında azalma yaşamıştır (Cetin ve ark., 2020). ASO'nın Türkiye'de narenciye, fidan, buğday, mısır, pamuk, soya ve yer fıstığı gibi tarımsal ürünlerin yetiştirildiği yüksek verimli bir tarım alanı olarak önemi göz önüne alındığında, doğru gerçek evapotranspirasyon ET_a tahmini optimal arazi ölçeğinde sulama suyu yönetimi için kritik öneme sahiptir. Uzaktan algılama (UA) teknikleri, büyük ölçekli sulama şebekelerinde yüksek mekânsal ve zamansal çözünürlükle ET_a tahminleri sağlayabilir. Bu çalışma büyük ölçekli bir sulama şebekesinde, Landsat görüntüleri ile yerel iklim verileri ve UA veri setlerini birleştirerek, bitkiler için ET_a hesaplamak amacıyla UA tabanlı gerçek evapotranspirasyon modellerini kullanmaktadır. Çalışma, 2020-2023 su yıllarını kapsayan periyotta Türkiye'deki ASO'da tuzlu lagünlere yakın stresli alanları (53,000 ha) ve Akarsu Sulama Bölgesi (ASB) olarak bilinen stressiz alanları (9,495 ha) kapsamaktadır.

ET_a hesaplamak için UA verileri kullanılan çeşitli modeller bulunmaktadır. Modeller içerisinde özellikle yüzey enerji dengesi (SEB) modelleri öne çıkmaktadır. SEB modelleri, geniş bölgelerde bitki bazlı ET_a değerlerinin mekânsal ve zamansal değişimlerini gösterebilmektedir. Lizimetre ve eddy covariance gibi noktasal ölçüm yapan sistemlere göre önemli bir avantaj sağlamaktadır. Bu araştırmada, UA verileri kullanılarak uygulanan SEB modelleri, ET_a tahminleri için kullanılmıştır. Modeller arasında, Bastiaanssen ve ark. (1998a) tarafından geliştirilen 'Yüzey Enerji Denge Algoritması (SEBAL) ile Allen ve ark. (2007a) tarafından önerilen 'İçselleştirilmiş Kalibrasyonlu Yüksek Çözünürlüklü Evapotranspirasyon Haritalama (METRIC)' bulunmaktadır. Çalışmada Türkiye'nin güneyinde yer alan ASO'daki iki bölgede, 2020-2023 su yıllarını kapsayan dönemde ET_a'yı tahmin etmek amacıyla, yerel iklim verileri ile UA verilerini birleştirerek standart METRIC ve SEBAL modelleri kullanılmıştır. Çalışma alanında 2020, 2021, 2022 ve 2023 su yıllarına ait ETa tahminleri için EEFlux-METRIC ve GeeSEBAL platformları da kullanılmıştır. Her iki platformda, Google Earth Engine ortamı aracılığıyla bulutta depolanan Landsat veri setlerini kullanmaktadır. Ayrıca, ET_a tahminleri için söz konusu platformlara sırasıyla 4 km × 4 km ve 9 km × 9 km mekânsal çözünürlüğe sahip CFSV2 ve ERA5 gibi küresel veri setleri de entegre edilmiştir. Araştırmada kullanılan SEB modelleri, iklim verileri ve UA verileri gibi geniş kapsamlı girdi setlerine ihtiyaç duymaktadır. Bunun yanı sıra, ET_a tahminlerinde UA tekniklerinin etkin bir şekilde kullanılabilmesi için uzman kullanıcıların katkısına da gereksinim duyulmaktadır. Bu nedenle, alternatif bir yaklaşım olarak Tarımsal Araştırmalar ve Politikalar Genel Müdürlüğü (TAGEM), Devlet Su İşleri (DSI, 2017) tarafından önerilen Normalleştirilmiş Fark Bitki İndeksi (NDVI) ile standart bitki katsayısı (K_c) arasındaki ilişki kullanılmıştır. Bu yöntem, belirlenen $K_{c\text{-NDVI}}$ ilişkisinden yararlanarak, referans evapotranspirasyon (ET_o) ile çarpılan, modifiye bir K_c üreterek ET_a'yı tahmin etmektedir. ET_a, $K_{c\text{-}NDVI}$ yaklaşımının SEB modelleri (METRIC ve SEBAL) ile karşılaştırılması yoluyla yorumlanmıştır. Bu modeller, uydu geçişi tarihlerinde çeşitli bitki türleri için referans evapotranspirasyon (ET_o) ve ET_c yöntemlerine göre değerlendirilmiştir. Ayrıca araştırmada buğday ve narenciye ile birinci ve ikinci ürün olarak yetiştiriciliği yapılan pamuk, mısır, soya, yer fıstığı gibi tarımsal ürünler için ET_a tahminleri yapılmıştır. Bu çalışmalara ek olarak, ASO'daki farklı bitkiler için bitki sağlık durumunu belirlemek amacıyla uydu geçiş tarihlerinde Yaprak Alan İndeksi (LAI) ile NDVI arasındaki ilişki de METRIC modeli kullanılarak değerlendirilmiştir. ET_a tahminleri, METRIC model ile stresli alanlar (ASO, tuzlu lagünlere yakın bölgeler) ile ASB'de yer alan stressiz alanlar arasında bir karşılaştırma yapılarak uygulanmıştır.

Bitki sınıflandırması, ENVI yazılımı aracılığı ile Yapay Sinir Ağı (YSA) modeli kullanılarak gerçekleştirilmiştir. Bu sınıflandırma işlemi 2020-2023 yılları arasında ASO'daki ASB'de bulunan bitkiler için, yer gözlem verileri ile yüksek çözünürlüklü UA verilerinin birleştirilmesi ile yapılmıştır. Ayrıca, aynı çalışma döneminde ASO'daki tuzlu lagünlere yakın bulunan her bitki türünü farklı gruplara ayırmak için, yetiştirilen bitkilere ait yer gözlem verileri de kullanılmıştır. Bu yaklaşım, çalışma alanında SEB modelleri, ET_c ve $K_{c\text{-}NDVI}$ yöntemleriyle elde edilen ET_a sonuçlarının yorumlanmasına önemli ölçüde katkı yapmıştır. METRIC modelinin, standart SEBAL modellerinin, EEFlux ve GeeSEBAL platformlarının performansı, stressiz alanlarda değerlendirilmiştir. Aynı zamanda, METRIC ve EEFlux, uydu geçiş tarihleri için stresli alanlarda da özel olarak değerlendirilmiştir. Ayrıca METRIC modeli, ASO'nın stressiz ve stresli alanları arasında çeşitli bitkiler için ET_a tahminindeki farklılıkları incelemek amacıyla uygulanmıştır. Tuzlu göllerin buharlaşması, uydunun çalışma alanının üzerinden geçtiği tarihler için METRIC modeli kullanılarak ayrıca tahmin edilmiştir. SEB modelleri ve $K_{c\text{-}NDVI}$ yöntemiyle tahmin edilen gerçek evapotranspirasyonu (ET_a), "iki aşamalı" prosedürle tahmin edilen ET_c ile karşılaştırmak amacıyla ASB'de yetiştirilen mısır, pamuk, soya ve yer fıstığı gibi bazı tarımsal ürünler için değerlendirilmiştir. Değerlendirme ölçütü olarak —Kök Ortalama Kare Hatası (RMSE), Ortalama Mutlak Hata (MAE), Determinasyon Katsayısı (R^2) ve Willmott Uyum İndeksi (d) gibi çeşitli istatistik bilgileri hesaplanmıştır. Bu değerlendirme ölçütleri METRIC, SEBAL ve $K_{c\text{-}NDVI}$ yöntemleri gibi modellerin performansı ET_c yöntemine kıyasla analiz edilmiş ve referans olarak kullanılmıştır.

Sınıflandırılmış bitki haritaları, yer gözlem verileri ile UA verileri birleştirilerek, ANN modeli uygulanarak 2020-2023 yılları için ASB'de yüksek genel doğrulukla üretilmiştir. Örneğin, 2021 yılında marul, patates, ikinci ürün susam, palmiye ve karpuz gibi bazı bitkiler %100 tahmin doğruluğu ile elde edilmiştir. Buna karşın, soğan ve buğday %90 ve üzerinde bir doğrulukla sınıflandırılmıştır. Diğer yandan narenciye, birinci ve ikinci ürün pamuk, soya, yer fıstığı ve mısır gibi bitkiler %77'den fazla doğrulukla tahmin edilerek sınıflandırılmıştır. Ancak meyve bahçelerinin sınıflandırılmasında, narenciye bahçeleriyle şekil benzerlikleri veya örtüşme özellikleri nedeniyle uyumsuzluklar yaşanmıştır. Bu uyumsuz sınıflandırmanın elma, nar ve şeftali gibi kış aylarında yaprak döken meyve ağaçları ile çok genç narenciye fidanlarının sıklıkla çıplak toprak gibi benzer arazi özelliklerini taşımasından kaynaklandığı düşünülmektedir. Denetimli sınıflandırma altında ANN modeli, 2020-2023 su yılları boyunca ASB'de yüksek doğrulukta, bitki türü sınıflandırması için güvenilir bir araç olduğunu kanıtlamıştır. Her bitki için araziden alınan yer gözlem verileri, ASO'nın stresli bölgelerinde yetiştirilen bitki türlerini belirlemek ve bunların gerçek evapotranspirasyon (ET_a) değerlerini tahmin etmek için kullanılmıştır. Bitkiler için araziden alınan yer gözlemlerine ek olarak, ASO'nın tuzluluk, alkalilik ve yüksek taban suyu seviyesi gibi stres faktörlerinin olduğu bölgelere ait verilerinde alınmış olması ek bir doğrulama sağladığından, araştırmanın genel değerini önemli ölçüde arttırmıştır.

Çalışma, uydu geçiş tarihlerinde METRIC modeli kullanılarak elde edilen gerçek evapotranspirasyon tahminleri ile FAO-PM modeli tarafından belirlenen ET_o arasında hem ASB'deki stressiz hem de ASO'nın stresli bölgelerinde güçlü bir korelasyon olduğunu göstermiştir. Değerlendirme ölçütlerinden korelasyon katsayıları ve RMSE gibi göstergeler, 2020-2023 döneminde METRIC ve SEBAL modelleri ile ET_c yöntemi arasında ABS'de tutarlı bir uyum olduğunu göstermiştir.

METRIC ve SEBAL modelleri ile ET_c yöntemi arasında yıllık ET_a tahminlerinde farklılıklar olduğu belirlenmiştir. Bu farklılıkların temel nedeni, ET_c yönteminin normal bitki koşullarına dayalı referans K_c değerlerini kullanmasından kaynaklanmış olabileceği düşünülmektedir. Buna karşın UA tabanlı modellerle kestirilen ET_a değerleri, gerçek arazi koşullarını yansıttığından daha temsili olarak değerlendirilmiştir. EEFlux-METRIC ve GeeSEBAL modelleri, özellikle Landsat 7 verilerinde tarama hattı hatalarını düzeltmede sınırlamalar göstermiştir. Oysaki standart modeller bu hataları önceden düzeltebilmektedir. EEFlux-METRIC ve GeeSEBAL modellerinden elde edilen ET_a değerleri özellikle yerel iklim verilerinin eksik olduğu durumlarda güvenilir ET_a değerleri olarak kullanılabilir.

Bu çalışma, gerçek evapotranspirasyonu iki farklı araç yardımıyla METRIC modeli kullanarak tahmin etmiştir. İlk araç MATLAB içindeki LandMOD ET haritalayıcısıdır. Landsat uydularının tüm türlerini (7, 8, 9) ve orta çözünürlüklü görüntüleme spektroradyometre (MODIS) verilerini desteklemektedir. R programlama dilinin su paketi içerisinde yer alan ikinci araç R-METRIC modelidir. Landsat 7 ve 8 verileri için özel olarak tasarlanmıştır. Bu araçlardan elde edilen ET_a sonuçlarını karşılaştırmak için 9 Eylül 2021 (Yılın Günü, yani DOY 190) ve 21 Ekim 2021 (DOY 294) dahil olmak üzere belirli tarihler analiz için seçilmiştir. Her iki araç kullanılarak elde edilen sonuçlar neredeyse aynı bulunmuştur. LandMOD ET Mapper ve R-METRIC model sonuçları arasındaki farklılıkların, her modelin iklim verisi gereksinimleri ve Landsat veri türlerindeki farklılıklarından kaynaklandığı ancak bu farklılıkların önemsiz düzeyde olduğu değerlendirilmektedir. R-METRIC modeli genellikle tek bir hava istasyonundan veri kullanır, iklim parametrelerini bir ağdan ortalayarak veya alanı alt bölgelere ayırarak her alt bölge için ET_a tahmin edecek şekilde sonuçları birleştirir. Ancak bu çalışmada ikinci yöntem gerekli olmadığından uygulanmamıştır. İkinci yöntem yerine MATLAB'deki LandMOD ET Mapper, güneş radyasyonu, sıcaklık, rüzgâr hızı ve bağıl nem gibi değişkenler için enterpolasyon yöntemleri kullanarak birden fazla hava istasyonunu dahil etmiştir. R-METRIC modeli ve LandMOD ET Mapper'dan elde edilen ET_a tahminleri benzer olmakla birlikte, LandMOD süreci özellikle veri hazırlığı ve Ters Mesafe Ağırlığı (IDW) gibi teknikler kullanılarak yapılan enterpolasyon sırasında daha fazla zaman gerektirmektedir. LandMOD ET Mapper, METRIC ve SEBAL modelleri, tek bir komut ile ET_a tahmini yapma imkânı sunmaktadır. Buna karşın R-METRIC yalnızca METRIC metodolojisini desteklemektedir. Girdi ve çıktılar üzerinde daha ayrıntılı kontrol sunmakla birlikte kullanıcıya her işlem adımını görme imkânı da vermektedir. Buna ek olarak NDVI, LAI, albedo ve çeşitli ısı akıları gibi ek sonuçları da sağlayabilmektedir. LandMOD ET Mapper, adım adım şeffaflık sağlamamasına rağmen METRIC ve SEBAL modelleri için birleştirilmiş K_c haritaları üretme konusunda başarılıdır ve Landsat ile MODIS verilerini de desteklemektedir. MATLAB'daki LandMOD'un önemli bir avantajı Landsat 9 ve İHA'lar gibi daha geniş bir veri kaynağı kullanılmasına imkân sağlamaktadır. Buna karşın R-METRIC, yalnızca Landsat 7 ve 8 verileriyle sınırlıdır. Bu fark özellikle Landsat 9 verilerini işleme konusunda araştırma için çok önemlidir. Farklılıklarına rağmen her iki araç da METRIC modelini kullanarak ASO ve diğer küresel bölgelerde ET_a'yı etkili bir şekilde tahmin etmektedir.

METRIC modeli, ASO'daki narenciye plantasyonlarında, fidanlarla karpuz veya fidanlarla lahana gibi kombinasyonları içeren karışık ekim uygulamaları için ET_a tahmin etme yeteneğini göstererek değerli bilgiler sunmuştur. Bu model, karışık ürün yetiştirilen narenciye fidan parsellerinde aynı dönemde yalnızca fidanlardan oluşan bahçelere kıyasla daha yüksek ET_a değerleri tahmin ederek arazideki fiili durumu yansıtan önemli bir detay sunmuştur. Ayrıca METRIC modeli, uydu tarihlerinde tuzlu lagünlerden buharlaşmayı (E) ve lagünlere bitişik meralar ile tarım alanlarından ET_a'yı tahmin ederek önemli mekânsal ve zamansal değişimleri ortaya çıkartmıştır. Bu değişimlerin büyük ölçeklerde kapsamlı bir şekilde geleneksel yöntemler kullanılarak belirlenmesi güçtür.

Bu çalışmada, METRIC ve SEBAL (Python aracılığıyla, yani PySEBAL) modelleriyle tahmin edilen ET_a, 2009 yılında Çukurova Üniversitesi Tarımsal Yapılar ve Sulama Bölümü Araştırma Alanlarında bulunan, 0.12 hektar büyüklüğündeki bir alanda ikinci ürün soya bitkisi için bir lizimetreden elde edilen ET_a ölçümleriyle karşılaştırılmıştır. 197. gün (16 Temmuz 2009) için METRIC modeli ile tahmin edilen ET_a değerleri 2.53 mm gün^{-1}, 213. gün (1 Ağustos 2009) için ise 2.81 mm gün^{-1} olarak belirlenmiştir. Buna karşın, bu tarihlerde lizimetre ölçümleri sırasıyla 2.9 mm gün^{-1} ve 2.5 mm gün^{-1} ET_a değerleri göstermiştir. Benzer şekilde, Sawadogo ve ark. (2020) aynı tarihlerde aynı piksel için PySEBAL tarafından türetilen ET_a değerlerini 2.3 mm gün^{-1} ve 3.1 mm gün^{-1} olarak rapor etmiştir. METRIC modeli kullanarak ikinci ürün soya için ET_a çıktıları lizimetre ölçümlerine karşı doğrulandığında ve PySEBAL modelinden elde edilen veriler ile karşılaştırıldığında daha üstün performans sergilediği söylenebilmektedir. SEB modellerinden elde edilen ET_a tahminleri, "iki adımlı" ET_c yöntemi kullanılarak türetilenlerle basit bir doğrusal regresyon modeli aracılığıyla karşılaştırılmıştır. SEB modellerinin ve $K_{c\text{-}NDVI}$ yaklaşımının performansını değerlendirmek için RMSE, MAE, R^2 ve Willmott uyum indeksi (d) gibi çeşitli istatistik değerlendirme ölçütleri hesaplanmıştır. Bu çeşitli istatistik verileri, METRIC, SEBAL ve $K_{c\text{-}NDVI}$'nin doğruluğunu değerlendirmek için kullanılmış ve ET_c yöntemi referans olarak alınmıştır. ET_a'nın istatistiksel analizi, METRIC, SEBAL ve $K_{c\text{-}NDVI}$ yöntemleri ile ET_c arasında, pamuk, mısır, soya, yer fıstığı, buğday ve narenciye gibi çeşitli mahsuller arasında güçlü bir uyum olduğunu göstermiştir.

$K_{c\text{-}NDVI}$ yöntemi, orta büyüme evrelerinde başlangıç ve hasat evrelerine göre ET_c yöntemi ile daha güçlü bir korelasyon olduğunu ortaya koymuştur. Pearson korelasyon katsayısı (r) 0.67 ile 0.99 arasında değişirken, RMSE değerleri 1.30 mm gün^{-1} ile 0.21 mm gün^{-1} arasında olmuştur. Ayrıca, belirli bitkiler için referans K_c ve NDVI arasındaki ilişkiyi gösteren $K_{c\text{-}NDVI}$ denklemlerinin, araştırmacılar ve paydaşlar tarafından kullanılması uygulanabilir. Bu, ET_c yönteminden farklı olarak ET_a tahmini için uyarlanmış bir yaklaşım sunmaktadır. Elde edilen sonuçlar, araştırma alanı ve Akdeniz benzeri bölgelerde kullanılmak üzere uygun ve umut verici bir metodoloji olduğuna işaret etmiştir.

Bu tezin temel bulgularından biri, ASB sınırları içerisinde yer alan Çotlu köyündeki bir narenciye plantasyonuna özel olarak uygulanan METRIC yaklaşımına dayalı bölgesel bir ET_a tahmin modelinin geliştirilmesidir. Çotlu meteoroloji istasyonuna yakınlığı nedeniyle seçilen Çotlu narenciye bahçesi, bu alandaki narenciye için ET_a tahminlerinin ASB'deki tüm narenciye alanlardaki ET_a değerlerinin ne ölçüde temsil ettiğini değerlendirmek amacıyla ayrıntılı olarak analiz edilmiştir. Bu analizde doğrusal regresyon analizi ile r, RMSE, MAE ve d gibi çeşitli istatistik değerlendirme ölçütleri kullanılmıştır. En yüksek doğruluk Çotlu yakınındaki narenciye için $ET_{a\text{-}METRIC}$ ile ASB'deki narenciye için ortalama $ET_{a\text{-}METRIC}$'in stres altında olmayan koşullarda karşılaştırıldığında bulunmuştur. Bu karşılaştırma sonucunda, güçlü bir korelasyon (r = 0.91), düşük hata (RMSE = 0.54 mm gün^{-1}, MAE = 0.40 mm gün^{-1}) ve mükemmel bir uyum (d = 0.95) bulunmuştur. Bu durum, tez metni içerisinde Şekil 4.8.1'de sunulmuştur. Önerilen denklem ($ET_{a\text{-}METRIC\text{-}ASB} = 0.8615 \times ET_{a\text{-}METRIC\text{-}Cotlu} + 0.2662$), Çotlu alanı için METRIC ile ET_a hesaplandıktan sonra, ASB'deki tüm narenciye mahsulleri için ET_a tahmini yapmak üzere kullanılabilir. Bu yöntem, farklı koşullar altında ASO'daki narenciye plantasyonlarındaki gerçek evapotranspirasyon (ET_a) değerini hesaplamak için güvenilir bir yaklaşım sunmaktadır. 2020 ve 2023 büyüme dönemlerinde uydu geçiş tarihlerinde ASO'daki belirli bitkiler için METRIC modelinin tahmin ettiği ET_a değerlerini, stres altında olmayan ($ET_{a\text{-}METRIC\text{-}NSA}$) ve stres altında olan ($ET_{a\text{-}METRIC\text{-}SA}$) alanlar arasında karşılaştırmak amacıyla istatistiksel ölçütler hesaplanmıştır. Türkiye'nin ASO'daki, METRIC modeli, ASB'deki stres altında olmayan alanlar ve Doğu Akdeniz kıyısındaki stresli bölgeler dahil olmak üzere çeşitli koşullarda ET_a'yı tahmin etmede son derece güvenilir olduğunu kanıtlamıştır. Fidanlar, ASB ve stresli alanlarda çok hassas ET_a tahminlerini göstererek, bitkiler arasında en düşük RMSE (0.61 mm gün^{-1}) ve MAE

(0.47 mm gün^{-1}) değerlerine ulaşmıştır. Birinci ürün pamuk bitkisi için, diğer bitkilere kıyasla biraz daha yüksek RMSE (1.10 mm gün^{-1}) ve MAE (0.98 mm gün^{-1}) değerleri elde edilmiş olmakla birlikte, en yüksek R^2 (0.96) ve Pearson korelasyon katsayısı (r = 0.98) elde edilerek güvenilir ET_a tahminleri yapılmıştır. Buğday, narenciye ve mısır bitkileri için stressiz ve stresli koşullarda güçlü korelasyonlar elde edilmiş olup, düşük hata değerleriyle bu bitkiler için ET_a kestirimleri yapılabilmiştir. Ancak, ikinci ürün soya bitkisi için, $ET_{a\text{-}METRIC\text{-}NSA}$ ve $ET_{a\text{-}METRIC\text{-}SA}$ alanları arasında daha düşük bir korelasyon (r = 0.81) ve R^2 (0.65) değerine sahip olmasına rağmen, soya çeşitleri arasında görece düşük bir RMSE (0.72 mm gün^{-1}) değerine ulaşarak kabul edilebilir bir hassasiyet göstermiştir. Model performansındaki farklılıklar, bitki türü, sulama yöntemleri ve yerel iklim koşullarına atfedilmiştir. Genel olarak, METRIC modelinin ET_a'yı doğru bir şekilde tahmin etme kapasitesi, ASO gibi su kıtlığı yaşayan bölgelerde su kaynakları yönetiminde ve suyun sektörlere paylaştırılmasında kritik bir rol oynamaktadır. Ayrıca, bu çalışmada, ABS'deki uydu geçişleri sırasında seçilen bitkiler için ortalama LAI ile ortalama NDVI arasındaki ilişki de araştırılmıştır. Elde edilen bulgular, NDVI–LAI ilişkisinin, ASB belirli bitkiler (birinci ve ikinci ürün mısır, pamuk, soya, yer fıstığı ve buğday) için ortalama NDVI ile ortalama LAI arasındaki ilişkinin üssel bir modelle ifade edilebileceğini ortaya koymuştur. Bu ilişkiden elde edilen denklemlerin, bitki örtüsünü değerlendirmek, üretimi tahmin etmek ve METRIC modeline gerek kalmadan LAI hesaplamak için kullanılabileceği sonucuna varılmıştır. Bu ilişkiden çıkartılan eşitlikler bitki örtüsü değerlendirmesi, üretim tahmini ve daha fazla özel uzmanlık ve veri gerektiren METRIC modeline gerek olmaksızın yaygın olarak kullanılabileceği söylenebilmektedir.

UA tabanlı ET_a modelleri ve $K_{c\text{-}NDVI}$ yaklaşımının uygulanması, çalışma alanında FAO-PM ve ET_c yöntemlerinden elde edilen ET_o ile güçlü bir uyum göstermiştir. Büyük ölçekli sulama şebeke alanlarında, METRIC ve SEBAL gibi UA tabanlı modeller, farklı bitkilerin çeşitli büyüme aşamalarında ET_a'yı yeterli doğrulukla tahmin etme imkânı sağlamıştır. Böylece, Akdeniz iklim kuşağında yer alan yarı kurak iklim koşullarında ve düz arazilerde yüksek mekânsal çözünürlüklü ET_a haritaları üretilebilmiştir. UA tabanlı ET_a (METRIC ve SEBAL) modellerinden üretilen gerçek evapotranspirasyon haritaları, tarımsal hidrolojiyi yakından ilgilendiren hidrolojik süreçlerin daha iyi anlaşılmasında ve su kaynaklarının havza düzeyinde yönetilmesinde kullanıcılara kritik bilgiler sunabilir. Ayrıca, METRIC ve SEBAL algoritmaları gerçek buharlaşma-terleme (ET_a) tahminlerinin yapılmasında son derece uygun araçlar olduğundan bu algoritmalardan elde edilen sonuçlar tarımsal planlama ve su yönetimi konusunda dünya genelindeki kurak ve yarı kurak bölgelerde önemli bilgiler sağlayabilir.

ACKNOWLEDGEMENTS

Without the assistance and direction of numerous individuals, completing my dissertation would not have been feasible. Above all, I would like to express my sincere gratitude to my esteemed and well-respected supervisor, Prof. Dr. Mahmut CETIN, for his invaluable advice, support, and mentoring during my PhD studies.

Words alone cannot adequately express my gratitude to those who have given me their sincere support during my PhD studies and dissertation completion. Still, with this note of thanks, I would like to acknowledge at least the love, kindness, and support I have received from them along the way.

I am grateful to my wife and son for creating the perfect environment and for their patience, support, and love during my studies. I am grateful to my parents for their unwavering support and for giving me the strength to complete this adventure. Throughout my PhD, my uncle has provided support in various ways, and I am always grateful to him and his family for that. I count myself very lucky to have a family that is so encouraging.

I thank Dr. Hakan AKSU and Dr. Nishan BHATTARAI for providing the required training and patiently answering my inquiries on this study. Moreover, I extend my gratitude to Prof. Dr. Mahmut CETIN, the coordinator of the TUJJB (Turkish National Geodesy and Geophysics Union) project, for supplying the necessary meteorological data and ground truth data for cropping pattern determination throughout my PhD studies. I am grateful to engineer Samet SALABAGIR and the Seyhan Left Bank Irrigation Union staff for their invaluable support. They facilitated my communication with farmers, provided essential meteorological data, and assisted in collecting ground truth data on crops. I am grateful to Research Assistant Muhammet Said GOLPINAR and engineers Burak TILKICI and Volkan CATALKAYA for their faultless support in the collection of my ground truth data in the irrigation landscapes of the Lower Seyhan Plain located in southern Türkiye.

I thank my friends, who have given me hope to continue my journey with their heartwarming words during tough times; I am pleased and grateful for having such friends in my life. I hold the utmost respect and gratitude for all the Agricultural Structures and Irrigation Department staff and faculty members at Cukurova University. They filled the void of being away from home and my parents during my PhD studies.

This thesis was supported by the Scientific Research Projects (BAP) Coordination Unit of Cukurova University [Project Number: FDK-2022-14907] and partially by the Scientific and Technological Research Council of Türkiye (TUBITAK) [Project Number: 122Y007]. I am incredibly thankful to Prof. Dr. Halil KARAHAN, the coordinator of the TUBITAK project, for providing financial support through a scholarship during my PhD studies.

Lastly, I wish to express my appreciation to my Thesis Monitoring Committee members, comprising my supervisor, Prof. Dr. Mahmut CETIN, Prof. Dr. Fatih TOPALOGLU, and Prof. Dr. Recep YURTAL, for their continuous guidance and constructive feedback throughout this research. I am also thankful to my jury members, Prof. Dr. Ahmet IRVEM and Dr. Hakan AKSU, for their insightful comments and support, which far exceeded the expectations of a typical academic evaluation.

This dissertation would not have been possible without the collective contributions of all these remarkable individuals to whom I am deeply indebted.

OMAR ALSENJAR

Adana, 2025

LIST OF TABLES

Table 3.1. The number of parcels visited over AID during four consecutive water years (2020, 2021, 2022 and 2023) 31

Table 3.2. The number of parcels near the lagoons/lakes of the Lower Seyhan Plain visited during four consecutive water years (2020, 2021, 2022 and 2023) over the stressed area 31

Table 3.3. Spectral bands, including a pan band for Landsat 7, Landsat 8, and Landsat 9 34

Table 3.4. Landsat scenes information (Landsat 7, Landsat 8, and Landsat 9) during the water years of 2020-2023, including scene names, acquisition dates, and overpass times 35

Table 3.5. Common crop types are grown in the study area, their growing periods and "length of crop growth stages" (Initial, developing, mid-season, and end-season), and corresponding K_c values (TAGEM-DSI, 2017; Cetin, 2020; Cetin et al., 2023b) 38

Table 3.6. Names and dates of Sentinel satellite images utilized to identify plant patterns in the research area during both winter and summer seasons 40

Table 3.7. Comparison of energy balance models (METRIC, EEFlux-METRIC, SEBAL, and GeeSEBAL) for ET_a estimation: Strengths, Limitations, and Applicability 52

Table 4.1. Some descriptive statistics for reference ET_o (mm day^{-1}) by the FAO-PM in the AID and stressed area of LSP for the years 2020-2023 59

Table 4.2. Outlines the aggregate count of parcels surveyed during both winter and summer seasons across the water years from 2020 to 2023 within both the AID and stressed regions of the LSP 59

Table 4.3. The land area (ha) cultivated plants in the stressed area during the winter season for the years 2020-2023 66

Table 4.4. The land area (ha) cultivated plants in the stressed area during the summer season for the years 2020-2023 67

Table 4.5. Some descriptive statistics of actual evapotranspiration by the METRIC model ($ET_{a\text{-}METRIC}$, mm day^{-1}) are available on October 21, 2021, within the AID and stressed areas 73

Table 4.6. Comparison of performance metrics of ET_a (mm day^{-1}) derived from the METRIC model, EEFlux, and ET_o (mm day^{-1}) by the FAO Penman-Monteith method across the AID 85

Table 4.7. Comparison of performance metrics for ET_a (mm day^{-1}) from the METRIC model, EEFlux, and ET_o (mm day^{-1}) calculated using the FAO Penman-Monteith method in the stressed area of the LSP 85

Table 4.8. Generated K_c equation between K_c and NDVI (Landsat) for some crops 115

Table 4.9. Validation of the $K_{c\text{-}NDVI}$ to K_c as outlined by the literature review 115

Table 4.10. Performance statistics of linear regression model for actual evapotranspiration by the ET_c and METRIC models for selected crops over the AID 129
Table 4.11. Performance statistics of linear regression model for actual evapotranspiration by the ET_c and SEBAL models for selected crops over the AID.................................. 130
Table 4.12. Performance statistics of linear regression model for actual evapotranspiration by the ET_c and $K_{c\text{-}NDVI}$ models for selected crops over the AID 131
Table 4.13. Student’s t-test results comparing the “two-step” approach (ET_c) with the METRIC and SEBAL models for citrus crops in 2021 132
Table 4.14. Student’s t-test results comparing the “two-step” approach (ET_c) with the METRIC, SEBAL and $K_{c\text{-}NDVI}$ models for wheat crops in 2021 133
Table 4.15. Student’s t-test results comparing the “two-step” approach (ET_c) with the METRIC, SEBAL and $K_{c\text{-}NDVI}$ models for corn-I crops in 2021............................... 133
Table 4.16. Student's t-test results comparing the “two-step” approach (ET_c) with the METRIC, SEBAL, and $K_{c\text{-}NDVI}$ models for cotton-I crop in 2021 133
Table 4.17. Performance statistics of linear regression model between $ET_{a\text{-}METRIC\text{-}NSA}$ and $ET_{a\text{-}METRIC\text{-}SA}$ for some crops 134
Table 4.18. Regression analysis summary (ANOVA; Regression, Residual) for the relationship between NDVI and LAI across various crop types: (a) Corn-I, (b) Corn-II, (c) Cotton-I, (d) Cotton-II, (e) Soybean-I, (f) Soybean-II, (g) Peanut-I, (h) Peanut-II, and (i) Wheat...147

LIST OF FIGURES

Figure 2.1. Akarsu Irrigation District (AID) 10
Figure 2.2. A diagram outlining the methodology employed to estimate ET_a using METRIC and crop evapotranspiration (ET_c) through a “two-step” procedure 14
Figure 2.3. Monthly fluctuations in $ET_{a\text{-METRIC}}$ and ET_o values 14
Figure 2.4. Yuregir plain 19
Figure 3.1. The study area location in the Lower Seyhan Plain (LSP) of the Mediterranean Region in Türkiye 25
Figure 3.2. The prevalent crop varieties cultivated, their respective cultivation periods, and the duration of distinct growth stages, including initial, development, mid-season, and late-season phases in the research area 25
Figure 3.3. Data sources and inputs utilized in this study 26
Figure 3.4. Study area and location of meteorological stations 27
Figure 3.5. General spatial distribution of ground truth data of crops, which was observed in both the AID location and the stressed region of the LSP during field visits 28
Figure 3.6. In-situ images of various crops collected for ground truth data to identify crop type in fields on 26.04 2022 over the AID of the LSP 29
Figure 3.7. In-situ images of various crops collected for ground truth data to identify crop type in field on 24.04. 2023 over the AID of the LSP 29
Figure 3.8. In-situ images of various crops collected for ground truth data to identify crop type in field on 25.08. 2022 over the stressed area near the coastal lagoons of the LSP 30
Figure 3.9. In-situ images of various crops collected for ground truth data to identify crop type in field on 31.03.2023 and 03.08.2023 over the stressed area near the coastal lagoons of the LSP 30
Figure 3.10. Landsat tiles that encompass the research area 33
Figure 3.11. Landsat sensors, spectral channels, and band passes are superimposed on atmospheric transmission percentage (grey background). MSS: Landsat 1 through -5; TM: Landsat 4 and 5; ETM^+: Landsat 7; OLI and TIRS: Landsat 8 and 9. (source: NASA/Landsat Legacy Project Team and American Society for Photogrammetry and Remote Sensing) 33
Figure 3.12. Digital elevation model (DEM) map for the study area in the LSP of Türkiye 37
Figure 3.13. A graphical representation depicting the crop coefficient curve spanning from the initial planting phase to the final harvesting stage of the crop 38
Figure 3.14. The flowchart outlining the methodology employed to estimate actual evapotranspiration (ET_a) utilizes SEB models, i.e., METRIC, EEFlux METRIC,

SEBAL, GeeSEBAL models and a "two-step" procedure for calculating crop evapotranspiration (ET_c), along with the $K_{c\text{-}NDVI}$ method 39
Figure 3.15. Training root mean square (RMS) versus the iteration value during the winter season of 2021 over the AID 41
Figure 3.16. The image processing steps for identifying the crop types cultivated in the irrigation district during both winter and summer seasons, along with their associated input data, pre-processing procedures, and utilized models 41
Figure 3.17. An example of calculating NDVI 44
Figure 3.18. A schematic diagram showcasing the various functions, data inputs, and resultant outputs utilized within the METRIC model. In this illustration, data inputs are represented by green rounded boxes, functional processes by blue boxes, and the outcome by a yellow box 45
Figure 3.19. Surface energy balance components 45
Figure 3.20. Energy balance over vegetation with different radiation components 46
Figure 3.21. Sensible heat flux in *Equation 3.8* 46
Figure 3.22. The methodology framework employed for estimating actual evapotranspiration ($ET_{a\text{-}EEFlux}$, mm day^{-1}) using the EEFlux-METRIC method and the standard METRIC model 49
Figure 3.23. Framework for estimating actual evapotranspiration ($ET_{a\text{-}Kc\text{-}NDVI}$, mm day^{-1}) using the $K_{c\text{-}NDVI}$ methodology 53
Figure 4.1. Daily temporal changes of calculated ET_o (mm day^{-1}) by the FAO-PM approach and total precipitation (mm) over the AID area for the years 2020-2023. Climatic information was recorded at the Cotlu station, as depicted in Figure 3.4 58
Figure 4.2. Daily temporal changes of calculated ET_o (mm day^{-1}) by the FAO-PM approach and total precipitation (mm) over the stressed area of the LSP for the years 2020-2023. Climatological data were documented at the Golkaya station, as illustrated in Figure 3.4 58
Figure 4.3. Crop distribution patterns during the winter and summer of 2020 in (a) AID) and (b) the stressed regions of the LSP in Türkiye 64
Figure 4.4. Crop distribution patterns during the winter and summer of 2021 in (a) AID and (b) the stressed regions of the LSP in Türkiye 64
Figure 4.5. Crop distribution patterns during the winter and summer of 2022 in (a) AID and (b) the stressed regions of the LSP in Türkiye 65
Figure 4.6. Crop distribution patterns during the winter and summer of 2023 in (a) AID and (b) the stressed regions of the LSP in Türkiye 65
Figure 4.7. The proportions of land area occupied by cultivated plants in the AID during the winter season, categorized by water years 66

Figure 4.8. The proportions of land area occupied by cultivated plants in the AID during the summer season, categorized by water years 66
Figure 4.9. Spatial distribution of land surface energy balance (LE, Rn, G, and H, W m^{-2}) components by the METRIC methodology over (a) AID and (b) stressed area on 21.10.2021 (DOY 294) 69
Figure 4.10. Spatial distribution of actual evapotranspiration ($ET_{a\text{-}METRIC}$, in mm day^{-1}) estimated using the METRIC methodology from the satellite image dated 21.10.2021 (DOY 294) for the designated polygon of interest, encompassing (a) the AID area and (b) the stressed area of the LSP 70
Figure 4.11. Spatial distribution of actual evapotranspiration ($ET_{a\text{-}METRIC}$, mm day^{-1}) estimated using the METRIC methodology from the satellite image dated 21.10.2021 (DOY 294) in the research area, (a) AID, and (b) stressed area........ 71
Figure 4.12. The temporal fluctuations in the average daily actual evapotranspiration ($ET_{a\text{-}METRIC}$, mm day^{-1}) values, obtained through the METRIC methodology, during satellite overpasses over the (a) AID and (b) stressed region of the LSP 74
Figure 4.13. The temporal changes in the average daily actual evapotranspiration ($ET_{a\text{-}METRIC}$, mm day^{-1}) values, obtained using the METRIC methodology, from September 30, 2019, to September 30, 2023, across the AID 75
Figure 4.14. Variations in $ET_{a\text{-}METRIC}$ values on a monthly basis across the hydrological years of 2020, 2021, 2022, and 2023 within the AID 75
Figure 4.15. ET_a values by the METRIC model over the non-stress area (AID, NS) from 2020 to 202 hydrological year. Horizontal lines in the box plots indicate the median, as well as the 25th and 75th percentiles. Dots on the plot signify outliers (Tukey, 1977; Iglewicz and Hoaglin, 1993), which are data points that lie beyond 1.5 times the interquartile range (IQR) from the first and third quartiles, respectively. The whiskers extending from the plot represent the minimum and maximum values 76
Figure 4.16. Spatial distribution of actual evapotranspiration ($ET_{a\text{-}EEFlux}$, mm day^{-1}) estimated using the EEFlux platform from satellite imagery on 30.07.2020 (DOY 212) for: (a) AID, and (b) stressed area........ 81
Figure 4.17. Temporal fluctuations in the average daily actual evapotranspiration ($ET_{a\text{-}METRIC}$, mm day^{-1}) values in (a) AID and (b) stressed area of the LSP as determined by the METRIC method, the EEFlux approach, and the ET_o by the FAO-PM method during satellite overpasses........ 82
Figure 4.18. Linear relationship between the ET_a (mm day^{-1}) by the standard METRIC approach and $ET_{a\text{-}EEFlux}$ during satellite images overpass dates over the (a) AID and (b) stressed area of the LSP........ 83

Figure 4.19. Linear relationship between ET_o (FAO-PM method) with ET_a derived from the METRIC model and $ET_{a\text{-EEFlux}}$ platform during satellite images overpass dates over the (a) AID area and (b) stressed area of the LSP 84
Figure 4.20. Spatial distribution of latent heat (LE-SEBAL, W m^{-2}) and actual evapotranspiration ($ET_{a\text{-SEBAL}}$, mm day^{-1}) using the SEBAL methodology from the satellite image captured on July 31, 2023 (DOY 212), is illustrated within the specified area of interest, covering the Akarsu Irrigation District (AID).................... 87
Figure 4.21. Spatial distribution of actual evapotranspiration ($ET_{a\text{-SEBAL}}$, mm day^{-1}) and crop coefficient (K_c) estimated using the SEBAL methodology from the satellite image of July 31, 2023 (DOY 212) in the Akarsu Irrigation District (AID) 88
Figure 4.22. Temporal variations in mean daily actual evapotranspiration ($ET_{a\text{-SEBAL}}$, mm day^{-1}) using the SEBAL model and ET_o by the FAO-PM method within the Akarsu Irrigation District (AID) during satellite overpasses... 90
Figure 4.23. Temporal changes in the daily average weighted actual evapotranspiration ($ET_{a\text{-SEBAL}}$, mm day^{-1}) values, using the SEBAL methodology and ET_o by the FAO-PM approach, across the Akarsu Irrigation District (AID) from September 30, 2019, to September 30, 2023... 90
Figure 4.24. Variations in actual evapotranspiration ($ET_{a\text{-SEBAL}}$, mm $month^{-1}$) values on a monthly basis across the water years of 2020, 2021, 2022, and 2023 within the Akarsu Irrigation District (AID).. 91
Figure 4.25. Actual evapotranspiration ($ET_{a\text{-SEBAL}}$, mm day^{-1}) values by the SEBAL model over the Akarsu Irrigation District (AID) from 2020 to 2023 hydrological year. Horizontal lines indicate the median, as well as the 25^{th} and 75^{th} percentiles. Dots on the plot signify outliers (Tukey, 1977; Iglewicz and Hoaglin, 1993), which are data points that lie beyond 1.5 times the interquartile range (IQR) from the first and third quartiles, respectively. The whiskers extending from the plot represent the minimum and maximum values 91
Figure 4.26. Linear relationship between ET_o by the FAO Penman-Monteith method and actual evapotranspiration ($ET_{a\text{-SEBAL}}$, mm day^{-1}) from the SEBAL model during satellite images overpass dates in the Akarsu Irrigation District (AID) for the years 2020-2023 92
Figure 4.27. Spatial distribution of actual evapotranspiration ($ET_{a\text{-GeeSEBAL}}$, mm day^{-1}) across the Akarsu Irrigation District (AID) on (DOY 228), equivalent to August 15, 2020, as generated by the GeeSEBAL model 93
Figure 4.28. Temporal variations in mean daily actual evapotranspiration (ET_a, mm day^{-1}) in the Akarsu Irrigation District (AID), using the SEBAL method, the GeeSEBAL

platform, and reference evapotranspiration (ET_o) from the FAO-PM method, during satellite overpasses 94
Figure 4.29. Temporal variation of actual evapotranspiration (ET_a, mm day^{-1}) by the SEBAL, METRIC, EEFlux, GeeSEBAL models, and the ET_o by the FAO-PM-56 method over Akarsu Irrigation District (AID) during satellite images overpass dates 95
Figure 4.30. Monthly variations in actual evapotranspiration (ET_a, mm month^{-1}) values for 2020–2023 hydrological year as follows as (a) 2020, (b) 2021, (c) 2022 and (d) 2023 in the Akarsu Irrigation District (AID) using the METRIC model, SEBAL algorithm, ET_o by the FAO-PM method, and ET_c method 99
Figure 4.31. The Location of the citrus plantation adjacent to the Cotlu meteorological station and the distribution of citrus fields across the Akarsu Irrigation District (AID) for 2020-2023 100
Figure 4.32. Temporal variations of average daily actual evapotranspiration ($ET_{a\text{-}METRIC}$, mm day^{-1}) estimated by the METRIC model for the citrus field near the Cotlu meteorological station and overall ET_a of citrus across the Akarsu Irrigation District (AID), compared with ET_o calculated using the FAO-PM method during satellite overpass dates 101
Figure 4.33. Spatial distribution of saplings with watermelon across the Akarsu Irrigation District (AID) during the summer season of 2022 101
Figure 4.34. Temporal fluctuations of average daily actual evapotranspiration ($ET_{a\text{-}METRIC}$, mm day^{-1}) values for sapling with watermelon obtained through the METRIC model across the entire study area, ET_o by the FAO-PM and $K_{c\text{-}METRIC}$ during satellite overpass dates 102
Figure 4.35. Spatial distribution of (a) sapling with watermelon and (b) sapling across the AID in the summer season of 2022 103
Figure 4.36. Temporal fluctuations of (a) average daily actual evapotranspiration ($ET_{a\text{-}METRIC}$, mm day^{-1}) and (b) K_c values for sapling with watermelon and only sapling, obtained through the METRIC model across the entire AID during satellite overpass dates 104
Figure 4.37. Spatial distribution of saplings with cabbage across the AID in the winter season of 2023 105
Figure 4.38. Temporal fluctuations of average daily actual evapotranspiration ($ET_{a\text{-}METRIC}$, mm day^{-1}) values for sapling with cabbage, obtained through the METRIC model across the entire AID during satellite overpass dates 105
Figure 4.39. Actual evapotranspiration ($ET_{a\text{-}METRIC}$, mm day^{-1}) map by the METRIC model for soybean-II on DOY 197 (16 July 2009) 107

Figure 4.40. Temporal variations in average daily actual evapotranspiration ($ET_{a\text{-}METRIC}$, mm day^{-1}) values for citrus and sapling determined using the METRIC model across satellite overpass dates within the AID and the stressed area of the LSP 110
Figure 4.41. Temporal variations in average daily actual evapotranspiration ($ET_{a\text{-}METRIC}$, mm day^{-1}) values for crops: (a) Wheat, (b) Cotton-I, (c) Cotton-II, (d) Corn-I, (e) Soybean-I, and (f) Peanut-II, as estimated using the METRIC model during satellite overpass dates within the AID and the stressed regions of the LSP 112
Figure 4.42. Temporal variations in average daily actual evapotranspiration ($ET_{a\text{-}METRIC}$, mm day^{-1}) values for pasture in the stressed region of the LSP, estimated using the METRIC model 114
Figure 4.43. Temporal variation of K_c as outlined by the literature review (TAGEM-DSI, 2017) and NDVI for corn-I in the 2022 115
Figure 4.44. Linear relationship between standard K_c by the TAGEM-DSI (2017) and $K_{c\text{-}NDVI}$ for corn-I 116
Figure 4.45. Temporal variation of ET_a for corn-I based on the $K_{c\text{-}NDVI}$ method and “two-step” procedure ET_c 116
Figure 4.46. Spatial distribution of wheat ET_a by the METRIC model and ET_a by $K_{c\text{-}NDVI}$ method on DOY 353 (December 19, 2019): ET_a in the unit of mm day^{-1}................ 117
Figure 4.47. Temporal variations of areal mean daily wheat ET_a (mm day^{-1}) values, acquired by the METRIC model and $K_{c\text{-}NDVI}$, at the time of satellite overpass over the AID 118
Figure 4.48. Temporal variations in the average daily ET_a values for: (a) Wheat,(b) Cotton-I, (c) Cotton-II, (d) Corn-I, (e) Corn-II, (f) Soybean-I, (g) Soybean-II, (h) Peanut-I, (i) Peanut-II, and (j) Citrus. ET_a estimations were done by the METRIC, SEBAL, $K_{c\text{-}NDVI}$, and ET_c models during satellite overpass dates within the AID of the LSP for the years 2020-2023.. 125
Figure 4.49. A linear relationship between actual evapotranspiration by the METRIC model ($ET_{a\text{-}METRIC}$, mm day^{-1}) for citrus near the Cotlu weather station compared to the mean value of citrus in the AID during the 2020–2023 study period. The dashed black lines represent the 1:1 lines.. 135
Figure 4.50. Temporal fluctuations of mean daily evaporation (E_{METRIC}, mm day^{-1}) of lagoons derived from the METRIC model during satellite overpass dates 137
Figure 4.51. Spatial variations in the average daily evaporation (E_{METRIC}, mm day^{-1}) of lagoons near the stressed area of the LSP, as determined by the METRIC model for some dates.. 139
Figure 4.52. Linear relationship between evaporation estimates from the METRIC approach and the KNF model during satellite image overpass dates over lagoons in the stressed region of the LSP 140

Figure 4.53. Spatial distribution of (a) LAI and (b) NDVI values using the METRIC model over the AID for several days during the summer of 2021. LAI is expressed in units of $m^2 m^{-2}$ 142
Figure 4.54. Temporal Variations in average Leaf Area Index (LAI) and Normalized Difference Vegetation Index (NDVI) values for various crop types: (a) corn-I, cotton-I, soybean-I, and peanut-I; (b) corn-II, cotton-II, soybean-II, and peanut-II; (c) wheat; across the Akarsu Irrigation District (AID) during satellite overpasses... 144
Figure 4.55. Exponential models between average NDVI and average LAI for various crop types: (a) Corn-I, (b) Corn-II, (c) Cotton-I, (d) Cotton-II, (e) Soybean-I, (f) Soybean-II, (g) Peanut-I, (h) Peanut-II, and (i) Wheat, in the Akarsu Irrigation District (AID) during satellite overpasses. Data excluded from calculations, indicated by Δ symbol, were identified as outliers through box plot analysis 146

SYMBOLS AND ABBREVIATIONS

DOY	: Day of year
“d”	: Index of agreement
dT	: Near surface air temperature difference
E	: Evaporation
SEB	: Surface Energy Balance
NSA	: Non-stressed area
SA	: Stressed area
EC	: Eddy covariance
e.g.	: For example
ET_a	: Actual evapotranspiration
ET_c	: Crop evapotranspiration
$ET_{a\text{-METRIC}}$	: Actual evapotranspiration estimated with METRIC
$ET_{a\text{-SEBAL}}$	: Actual evapotranspiration estimated with SEBAL
$ET_{a\text{- Kc-NDVI}}$	: Actual evapotranspiration estimated with K_c and NDVI
ET_o	: Refernce evapotranspiration
ETM^+	: Enhanced Thematic Mapper Plus
ET_{ins}	: Instantaneous evapotranspiration
ET_rF	: Reference evapotranspiration fraction
ET_{24}	: Evapotranspiration for 24 hours
RS	: Remote sensing
GIS	: Geographic information systems
LE	: Latent heat flux
G	: Soil heat flux
H	: Sensible heat flux
K_c	: Crop coefficient
LAI	: Leaf area index
MBE	: Mean bias error
METRIC	: Mapping EvapoTranspiration at high Resolution using Internal Calibration
NDVI	: Normalized Difference Vegetation Index
NIR	: Near-infrared band
OLI	: Operational Land Imager
IRTs	: Infrared thermometers
QC	: Quality control
RH	: Relative humidity
R_n	: Net radiation

SR : Solar radiation
RMSE : Root Mean Square Error
R^2 : Coefficient of determination
SAVI : Soil-adjusted vegetation index
SEBAL : Surface Energy Balance Algorithm for Land
SEBS : Surface Energy Balance Systems
Std. Dev. : Standard deviation
T : Transpiration
Ta : Air temperature
Td : Dew point temperature
TIRS : Thermal Infrared Sensor
T_s : Surface temperature
USGS : United States Geological Survey
SEBS : Surface Energy Balance Systems
km : Kilometer
r : Pearson correlation coefficient
SD : Standard deviation
Q1 : Quartile one
Q2 : Quartile two
Q3 : Quartile three
IQR : Interquartile Range
% : Percent

1. INTRODUCTION

As climate change continues to impact various regions globally, including Türkiye, accurately measuring and/or estimating evapotranspiration (ET) becomes crucial. Carr (1990) stated that approximately 60 percent of the precipitation is lost through evaporation. Precise ET measurements are vital for understanding and managing water resources, forecasting agricultural productivity, and assessing ecosystem health—factors critical for adapting to and mitigating the effects of climate change. Furthermore, as global demand for freshwater resources intensifies, it is increasingly important to evaluate agricultural water usage accurately. Data on crop water consumption, or consumptive use, is essential for several purposes, including optimizing agricultural water management, improving irrigation techniques, planning water resources, and allocating water rights (Allen et al., 2011). Population growth and increased water consumption have led to higher competition for the limited water supply, resulting in potential shortages for other users depending on the same source. Reducing water availability for irrigation can diminish agricultural yields and jeopardize food security. Nevertheless, there is significant potential to enhance water management within agricultural systems, and accurate ET estimation is pivotal for achieving this goal.

On the other hand, ET plays a pivotal role in the hydrological cycle. It encompasses the transfer of water from surface bodies of soil and water into the air by vaporization, as well as plant transpiration. ET can be classified into two types: potential evapotranspiration (ET_p), which represents the maximum rate of evapotranspiration that could occur if there were no limitations on water availability, and actual evapotranspiration (ET_a), which reflects the amount of water evaporated and transpired from a surface, taking into account any constraints on water availability. Therefore, accurately estimating the value of ET_a is essential for hydrological models as well as drought forecasting to represent the water balance effectively.

The significance of ET_a in the hydrological cycle lies in its application across various endeavours, such as drought monitoring and mitigation, climate forecasting, water asset administration, and agricultural strategizing. According to Madugundu et al. (2017), ET_a is one of the most critical factors affecting the hydrologic cycle in semi-arid climates. Similarly, Hoedjes et al. (2008) emphasize that accurately determining ET_a is essential for optimizing agricultural water management under different irrigation schemes. It is widely acknowledged that variations in ET_a rates across spatial scales are influenced by climatic factors, soil properties, and plant characteristics (Allen et al., 1998; Allen et al., 2007a).

Numerous conventional techniques are available for estimating ET_a, which can be categorized into (a) direct measurements using advanced instruments like lysimeters, eddy covariance systems, and Bowen ratio, and (b) indirect methods employing empirical formulas. One of the most commonly employed indirect methodologies in recent research is the FAO-56 Penman-Monteith (PM) model. Furthermore, the PM model is regarded as a benchmark by researchers, farmers, and the United Nations Food and Agriculture Organisation (FAO) because it thoroughly incorporates all meteorological factors (Santos et al., 2019). The evapotranspiration of vegetation/crop (ET_c) is determined by multiplying the reference evapotranspiration (ET_o) by the vegetation/crop coefficient (K_c), which varies according to the crop type and its various growth stages (Alsenjar et al., 2023a). Nonetheless, Allen et al. (2007b) mentioned that concerns have been raised regarding the suitability of standardized K_c values for accurately representing real-world conditions of plant growth and vegetation, especially in areas experiencing water scarcity. It has been noted that predicting precise agricultural development stage dates may pose challenges, especially for extensive plants and fields (Allen et al., 2007b). Determining ET_a at a large irrigation scale using traditional methods is often the most challenging variable. These methods necessitate skilled personnel, specialized instruments, and financial resources. Moreover, due to the dynamic nature and regional variations in ET_a, these methods cannot be easily extrapolated to larger areas (Seemann et al., 2003). Additionally, conventional approaches overlook temporal and spatial variations in soil, climate, and crop effects on ET_a, limiting their applicability to agricultural parcels or regional levels (Allen et al., 2011). Consequently, the remote sensing (RS)-driven surface energy balance (SEB) technique has been utilized to determine ET_a across extensive geographical areas with high resolution (Karahan et al., 2024).

SEB models utilizing RS techniques were employed for ET_a estimation, including the Surface Energy Balance Algorithm for Land (SEBAL) developed by Bastiaanssen et al. (1998a), the Surface Energy Balance System (SEBS) proposed by Su (2002), Mapping Evapotranspiration at High Resolution with Internalized Calibration (METRIC) introduced by Allen et al. (2007a), and among others. RS-based ET_a estimation models have been utilized to forecast ET_a by combining RS and ground truth data.

The precision of ET_a estimations relies on the complexity of the model and the quantity of input variables and assumptions it incorporates. More complex models are typically developed to account for subprocesses and offer a more realistic estimate of ET_a. However, the ET_a values are computed instantaneously over the study site on the date when the satellite passes overhead. These instantaneous ET_a values may not be helpful for various applications that typically require daily, monthly, and seasonal values. Hence, techniques that enable extrapolating instantaneous ET_a values to more extended periods, such as scaling up instantaneous ET (ET_i) to daily values (ET_d), are employed (Allen et al., 2007a; Karahan et al., 2024). These techniques include utilizing methods like a constant evaporative fraction (EF), constant reference evaporative fractions (ET_rF), constant global shortwave radiation method (SR), and constant extra-terrestrial radiation method. In the same context, our investigation employs the METRIC and SEBAL techniques to compute ET_a for each pixel within the satellite images. The METRIC model scales up instantaneous ET (ET_i) to daily values (ET_d) using ET_rF, whereas the SEBAL model utilizes EF.

The METRIC model, utilizing satellite image processing, incorporates multiple sub-models to calculate ET_a for individual pixels and crop types. Implementing the METRIC model necessitates various RS data sets, including but not limited to visible and thermal infrared sensor bands, digital elevation model (DEM), surface temperature (T_s), normalized difference vegetation index (NDVI) emissivity, and surface albedo. The METRIC algorithm computes the latent heat flux (LE) while a satellite passes overhead by considering the remaining energy within the SEB, thereby estimating ET_a. This is accomplished by employing remote sensing data with meteorological parameters, as detailed by Allen et al. (2007a). According to Allen et al. (2007a), the development of the METRIC method originated from the SEBAL algorithm. One distinctive feature of the SEBAL model is its use of the temperature gradient close to the Earth's surface, denoted as dT, to indicate satellite-derived T_s. Conversely, the innovative aspect of the METRIC model is its choice of two boundary conditions, namely hot and cold pixels, for calibration within the SEB framework. This process of selecting boundary conditions is complex and requires expert judgment to achieve optimal calibration.

The R-METRIC model and LandMOD ET mapper toolbox-MATLAB, derived from the standard METRIC model, incorporate an automated hot-cold pixel selection technique, thereby reducing the potential for human error (Olmedo et al., 2016; Bhattarai et al., 2017). The standard METRIC algorithm is used to compute ET_a for each pixel and crop type based on the RS data coupled with local climatic parameters. During the last ten years, the METRIC algorithm has been utilized to predict ET_a on both small-scale agricultural fields and larger regional areas encompassing diverse crops such as citrus orchards, peanut, cotton, wheat, banana orchards, soybeans, maize, cover crops, alfalfa, pistachios, vineyards, olive orchards, sugarcane, and forests, among others, in different locations of the world. Automated calibration algorithms for the METRIC model necessitate various datasets, including satellite imagery, cloud coverage identification, DEM, local climate information, soil categorization maps, and land use/land cover or crop pattern maps. These datasets require preprocessing before applying the METRIC model, thereby consuming valuable time for users. The earth engine evapotranspiration flux (EEFlux) application was implemented on the Google Earth Engine (GEE) platform to address this issue, utilizing the METRIC model. The EEFLux was developed in 2012 through collaboration among the Desert Research Institute and the Universities of Idaho and Nebraska (Foolad et al., 2018; Alsenjar and Cetin, 2023). This solution aims to reduce time and cost burdens. Furthermore, the platform enables rapid ET_a and K_c data generation at a spatial resolution of 30 m for individual Landsat scenes and additional RS products.

In certain situations, creating ET_a maps using complex equations and RS data can present challenges and may require input data that is not readily accessible. In this context, developing a streamlined and expedited approach for generating ET_a maps using fewer input parameters is possible. This would be particularly beneficial in situations where available input data are scarce or where a higher level of uncertainty in the resulting ET_a estimates is deemed acceptable. One approach involves a simplified satellite imagery method, leveraging the NDVI and K_c sourced from existing literature. This involves deriving a novel K_c value based on the relationship between NDVI and K_c, thereby establishing K_{cnew} ($K_{c\text{-}NDVI}$) for estimating ET_a (Rouse et al., 1974; Glenn et al., 2011). Rafn et al. (2008) noted that NDVI indicates the proportion of crop coverage, offering valuable information on the present condition of crops (Glenn et al., 2011). For well-irrigated vegetation, a crop-specific correlation through K_c as well as NDVI is commonly observed. The earlier ET_a methods were developed to estimate ET_a accurately to enhance sustainable water management on a large scale for irrigation. This study is important for mitigating the effects of climate change on water resources in the Mediterranean Basin and other regions worldwide.

Anonymous (2012) emphasized that Türkiye is situated in the Mediterranean Basin, which is warm in the winter and hot and dry in the summer. In recent years, the vulnerability of the Mediterranean region to climate change effects has escalated, marked by a rise in the frequency and intensity of extreme weather conditions. Numerous recent studies have concluded that Türkiye confronts significant challenges due to climate change, including heightened occurrences and severity of extreme weather phenomena such as floods and droughts, escalating annual temperatures, and diminishing levels of precipitation (Yilmaz and Imteaz, 2014; Irvem et al., 2018). The impacts of climate change manifest through changes in air temperature and precipitation, predominantly affecting crop growth and yields while also intensifying the evapotranspiration rate of crops. Additionally, these changes place strain on already scarce freshwater resources.

Accurate ET_a estimation is essential for effective large-scale irrigation management. In Türkiye's Lower Seyhan Plain (LSP), traditional ET_a estimation relies on a two-step approach using crop evapotranspiration (ET_c) methods, which generalize ET_a across the region. However, surface energy balance (SEB) models, such as METRIC and SEBAL, offer higher accuracy by capturing spatial and temporal variations influenced by soil salinity, crop health, water availability, and irrigation practices. This study advances ET_a estimation by integrating METRIC, SEBAL models, and the $K_{c\text{-}NDVI}$ approach with existing methods, introducing key improvements:

- **Enhanced Accuracy** – Validation of METRIC and SEBAL against lysimeter measurements and ET_c-based methods using statistical metrics (RMSE, MAE, R^2, and Willmott's index) ensures reliability.
- **Refined Climatic Data Integration**—The LandMOD ET Mapper incorporates multiple weather stations and advanced interpolation techniques to improve data precision.
- **Optimized $K_{c\text{-}NDVI}$ Approach** – Strengthening the relationship between $K_{c\text{-}NDVI}$ and ET_a across various crops enhances its applicability for crop-specific water use estimation.

This study investigates ET_a estimation using remote sensing in Türkiye's Lower Seyhan Plain (LSP), providing a region-specific application. However, the contribution of this research to Türkiye's existing water management policies can be clarified as follows:

- **Supporting Water Resource Management:** This study's findings offer a detailed and accurate approach to estimating ET_a, which is essential for understanding crop water demand and improving irrigation practices. By incorporating remote sensing-based ET_a models, this study provides valuable data to optimize water use in agricultural fields, helping water resource managers make informed decisions, especially in areas facing water scarcity.
- **Enhancing Irrigation Efficiency:** Integrating models like METRIC, SEBAL, and $K_{c\text{-}NDVI}$ can help develop more efficient irrigation schedules, thereby reducing water wastage and improving crop yield. This aligns with Türkiye's goal of achieving sustainable water management, especially in arid and semi-arid regions such as the Lower Seyhan Plain, where agriculture heavily depends on irrigation.
- **Contributing to Policy Development:** The study's results can inform future water management policies by providing evidence-based insights into regional water usage patterns and the effectiveness of different irrigation strategies. The research can be used to refine national water policies and enhance their alignment with climate variability, crop water needs, and long-term sustainability.
- **Facilitating Decision-Making in Water-Scarce Regions:** With increasing challenges related to water scarcity, the methods proposed in this study can serve as a tool for policymakers to assess the impact of current water management strategies and adjust them to ensure efficient and equitable water distribution, especially in areas like the Lower Seyhan Plain.

By estimating ET_a across a large irrigated catchment under diverse environmental conditions, this study enhances irrigation scheduling, improves regional and field-scale water demand assessments, and strengthens agricultural water resource management. The integration of weather station data and remote sensing within energy balance models further reinforces the reliability of ET_a estimation for large-scale applications. This research offers key advancements over previous ET_a estimation studies:

- **Higher Resolution and Accuracy**: Using high-resolution Sentinel-2 data and ANN classification enhances crop differentiation, improving ET_a estimates.
- **Reduced Computational Effort**: The LandMOD ET Mapper in MATLAB streamlines data preprocessing and model implementation, significantly reducing computational

time compared to traditional approaches. Unlike R-based implementations, MATLAB handles large datasets (multiple images, weather stations) more efficiently, minimizing memory-related crashes and slowdowns.

- **Validation with Multiple Datasets**: Unlike many studies relying solely on remote sensing outputs, this research cross-validates ET_a estimates with lysimeter measurements and ET_c calculations, ensuring higher reliability.

The research aims to estimate actual evapotranspiration (ET_a) using several surface energy balance (SEB) models—namely METRIC, EEFlux METRIC, SEBAL, and GeeSEBAL—along with the $K_{c\text{-}NDVI}$ method and a "two-step" approach of ET_c in stressed and non-stressed areas of the Lower Seyhan Plain (LSP) in the Eastern Mediterranean region of Türkiye over the 2020-2023 water years. The study also involves comparing the ET_a results from these SEB models with direct ET_a measurements obtained in previous research for specific crops and locations within the study area. Additionally, statistical analyses are conducted to evaluate differences in mean ET_a values across various SEB methods and the "two-step" approach of ET_c for selected crop types.

The objectives of the research are to:

- Evaluate the effectiveness of RS-based ET_a estimation using the METRIC, EEFlux METRIC, SEBAL, and GeeSEBAL models in two regions of the LSP under varying conditions, i.e., non-stressed (standard) and stressed (non-standard).
- Predict daily ET_a using the METRIC, SEBAL, $K_{c\text{-}NDVI}$, and ET_c models for specific crop types during satellite overpass dates.
- Estimate and produce comprehensive ET_a maps covering the entire study area, including the non-stressed (standard) and stressed areas (non-standard) of the LSP.
- Compare the outcomes derived from EEFlux with those of conventional METRIC applications to demonstrate the effectiveness of EEFlux products in their current state and analyze the main distinctions between the two applications.
- Compare the estimated ET_a and K_c values derived from SEB models with those obtained from literature reviews for specific crop types and studies conducted across the study area.
- Compare the estimated ET_a values for some crops obtained from the METRIC model in non-stressed areas (Akarsu Irrigation District) and stressed areas (near the Mediterranean Sea of Türkiye) during the satellite overpass.
- Assess the relationship between leaf area index (LAI), NDVI, K_c, and ET_a by the METRIC model for some crop types in the non-stressed area.

Research hypothesis and questions

Effectiveness of RS-based ET_a estimation in the Lower Seyhan Plain of Türkiye:

- *Hypothesis: The METRIC, EEFlux METRIC, SEBAL, and GeeSEBAL models provide accurate and consistent ET_a estimations in the LSP region.*

How effective are the METRIC, EEFlux METRIC, SEBAL, and GeeSEBAL models in estimating ET_a under non-stressed and stressed conditions in the LSP regions?

Daily ET_a Prediction:

- *Hypothesis: The $K_{c\text{-}NDVI}$ and ET_c models provide reliable predictions of daily ET_a values comparable to those from METRIC and SEBAL-based models.*

  How do the $K_{c\text{-}NDVI}$ and ET_c models compare to METRIC and SEBAL-based models in predicting daily ET_a values?

Comprehensive ET_a Maps:

- *Hypothesis: Comprehensive ET_a maps generated from RS-based models can accurately depict spatial variations in ET_a across both non-stressed and stressed areas of the LSP.*

  Can comprehensive ET_a maps generated from RS-based models accurately represent spatial variations in ET_a across the LSP's non-stressed and stressed areas?

EEFlux vs Conventional METRIC Applications:

- *Hypothesis: EEFlux products demonstrate comparable or superior accuracy in ET_a estimation to conventional METRIC applications in non-stressed and stressed areas during satellite overpass dates.*

  How do the outcomes from EEFlux compare to those from conventional METRIC applications in terms of ET_a estimation accuracy?

Comparison with Literature Values:

- *Hypothesis: ET_a and K_c values estimated from SEB models closely match those obtained from literature reviews for specific crop types in the study area.*

  Are the ET_a and K_c values derived from SEB models consistent with those obtained from literature reviews for specific crop types in the study area?

ET_a Estimations in Different Conditions:

- *Hypothesis: ET_a values estimated for crops in the non-stressed Akarsu district do not differ from those in stressed areas near the Mediterranean Sea of Türkiye at the time of the satellite overpass.*

  How do ET_a estimations for crops in non-stressed areas compare to those in stressed areas during satellite overpasses?

Relationship between LAI, NDVI, K_c, and ET_a:

- *Hypothesis: For specific crop types in the non-stressed area, there is no significant positive or negative correlation between LAI, NDVI, K_c, and ET_a values estimated by the METRIC model.*

  What is the mathematical relationship between LAI, NDVI, K_c, and ET_a values estimated by the METRIC model for specific crop types in the non-stressed area?

The study introduces an enhanced approach for estimating ET_a using remote sensing models, such as METRIC, SEBAL, and the $K_{c\text{-}NDVI}$ method, specifically tailored to the unique conditions of the Lower Seyhan Plain. It represents a novel application of these methods in a semi-arid region, providing valuable insights into the spatial and temporal variations in crop water use while addressing local environmental and climatic challenges. Additionally, the study offers significant advancements in integrating satellite-based models into regional water management practices, making a notable contribution to agricultural water management and remote sensing.

2. PRELIMINARY WORK

As it is commonly understood, RS-based ET_a models assess every pixel, identifying individual crop types as well as the entirety of the area (Cetin et al., 2023b). Consequently, it is imperative to classify each crop type and ascertain the proportion of each crop throughout the water year. The insights garnered from crop classification are pivotal, offering a valuable understanding of the variety of crops cultivated within a particular region, thus furnishing crucial data on regional cropping patterns. Various approaches have been employed to classify cropping patterns, encompassing field visits and RS data such as Sentinel-2.

The Sentinel-2 satellite system, launched as part of the European Commission's (EC) Copernicus program, consists of the Sentinel-2A and Sentinel-2B satellites; the presence of two satellites allows repeated surveys every five days at the equator and every 2-3 days at mid-latitudes (EOS, 2019). Satellite imagery is defined by specific features, including wavelengths, bandwidths, and spectral bands, which are used to derive key indices like the Normalized Difference Vegetation Index (NDVI). In this context, NDVI is a powerful metric for distinguishing between water and vegetation and is widely employed for mapping and monitoring crop health (Alsenjar et al., 2023a). Some of the literature reviews reported below on how to classify crops using different types of bands, including NDVI.

Yilmaz (2018) conducted a classification study on crops, namely pepper, corn, eggplant, wheat, tomato, cotton, grapes, clover, and olive, in the Gediz Plain in the western part of Türkiye. This study encompassed an area of 520 km^2. The study area's coordinates are as follows: upper left longitude: 27.844ºE, latitude: 38.625ºN, lower right longitude: 28.181ºE, latitude: 38.463ºN. Eight Sentinel-2 satellite images from 2017, encompassing the research region, were chosen for analysis. Additionally, NDVI bands were derived from each selected satellite image. Ground truth data were acquired through fieldwork and the farmer registration system (FRS). The accuracy of the FRS data was verified parcel by parcel and cross-referenced with fieldwork observations. Object-based classification using the random forest (RF) algorithm was employed for crop detection, with a segmentation-based approach utilized during the classification process. The classification process resulted in an overall accuracy of 94% and a Kappa value of 93.65%.

Irfanoglu and Balcik (2018) employed a parcel-based approach utilizing the RF algorithm for crop classification within agricultural regions (3,322 km^2) encompassing the Artuklu, Kiziltepe, and Derik districts of Mardin city (WGS 84, UTM-Zone 37 N, DOM 39), utilizing multi-temporal Sentinel-2 images from 2018. The identified crops included corn, wheat, cotton, chickpeas, and lentils. Six image acquisition dates were selected for analysis. The classification utilized 10 m spatial resolution bands, including Blue (B), Green (G), Red (R), and Near Infrared (NIR), along with the computation of the NDVI band for each image date, incorporated as an additional band in the classification process. The RF algorithm classified the stack of 30 bands, consisting of five bands (B, G, R, NIR, NDVI) for each image. Training samples and result accuracy assessment were conducted using the existing FRS. The classification process yielded an overall accuracy of 96.35% and a Kappa value of 93.13%.

Alsenjar et al. (2023a) employed the artificial neural network (ANN) algorithm to classify crops during the winter-summer seasons of the 2021 water year across the AID (Figure 2.1) as part of this PhD thesis, utilizing Sentinel-2 imagery with a 10-meter resolution alongside ground truth data. In winter, crops such as wheat, onion, potatoes, and lettuce were identified, while during the summer, first crop types (I) and second crops (II), including corn, peanuts, cotton, soybean, watermelon, and others, were cultivated. Citrus orchards accounted for over 30% of the AID throughout the year. The confusion matrix of the ANN algorithm demonstrated high agreement rates of more than 89% for wheat, potato, lettuce, onion, citrus, sesame-II, watermelon, and palm, and moderate agreement rates (fruit 58.33% in winter, 42.86% in summer) with ground truth data during the growing seasons. Additionally, agreement exceeded 80% for first and second crops (corn, soybean cotton, and peanut) during summer. Implementing the ANN approach facilitated the production of highly precise classified maps depicting crop distribution across extensive irrigation catchment areas.

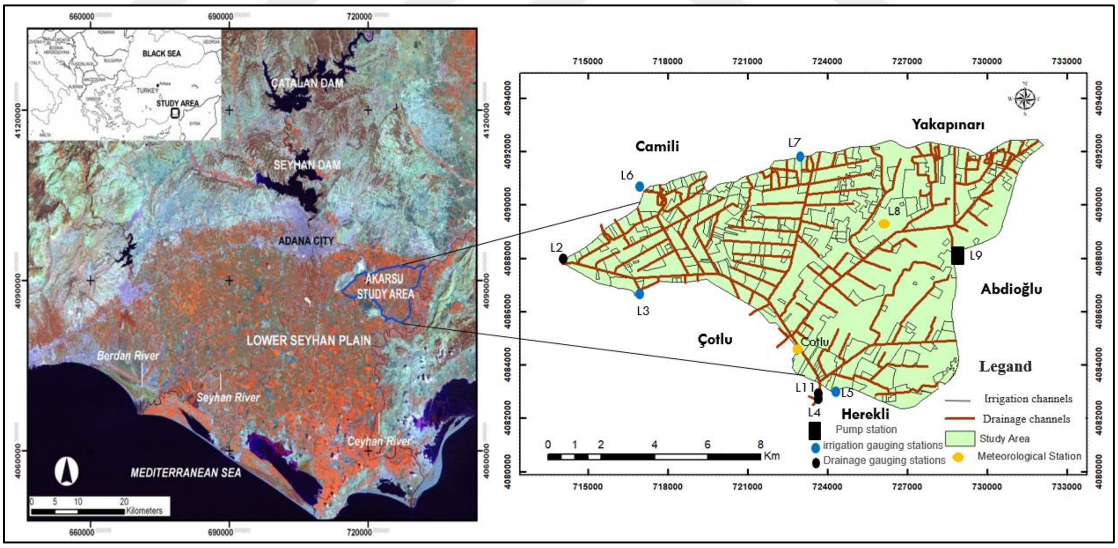

Figure 2.1. Akarsu Irrigation District (AID) (Alsenjar et al., 2023a)

In another research conducted by Alsenjar et al. (2023b), the ANN technique was employed to categorize crop patterns across the AID region (refer to Figure 2.1). This involved integrating ground truth data acquired through surveys conducted across various crop fields during winter and summer, along with Sentinel-2 data from 2020. The ANN algorithm was utilized for crop-type classification, employing the neural net classification module within the supervised classification framework. The crop types identified through the ANN method aligned with the ground truth crop data, resulting in an overall classification accuracy of 90%. This information is crucial in regions experiencing increased evapotranspiration (ET) rates, as it helps identify which crops consume more water, enabling the development of targeted and efficient water resource management strategies.

Rising ET rates have been observed worldwide in arid and semi-arid regions, including Türkiye (Alsenjar et al., 2023a). This trend places additional strain on scarce water resources, such as freshwater and groundwater, to meet the water demands of crops in drought-prone areas. Therefore, studying and accurately estimating ET_a in these areas can contribute to adequately managing water resources (Alsenjar and Cetin, 2023). Many studies were applied to compute/estimate ET_a for different crops using satellite/RS-ET_a techniques at small, large, and regional scales. ET_a-direct methods focused on localized points of the world. Several literature reviews were summarized in this study, focusing on research that employed remote sensing (RS) techniques to estimate ET_a in areas with environmental and climatic conditions comparable to those of the study area.

The METRIC model, introduced by Allen et al. (2007a), is a revised version of the widely recognized SEBAL model (Bastiaanssen, 1995; Bastiaanssen et al., 1998a). Alsenjar and Cetin (2023) stated that the METRIC model calculates ET_a by deriving it as a residual from the SEB equation, utilizing data acquired from satellite imagery and in-situ meteorological data. One of the advantages of the METRIC model is its applicability in flat and mountainous landscapes (Allen et al., 2013; Alsenjar et al., 2023b; Cetin et al., 2023a). Alsenjar et al. (2023b) reported that the METRIC model has been extensively utilized across numerous countries to assess ET_a using satellite images combined with climatic data within diverse agro-climatic zones, encompassing field-level assessments and large-scale geographic areas. It has been utilized successfully in various crops, including wheat, corn, soybean, and alfalfa, demonstrating favorable outcomes with errors ranging from 3 to 20%. Additionally, in recent years, it has been applied to sparsely vegetated areas such as vineyards and olive orchards (Allen et al., 2007a; Allen et al., 2007b; Mkhwanazi and Chávez, 2012; Patil et al., 2015). In addition, the METRIC model was employed in Idaho to examine the coherence of water rights and the utilization of groundwater as part of water asset planning efforts. Furthermore, the METRIC model was applied in the Rio Grande Valley, New Mexico, to assess the adequacy of the water system and to manage salinity levels (Trezza et al., 2013). Several studies have tested the accuracy of estimation of $ET_{a\text{-METRIC}}$ with ET_a using direct and indirect methods for different crops at local, regional, and global scales. The METRIC model has been extensively utilized for estimating ET_a across various crops at field and regional scales, with reported errors falling within 3-20% (Allen et al., 2007a).

Gowda et al. (2008) conducted a study assessing the performance of the METRIC model in the Texas plains region. They used Landsat 5 TM (Thematic Mapper) data for their analysis on June 27 and July 29, 2005. The researchers discovered a strong correlation between the ET estimations generated by the METRIC model and those derived from a soil water budget model.

Another research by Aksu and Arikan (2017) employed moderate resolution imaging spectroradiometer (MODIS) data within the METRIC model to produce ET_a maps for major land cover types that cover 3,560 km^2 of the Buyuk Menderes basin during the irrigation season, i.e., from April to September 2010. As widely recognized, MODIS data offers a spatial resolution of 1,000 m by 1,000 m and daily temporal resolution. In this study, the results from the METRIC model were compared with crop evapotranspiration (ET_c), which was calculated using reference evapotranspiration estimated by the Penman-Monteith ASCE method and adjusted using a crop coefficient (K_c) specific to olive trees. Additionally, for Bafa Lake, located in the Buyuk Menderes Basin, class A-pan evaporation measurements from the Kusadasi meteorological station were used to validate the lake's evaporation (E) estimates produced by the METRIC model. The findings indicated a strong concurrence between the evaporation values computed by the METRIC model and the class A-pan data and ET_c estimates, suggesting that METRIC has the potential for estimating evaporation (E) utilizing satellite data in regions with limited data availability.

Bhattarai et al. (2017) applied the automated approach to compute ET_a using the METRIC model in four sites in the USA. Three distinct land cover types are marshes, crops, and grassland in Florida, while one is cropland in Oklahoma. The recently developed fully automated model, which relies on selecting NDVI, LST, and LAI, exhibited superior performance and showed greater consistency compared to an established semi-automated approach that utilized statistical methods to isolate the hottest and coldest pixels within an image. The daily estimates of ET_a obtained from the automated SEBAL and METRIC models closely aligned with their manual counterparts, as evidenced by high levels of agreement (e.g., NSE≥0.94 and RMSE≤0.35 mm day^{-1}).

He et al. (2017) reported that the METRIC model was applied to estimate ET_a across an almond orchard with 60 ha in California, USA. The almond trees stood at approximately 7 meters in height throughout the study period from 2009 to 2012. The model's outcomes are assessed against the flux tower data. The METRIC model is fueled by 46 satellite images from Landsat 5 and 7 with spatial resolution 30 m by 30 m spanning the timeframe from April to November 2009-2012, while 30-minute flux tower data are integrated as inputs. The results from the METRIC model are generally consistent with the flux tower measurements. However, during periods of cloudy or rainy weather, specifically from December to March, the uncertainty in the calculations increases due to interpolation errors.

Madugundu et al. (2017) utilized the METRIC model to generate ET_a values for 50 hectares of alfalfa irrigated fields in the eastern region of Saudi Arabia from June to October 2013. The RS data utilized for the METRIC model were obtained from eight Landsat 8 satellite images. The findings demonstrated a strong correlation between the outcomes of the METRIC model and those obtained through the eddy-covariance (EC) method. Moreover, the METRIC model reflects an underestimation of 4.2% in daily ET_a compared to the EC method, which deviates from typical findings reported in the existing literature. Variations are observed in the EC and Landsat-derived latent heat flux estimates (LE). This could be attributed to the advection process in hourly ET_a estimations and the variability in canopy density within the studied footprint.

In the research conducted by Tasumi (2019), the METRIC model was employed to predict ET_a for rain-fed wheat, irrigated short crops, city centers, and Urmia Lake from 2014 to 2016 in Iran's western region of the Urmia Lake Basin. The METRIC model could predict evaporation (E) from freshwater lakes and saline bodies of water like Urmia Lake. The METRIC model utilizes 34 Landsat 8 satellite images as input data. Because a lysimeter and eddy covariance were inaccessible for estimating ET_a in the study area, ET_a values were contrasted with those derived from the Penman-Monteith model, which served as the ET_o. The findings of this investigation demonstrated a strong correlation between the predicted ET_a using the METRIC model and the ET_o by the Penman-Monteith approach. However, there is a tendency to overestimate ET_a on uncovered soil, which presents a significant issue in mountainous terrains. The evaporation findings from saline lakes typically surpass those of freshwater lakes. This phenomenon can be ascribed to saline lakes' tendency to exist in arid and semi-arid regions, where low humidity levels facilitate heightened evaporation rates.

An article titled "Actual evapotranspiration estimation using METRIC model and Landsat satellite images over an irrigated field in the Eastern Mediterranean Region of Türkiye" was published by Alsenjar et al. (2023b) in the Journal of Mediterranean Geoscience Review in 2023. In the research, Alsenjar et al. (2023b) applied the METRIC model to compute daily and monthly ET_a for wheat and citrus in the winter and first-crop type (I), corn-I and peanut-I, and citrus in the summer seasons of 2020 over an irrigated area, i.e., Akarsu Irrigation District (AID) (Figure 2.1), with 9,495 ha as part of PhD's study area. The AID is situated within the latitude range of 36°57′32″ to 36°50′43″N and the longitude range of 35°40′22″ to 35°28′42″E in the Lower Seyhan Plain (LSP) in Türkiye. The research results by Alsenjar et al. (2023b) are part of this PhD thesis. Figure 2.2 shows the proposed methodology to predict ET_a over the AID area with data used and RS data in the 2020 water year. Seven Landsat satellite images (path 175, row 34) with a spatial resolution of 30 m by 30 m were used in the research site. In the 2020 hydrological year, the total ET_o was calculated at 1,238 mm, surpassing the ET_a estimated by METRIC, which amounted to 1,191 mm. Figure 2.3 shows the difference between ET_o by the FAO-PM method and ET_a by the METRIC model. In this article, the annual ET_c totals approximately 823 mm, constituting 69% of the ET_a. This notable discrepancy between the annual calculated ET_c and the yearly estimated ET_a by the METRIC model suggests that the crop coefficient (K_c) values employed in the ET_c approach during different stages of crop development tend to be lower than those derived from the reference evapotranspiration fraction (ET_rF_i) function used in ET_a estimation. The findings demonstrated satisfactory consistency between ET_a and ET_c estimations. The ET_a maps depicted variations corresponding to changes in crop types across the study area during the summer and winter seasons of 2020.

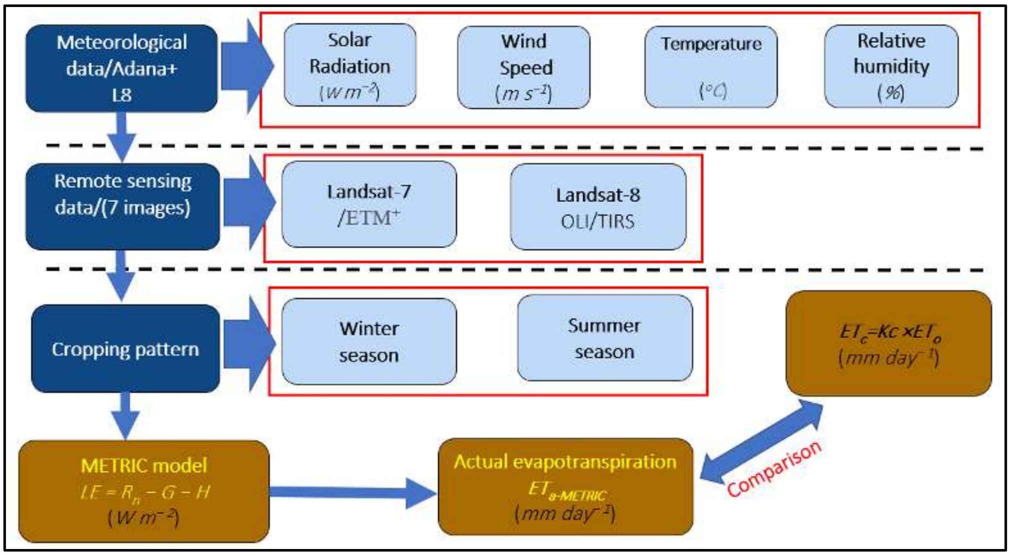

Figure 2.2. A diagram outlining the methodology employed to estimate ET_a using METRIC and crop evapotranspiration (ET_c) through a "two-step" procedure (Cetin, 2020; Alsenjar et al., 2023b)

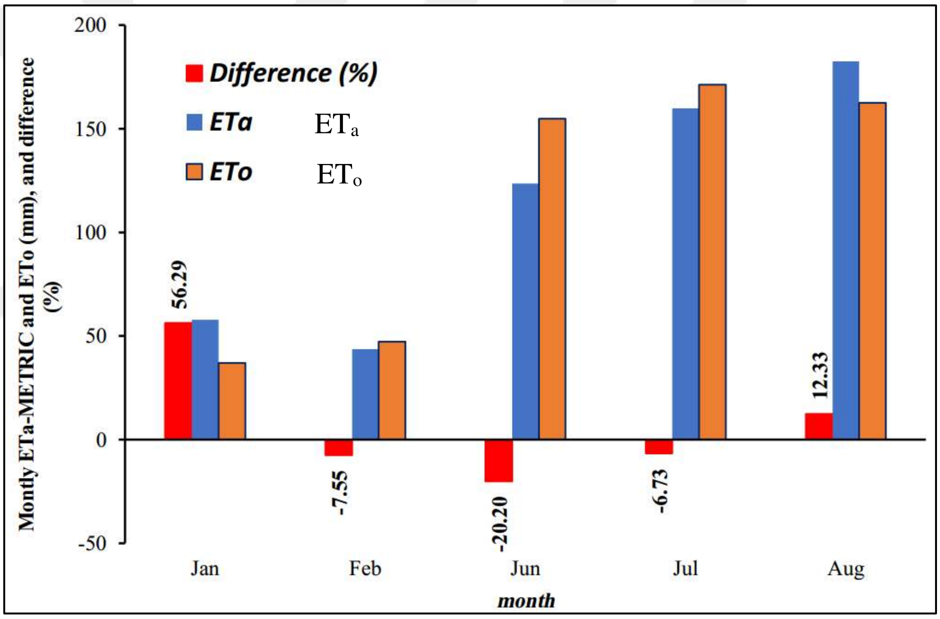

Figure 2.3. Monthly fluctuations in $ET_{a\text{-}METRIC}$ and ET_o values (Alsenjar et al., 2023b)

Cetin et al. (2023b) utilized the METRIC model to compute daily, monthly, and seasonal ET_a for irrigated wheat, potato, lettuce, corn-I, peanut-I, soybean-II, and citrus crops within the AID with an area of about 95 km^2 during the 2021 hydrological year. Throughout the two growing seasons, this study employed 17 satellite images from Landsat 7 and Landsat 8, all of which exhibited a cloud cover of less than 10% in the processed data. The yearly ET_o calculated at 1,308.0 mm was higher than the estimated ET_a of 1,254.5 mm. The total annual ET_c across the study area amounted to approximately 71% of ET_a, highlighting that the K_c values utilized during various stages of crop development in the ET_c approach tend to be lower than those derived from the ET_rF_i in ET_a estimation. The ET_a values demonstrate notable proximity to the corresponding ET_c values for wheat, with discrepancies ranging between 0.32 and 1.78 mm day^{-1}. The ET_a values are remarkably similar to the ET_c values across various crops, including potato, lettuce, corn-I, peanut-I, and soybean-II. For citrus during the 2021 water year, the estimated ET_a for citrus-planted regions tended to surpass the corresponding ET_c for the identical crop. This variance could potentially stem from utilizing K_c values (standard K_c) sourced from existing literature by General Directorates of Agricultural Research and Policies and State Hydraulic Works (2017), i.e., TAGEM-DSI (2017), which were chosen based on the phenological stages of citrus. This study confirmed that the outcomes derived from the METRIC model, namely ET_a and ET_c, were employed as inputs for the water balance analysis. Moreover, these findings facilitated the development of a methodology to evaluate water balance closure discrepancies at the catchment level.

As is known, the standard METRIC model needs more complex data, and users are experienced in manipulating RS data. For this reason, the EEFLux was used to predict ET_a using the GEE platform based on global climatic data coupled with Landsat satellite data at 30 m spatial resolutions. EEFlux has grown steadily because it enables users with minimal experience to efficiently process remote sensing (RS) data and compute ET_a and K_c for various regions worldwide. The EEFlux platform offers rapid generation of ET_a at a spatial resolution of 30 m alongside additional data products, including T_s, NDVI, DEM, and albedo.

In the research conducted by Foolad et al. (2018), the evaluation of EEFlux METRIC against the conventional METRIC method demonstrated favorable conformity in both ET_rF and ET_a estimations across diverse agricultural regions in the western and central United States. In EEFlux METRIC, gridded weather data was utilized as input, whereas METRIC utilized local weather data. A total of 58 Landsat images were utilized as input data. Conversely, distinctions between EEFlux and METRIC were notably more pronounced for non-agricultural land. The variances observed in this section may arise from EEFlux encountering challenges in accurately factoring in background evaporation during the calibration endpoint for hot pixels. The bias in hot pixels assigned to K_c (ET_rF) tends to influence non-agricultural pixels significantly more than agricultural ones. This is primarily because non-agricultural pixels typically exhibit lower ET_a, making them more susceptible to errors or biases in the overall surface energy balance.

Venancio et al. (2020) utilized the EEFlux METRIC platform to estimate ET_a and K_c for an 80-hectare soybean plantation during the 2016/17 growing season in the western area of Bahia state, Brazil. Six clear-sky Landsat satellite images were employed and processed utilizing the EEFlux platform. The assessment of ET_a EEFlux versus ET_a by modified FAO (MFAO) approach revealed favorable concordance, as evidenced by Willmot’s index of agreement (d-index), which registered values of 0.85, 0.83, and 0.89 for central pivots 1, 2, and 3, respectively. Nonetheless, EEFlux tends to underestimate ET_a marginally. The K_c values derived from EEFlux demonstrated strong agreement with the K_c values examined in this investigation, except for phase II, where a notable disparity was observed. The results of this study showed that ET_a and K_c estimates from EEFlux are readily accessible and freely available, thus serving as exceptional data reservoirs for the scientific community and practitioners engaged in agricultural remote sensing applications.

In the study by Nisa et al. (2021), three single-source surface energy balance (SEB) models—SEBS, QWaterModel, and METRIC-EEFlux—were evaluated against an eddy covariance (EC) system for estimating daily ET_a in a 15-hectare irrigated field planted with maize and forage crops in a Mediterranean environment in southern Italy. QWaterModel, a QGIS plugin, calculates ET_a using land surface temperature (LST) maps and is based on the energy balance model DATTUTDUT (Deriving Atmosphere Turbulent Transport Useful to Dummies Using Temperature). For the analysis, thirty-six nearly cloud-free images captured by Landsat 5 and 7 were utilized through the GEE platform for the period spanning from 2008 to 2009. According to the results of this study, SEBS and METRIC-EEFlux exhibited satisfactory consistency with measured ET_a in patterns and quantities. Addressing errors caused by scan line defects in Landsat 7's sensor can enhance the quality of the METRIC-EEFlux ET_a output.

Kumar et al. (2023) utilized the EEFlux model to estimate ET_a for wheat crops during the rabi season of 2019–2020 in the Bhagwatipur distributary, Bihar, India. The study incorporated eight Landsat 7 and 8 satellite images along with climatic data as input. The research compared the EEFlux and CROPWAT 8.0 models (Modified Penman-Monteith Model). The regression analysis indicated a coefficient of determination (R^2) of 0.79 between ET_a estimated by the EEFlux model and ET_a derived from the FAO-PM model. The mean bias error (MBE) was calculated as 0.60 mm day^{-1}, while the root mean square error (RMSE) was determined to be 0.86 mm day^{-1}. The satellite-based method readily evaluates ET_a for the designated area, functioning as a dependable tool for scheduling irrigation practices.

Alsenjar and Cetin (2023) employed the EEFlux platform to assess ET_a within the AID, spanning an expanse of 9,495 hectares in our research domain within the LSP, Türkiye, throughout the 2020 hydrological year. The AID has been operating under an irrigation system for the past six decades and is considered to be in standard condition. Sixteen Landsat images were utilized as RS data in the study. Local weather information from two meteorological stations within the catchment area was compared with gridded global data from CFSv2 during the 2020 water year. The outcomes derived from EEFlux exhibited strong consistency with METRIC across the entirety of the research area. Furthermore, a robust correlation (r= 0.93 and RMSE= 0.74 mm day^{-1}) was observed between ET_o and ET_a, determined by the METRIC model. The coefficient of determination (R-squared) and RMSE between ET_o and ET_a computed via EEFlux stood at 0.77 and 1.42 mm day^{-1}, respectively. In addition to the METRIC model and the EEFlux platform, another variation of the SEBAL model is available, which also estimates ET_a using remote sensing (RS) data combined with climatic parameters in different regions of the world.

Bastiaanssen et al. (1998a) designed the SEBAL model to compute ET_a based on the RS data with minimal ground truth data. The SEBAL has been tested with the in-situ ET_a measurements across various climate conditions in Türkiye, Iran, Egypt, India, Sri Lanka, Pakistan, Spain, and Argentina, etc., to assess crop consumptive use uniformity, crop water stress, and irrigation efficiency (e.g., Bastiaanssen, 2000).

Trezza (2002) employed Landsat satellite data (Landsat 5 TM imagery and Landsat 7 ETM^+ imagery) along with the SEBAL model to determine the water demand of crops in the Idaho region. The author evaluated the precision of the model by contrasting it with weighing lysimeter data obtained from the Kimberley Agricultural Research Institute of Idaho. The outcomes generated by the SEBAL approach exhibited a variance of under 5% when compared to the results derived from weighing lysimeter data.

Bastiaanssen et al. (2005) reported that the SEBAL model has been utilized to estimate ET_a for different crop types across over 30 countries of the four Continents (Europe, Asia, Africa, and the Americas), assessing its performance at both farm and regional scales. These crop types are cherry, wheat, apple, alfalfa, nut, grassy hay, and pasture. Their findings indicated an 85% daily accuracy rate for comparisons between different direct ET_a measurements (eddy covariance, Bowen ratio, lysimeter, scintillometer) and ET_a by the SEBAL model at the farm scale, increasing to 95% for seasonal evaluations. Additionally, the algorithm exhibited a 96% accuracy at the regional scale.

Ramos et al. (2009) examined the 4-year ET_a (1997–2000) of the Flumen region in the Ebro plain of northeastern Spain. The Flumen District encompasses an estimated area of 33,730 ha. Two lysimeters were used, one for grass crops and the second for wheat and maize crops. In total, 15 Landsat satellite images (Landsat 5 and 7) were used alongside climatic data from 1997-2000 as RS input data. They utilized the SEBAL algorithm to analyze these values and juxtaposed them with data obtained from lysimeters. The estimated ET_a values derived from the SEBAL approach for the grass exhibited a bias of 0.3 mm day^{-1} compared to the lysimetric measurements and a bias of 0.36 mm day^{-1} compared to ET_o by the Penman-Monteith method. Additionally, there was strong agreement between the estimated ET_a of maize and wheat, and the ET_a was determined through lysimetric measurements in the research. Furthermore, at the regional scale, a discrepancy of 20% was observed between the ET_a values calculated using the SEBAL method and those derived from the Penman-Monteith method.

In their study, Ruhoff et al. (2012) examined the precision of the SEBAL model in predicting ET_a in a Brazilian savanna environment compared to measurements obtained through eddy-covariance (EC) techniques. They utilized 28 Terra MODIS remote sensing images spanning from February to November 2001 for their analysis. The findings from comparing daily ET_a values obtained from the SEBAL model with those derived from the in-situ EC correlation method for sugarcane and savannah cultivars showed R^2 of 0.76 and 0.66, respectively.

In their research, Zamani and Rahimzadegan (2018) utilized the SEBAL, METRIC, and SEBS models to assess evaporation rates from freshwater bodies within the vicinity of the Amirkabir dam reservoir and the surrounding agricultural lands in Iran's semi-arid climate. A total of 16 Landsat satellite images with type Landsat 5 and Landsat 8 were used from 2011 to 2017. In this regard, three models' estimated evaporation (E) values were compared with the Pan evaporation measurements conducted within the study area. The results indicated that the SEBAL model was inefficient. In contrast, the SEBS and METRIC models demonstrated appropriate performance in estimating evaporation from the designated water body compared to the evaporation pan data.

Atasever and Ozkan (2018) employed the SEBAL model to determine ET_a using Landsat 8 imagery in the AID region in the LSP of Türkiye, which is a component of this PhD thesis, on the dates January 22, April 28, and July 01, in 2015. ET_a values obtained from SEBAL models were compared with ET_o estimates at ground truth locations, calculated using the FAO Penman-Monteith model. The statistical analyses, including matched pairs t-test and nonparametric Wilcoxon signed rank test, indicated no significant disparity between the ET_a values derived from the proposed method and those of the ground truth points.

Rahimzadegan and Janani (2019) utilized the SEBAL model for estimating ET_a over a 100-hectare pistachio plantation in the Safaeieh area of Semnan province, Iran, utilizing 29 Landsat 8 datasets spanning from 2013 to 2017. The findings were authenticated and juxtaposed with ET_a outcomes under standardized conditions determined by the Intelligent Meteorological instrument (iMetos-Pessl). The study's results reveal that the correlation coefficient (r) and RMSE for the pistachio plant's estimated ET_a are 0.89 and 2.5 mm day^{-1}, respectively. In general, the outcomes demonstrate the adequate performance of the SEBAL model in predicting the ET_a of pistachio crops.

Sawadogo et al. (2019) employed the SEBAL model using the Python script (PySEBAL) to estimate ET_a for soybean-II. They conducted a comparison with lysimeter field data obtained from the center of a 0.12-hectare field at the Research Fields of the Agricultural Structures and Irrigation Department, Faculty of Agriculture, University of Cukurova, situated in Adana, Türkiye (37°1'N, 35°21'E, and 20 m above mean sea level). Five Landsat 5 Thematic Mapper (TM) clear-sky images and meteorological data were employed in this study in 2009 (from July to October). The results revealed a strong agreement between the PySEBAL model and the lysimeter, with an R-squared value of 0.73, an RMSE of 0.51 mm day^{-1}, an MBE of 0.04 mm day^{-1}, and a Willmott's index of agreement (d) of 0.90. Therefore, the PySEBAL model accurately estimates the ET_a of soybean crops in Adana, Türkiye.

Shamloo et al. (2021) utilized the SEBAL algorithm to estimate ET_a in the Yuregir plain (Figure 2.4) with 125,000 ha, located at 37.00ºN latitude and 35.33ºE longitude in UTM Zone 36 N-WGS 84. The Yuregir delta plain is enclosed by the Mediterranean Sea in the south, the foothills of the Taurus Mountains in the north, and the Ceyhan and Seyhan rivers in the east and west. The investigation was conducted to estimate the ET_a of corn and determine the K_c from March to September 2018. ET_a computed by the SEBAL model was contrasted with ten experimental models: Penman, FAO24 Penman, Kimberly Penman (KP), FAO56 Penman-Monteith (FAO-56 PM), Priestley-Taylor (PT), De Bruin-Keijman (DK), Makkink (mak), Turk, Hargreaves (Har), and

Mcloud (Mcl). Twelve Landsat 8 images, each with a spatial resolution of 30 m × 30 m, spanning from March to December 2018 (the typical plant growth period), were employed in the study. The estimated ETa values displayed the strongest correlation (r= 0.91) and the lowest error (RMSE= 1.14 mm day^{-1}) compared with the FAO Penman-Monteith method. Moreover, the SEBAL method exhibited the highest correlation values of 0.89, 0.87, and 0.68 with the Turk, Makkink, and Hargreaves experimental methods. The crop coefficients (K_c) estimated using SEBAL demonstrated strong agreement across all methods, with the FAO Penman-Monteith method showing the highest correlation (r = 0.98) and a very low RMSE (0.05). However, this study has certain limitations. It primarily focused on estimating ET_a for corn using the SEBAL model without considering other crop types within the Yuregir Plain, including those in the Akarsu Irrigation District (AID). Additionally, the average ET_a values derived from SEBAL only represent the corn fields, as the research did not include a detailed classification of different crops across the study area. Furthermore, the study lacks adequate information on the meteorological data utilized, such as the locations and distribution of the meteorological stations. Lastly, ET_a was not estimated to be the most water-stressed area within the Yuregir Plain.

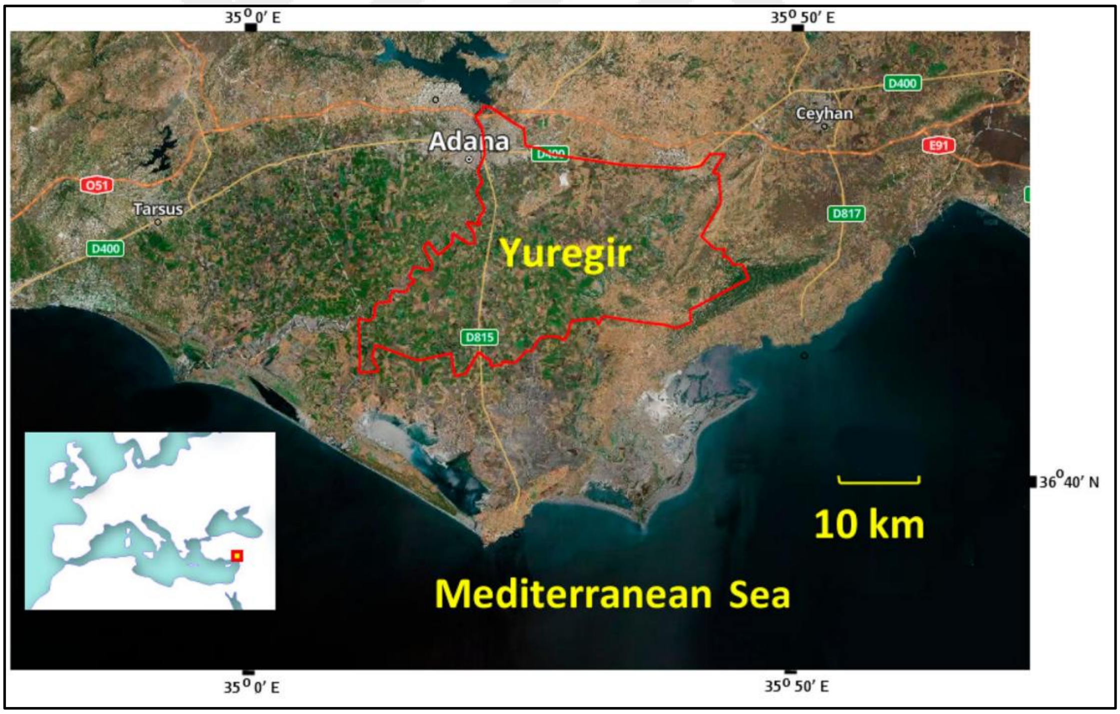

Figure 2.4. Yuregir plain (Shamloo et al., 2021)

Long et al. (2011), as well as Laipelt et al. (2020), reported that the standard SEBAL algorithm is more sensitive to the near-surface temperature gradient and less sensitive to meteorological inputs. While regions like North America and Europe benefit from extensive monitoring networks that yield high-quality meteorological data, other areas of the world lack the dense network of localized measurements required for precise ET_a estimations, as highlighted in studies by Fick and Hijmans (2017) and Menne et al. (2012). Therefore, the GeeSEBAL platform is established as an open-source implementation for ET_a estimation based on the SEBAL model at a resolution scale of 30 m through the GEE platform. The GeeSEBAL application relies on Landsat images and global meteorological data from ERA5 Land reanalysis. Several studies have been carried out to estimate ET_a using GeeSEBAL under different climatic conditions.

In the research conducted by Laipelt et al. (2021), GeeSEBAL emerged as a novel tool within the GEE platform for implementing the SEBAL model. The study applied and validated this tool across various biomes in Brazil by comparing daily ET_a estimates with eddy covariance (EC) data obtained from 10 flux towers. By leveraging 224 Landsat images and ERA5 Land meteorological data, the results demonstrated that GeeSEBAL holds substantial promise for long-term assessment of actual evapotranspiration (ET_a) in various regions. This potential might be attributed to its lower sensitivity to meteorological inputs, evidenced by an average root mean square deviation (RMSD) of 0.71 mm day^{-1} when using in situ meteorological measurement. Moreover, GeeSEBAL demonstrated its capability to evaluate ET_a across diverse Brazilian biomes over extended periods, thereby contributing to an enhanced comprehension of the effects of land cover changes on ET_a in recent decades.

In the research by Henrique et al. (2022), the effectiveness of GeeSEBAL was confirmed through validation against eddy covariance measurements obtained from five flux towers in the southern Brazil region. The study utilized 132 cloud-free Landsat images and gridded weather data within the GeeSEBAL framework. The findings highlighted that GeeSEBAL represents a viable option for estimating ET_a in croplands and managing water resources, particularly in subtropical humid climates and regions with limited data availability.

The study conducted by Gonçalves et al. (2022) utilized GeeSEBAL to estimate ET_a in a 24-hectare commercial field located in the western region of São Paulo state, Brazil. The field, situated at latitude 20°43'43.6" S and longitude 51°16'30.3" W, is approximately 360 m above mean sea level. The study focused on sugarcane and monitored two growing seasons from June 2016 to June 2018. In total, 77 Landsat images and ERA5-Land data were utilized as input data for the GeeSEBAL platform. The SEB components (latent heat (LE), net radiation (R_n), sensible heat flux (H), and soil heat flux (G)) modeled using the GeeSEBAL model exhibited strong agreement with values obtained from the eddy covariance system, considering both satellite overpass time and modeled ET_a throughout the growing seasons. As a result, the K_c values demonstrated comparable performance to those measured and reported by Allen et al. (1998).

Pakdel et al. (2023) utilized the GeeSEBAL platform to produce ET_a maps across the Lockyer Catchment in Australia, spanning an area of 3,000 km^2. Their study employed ER5A reanalysis data with a spatial resolution of 9 km alongside Landsat satellite images with a resolution of 30 m, covering long-term periods. The findings revealed a significant correspondence between ET_a derived from GeeSEBAL and ET_o.

As recognized, the conventional METRIC and SEBAL models necessitate multiple input datasets like DEM, T_s, NDVI, albedo, emissivity, and climatic variables, among others. Nevertheless, these datasets entail preprocessing before applying these models, typically conducted by proficient experts with RS techniques (Foolad et al., 2018). Consequently, an alternative approach employing the vegetation index method has been devised to produce ET_a maps, requiring fewer input parameters. The vegetation index method (Kamble et al., 2013; El-shirbeny et al., 2015; Reyes-González et al., 2018) is based on the relationship between crop coefficient (K_c) and NDVI to generate a new crop coefficient ($K_{c\text{-}NDVI}$).

Kamble et al. (2013) conducted research where they established a straightforward linear correlation between NDVI derived from moderate resolution imaging spectroradiometer data (MODIS) and K_c calculated from flux data obtained for various crops (including maize, grass, and soybean) and different cropping practices across three growing seasons in 2006 and 2007, using AmeriFlux towers in the USA. The study aimed to develop a relationship between NDVI and K_c for rainfed and irrigated agriculture. Validation of the developed regression model ($K_{c\text{-}NDVI}$= 1.4571×NDVI-0.1725) showed a strong correlation between the estimated crop coefficient (K_c) derived from the $K_{c\text{-}NDVI}$ relationship and the measured K_c values, with r values of 0.954 and 0.949 for 2006 and 2007, respectively. The RMSE at irrigated maize field for K_c was 0.16 in 2006 and 0.19 in 2007. However, there was a systematic bias of approximately ±5%, possibly attributable to variations in crop evapotranspiration due to wet conditions in 2006 and dry conditions in 2007, which were not accounted for in the K_c formulation used in the study.

In the research conducted by Reyes-Gonzalez et al. (2015), RS proved to be a valuable tool in the Region of Laguna, Mexico, for generating updated K_c based on NDVI and for estimating ET_a. The study involved deriving new K_c values for maize and alfalfa by establishing the relationship between NDVI extracted from satellite imagery and K_c values obtained from the FAO-56 database (Allen et al., 1998). This is known as the $K_{c\text{-}NDVI}$ method. Through the $K_{c\text{-}NDVI}$ method, which involved multiplying these newly derived regional K_c values with ET_o, ET_a was estimated. The findings demonstrated a robust correlation between NDVI and K_c-FAO-56 for both forage crops. The $K_{c\text{-}NDVI}$ method was shown to be capable of estimating ET_a with minimal input data. Furthermore, the introduction of new K_c values has the potential to optimize irrigation water usage and promote water resource conservation efforts.

In the study presented by Reyes-González et al. (2018), the $K_{c\text{-}NDVI}$ method was applied with the METRIC model to calculate ET_a in eastern South Dakota in the USA during the 2015 and 2016 growing seasons. The $K_{c\text{-}NDVI}$ method uses two input parameters (K_c and NDVI) to compute ET_a. The METRIC model uses four primary input parameters: a) Landsat image, b) DEM map, c) land cover map, and d) weather data to estimate ET_a. The comparison showed that ET_a values calculated by the METRIC model were higher than the ET_a values estimated with the $K_{c\text{-}NDVI}$ method by 18 and 11%

for the 2015 and 2016 growing seasons, respectively. The $K_{c\text{-}NDVI}$ method can estimate ET_a with minimum input parameters at focused regional and field scales for short periods.

Kumar et al. (2021) developed a straightforward relationship between K_c derived from Landsat data and NDVI to establish a new K_c for the Kangsabati River basin in eastern India during 2014–2015. The study utilized six multi-date, cloud-free Landsat 8 images with path and rows 139/44 and 139/45. The Vegetation Index-based ET_a estimates were evaluated against lysimeter data for different crop growth stages throughout the season. The result showed a strong determination coefficient between ET_a estimated using vegetation-based K_c vs. lysimeter ET_a ($R^2 = 0.81$) and crop coefficient FAO 56 Penman-Monteith (ET_c/ET_a) vs. lysimeter ET_a ($R^2 = 0.63$). For the relationship between the vegetation-based crop coefficient and lysimeter-measured ET_a, the slope was 1.01, and the intercept was -0.15. The slope and intercept for the FAO-56 Penman-Monteith crop coefficient (ET_c) versus lysimeter-measured ET_a were 0.65 and 0.70, respectively.

Research conducted across various regions worldwide, including Türkiye, indicates that while many studies yield comparable results, notable differences also exist between ET_a estimates derived from SEB models and those obtained through direct measurement methods. Nonetheless, a common theme among these studies is comparing and evaluating different approaches for estimating crop water requirements. These studies consistently highlight the substantial agreement between remote sensing-based actual evapotranspiration (RS-ET_a) models and traditional crop evapotranspiration (ET_c/ET_a) methods. Such approaches are preferred to effectively manage spatial variability and provide more reliable and accurate estimates, especially for large-scale environmental and water resource evaluations.

3. MATERIALS AND METHODS

This section thoroughly examines the Lower Seyhan Plain (LSP), concentrating on its geographical characteristics, climatic factors, and surface water reservoir availability. Additionally, it briefly discusses the agricultural patterns observed in two specific areas within the LSP. The final part of this section introduces the remote sensing evapotranspiration (RS-ET_a) methodology in detail and the data sets used in this research study.

3.1. Study Area

The research area, commonly known as Yuregir Plain, constitutes a segment of the LSP within the Eastern Mediterranean region of Türkiye, encompassing a total expanse of 1,434 km^2; this area is situated along the southern coastal Mediterranean region close to the Adana province of Türkiye, as illustrated in Figure 3.1. It is located between the Seyhan (on the west) and Ceyhan (on the east) rivers, which is flat terrain with a slope of 0.5-1.0 % (Ozcan and Cetin, 1996; Ozcan et al., 2003). The highest altitude within the LSP reaches approximately 30 m above sea level. The study area comprises two regions: the Akarsu Irrigation District (AID; non-stressed, i.e., NSA, Figure 3.1) area, covering 9,495 ha under normal standard conditions (non-stressed area), and the second region, i.e., non-standard development (53,000 ha; stressed area, i.e., SA, Figure 3.1) situated adjacent to the Eastern Mediterranean Region of Türkiye.

The Mediterranean climate, prevalent across the LSP, is characterized by hot and arid summers, contrasted with mild and rainy winters, as outlined by Cetin et al. (2007, 2020). According to Cetin et al. (2020), the basin receives an annual average precipitation of 650 mm. The region experiences an average temperature of approximately 19°C, with January marking the coldest month at around 9°C on average, while August is the warmest month with an average temperature of 29°C. Alsenjar et al. (2023b) reported a notable increase in temperature and evaporation (E) rates during the irrigation season (IS), particularly in July and August, compared to the rainy seasons in the Eastern Mediterranean Region of Türkiye. According to Cetin et al. (2020), relative humidity typically exceeds 80% during summer, whereas it falls below 50% in periods without rainfall and irrigation. In Türkiye, the winter typically spans from December 1st to late February, while the summer season extends from June 1st until the end of August (Alsenjar et al., 2023a; Alsenjar et al., 2023b; Cetin et al., 2023b). However, as a typical consequence of the Mediterranean climate, there is no clear transition between seasons in and around the study area.

In the study area, there are two distinct geological age categories. The first category encompasses a variety of ages, including limestones, conglomerates, and marl, while the second category comprises Holocene deposited alluvial materials (Cetin et al., 1999). The region near the Mediterranean Sea experiences persistent soil salinity and alkalinity issues, along with a high groundwater table characterized by significant salinity concerns. In contrast, the other part of the study area (AID, i.e., NSA) has no high salinity values (Cetin et al., 2000). Within the AID area, soil pH ranges from 7.61 to 7.87, and soil saturation extract electrical conductivity (EC) fluctuates between 0.12 and 0.19 dS m^{-1}. In other words, the soils within the AID of the research area are generally categorized as having low or minimal salinity. In the AID, there are five soil types, namely the Arikli (33.99%), Incirlik (28.22%), Yenice (14.65%), Gemisure (6.27%), and Canakci (6.06%) soil series. These soil series collectively account for 89.19% of the AID and cover the entire study area. According to Dinç et al. (1995), the Arikli series exhibits clay content ranging from around 55-67%, the Canakci series from 22-35%, the Incirlik series from 60-62%, the Yenice series from 51-58%, and the Gemisure series from 72-77% within the AID. The second part of the study area is located in the coastal lagoons (Akyatan, Tuzla) of the LSP. This area exhibits elevated concentrations of saline water in combination with unsuitable soil conditions (Akça et al., 2020) for irrigated agriculture as well as traditional agricultural practices. In the stressed region surrounding the coastal logons of the LSP, a range of soil types exists, encompassing Arikli, Arpaci, Mursel, Oymakli, Canakcı, Helvaci, Gemisure, Pekmez, Baharli, Golyaka, Karatas, and Ismailiye (Dinç et al., 1990; Dinç et al., 1991a; Dinç et al., 1991b). In 2009, the region underwent irrigation facilitated by DSI (State Hydraulic Works), officially designated as the 4^{th} Stage Irrigation Area. The study area has many irrigation and drainage canals and a myriad of drainage observation wells (Cetin et al., 2000) under the responsibility of the water user association. The DSI diverted irrigation water to the research site from Seyhan Dam, characterized by high-quality water attributes with an EC ranging from 0.4 to 0.5 dS m^{-1} (Çetin and Kirda, 2003; Akça et al., 2020).

The Seyhan Plain holds significant agricultural promise for the Turkish economy, with most of its territory designated irrigated zones. The research area encompasses various crop varieties, including but not exclusively limited to citrus fruits, soybeans, peanuts, corn, cereals, cotton, potatoes, watermelon, onions, pasture, and vegetables. Predominant winter crops consist of wheat, onions, potatoes, and lettuce, while summer crops are mainly cotton, soybeans, corn, peanuts, and watermelon. Furthermore, citrus orchards occupy a significant portion of the study area (Ozcan et al., 2003; Alsenjar et al., 2023b). Figure 3.2 illustrates the typical crops cultivated in the study area, depicting their growing periods and the durations of different growth stages, including initial, development, mid-season, and late-season phases (TAGEM-DSI, 2017; Cetin et al., 2023b).

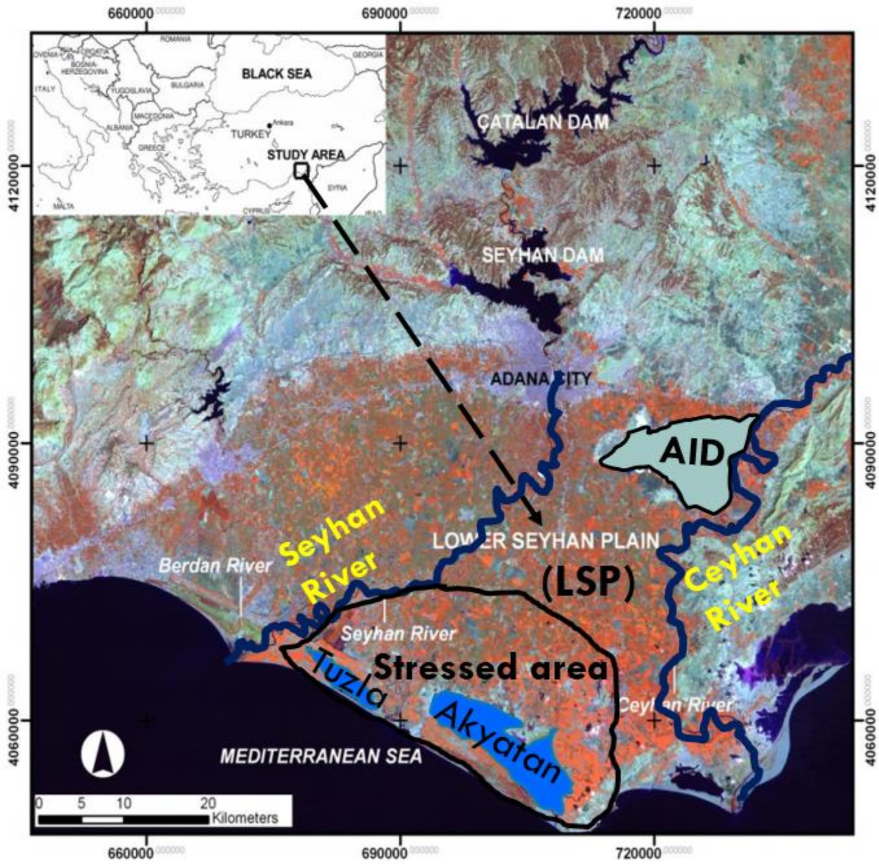

Figure 3.1. The study area location in the Lower Seyhan Plain (LSP) of the Mediterranean Region in Türkiye

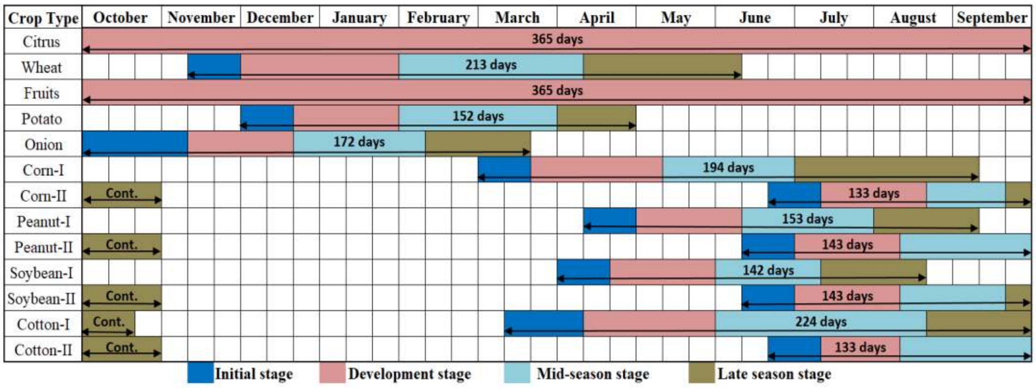

Figure 3.2. The prevalent crop varieties cultivated, their respective cultivation periods, and the duration of distinct growth stages, including initial, development, mid-season, and late-season phases in the research area (Cetin et al., 2023b)

3.2. Datasets

The chosen study area encompasses the flat terrain of the LSP. This research utilizes meteorological data, high-resolution remote sensing data, field surveys to identify crop types during growth periods, and standard crop coefficients (K_c). All data employed in this study, including meteorological records, remote sensing data, field observations, and K_c, will be elaborated upon in subsequent sections. Figure 3.3 illustrates the datasets employed in this study, each of which will be elaborated upon in the subsequent sections.

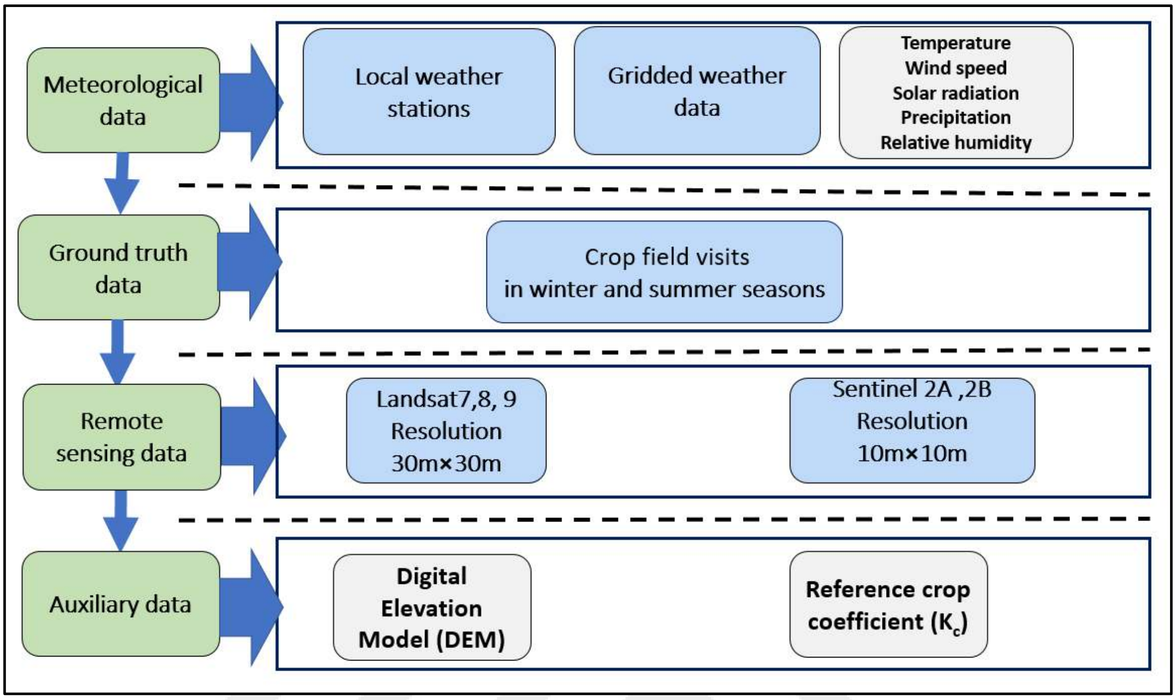

Figure 3.3. Data sources and inputs utilized in this study

3.2.1. Meteorological data

This study relies on the standard METRIC and SEBAL models, ET_c estimations, and $K_{c\text{-}NDVI}$ that necessitate local climatic data at hourly and daily intervals during the 2020-2023 water years. Figure 3.4 illustrates the sites of used meteorological stations across the study area, encompassing the Akarsu region and the stressed area within the LSP. Meteorological data typically include parameters such as temperature (°C), relative humidity (%), precipitation (mm), wind speed (m s^{-1}) at 2 m height, and solar radiation (W m^{-2}); they were obtained from stations situated within the study area. Specifically, two meteorological stations, L8 and Cotlu, located within the AID, and one station (Agzibuyuk-Cotlu) near the AID (refer to Figure 3.4) were utilized to compute ET_o. Additionally, meteorological stations at Golkaya, Gumusyazi, and Bebeli were employed to gather climatic variables for running the SEB models and conducting ET_o calculations in the stressed region adjacent to the coastal lagoons of the LSP. On the other hand, the EEFlux-METRIC and GeeSEBAL models utilize CFSV2 gridded weather data with a spatial resolution (4 km ×4 km) on a global scale and global weather data sourced from the ERA5 land reanalysis dataset with a spatial resolution (9 km× 9 km), respectively. Climatic data underwent quality control (QC) checks spanning the water years from 2020 to 2023. This process entails verifying and guaranteeing data or procedures' accuracy, reliability, and consistency. Specifically, this includes addressing issues such as data gaps, outliers, constant values, and abrupt changes or jumps in the data. This study utilizes climatic data during the

2020-2023 water years to improve ET_a estimation accuracy using remote sensing-based models validated with direct measurements and ET_c calculations. The study does not assess long-term climatic variability, as RS-based models rely on meteorological data during satellite overpass dates rather than extended time series.

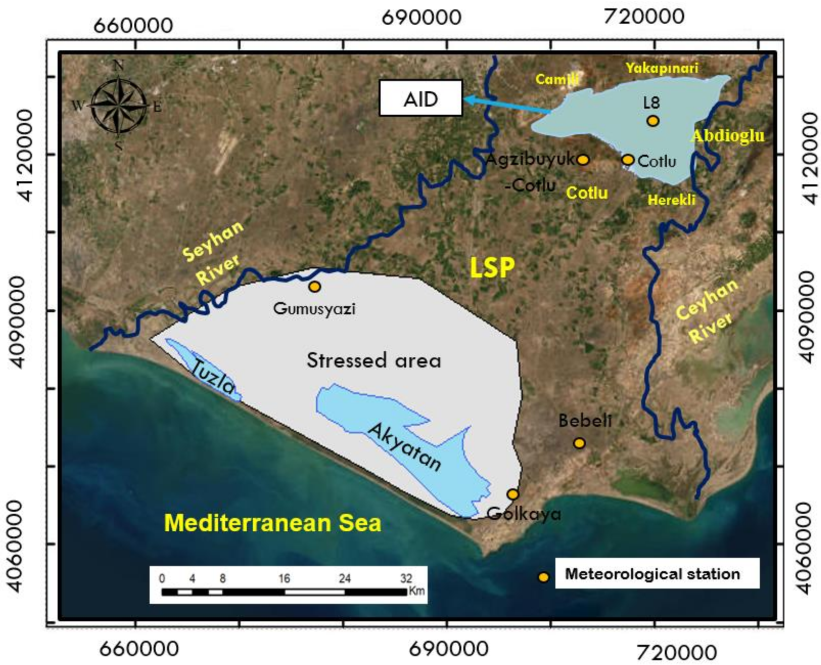

Figure 3.4. Study area and location of meteorological stations

3.2.2. Ground truth data of crops

Ground truth data, also termed field visits or observations for cropping pattern mapping, encompass firsthand information collected through physical visits and direct observations within the study area. This methodology entails gathering data directly from the study area, including details regarding crop types, land use patterns, and other pertinent parameters. Ground truth data play a crucial role in validating RS data, calibrating models, and improving the accuracy of analyses and predictions. Regarding cropping patterns, ground truth data or field visits entail observing and documenting cultivated crop types, their spatial distribution, growth stages, and the farming practices implemented by agricultural practitioners. Ground truth data are needed to validate crop type classification obtained through remote sensing, allowing for estimating crop water requirements (ET_c) for each crop type and the study area. Furthermore, observations of crop types (ground truth data) are utilized to estimate ET_a using Surface Energy Balance (SEB) models at both pixel and study area scales.

Ground truth data were gathered from the Akarsu district and specific plots near the lakes of the Yuregir Plain within the LSP during the growing seasons spanning the 2020-2023 water years. This collection was conducted considering the onset of the irrigation season and the peak irrigation period, representing two distinct production phases. All field investigations/campaigns involved the observation of cultivated crops and bare soil or fallow fields, with vegetation noted on a map representing the study area. Subsequently, the coordinates of each visited parcel were recorded using handheld GPS devices (GPS essentials program) [UTM, Datum=WGS84] and duly stored. After the fieldwork, the terrestrial data were transferred to a computer environment using the ArcGIS program. This process facilitated identifying the distribution of winter and summer crops (land-use types) within the visited parcels. Figure 3.5 illustrates the overall spatial arrangement of crops determined through on-site visits in both the AID location and the stressed region of the LSP. Table 3.1 and Table 3.2 indicate the number of parcels visited during the study period in both the non-stressed area (NSA) and the stressed area (SA). Additionally, photographs were taken to establish the types of crops as accurate data for crop identification during field visits conducted every twice per water year, i.e., winter and summer seasons in regions (AID, i.e., NSA) under normal conditions and in areas experiencing stress throughout the research period, as illustrated in Figure 3.6- Figure 3.9.

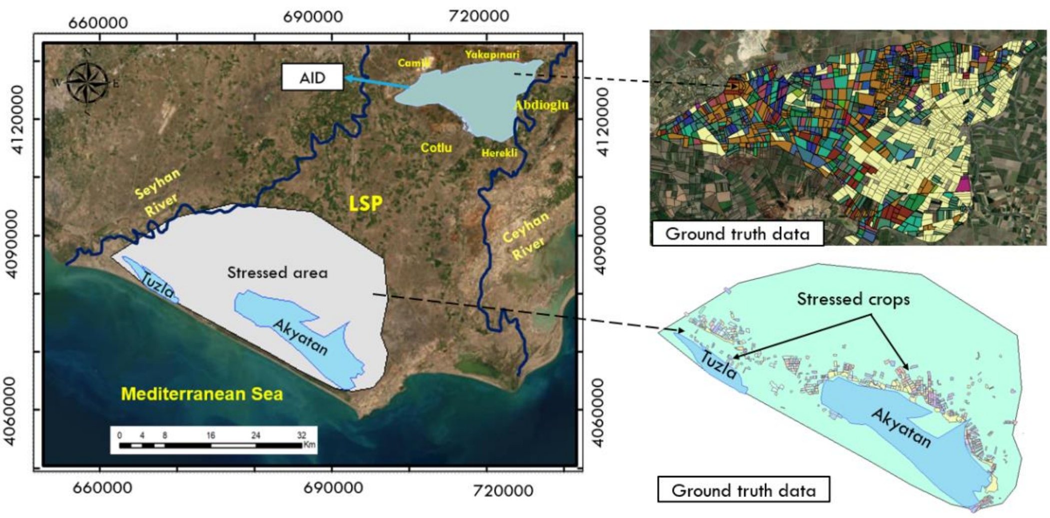

Figure 3.5. General spatial distribution of ground truth data of crops, which was observed in both the AID location and the stressed region of the LSP during field visits

Figure 3.6. In-situ images of various crops collected for ground truth data to identify crop type in fields on 26.04 2022 over the AID of the LSP

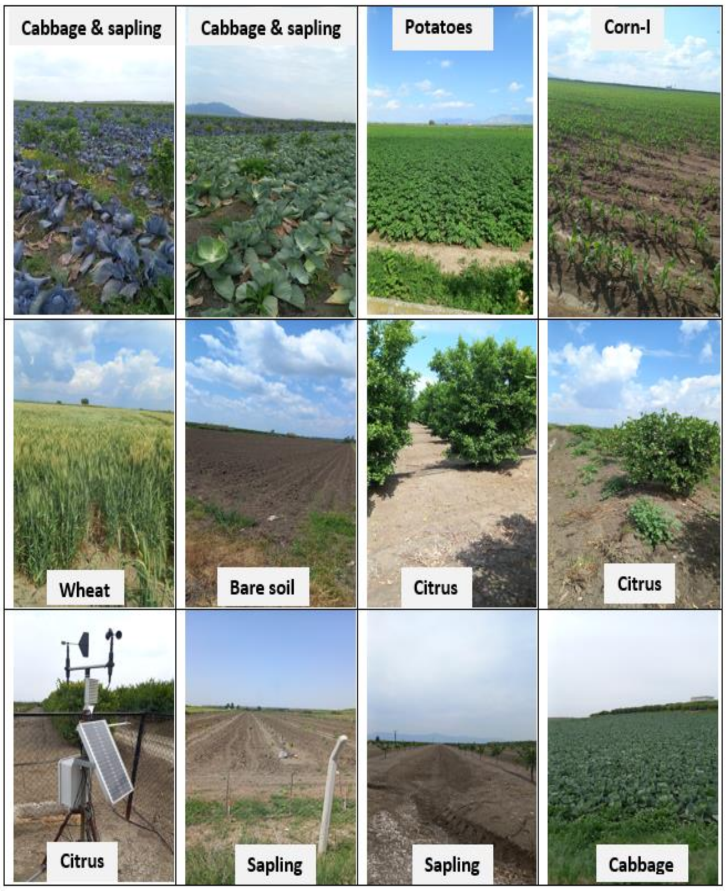

Figure 3.7. In-situ images of various crops collected for ground truth data to identify crop type in field on 24.04. 2023 over the AID of the LSP

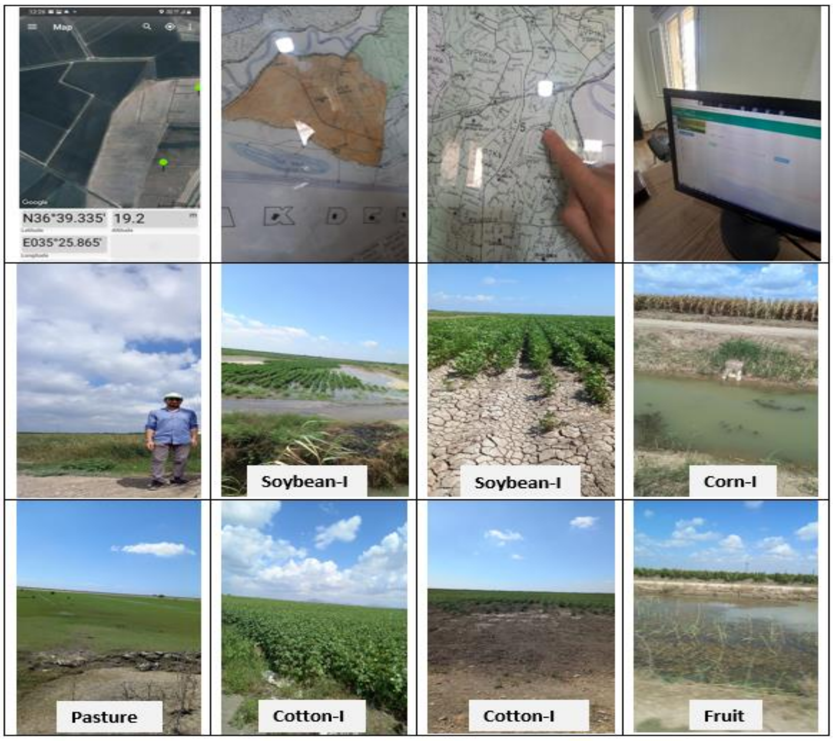

Figure 3.8. In-situ images of various crops collected for ground truth data to identify crop type in field on 25.08. 2022 over the stressed area near the coastal lagoons of the LSP

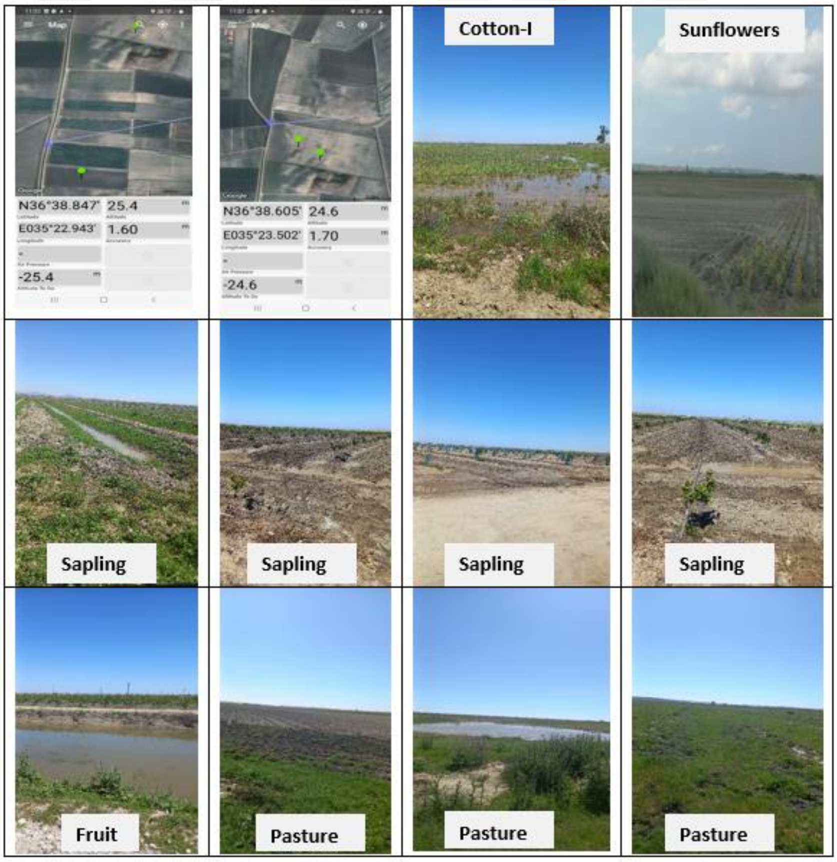

Figure 3.9. In-situ images of various crops collected for ground truth data to identify crop type in field on 31.03.2023 and 03.08.2023 over the stressed area near the coastal lagoons of the LSP

Table 3.1. The number of parcels visited over AID during four consecutive water years (2020, 2021, 2022 and 2023)

	2020		2021		2022		2023	
Crop	**Winter**	**Summer**	**Winter**	**Summer**	**Winter**	**Summer**	**Winter**	**Summer**
Cereals	159	0	200	0	252	0	238	0
Fruit (pomegranate, apricot, peach, date and plum)	16	14	18	10	15	19	23	31
Bare soil	432	25	369	27	405	42	426	20
Citrus	617	631	622	626	574	556	554	558
Potatoes	38	0	28	0	22	0	25	0
Onion	16	0	26	0	6	0	17	0
Others	0	9	4	1	7	9	7	4
Peanut-I	0	83	0	129	0	49	0	67
Peanut-II	0	44	0	40	0	38	0	93
Sapling	31	26	49	64	153	182	203	215
Corn-I	0	202	0	228	0	257	0	302
Corn-II	0	61	0	32	0	23	0	48
Cotton-I	0	67	0	74	0	80	0	42
Cotton-II	0	42	0	75	0	108	0	63
Soybean-I	0	29	0	26	0	15	0	7
Soybean-II	0	57	0	119	0	81	0	69
Watermelon - Melon	0	0	0	3	0	4	0	4
Total	**1,309**	**1,290**	**1,316**	**1,454**	**1,434**	**1,463**	**1,493**	**1,523**

Table 3.2. The number of parcels near the lagoons/lakes of the Lower Seyhan Plain visited during four consecutive water years (2020, 2021, 2022 and 2023) over the stressed area

	2020		2021		2022		2023	
Crop	**Winter**	**Summer**	**Winter**	**Summer**	**Winter**	**Summer**	**Winter**	**Summer**
Cereals	49	0	69	0	47	0	34	0
Fruit (pomegranate, apricot, peach, date and plum)	3	3	4	4	5	5	6	6
Bare soil	90	90	95	95	91	91	98	98
Citrus	67	67	67	67	67	67	70	70
Potatoes	0	0	0	0	0	0	1	0
Onion	0	0	0	0	0	0	0	0
Others	15	0	13	0	5	0	6	0
Peanut-I	0	9	0	15	0	9	0	17
Peanut-II	0	2	0	0	0	0	0	16
Sapling	138	138	151	151	170	170	172	172
Corn-I	0	36	0	20	0	11	0	51
Corn-II	0	0	0	1	0	2	0	3
Cotton-I	0	66	0	45	0	64	0	62
Cotton-II	0	25	0	28	0	28	0	17
Soybean-I	0	10	0	3	0	4	0	5
Soybean-II	0	9	0	13	0	5	0	2
Watermelon - Melon	0	0	0	0	0	0	0	4
Total	**362**	**455**	**399**	**442**	**385**	**456**	**387**	**523**

3.2.3. Remotely sensed data

Over the past few decades, Landsat has become an important operational satellite for Earth observation. Its notable high spatial resolution images have led to extensive utilization of them across various research and non-research domains. In this study, 70 Landsat satellite scenes (path 175, rows 34 as shown in Figure 3.10) with a spatial resolution of 30 m by 30 m were downloaded from the United States Geological Survey (USGS) Earth Explorer website (www.earthexplorer.usgs.gov, accessed on 16 February 2023 and 18 October 2023) to cover the period from 30.09.2019 to 30.09.2023. Landsat imagery, commonly accessible at 8 to 16-day intervals, encompasses satellite scenes from Landsat 7 (Enhanced Thematic Mapper Plus, i.e., ETM^+), Landsat 8, and Landsat 9. These satellites have two sensors onboard: a) a Thermal Infrared Sensor (TIRS) and b) an Operational Land Imager (OLI), which gathers data almost simultaneously. Figure 3.11 compares the OLI and thermal spectral bands to Landsat satellite images. Table 3.3 shows both Landsat 7, Landsat 8, and Landsat 9 shortwave and thermal bands. Table 3.4 lists the dates of the 70 Landsat satellite images used in this research, along with their corresponding day of the year (DOY). Subsequently, the Environment for Visualizing Images (ENVI) software was used to apply a cloud mask when cloud coverage exceeded 50% on four satellite image dates, specifically on DOY 28, DOY 60, DOY 121, and DOY 030 of grayscale fill, as shown in Table 3.4. Before using Landsat 7 ETM^+ data, any scan line errors were rectified, and gaps were filled using Quantum Geographic Information System (QGIS 3.24.3) and the Landsat toolbox within ArcGIS 10.4.1. These images were utilized to estimate ET_a using RS data in conjunction with hourly and daily climatic variables sourced from meteorological stations within the study area. This study quantifies errors in satellite data (radiometric calibration, atmospheric corrections, and geometric rectifications) before applying the SEB models. It also performs quality control on meteorological data to assess potential deviations in ET_a estimates. All corrections were made before applying these models.

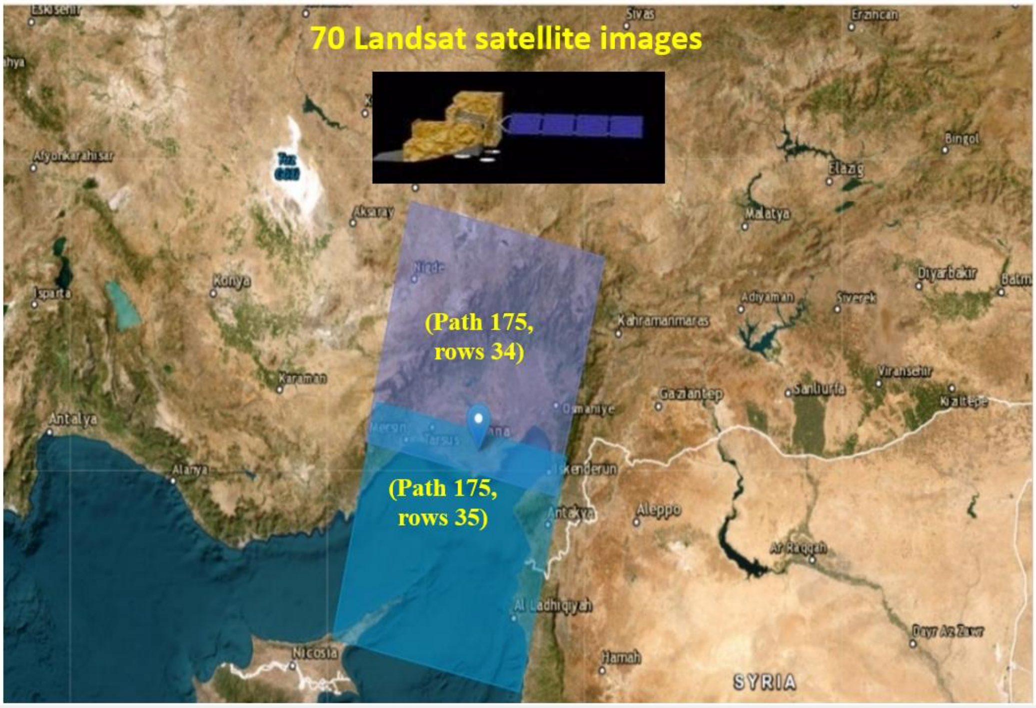

Figure 3.10. Landsat tiles that encompass the research area

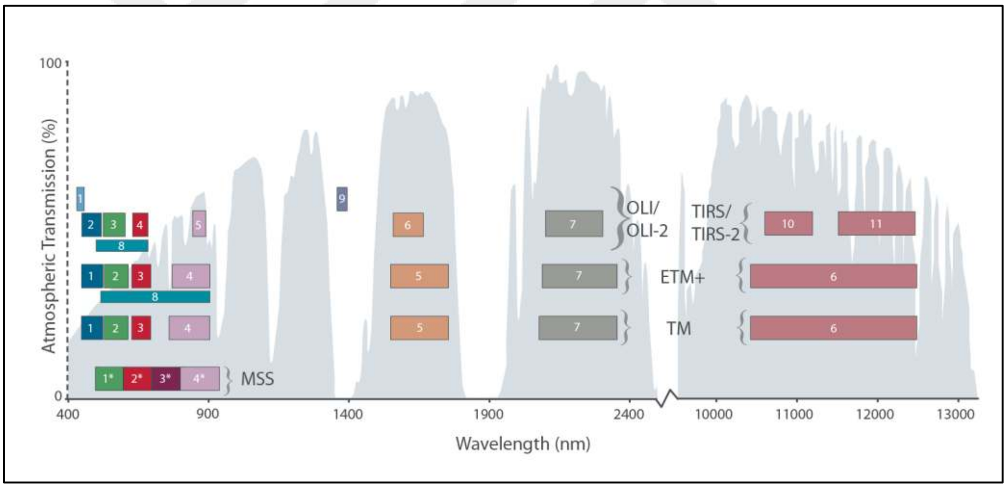

Figure 3.11. Landsat sensors, spectral channels, and band passes are superimposed on atmospheric transmission percentage (grey background). MSS: Landsat 1 through -5; TM: Landsat 4 and 5; ETM^{+}: Landsat 7; OLI and TIRS: Landsat 8 and 9. (source: NASA/Landsat Legacy Project Team and American Society for Photogrammetry and Remote Sensing)

Table 3.3. Spectral bands, including a pan band for Landsat 7, Landsat 8, and Landsat 9

<table>
<tr><th colspan="4">Landsat 7 Enhanced Thematic Mapper</th><th colspan="4">Landsat 8 and Landsat 9 OLI and TIRS Sensors</th></tr>
<tr><th>Band No.</th><th>Description</th><th>Wavelength</th><th>Resolution (m)</th><th>Band No.</th><th>Description</th><th>Wavelength</th><th>Resolution (m)</th></tr>
<tr><td>Band 1</td><td>Visible blue (Blue)</td><td>0.45 to 0.52 µm</td><td>30</td><td>Band 1</td><td>Coastal / Aerosol</td><td>0.433 to 0.453 µm</td><td>30</td></tr>
<tr><td>Band 2</td><td>Visible green (Green)</td><td>0.52 to 0.60 µm</td><td>30</td><td>Band 2</td><td>Visible blue (Blue)</td><td>0.450 to 0.515 µm</td><td>30</td></tr>
<tr><td>Band 3</td><td>Visible red (Red)</td><td>0.63 to 0.69 µm</td><td>30</td><td>Band 3</td><td>Visible green (Green)</td><td>0.525 to 0.600 µm</td><td>30</td></tr>
<tr><td>Band 4</td><td>Near-infrared (NIR)</td><td>0.76 to 0.90 µm</td><td>30</td><td>Band 4</td><td>Visible red (Red)</td><td>0.630 to 0.680 µm</td><td>30</td></tr>
<tr><td>Band 5</td><td>Near-infrared (SWIR-1)</td><td>1.55 to 1.75 µm</td><td>30</td><td>Band 5</td><td>Near-infrared (NIR)</td><td>0.845 to 0.885 µm</td><td>30</td></tr>
<tr><td>Band 6</td><td>Thermal (TIR)</td><td>10.4 to 12.3 µm</td><td>60</td><td>Band 6</td><td>Short wavelength infrared (SWIR-1)</td><td>1.56 to 1.66 µm</td><td>30</td></tr>
<tr><td>Band 7</td><td>Mid-infrared (SWIR-2)</td><td>2.08 to 2.35 µm</td><td>30</td><td>Band 7</td><td>Short wavelength infrared (SWIR-2)</td><td>2.10 to 2.30 µm</td><td>60</td></tr>
<tr><td>Band 8</td><td>Panchromatic (Pan)</td><td>0.52 to 0.90 µm</td><td>15</td><td>Band 8</td><td>Panchromatic (Pan)</td><td>0.50 to 0.68 µm</td><td>15</td></tr>
<tr><td colspan="4" rowspan="4">-</td><td>Band 9</td><td>Cirrus</td><td>1.36 to 1.39 µm</td><td>30</td></tr>
<tr><th>Band No.</th><th>Description</th><th>Wavelength</th><th>Resolution (m)</th></tr>
<tr><td>Band 10</td><td>Long wavelength infrared (TIR-1)</td><td>10.3 to 11.3 µm</td><td>100</td></tr>
<tr><td>Band 11</td><td>Long wavelength infrared (TIR-2)</td><td>11.5 to 12.5 µm</td><td>100</td></tr>
</table>

Table 3.4. Landsat scenes information (Landsat 7, Landsat 8, and Landsat 9) during the water years of 2020-2023, including scene names, acquisition dates, and overpass times

Image No.	Day of the year (DOY)	Landsat scene_ID	Landsat satellite type	Cloud Cover %	Acquisition dates	Overpass local Time (AM)	Water year
1	273	LC81750342019273LGN00	8	0	30.9.2019	11:16:02.5052379	
2	297	LE71750342019297SG100	7	16	24.10.2019	10:59:54.3561211	
3	321	LC81750342019321LGN00	8	4	17.11.2019	11:16:01.7353690	
4	353	LC81750342019353LGN01	8	1	19.12.2019	11:15:58.3225900	
5	28	LE71750342020028NPA00	7	**67**	28.01.2020	10:55:13.3874493	
6	60	LE71750342020060SG100	7	**66**	29.02.2020	10:53:33.8472536	
7	68	LC81750342020068LGN00	8	2	08.03.2020	11:15:36.2460760	
8	108	LE71750342020108SG100	7	6	17.04.2020	10:50:52.5176873	2020
9	148	LC81750342020148LGN00	8	4	27.05.2020	11:15:08.7684079	
10	180	LC81750342020180LGN00	8	1	28.06.2020	11:15:26.9694210	
11	196	LC81750342020196LGN00	8	1	14.07.2020	11:15:33.4238989	
12	212	LC81750342020212LGN00	8	0	30.07.2020	11:15:37.9038700	
13	228	LC81750342020228LGN00	8	0	15.08.2020	11:15:42.0945460	
14	244	LC81750342020244LGN00	8	0	31.08.2020	11:15:50.3682170	
15	260	LC81750342020260LGN00	8	1	16.09.2020	11:15:56.5028510	
16	300	LE71750342020300SG100	7	8	26.10.2020	10:38:56.1154274	
17	316	LE71750342020316NPA00	7	3	11.11.2020	10:37:51.0228172	
18	364	LE71750342020364NPA00	7	1	29.12.2020	10:34:21.8153233	
19	22	LC81750342021022LGN00	8	9	22.01.2021	11:15:49.9861710	
20	54	LC81750342021054LGN00	8	7	23.02.2021	11:15:43.2139690	
21	79	LE71750342021078SG100	7	5	19.03.2020	10:28:24.8443048	
22	118	LC81750342021118LGN00	8	8	28.04.2021	11:15:15.8809360	
23	134	LC81750342021134LGN00	8	1	14.05.2021	11:15:15.9098560	2021
24	158	LE71750342021158SG100	7	1	07.06.2021	10:21:43.6865663	
25	182	LC81750342021182LGN00	8	4	01.07.2021	11:15:35.1871370	
26	190	LE71750342021190SG100	7	3	09.07.2021	10:19:04.5579664	
27	198	LC81750342021198LGN00	8	5	17.07.2021	11:15:36.9021800	
28	214	LC81750342021214LGN00	8	0	02.08.2021	11:15:45.3409259	
29	230	LC81750342021230LGN00	8	2	18.08.2021	11:15:51.0643500	
30	262	LC81750342021262LGN00	8	9	19.09.2021	11:15:59.0216650	
31	278	LC81750342021278LGN00	8	1	05.10.2021	11:16:04.4435930	
32	294	LC81750342021294LGN00	8	0	21.10.2021	11:16:07.4309270	
33	326	LC81750342021326LGN00	8	6	22.11.2021	11:16:02.0432969	
34	358	LC81750342021358LGN00	8	4	24.12.2021	11:15:59.4307040	
35	001	LE71750342022001NPA00	7	13	01.01.2022	10:03:01.7753300	
36	017	LE71750342022017NPA00	7	3	17.01.2022	10:01:30.1854341	
37	049	LE71750342022049NPA00	7	6	18.02.2022	09:58:18.1083401	
38	081	LE71750342022081NPA00	7	19	22.03.2022	09:55:10.7155745	
39	089	LC81750342022089LGN00	8	7	30.03.2022	11:15:25.6965150	2022
40	113	LC91750342022113LGN00	9	2	23.04.2022	11:15:26.7327310	
41	121	LC81750342022121LGN00	8	**60**	01.05.2022	11:15:28.7371250	
42	140	LE71750342022140SG100	7	12	20.05.2022	09:50:56.6332014	
43	157	LE71750342022157SG100	7	23	06.06.2022	09:50:06.2292853	
44	169	LC81750342022169LGN00	8	1	18.06.2022	11:15:53.3072380	
45	186	LE71750342022186SG100	7	0	05.07.2022	09:42:29.8002719	
46	201	LC81750342022201LGN00	8	1	20.07.2022	11:15:58.6410700	

Image No.	Day of the year (DOY)	Landsat scene_ID	Landsat satellite type	Cloud Cover %	Acquisition dates	Overpass local Time (AM)	Water year
47	209	LC91750342022209LGN00	9	0	28.07.2022	11:15:42.4933480	
48	220	LE71750342022220SG100	7	29	08.08.2022	09:39:50.3921524	
49	237	LE71750342022237SG100	7	9	25.08.2022	09:38:18.9640686	
50	249	LC81750342022249LGN00	8	8	06.09.2022	11:16:15.2109079	
51	271	LE71750342022271SG100	7	3	28.09.2022	09:34:51.9536731	
52	297	LC81750342022297LGN00	8	0	24.10.2022	11:16:18.0041120	
53	305	LE71750342022305NPA00	7	0	01.11.2022	09:30:39.7271478	
54	344	LE71750342022344SG100	7	33	10.12.2022	09:30:47.2239022	
55	361	LC81750342022361LGN00	8	6	27.12.2022	11:16:05.6881030	
56	030	LE71750342023030NPA00	7	**66**	30.01.2023	09:21:42.8842895	
57	052	LE71750342023052SG100	7	15	21.02.2023	09:22:38.4412600Z	
58	069	LE71750342023069SG100	7	46	10.03.2023	09:18:17.6146932	
59	091	LE71750342023091SG100	7	42	01.04.2023	09:17:34.3303402	
60	108	LC81750342023108LGN00	8	9	18.04.2023	11:15:12.8746539	
61	124	LC81750342023124LGN00	8	31	04.05.2023	11:15:07.6881360	2023
62	157	LE71750342023157SG100	7	32	06.06.2023	09:10:50.8614907	
63	172	LC81750342023172LGN00	8	27	21.06.2023	11:15:09.4635820	
64	196	LC91750342023196LGN00	9	0	15.07.2023	11:15:17.6790280	
65	212	LC91750342023212LGN00	9	4	31.07.2023	11:15:22.8236480	
66	228	LC91750342023228LGN00	8	2	16.08.2023	11:15:27.4594450	
67	236	LC81750342023236LGN00	8	2	24.08.2023	11:15:41.0675900	
68	244	LC91750342023244LGN00	9	11	01.09.2023	11:15:38.2409350	
69	268	LC81750342023268LGN00	8	0	25.09.2023	11:15:47.2496279	
70	284	LC81750342023284LGN00	8	0	11.10.2023	11:15:51.2437789	

3.2.4. Digital elevation model (DEM)

The Digital Elevation Model (DEM) data were obtained from the United States Geological Survey (USGS) website (http://earthexplorer.usgs.gov, accessed on 16 February 2023), with a spatial resolution of 30 m, which aligns well with Landsat data. The DEM served as input for SEB models. Typically, DEM is utilized in mountainous regions where its utility is crucial, but its necessity in flat areas for SEB models is less pronounced (Olmedo et al., 2016; Alsenjar et al., 2023b; Cetin et al., 2023a; Cetin et al., 2023b). Nevertheless, this study incorporated DEM to evaluate its impact on the outcomes and facilitate comparisons. Figure 3.12 depicts the DEM for the AID region and the stressed site within the LSP.

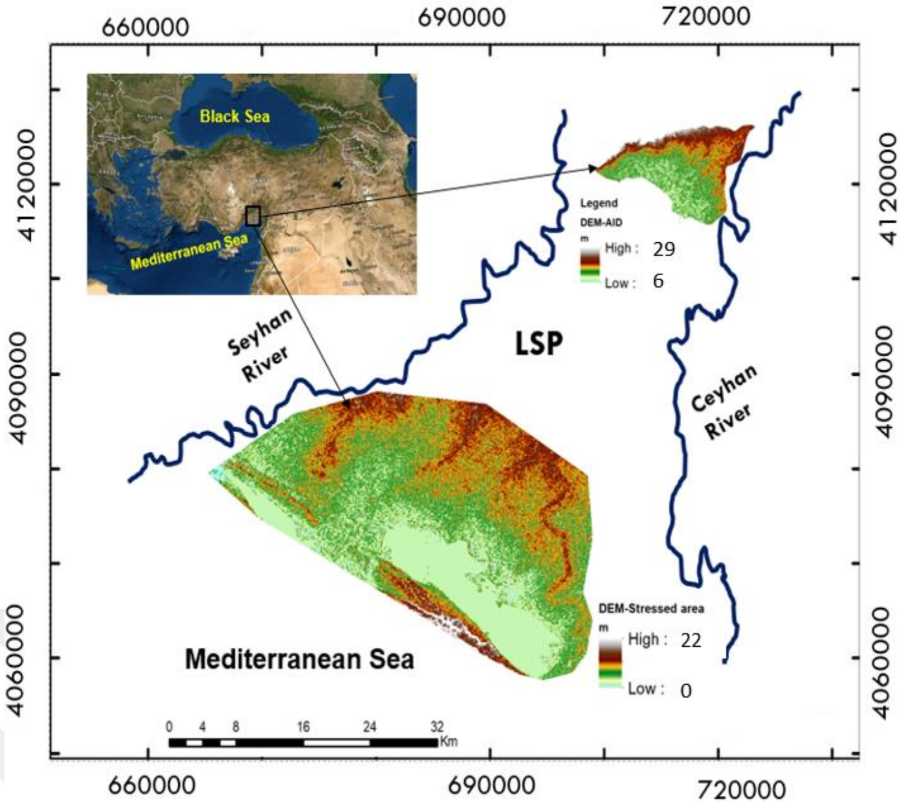

Figure 3.12. Digital elevation model (DEM) map for the study area in the LSP of Türkiye

3.2.5. Standard crop coefficient K_c

Crop coefficients (K_c) are crucial to determine precisely crop water requirements in an area. They are dimensionless values used to adjust reference evapotranspiration to reflect the specific water needs of different crops. The K_c values change throughout the growing season to match the crop's development stages, which include primarily the initial establishment, the mid-season (which encompasses the second and third stages), and the late-season. K_c were applied to each crop type across the study area. The standard K_c values were provided by the literature TAGEM (General Directorate of Agricultural Research and Policies) –DSI, i.e., State Hydraulic Works (2017), as shown in Table 3.5. Figure 3.13 shows that these K_c values were obtained from crop curves corresponding to each crop type grown during specific times and growth stages.

Table 3.5. Common crop types are grown in the study area, their growing periods and "length of crop growth stages" (Initial, developing, mid-season, and end-season), and corresponding K_c values (TAGEM-DSI, 2017; Cetin, 2020; Cetin et al., 2023b)

Crop type	Sowing-planting time	Period-I	Period-II	Period-III	Period-IV	Length Vegetation period	K_{cini}	K_{cmid}	K_{cend}
Wheat	11-Nov	20	62	71	60	213	0.84	1.11	0.2
Corn-I	01-Mar	20	50	50	74	194	0.45	1.14	0.27
Corn-II	21-Jun	20	40	30	43	133	0.33	1.14	0.31
Soybean-I	1-Apr	20	40	40	42	142	0.35	1.09	0.44
Soybean-II	11-Jun	20	40	40	43	143	0.36	1.1	0.46
Peanut-I	11-Apr	20	40	50	43	153	0.35	1.1	0.57
Peanut-II	11-Jun	20	40	50	33	143	0.36	1.11	0.57
Cotton-I	11-Mar	31	50	80	83	244	0.32	1.13	0.55
Cotton-II	21-Jun	20	30	40	43	133	0.32	1.13	0.55
Potatoes	1 Dec	20	40	60	32	152	0.89	1.11	0.71
Onion	1-Oct	41	40	51	40	172	0.56	0.97	0.97
Citrus	1-Jan	60	90	125	90	365	0.91	0.52	0.58
Watermelon-Melon	1-Apr	20	30	30	42	122	0.52	0.96	0.71
Lettuce	1-Oct	10	20	25	10	65	0.6	0.96	0.91
Sesame-II	12-Jun	20	31	40	21	112	0.37	1.04	0.2
Appel	21-Mar	20	41	118	49	228	0.52	0.87	0.68
Peach	21-Feb	30	50	115	40	235	0.59	0.87	0.69
Plum	11-Feb	30	40	118	49	237	0.47	0.88	0.69
Pomegranate	11-Mar	30	45	133	40	248	0.5	0.87	0.7
Fruit-Average	1-Mar	28	44	121	55	248	0.5	0.87	0.68

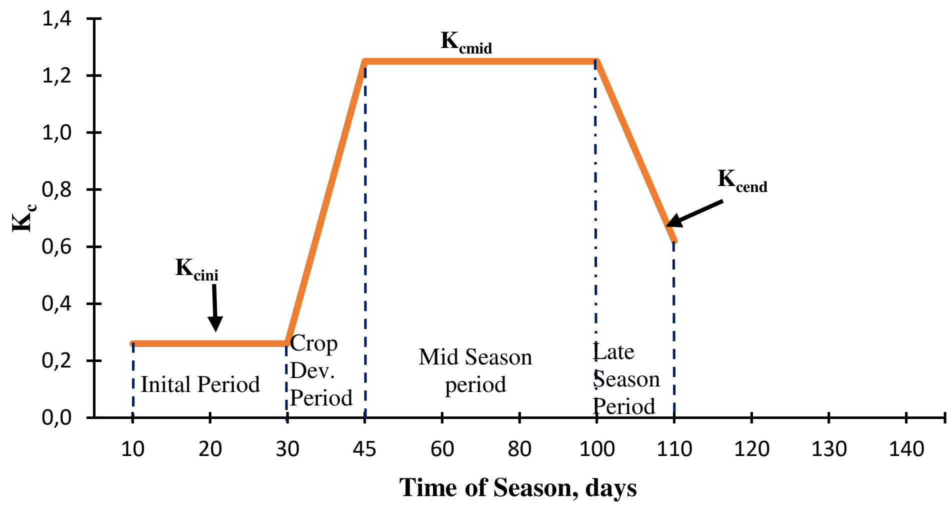

Figure 3.13. A graphical representation depicting the crop coefficient curve spanning from the initial planting phase to the final harvesting stage of the crop (modified from Allen et al., 1998)

3.3. Methods

Figure 3.14 depicts the flowchart illustrating the methodology employed in this study. It provides a comprehensive overview of the methods utilized with detailed explanations.

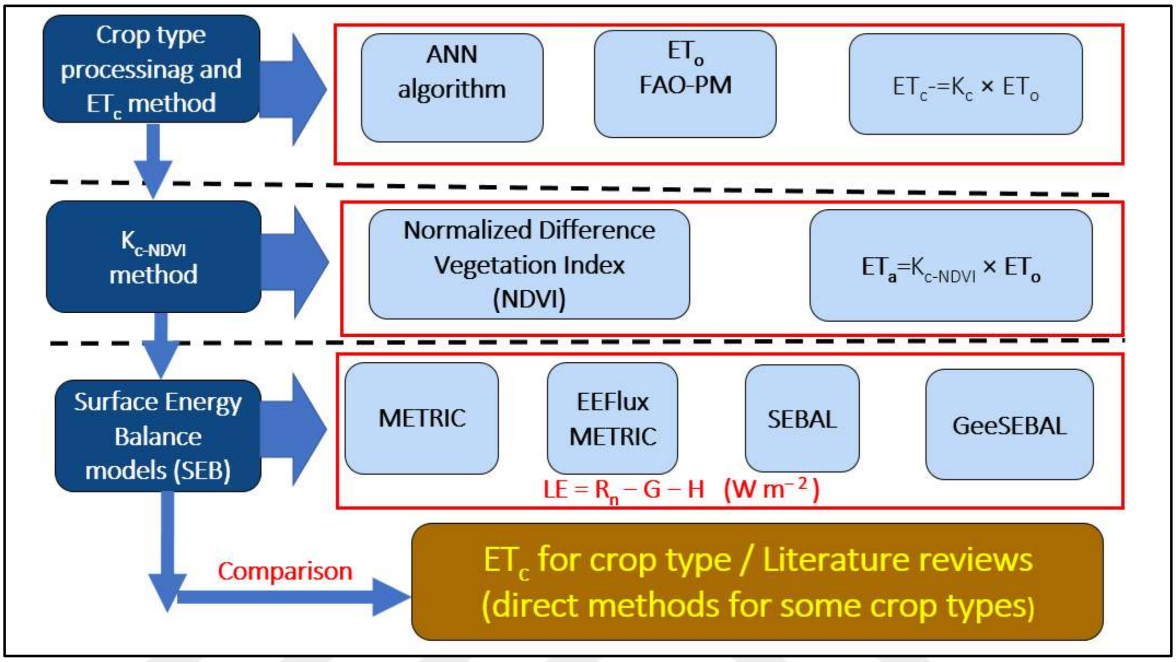

Figure 3.14. The flowchart outlining the methodology employed to estimate actual evapotranspiration (ET_a) utilizes SEB models, i.e., METRIC, EEFlux METRIC, SEBAL, GeeSEBAL models and a "two-step" procedure for calculating crop evapotranspiration (ET_c), along with the $K_{c\text{-}NDVI}$ method

3.3.1. Crop type processing

In this study, identifying the specific crop type is pivotal for estimating ET_a through SEB models and the ET_c method as well as for quantifying irrigation water requirements at a catchment scale (Alsenjar et al., 2023a). Typically, at least two different crops are grown each year in the research area (Cetin et al., 2023a; Cetin et al., 2023b). Thus, determining the spatial behavior of vegetation patterns during the field's winter and summer seasons is essential. Satellite data is utilized to achieve this aim. Crop-type processing consists of three main steps as described below: pre-processing, processing, and post-processing.

Pre-processing

Ground truth data were collected by noting and recording each crop type grown in the winter and summer in the study area for the years 2020-2023. In this context, as an example, a total of 1316 parcels were visited in the winter of 2021 by noting the coordinates of the parcels and the existing plant species or land use types at that time in the AID. Then, clear-sky satellite images were downloaded (Landsat with resolution 30 m×30 m/Sentinel-2A-2B-2C with spatial resolution

10 m×10 m). Sentinel-2A-2B images were obtained from https://scihub.copernicus.eu/dhus/#/home, with specific information provided in Table 3.6. Then, the correction of RS data by refining the data by removing outliers, null entities, cloudiness, shadow, and cloud mask by using a) radiometric calibration to calibrate image data to radiance, reflectance, or brightness temperatures and b) the atmospheric correction module, which eliminates atmospheric effects, is a critical pre-processing step in the analysis of surface reflectance images using the Environment for Visualizing Images (ENVI) program. To show the changes in the growth of stages, the Normalized Difference Vegetation Index (NDVI) was calculated. The resulting NDVI values were included in the study to increase the accuracy of artificial neural network (ANN) classification.

Table 3.6. Names and dates of Sentinel satellite images utilized to identify plant patterns in the research area during both winter and summer seasons

Sentinel-2 scene_ID	Satellite date	Day of year (DOY)
S2B_MSIL2A_20200413T082559_N0214_R021_T36SYF_20200413T115830	13.04.202	104
S2B_MSIL2A_20200702T082609_N0214_R021_T36SYF_20200702T122946	02.07.2020	184
S2A_MSIL1C_20200806T082611_N0209_R021_T36SYF_20200806T100018	06.08.2020	219
S2B_MSIL2A_20210319T082639_N0214_R021_T36SYF_20210319T112002	19.03.2021	78
S2B_MSIL2A_20210329T082559_N0214_R021_T36SYF_20210329T111602	29.03.2021	88
S2A_MSIL2A_20210413T082601_N0300_R021_T36SYF_20210413T105415	13.04.2021	103
S2B_MSIL2A_20210627T082559_N0300_R021_T36SYF_20210627T112602	27.06.2021	178
S2A_MSIL2A_20210811T082601_N0301_R021_T36SYF_20210811T114551	11.08.2021	223
S2B_MSIL2A_20220413T082559_N0400_R021_T36SYF_20220413T105828	13.04.2022	103
S2B_MSIL1C_20220702T082609_N0400_R021_T36SYF_20220702T091957	02.07.2022	183
S2B_MSIL2A_20220729T081609_N0400_R121_T36SYF_20220729T100550.	29.07.2022	210
S2B_MSIL2A_20220828T081609_N0400_R121_T36SYF_20220828T101438	28.08.2022	240
S2A_MSIL2A_20230331T081601_N0509_R121_T36SYF_20230331T114600	31.03.2024	90
S2B_MSIL1C_20230624T081609_N0509_R121_T36SYF_20230624T090714	24.06.2023	175
S2B_MSIL2A_20230724T081609_N0509_R121_T36SYF_20230724T104606	24.07.2023	205
S2B_MSIL1C_20230826T082609_N0509_R021_T36SYF_20230826T104420	26.08.2023	238

Processing

Regions of Interest (ROIs) are specific areas within a raster dataset that are selected for detailed analysis, such as areas containing crops or water bodies. Subsequently, each Region of Interest (ROI) from the ground truth data of crop types was integrated into the ENVI software by delineating individual classes or importing polygon and point shape files. This integration was performed through supervised classification. The ANN algorithm was implemented using the ENVI software's neural net classification module, employing the logistic activation method (Alsenjar et al., 2023a; Cetin et al., 2023a). Input layers and three hidden layers were configured, resulting in the generation of one output map. Training data comprised 80% of the ground truth dataset, while the remaining 20% was allocated for testing purposes (Mahlayeye et al., 2022; Alsenjar et al., 2023a; Alsenjar et al., 2023b; Cetin et al., 2023a; Cetin et al., 2023b)**.** The input layer represents the ROIs, with the connections between layers characterized by varying weights, which are adjusted during training to produce the lowest RMS used in classification. Figure 3.15 is an example of the winter season of 2021 for achieving the desired output. The ANN model relies on feed-forward and backpropagation processes to facilitate training. Figure 3.16 illustrates the operational workflow of the ANN algorithm in this study.

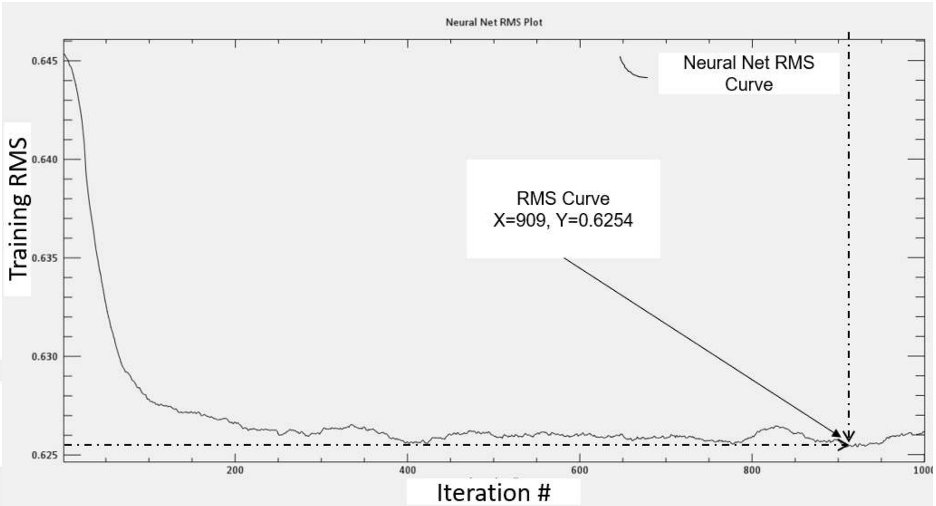

Figure 3.15. Training root mean square (RMS) versus the iteration value during the winter season of 2021 over the AID (Alsenjar et al., 2023a)

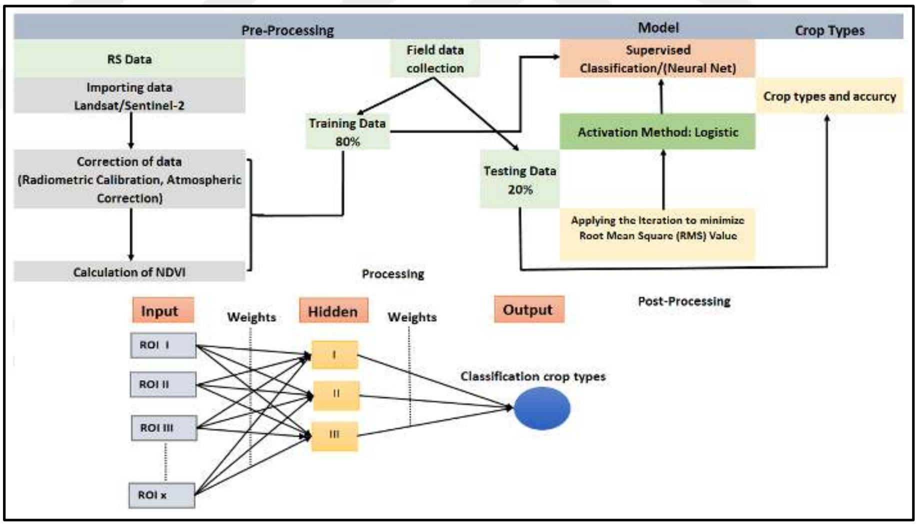

Figure 3.16. The image processing steps for identifying the crop types cultivated in the irrigation district during both winter and summer seasons, along with their associated input data, pre-processing procedures, and utilized models (Alsenjar et al., 2023b; Cetin et al., 2023a; b)

Post-processing

The ANN algorithm requires validation of the estimated cropping pattern map using ground truth data (Irfanoglu and Balcik, 2018; Alsenjar et al., 2023a; Cetin et al., 2023a; b). To achieve this, the following steps were implemented:

Sieve classes: Sieve classes remove isolated classified pixels using blob grouping to solve the problem of isolated pixels in classification images.

Clump classes: It clumps adjacent similarly classified areas using morphological operators.

Use combine classes. It is to merge classes in classified images selectively.

Use majority/minority analysis: It was applied to the classification image to enhance its accuracy. Specifically, majority analysis was used to correct isolated spurious pixels by assigning them to the dominant class within a larger contiguous area. This approach helps refine the classification by consolidating pixels incorrectly classified as outliers into the appropriate class.

Confusion matrix: It was utilized to evaluate the accuracy of the classification results by comparing them against ground truth data. This matrix provides a detailed comparison between the classified results and the actual reference information, allowing for an assessment of the classification performance.

3.3.2. Reference evapotranspiration (ET_o) calculation

The reference Evapotranspiration (ET_o) values were calculated using meteorological datasets acquired from weather stations in the study area (refer to Figure 3.4) by employing the FAO Penman-Monteith method in Equation (3.1), as described by Allen et al. (1998), Cetin (2020) and İrvem and Ozbuldu (2022). The following equation was applied for short grass, with an albedo set at 0.23 and an aerodynamic resistance of 70 s m^{-1}.

$$ET_o = \frac{0.408\times \Delta\times (R_n - G) + \gamma\times\frac{900}{T+273}\times u_{2}\times (e_s - e_a)}{\Delta + \gamma\times (1 + 0.34\times u_2)} \quad (3.1)$$

where

ET_o is the reference evapotranspiration (mm day^{-1}),

R_n is the net radiation at the crop surface (MJ m^{-2} day^{-1}),

G is the soil heat flux density (MJ m^{-2} day^{-1}),

T is the mean daily air temperature at 2 m height (°C)

u_2 is the wind speed at 2 m height (m s^{-1}),

e_s is the saturation vapor pressure (kPa),

e_a is the actual vapor pressure (kPa),

$e_s - e_a$ is the saturation vapor pressure deficit (kPa),

Δ and γ are the slope (kPa°C^{-1}) of the vapor pressure curve and the psychrometric constant (kPa°C^{-1}), respectively.

3.3.3. Crop evapotranspiration (ET_c) estimation

In this research, the effectiveness of the METRIC, SEBAL, and $K_{c\text{-}NDVI}$ models was assessed against independently calculated ET_c values obtained through the FAO-56 method, following the methodology outlined in Tasumi (2019), Cetin (2020), and Cetin et al. (2023b). Hence, ET_c was determined by multiplying ET_o by a crop coefficient K_c, adjusted based on the specific crop type and growth stages. This process followed a "two-step" approach, as described by Allen et al. (1998), Steduto (2000), Cetin (2020), and Cetin et al. (2023b).

$$\mathrm{ET_c} = \mathrm{K_c} \times \mathrm{ET_o} \tag{3.2}$$

In this context, ET_c represents crop evapotranspiration in millimeters per day, i.e., mm day^{-1}, while K_c represents the "*dimensionless crop coefficient*". Local K_c values for various crop growth stages were sourced from literature provided by TAGEM-DSI (2017).

3.3.4. NDVI calculation

The Normalized Difference Vegetation Index (NDVI) is a quantitative measure for evaluating the density and condition of vegetation cover within a specific region, as shown in Figure 3.17. It finds extensive application in remote sensing and satellite imagery analysis to track vegetation alterations over temporal periods. NDVI is calculated using the reflectance of two wavelengths of light: near-infrared (NIR) and visible red (R) (Rouse et al., 1974). The formula for NDVI is:

$$\mathrm{NDVI} = \frac{(\mathrm{NIR}-\mathrm{R})}{(\mathrm{NIR}+\mathrm{R})} \tag{3.3}$$

NDVI values range from -1 to +1. NDVI takes negative values for water bodies while high and positive for dense vegetation (Rouse et al., 1974). NDVI values are used in the METRIC model and $K_{c\text{-}NDVI}$ method, especially in soil heat flux (G), obtained according to Bastiaanssen (2000).

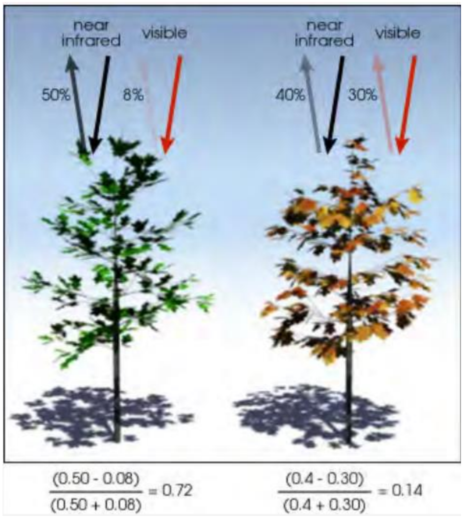

Figure 3.17. An example of calculating NDVI (Alsenjar et al., 2023b)

3.3.5. Mapping EvapoTranspiration at high Resolution and with Internalized Calibration (*METRIC*) model and EEFlux-METRIC

The standard METRIC model

The METRIC model, an image processing model that relies on satellite data, comprises various sub-models to compute ET_a as the residual of surface energy balance. Key inputs for the METRIC model include Thermal Infrared Sensor bands, image metadata files, and Operational Land Imager (OLI) bands. Additionally, a digital elevation model (DEM) generates aspect and slope information necessary for adjusting surface temperature (T_s) and accounting for mountainous terrain corrections within the model. The METRIC model can be used for flat and high-terrain areas (Olmedo et al., 2016). Figure 3.18. presents a schematic illustration delineating the functionalities, data inputs, and outputs employed within the METRIC model.

The METRIC model was employed to estimate the following: (a) surface energy balance components (SEB shown in Figure 3.19), including latent heat (LE), net radiation (R_n), sensible heat (H), and soil heat flux (G) and (b) ET_a for each pixel, crop type and the entire study area (Equation 3.4) utilizing Landsat satellite imagery and meteorological data from weather stations at the time of satellite overpass. This was primarily conducted following the methodologies outlined by Allen et al. (2007a) using the R-METRIC model (Olmedo et al., 2016) with a water package in the R program and LandMOD ET mapping toolbox in MATLAB (Bhattarai et al., 2017). In this context, latent heat flux (LE) is calculated as the following:

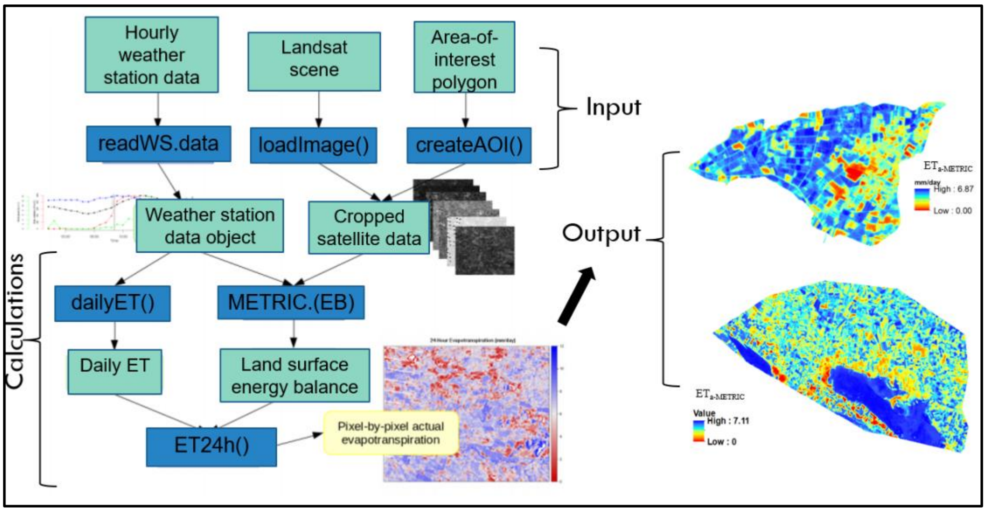

Figure 3.18. A schematic diagram showcasing the various functions, data inputs, and resultant outputs utilized within the METRIC model. In this illustration, data inputs are represented by green rounded boxes, functional processes by blue boxes, and the outcome by a yellow box (Olmedo et al., 2016)

$$LE = R_n - G - H \tag{3.4}$$

where R_n, G, and H have the same units (typically expressed in W m^{-2}).

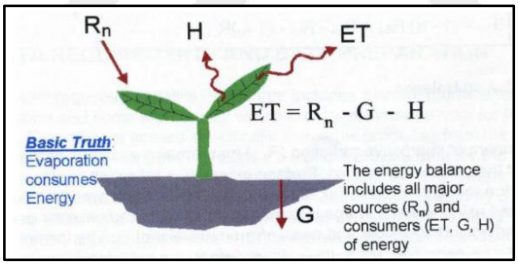

Figure 3.19. Surface energy balance components (Allen et al., 2007a)

From satellite imagery, net radiation (R_n) is determined using surface reflectance and surface temperature (T_s). It represents the disparity between incoming shortwave radiation and outgoing longwave radiation, formulated as follows:

$$R_n = R_s\downarrow - \alpha \times R_s\downarrow + R_L\downarrow - R_L\uparrow - (1 - \varepsilon_o) \times R_L\downarrow \tag{3.5}$$

This equation comprises various components: $R_s\downarrow$ represents the incoming shortwave solar radiation (W m^{-2}), α denotes the surface albedo (a dimensionless value), $R_L\downarrow$ represents the incoming longwave radiation (W m^{-2}), $R_L\uparrow$ stands for the outgoing longwave radiation (W m^{-2}), and ε_o signifies the surface thermal emissivity (also dimensionless) as shown in Figure 3.20.

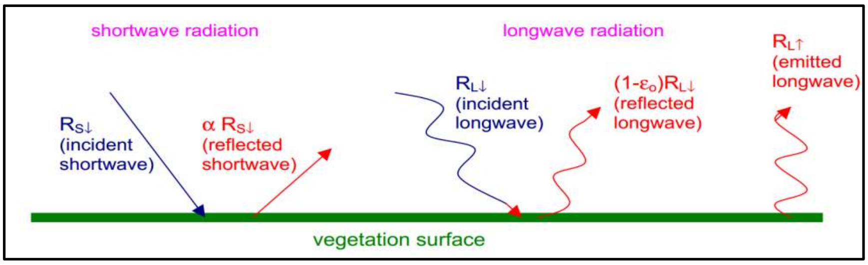

Figure 3.20. Energy balance over vegetation with different radiation components (Allen et al., 2007a)

In the METRIC model, soil heat flux (G) is computed following Tasumi's (2003) approach. It represents the heat storage rate within the soil and vegetation (Allen et al., 2007a). This computation involves determining the G-to-R_n ratio, considering surface temperature, albedo, and NDVI as contributing factors.

$$\frac{G}{R_n} = 0.05 + 0.18 \times e^{-0.521\times LAI} \quad (LAI \geq 0.5) \tag{3.6}$$

$$\frac{G}{R_n} = 1.80 \times (T_s - 273.15) / R_n + 0.084 \quad (LAI < 0.5) \tag{3.7}$$

In Equation 3.7, T_s denotes surface temperature (measured in degrees Kelvin) derived from satellite imagery. The equation indicates that when the Leaf Area Index (LAI) is below 0.5, the ratio of G to R_n exhibits an increase with elevated T_s rates and declines as LAI rises (Allen et al., 2007a).

Sensible heat flux (H) was calculated using the aerodynamic-based heat transfer equation as follows:

$$H = \frac{\rho_{air} \times C_p \times dT}{r_{ah}} \tag{3.8}$$

where ρ_{air} represents air density (kg m^{-3}), C_p denotes the specific heat of the air (1004 J kg^{-1} K^{-1}), dT represents the temperature difference between two heights z_1 (0.1 m) and z_2 (2 m), and r_{ah} signifies the aerodynamic resistance to heat transfer (s m^{-1}) as shown in Figure 3.21.

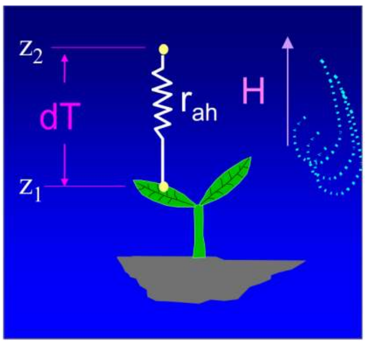

Figure 3.21. Sensible heat flux in *Equation 3.8* (Allen et al., 2007a)

One of the most critical issues in applying the METRIC model is the determination of hot and cold cells in the study area. During image processing, T_s, albedo, NDVI, and LAI values, along with the properties of the specified pixel (e.g., soil, plant, water), are assessed together. For instance, in a hot pixel (bare soil), NDVI and LAI values are very low, while T_s is high. Conversely, NDVI and LAI values are very high in cold pixels (irrigated crop, river, lake) and low in T_s. Therefore, the accuracy of selecting hot and cold pixels when applying the METRIC model is evaluated based on NDVI, T_s, and LAI.

Using the values of latent heat flux (LE), the instantaneous values of ET_a were calculated for each pixel:

$$\mathrm{ET_{inst}} = \frac{3600 \times \mathrm{LE}}{\lambda \times \rho w} \tag{3.9}$$

where ET_{inst} represents the instantaneous ET_a at the time of satellite overpass (mm h^{-1}); The conversion factor 3600 is utilized to convert from seconds to hours; LE denotes the latent heat flux (W m^{-2}) utilized by evapotranspiration, ρw represents the density of water which is 1000 kg m^{-3}; and λ signifies the latent heat of vaporization (J kg^{-1}), which is computed as:

$$\lambda = [2.501 - 0.00236 \times (\mathrm{T_s} - 273.15)] \times 10^6 \tag{3.10}$$

Daily values of evapotranspiration ET (ET_{24}) (mm day^{-1}) for each pixel were determined using the following method:

$$\mathrm{ET_{24}} = \mathrm{ET}_r\mathrm{F} \times \mathrm{ET_r 24} \tag{3.11}$$

where ET_rF represents the reference evapotranspiration fraction, ET_r24 signifies the cumulative short grass reference evapotranspiration (ET_o) for the day (mm day^{-1}), and ET_{24} represents the ET_a for the entire 24-hour period (mm day^{-1}). The values for ET_rF are determined based on ET_{inst} for each pixel, while ETr is obtained from weather data as:

$$\mathrm{ET_rF} = \frac{\mathrm{ET_{inst}}}{\mathrm{ET_r}} \tag{3.12}$$

Accumulated values of ET_a for a specific period of t-day duration (month or season) are computed according to Equation 3.13. This calculation involves interpolating ET_rF values for the days between satellite images and deriving ET_r from meteorological data collected on the ground. Subsequently, the annual ET_a is determined by aggregating the daily ET_a values.

Monthly ET, in total, is determined as follows:

$$\mathrm{ET_m} = \sum_{i=1}^{m}[(\mathrm{ET_rF_i} \times \mathrm{ET_r24_i})] \tag{3.13}$$

where ET_m represents the cumulative evapotranspiration for a month ending on day m (m=28-day for February, m=30-day for September, etc.), ET_rF_i denotes the interpolated reference evapotranspiration fraction (ET_rF) for day i, and ET_r24_i signifies the 24-hour reference evapotranspiration for day i. All units are expressed in millimeters per day.

Following the estimation of daily ET_a for individual pixels and the classification of crop types (Alsenjar et al., 2023b; Cetin et al., 2023a; Cetin et al., 2023b) through remote sensing across the study area, it has become straightforward to calculate daily ET_a for each crop type c, i.e., $\mathrm{ET_{a_c}}$ as shown in Equation 3.14.

$$\mathrm{ET_{a_c}} = \frac{\sum_{i=1}^{m_c}[\mathrm{ETa_{ci}} \times \mathrm{A_{ci}}]}{\sum_{i=1}^{m_c}\mathrm{A_{ci}}} \tag{3.14}$$

The mean ET_a for the whole of the study area can be computed as follows

$$\mathrm{ET_{a\,study\ area}} = \frac{\sum_{c=1}^{l}[\mathrm{ET_{a_c}} \times \mathrm{A_c}]}{\sum_{c=1}^{l}\mathrm{A_c}} \tag{3.15}$$

where $\mathrm{ETa_{ci}}$ represents the actual evapotranspiration for the crop type c in pixel i (mm day^{-1}), and $\mathrm{A_{ci}}$ signifies the area covered by crop type c in pixel i(measured in square meters), $\mathrm{m_c}$ and l stands for the total number of pixels for crop type c, and the number of crop types growing in the study area, respectively. $ET_{a\,study\ area}$ denotes the average value of ET_a for the entire study area on a given day i (mm day^{-1}) for each i crop type.

Following the same methodology outlined in Equation 3.13, the cumulative ET_a for each crop type and the entire study area can be derived for any given timeframe, such as a month, season, or year.

The Earth Engine evaporation Flux (EEFlux) estimation of evapotranspiration

The Earth Engine Evapotranspiration Flux (EEFlux) tool has been created and implemented on the Google Earth Engine (GEE) platform, utilizing the METRIC model developed by Allen et al. (2007a). This tool estimates ET_a using Landsat satellite data and CFSv2 gridded weather data, providing outputs at a spatial resolution of 30 m accessible at https://eeflux-level1.appspot.com/. EEFlux also provides other parameters, such as NDVI, DEM, albedo, etc.

The EEFlux METRIC model shares similarities with the METRIC model regarding the procedure, utilizing the same equations in Section 3.3.5. However, notable distinctions exist between them, particularly regarding calibration methods (automatic versus manual) and input datasets.

A significant disparity between EEFlux and METRIC lies in using weather data sources for calibration and calculations. METRIC typically relies on ground-based hourly weather data from agricultural weather stations to compute ET_r to solve the SEB equation during calibration and estimate any background evaporation from recent precipitation events. In contrast, EEFlux employs gridded hourly and daily weather data stored on the Earth Engine platform. For this study, the CFSV2 gridded weather dataset with a resolution of 4 km is utilized. This section of the study compares automatically calibrated EEFlux products with METRIC products, as illustrated in Figure 3.22.

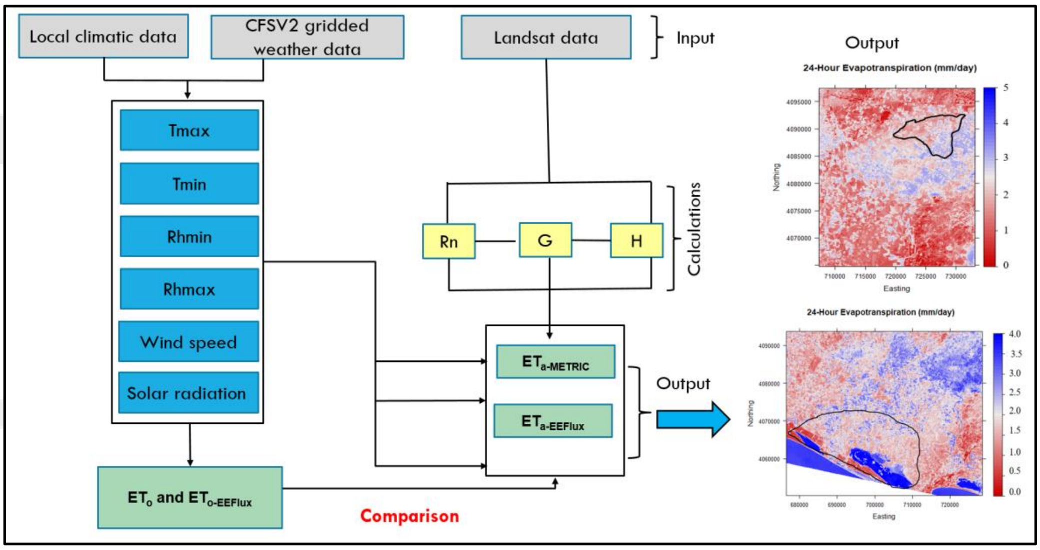

Figure 3.22. The methodology framework employed for estimating actual evapotranspiration ($ET_{a\text{-}EEFlux}$, mm day^{-1}) using the EEFlux-METRIC method and the standard METRIC model

3.3.6. Surface Energy Balance Algorithm for Land (*SEBAL*) model and GeeSEBAL

SEBAL algorithm

This research used the conventional SEBAL method (Bastiaanssen et al., 1998a) to compute ET_a utilizing Landsat satellite imagery alongside pertinent local climatic data by LandMOD ET mapping toolbox in MATLAB (Bhattarai et al., 2017). The latent heat flux (LE) equation, as expressed in Equation 3.4. R_n (W m^{-2}) is represented using the same equation described in Equation 3.5. G is the soil heat flux (W m^{-2}) as outlined by Equation 3.16 (Bastiaanssen, 2000), and H is the sensible heat flux (W m^{-2}) expressed using the same equation as described in Equation 3.8.

$$\frac{G}{Rn} = \alpha \times (T_s - 273.15)(0.0038 \times \alpha + 0.0074 \times \alpha^2)(1 - 0.98 \times NDVI^4) \quad (3.16)$$

where α is the surface albedo, calculated using the corrected irradiance from the satellite images, and T_s stands for surface temperature in Kelvin is estimated based on Allen et al. (2007a). When the NDVI value is below zero, indicating a water surface, the G/R_n ratio is assigned a value of 0.5 because of water surfaces' distinct thermal and radiative characteristics (Allen et al., 2007a). Additionally, regions where the surface temperature (T_s) is below four °C are identified as snow-covered areas, characterized by an albedo exceeding 0.45, with the G/R_n ratio also set to 0.5.

As mentioned above, to estimate H in Equation 3.8, the parameters within the equations are influenced by temperature gradient, surface roughness, and wind speed. However, solving Equation (3.8) becomes challenging due to two unknown parameters, i.e., r_{ah} and dT. To address this issue, the SEBAL algorithm adopts a strategy involving the utilization of two hot and cold pixels, along with wind speeds measured at a specified height. This approach simplifies calculations and facilitates overcoming the complexity arising from the unknown parameters. By combining aerodynamic resistance with maximum and minimum temperature differentials observed over specially selected earth surfaces (hot and cold pixels), the algorithm enables the assessment of air temperature differences near the surface. Subsequently, reliable values of H are derived, assuming a linear relationship between surface temperature and heat transfer gradients observed in the two pixels. This process enables estimating dT values in Equation 3.8 within these pixels.

As known, the SEB components, i.e., R_n, G, and H, are instantaneous values at the satellite's transit point in time, and the latent heat flux values are also instantaneous. Therefore, in the SEBAL model, the instantaneous evapotranspiration flux is calculated in Equation 3.9.

As mentioned in the introduction section, in the SEBAl model, a constant evaporative fraction (EF) is used to convert from instantaneous ET_i for each pixel to daily ET_a in Equation 3.20, where ET_r (ET_o, i.e., reference ET) is obtained from weather data as:

$$\mathrm{EF} = \frac{\mathrm{ET_{inst}}}{\mathrm{ET_r}} \tag{3.20}$$

Daily evapotranspiration values (ET_{24}) are frequently deemed more practical than instantaneous values (ET_{inst}) in agriculture water management and hydrological modeling. The calculation of daily evapotranspiration values proceeded as follows:

$$\mathrm{ET_{24}} = \mathrm{EF} \times \mathrm{ET_{r24}} \tag{3.21}$$

Finally, ET_{r24} signifies the total evapotranspiration accumulated over the imaging day, computed by summing up the hourly values throughout that day.
Afterwards, the annual ET_a is calculated by summing up the daily ET_a values for each crop type and the entire study area using the same Equations in 3.13, 3.14, and 3.15, respectively.

GeeSEBAL platform

The GeeSEBAL platform (Laipelt et al., 2021) is an openly available adaptation of the SEBAL model designed to utilize the Google Earth Engine (GEE, version 0.1) for estimating ET_a at a resolution scale of 30 m through an Earth Engine application (https://etbrasil.org/geesebal). It employs SEBAL model computations (the same equations are mentioned in the SEBAL model) to ascertain ET_a for individual pixels during satellite passes. The SEBAL model estimates LE as a residual of other energy fluxes observed during satellite overpasses, primarily relying on the methodology outlined by Bastiaanssen et al. (1998a) and Bastiaanssen et al. (1998b). The primary distinction between the standard SEBAL model and the GeeSEBAL product lies in weather data input. While the standard SEBAL model relies on local climatic data, i.e., in-situ weather data, the GeeSEBAL platform utilizes global meteorological data from ERA5 land reanalysis with a resolution of around 9 km. This approach compares the ET_a outcomes obtained from the standard SEBAL model with those generated by the GeeSEBAL platform. This comparison assesses the accuracy of the GeeSEBAL product across the AID for the water years of 2020-2021.

This study detailed the four energy balance models (SEB-METRIC, EEFlux-METRIC, SEBAL, and GeeSEBAL) for ET_a estimation. Table 4.7 summarizes each model's strengths and limitations regarding computational complexity, required inputs, accuracy, and suitability for different climatic conditions.

Table 3.7. Comparison of energy balance models (METRIC, EEFlux-METRIC, SEBAL, and GeeSEBAL) for ET_a estimation: Strengths, Limitations, and Applicability

Model	Strengths	Limitations	Computational Complexity	Required Inputs	Usability in Different Climatic Conditions
METRIC	- High accuracy in ET_a estimation - Accounts for local weather variability - Well-validated in agricultural regions	- Requires detailed meteorological and ground-based data - Sensitive to selection of hot/cold pixels	High	- Landsat imagery - climatic data - Surface temperature	- Performs well in irrigated and semi-arid areas but sensitive to extreme weather conditions
EEFlux-METRIC	- Automated processing via Google Earth Engine - No need for local ground data - Cloud-based processing reduces computational demand	- Less flexible for customized calibration - Hot/cold pixel selection is automated, which may reduce accuracy in heterogeneous landscapes - Can be affected by cloud cover and missing pixels in Landsat images	Medium	- Landsat imagery - Pre-loaded climatic data	- Works well in general conditions but may struggle with local microclimates
SEBAL	- Lower input requirements than METRIC - Does not require weather station data for initial estimation - Suitable for large-scale applications	- More sensitive to errors in net radiation and surface roughness estimation - Less accurate under strong advection conditions	Medium	- Landsat imagery - Surface temperature	- Performs well in flat terrains and semi-arid regions but struggles in areas with strong advection
GeeSEBAL	- Fully automated on Google Earth Engine - No need for manual selection of reference pixels - Suitable for large-scale studies	- Reduced flexibility for local calibration - Can be affected by cloud cover and missing pixels in Landsat images	Low	- Landsat imagery - Automated climate inputs	- Works well in regions with consistent climate patterns but may be less accurate in complex microclimates

3.3.7. $K_{c\text{-}NDVI}$ method

The process of estimating ET_a maps using SEB models through intricate equations and analysis of remotely sensed shortwave and thermal infrared imagery can pose challenges, mainly when required input data is unavailable or when there is a tolerance for higher uncertainty in the resulting ET_a estimates. Consequently, an opportunity arises to develop a more straightforward and efficient method for generating ET_a maps using fewer input parameters, particularly in cases where data availability is limited or more significant uncertainty is acceptable. The advantage of deriving new K_c values from the relationship between K_c and NDVI lies in its ability to provide actual K_c estimates corresponding to the satellite overpass dates based on fewer inputs rather than relying solely on standardized K_c values from reference sources, as detailed by TAGEM-DSI (2017). To address this, a novel approach involves creating a new K_c derived from the relationship between K_c values obtained from literature reviews by TAGEM-DSI (2017) and the NDVI, as shown in Figure 3.23. This correlation is the basis for developing linear regression equations for some crops. As a result, a new K_c, termed $K_{c\text{-}NDVI}$, is established, which integrates the relationship between K_c and NDVI. This newly derived $K_{c\text{-}NDVI}$ is then multiplied by ET_o to estimate ET_a maps, as outlined in Equation 3.22 (Reyes-González et al., 2018). The unit of ET_a and ET_o is mm day^{-1}.

$$\mathrm{ET_a} = \mathrm{K_{c-NDVI}} \times \mathrm{ET_o} \tag{3.22}$$

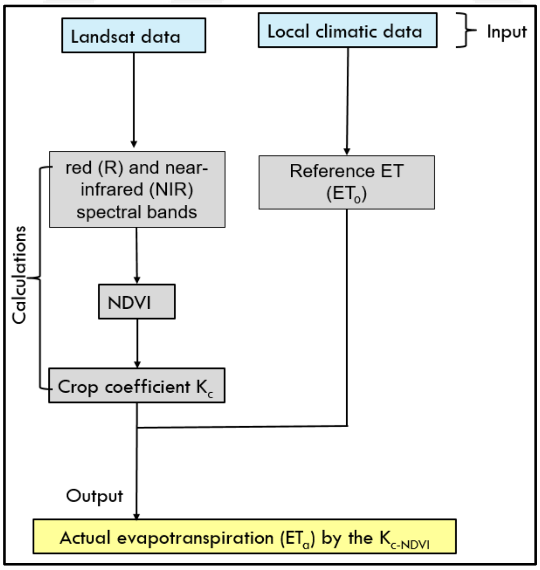

Figure 3.23. Framework for estimating actual evapotranspiration ($ET_{a\text{-}Kc\text{-}NDVI}$, mm day^{-1}) using the $K_{c\text{-}NDVI}$ methodology

The $K_{c\text{-}NDVI}$ method employed in this study links the crop coefficient (K_c) with NDVI to generate high-resolution ET_a estimates with minimal ground data. While its advantages are highlighted, its limitations have not been fully addressed compared to other methods. These limitations include potential inaccuracies during extreme crop stress, where NDVI may not accurately reflect crop health. The method requires region-specific calibration and may vary across crop types and growth stages. While the $K_{c\text{-}NDVI}$ method is simple, computationally efficient, and well-suited for long-term ET_a trend analysis, it assumes a direct proportionality between NDVI and K_c, which may not hold under water stress or extreme weather conditions. It is effective in homogeneous croplands but may be less reliable in mixed vegetation or stressed conditions, relying on satellite-derived NDVI and crop-specific K_c relationships.

3.3.8. Estimation of evaporation over lagoons in the LSP using the METRIC and Kohler-Nordenson-Fox models

The METRIC model calculates ET_a for crops and determines evaporation from freshwater and saline lakes. Consequently, this study utilized the Kohler-Nordenson-Fox (KNF) model (Kohler et al., 1955), an empirical method, to estimate Epan and compare the evaporation results from the METRIC model with those from the KNF model. When estimating evaporation, the KNF model considers critical factors such as air temperature, solar radiation, wind speed, and relative humidity.

$$\mathrm{Epan} = \frac{\Delta \times R_n + \Upsilon \times \rho \times E_a}{\Upsilon \rho} \tag{3.23}$$

Here;

Epan is daily container evaporation amount (mm day^{-1}),

Δ is the slope of the saturation vapor pressure curve at the current temperature of the air,

γ p is psychrometric constant (0.001568xP) (kPa $°C^{-1}$),

P is atmospheric pressure (kPa),

R_n is equivalent of the evaporation of daily net radiation (mm day^{-1}) calculated according to the principles outlined by Allen et al. (1998),

E_a is the aerodynamic function (mm day^{-1}), determined using Equation 3.24.

$$E_a = 25.4 \times [0.296 \times (e_s - e_a)^{0.88} \times (0.37 + 0.00255 \times \mathrm{up})] \tag{3.24}$$

Where:

e_s is the saturation vapor pressure (kPa),

e_a is the actual vapor pressure (kPa),

$e_s - e_a$ is the saturation vapor pressure deficit (kPa), and up is the wind speed at 15.2 cm above Class A container (km day^{-1}).

3.3.9. Statistical comparisons

In this research, daily estimates of actual evapotranspiration (ET_a) were computed using various Surface Energy Balance models (SEB), including METRIC, EEFlux, SEBAL, GeeSEBAL, $K_{c\text{-}NDVI}$ for the study area during satellite overpass periods in the growing seasons of 2020 and 2023. To evaluate the accuracy of these SEB models, their ET_a estimates were compared to those obtained using a "two-step procedure" (ET_c) through a simple linear regression model ($ET_{a\text{-}SEB} = a + b \times ET_c$). In this model, $ET_{a\text{-}SEB}$ from the different models was denoted by 'y', while ET_c was represented by 'x'. The performance of the SEB models and the $K_{c\text{-}NDVI}$ method were assessed by determining several metrics, including Root Mean Square Error (RMSE), Mean Absolute Error (MAE), Coefficient of Determination (R^2), and the Willmott index of agreement (d). These metrics were used to compare the performance of METRIC, SEBAL, EEFlux products, GeeSEBAL, and $K_{c\text{-}NDVI}$ against the ET_c method, which served as the reference. A Student's t-test was also conducted to assess whether the mean differences between ET_c values and ET_a estimates from SEB models for specific crop types significantly deviated from unity. The test was performed at a 95% confidence level, following an F-test to determine whether the variances of the datasets were equal or unequal. The equal variance Student's t-test and the unequal variance t-test were described in Equations 3.29 and 3.30, respectively. The ArcGIS software tool "ArcGIS Zonal Statistics as Table" was utilized to calculate ET_a statistics for each crop type.

$$\mathrm{MAE} = \frac{\sum_{i=1}^{n} |x_i - y_i|}{n} \tag{3.25}$$

$$\mathrm{RMSE} = \sqrt{\frac{\sum_{i=1}^{n} (x_i - y_i)^2}{n}} \tag{3.26}$$

$$R^2 = \left(\frac{\sum_{i=1}^{n} (x_i - \bar{x}) \times (y_i - \bar{y})}{\sqrt{\sum_{i=1}^{n} (x_i - \bar{x})^2} \times \sqrt{\sum_{i=1}^{n} (y_i - \bar{y})^2}} \right)^2 \tag{3.27}$$

$$d = 1 - \frac{\sum_{i=1}^{n} (x_i - y_i)^2}{\sum_{i=1}^{n} (|x_i - \bar{x}| + |y_i - \bar{x}|)^2} \tag{3.28}$$

$$t = \frac{|\overline{x_1} - \overline{x_2}|}{\sqrt{S^2 \left(\frac{1}{n_1} + \frac{1}{n_2} \right)}} \tag{3.29}$$

$$t = \frac{|\overline{x_1} - \overline{x_2}|}{\sqrt{\left(\frac{S_1{}^2}{n_1} + \frac{S_2{}^2}{n_2} \right)}} \tag{3.30}$$

In this context, 'x' represents the independently estimated ET (Tasumi, 2019) using the FAO-56 method, also referred to as the "two-step procedure" (ET_c). 'y' denotes the actual evapotranspiration ($ET_{a\text{-}SEB}$) estimated by the Surface Energy Balance (SEB) approach.

4. RESULTS AND DISCUSSION

4.1. Reference evapotranspiration (ET_o) and precipitation

Considering the significant influence of meteorological factors on ET_o and ET_c, a comprehensive investigation of climatic conditions is essential for a robust assessment of the study area for 2020-2023. Rainfall quantities and additional meteorological observations about climate conditions were scrutinized daily throughout the 2020-2023 hydrological years. Figure 4.1 and Figure 4.2 display the temporal variations of calculated daily ET_o using the FAO-PM method and the cumulative precipitation at Cotlu weather station in the AID and Golkaya meteorological station in the stressed areas of LSP, respectively, during the years 2020-2023. According to Figure 4.1, the cumulative annual ET_o at Cotlu weather station exceeded that at Golkaya meteorological in the stressed section of the LSP during the water years of 2020 to 2023. At Cotlu station within the AID, the annual total evapotranspiration (ET_o) ranged from 1,223 to 1,309 mm. In contrast, the LSP's stressed region varied between 981 and 1,092 mm during the same study period. The difference in annual ET_o between the AID area and the stressed region of the LSP could be explained by the fact that the stressed area experienced lower relative humidity and wind speeds compared to the AID area for the years 2020-2023. Table 4.1 presents descriptive statistics of calculated ET_o across the study areas, including the AID and the stressed region of the LSP. Between 2020 and 2023, the average daily ET_o was at approximately 3.43 mm in the AID and 2.79 mm in the stressed region of the LSP. As indicated in Table 4.1, the minimum ET_o value was 0.47 mm day^{-1} (DOY 354, December 20, 2021), while the maximum reached 9.7 mm day^{-1} on May 17, 2020 (DOY 137) in the AID during the water years 2020-2023. Conversely, in the stressed area of the LSP, the lowest and highest ET_o values were 0.39 mm day^{-1} (DOY 361, December 27, 2019) and 6.92 mm day^{-1} (DOY 174, June 23, 2023), respectively. Notably, ET_o surpassed 5.0 mm day^{-1} on numerous occasions during the summer days across the study area.

The mean total precipitation in the AID was at 711 mm, surpassing that in the stressed region of the LSP, which recorded 637 mm over the four water years. Nonetheless, the maximum yearly precipitation value reached 1,050 mm in 2020 within the stressed area, compared to 962 mm in the AID during the same year. Moreover, the mean annual total precipitation in the AID was 711 mm, approximately 9.3% (61 mm) higher than the basin's average annual precipitation (Cetin et al., 2020). Nevertheless, it was 13 mm less than the stressed region's annual rainfall. As evident from Figure 4.1 and Figure 4.2, precipitation exhibited a notable increase during the non-irrigation season (NIS) compared to the irrigation season (IS), with the rainy period typically spanning from late October to late May across the observed four water years (2020-2023) in both the AID and the stressed region of the LSP. The annual ET_o and total precipitation outcomes were consistent with the research of Ibrikci et al. (2015), Alsenjar et al. (2023a), Alsenajr et al. (2023b), Cetin et al. (2023a) and Cetin et al. (2023b) across the AID region. However, Ibrikci et al. (2015) noted that the precipitation levels are inadequate to meet the water requirements of crops, leading to approximately 70% of local crops being grown during the irrigation season. Consequently, irrigation and sufficient annual precipitation are crucial for optimal crop yields.

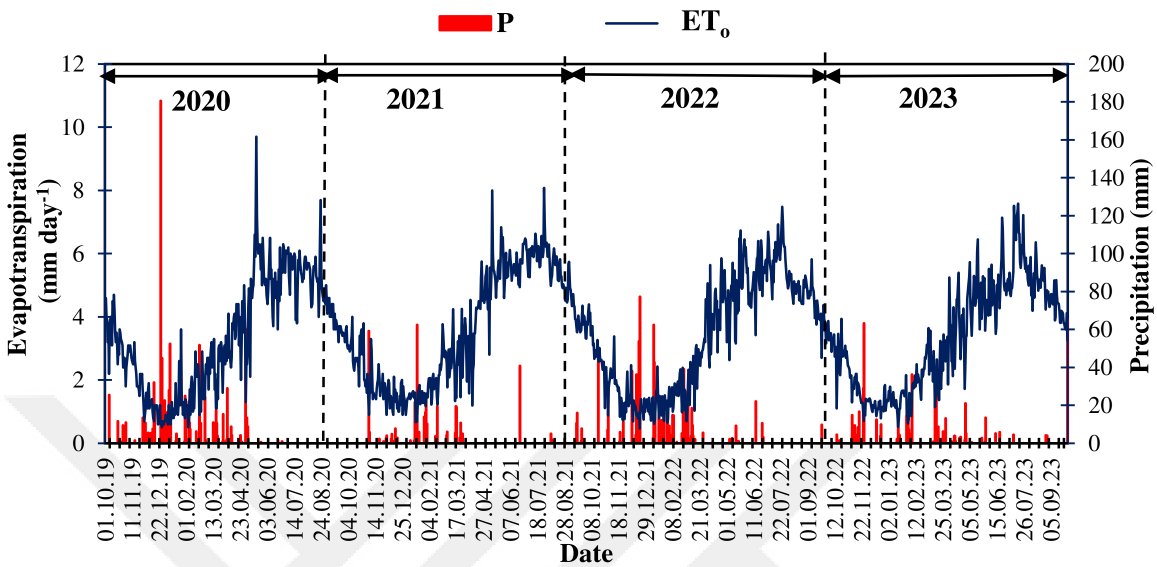

Figure 4.1. Daily temporal changes of calculated ET$_o$ (mm day^{-1}) by the FAO-PM approach and total precipitation (mm) over the AID area for the years 2020-2023. Climatic information was recorded at the Cotlu station, as depicted in Figure 3.4

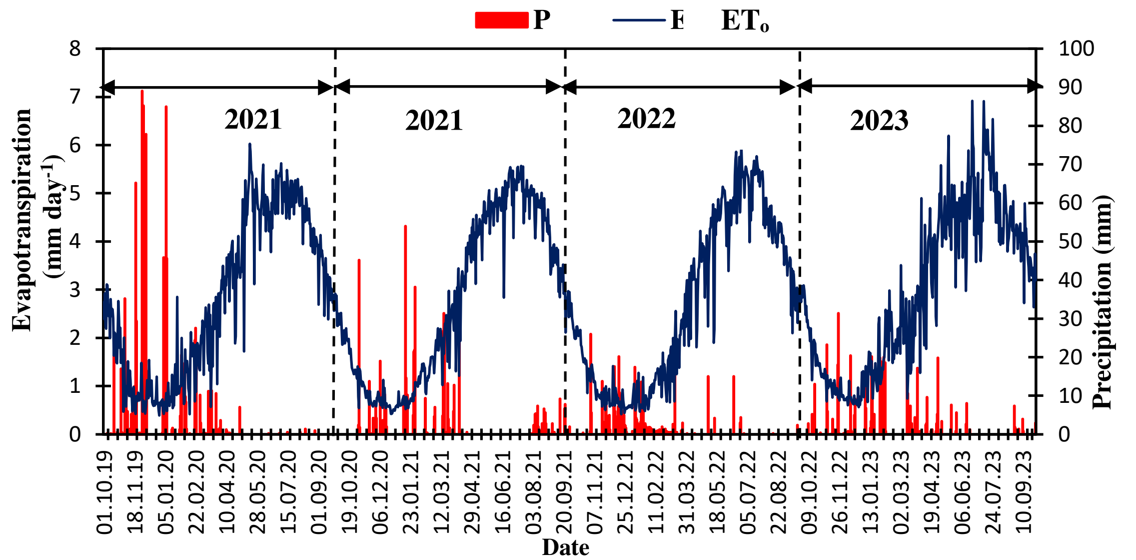

Figure 4.2. Daily temporal changes of calculated ET$_o$ (mm day^{-1}) by the FAO-PM approach and total precipitation (mm) over the stressed area of the LSP for the years 2020-2023. Climatological data were documented at the Golkaya station, as illustrated in Figure 3.4

Table 4.1. Some descriptive statistics for reference ET_o (mm day^{-1}) by the FAO-PM in the AID and stressed area of LSP for the years 2020-2023

	ET_o in the AID (NSA)				**ET_o in the stressed area (SA)**			
Water year	**2020**	**2021**	**2022**	**2023**	**2020**	**2021**	**2022**	**2023**
Mean	3.38	3.59	3.39	3.35	2.80	2.72	2.69	2.94
Median	3.30	3.44	3.42	3.34	2.74	2.47	2.34	2.85
Standard deviation	1.76	1.80	1.79	1.69	1.65	1.69	1.71	1.66
Kurtosis	-0.78	-1.33	-1.29	-0.98	-1.38	-1.51	-1.39	-1.17
Skewness	0.18	0.16	0.07	0.23	0.11	0.16	0.25	0.22
Range	9.20	7.41	7.02	7.07	5.64	5.15	5.62	6.35
Minimum	0.50	0.67	0.47	0.51	0.39	0.42	0.42	0.56
Maximum	9.70	8.08	7.48	7.59	6.03	5.57	6.04	6.92

4.2. Crop type classification and plant distribution mapping

Table 4.2 demonstrates that field visit data were depicted through spatial datasets acquired from field surveys conducted in both winter and summer seasons throughout the water years spanning from 2020 to 2023 within both the AID (NSA) and stressed regions (SA) near the coastal area of the LSP.

Table 4.2. Outlines the aggregate count of parcels surveyed during both winter and summer seasons across the water years from 2020 to 2023 within both the AID and stressed regions of the LSP

	AID (NSA)		**Stressed area (SA)**	
Growing season	Winter	Summer	Winter	Summer
2020	1,309	1,290	362	455
2021	1,316	1,454	399	442
2022	1,434	1,463	385	456
2023	1,493	1,523	387	523

The ANN algorithm was utilized to classify crop types within the area across the years 2020–2023. In their study, Mahlayeye et al. (2022) reported using the ANN model in the ENVI program, where 80% of the dataset was allocated for training and 20% for testing. This approach was also adopted in this research. Classified images that underwent classification were refined for each parcel within the piece data of the study area, focusing on winter and summer product patterns for 2020-2023. Potential errors were rectified by assigning the (majority) values based on the highest pixel count within each parcel, as described in the post-processing section in the methodology. The obtained results were validated using test data. Ultimately, a high classification accuracy exceeding 90%, on average, was achieved for most crops across the study area, irrespective of the winter or summer season, from a substantial number of parcels during field studies.

Classified maps were generated to identify the predominant plant species and their distributions in the research area across the water years of 2020-2023. This involved utilizing field survey data in conjunction with Sentinel-2 satellite images. Crop distribution maps were generated using the Artificial Neural Network (ANN) algorithm for winter and summer, as illustrated in Figure

4.3-Figure 4.6. As mentioned earlier, field data were collected -twice a year- during each water year throughout the 2020-2023 water years. Consequently, RS data was required to generate the classified maps, prompting an archive scan. Given that crops in the study area are typically cultivated as "first, i.e., I" and "second, i.e., II" crops, a single satellite scan was insufficient to differentiate between them, particularly during the summer season. In other words, the second crop type is typically planted after June 25th each year, following the harvest of the first crop, which is usually wheat and rarely winter vegetables. Consequently, the physical characteristics of the crops, such as leaf shape and coverage, can appear quite similar between the first and second crops. Additional auxiliary images were used to help differentiate between these crops. Specifically, the NDVI (Normalized Difference Vegetation Index) was added with the red, green, blue, and near-infrared (NIR) bands to achieve more accuracy in classifying crops. For example, in the 2023 water year, an aid image from August 24, 2023, was utilized to classify the second crop, as detailed in Table 3.6. The resulting "I. Product" and "II. Product" maps were merged within a GIS environment to create a unified cropping map illustrating the summer plant pattern (as depicted in Figure 4.3a-Figure 4.6a). Conversely, a single satellite image proved adequate during winter, as indicated in Table 3.6. Notably, all satellite images were carefully selected to mitigate the impact of cloud coverage, which is prevalent in the research area. This approach of plant pattern classification from images of different dates facilitated the production of highly accurate plant pattern distribution maps for the research area. Figure 4.3-Figure 4.6 depict the spatial distribution patterns of crops across the AID and the stressed region of the LSP during the winter and summer seasons from 2020 to 2023.

When examining the plant pattern distribution in the AID for the years 2020-2023, Figure 4.3a-Figure 4.6a indicate that citrus cultivation areas, i.e., citrus plantations, are extensive and contiguous in the eastern part of the AID. In particular, due to soil characteristics, citrus plantations in other AID regions are less densely distributed. Citrus orchards are generally distributed across large areas along the Ceyhan River. It is important to note that cultivated field crops become increasingly common as one moves from east to west within the AID area. The dominant soil series in the AID significantly influences this composition of plant patterns. In addition to citrus plantations, fruit orchards such as pomegranate, peach, and greenhouse bananas cover a relatively small area. These orchards comprise only about 1% of the AID area during winter and summer seasons.

As evident from Figure 4.3a-Figure 4.6a, the winter crop pattern map reveals a notable abundance of empty areas, i.e., fallow pieces, distributed extensively in clusters across the AID, excluding citrus groves or plantations. These empty or uncultivated parcels undergo spatial fluctuations and changes during winter. It is important to highlight that cereals, especially wheat, are the predominant winter crop in AID. A significant portion of the land in AID is left fallow during the winter months, as depicted in the winter plant pattern map (Figure 4.3a-Figure 4.6a). Examining the summer crop pattern map, especially for the first crop type (I) (Figure 4.3a-Figure 4.6a), shows that areas labeled as "empty land/bare soil" during the winter are utilized for cultivating field crops in the summer. These areas are planted with the first crops, typically sown after March 20 each year, as detailed in Figure 3.2.

Figure 4.3-Figure 4.6 illustrate the rates of crop cultivation in the field during both the winter and summer seasons for the water years from 2020 to 2023. An examination of Figure 4.3a-Figure 4.6a shows that citrus plantations are the predominant type of vegetation, comprising over 43% (4,083 ha) and 44.95% (4268 ha) on average of the agricultural area in the AID during both the winter and summer months, respectively, for the water years 2020-2023. In other words, the number of citrus-planted areas in the AID has been increasing day by day for economic reasons. Within the AID, spanning an area of 9,495 hectares, the primary field crops cultivated during the winter months from 2020 to 2023 include wheat, potatoes, lettuce, cabbage, and onions. Spatial analysis of Figure 4.3a-Figure 4.6a indicates that wheat emerges as the predominant crop among these. Figure 4.3a-Figure 4.6a reveal that these crops are predominantly cultivated in the northern and northwestern regions of the AID, where reddish Mediterranean soils known as terra rossa, Italian for “red soil,” are prevalent. These soils' physical and chemical characteristics generally favour growing potatoes, onions, lettuce, and cabbage. Consequently, it has been observed that the parcel locations where these crops are cultivated align well with the soil properties within the AID.

As seen from Figure 4.3a-Figure 4.6a, wheat was grown on an average of 15.5% (covering 1,472 ha) of the land during the winter months, as shown in Figure 4.7. Notably, 36.8% (3,494 ha) of the land (more than 1/3 of the AID) was left empty, i.e., fallow land, for primary crop cultivation for 2020-2023. In the summer of 2020-2023, no planting was done in all the empty areas in the winter. It was determined that 161.42 ha (1.7%) on average of the AID was vacant land; in other words, it was left empty without irrigation, although irrigation water was available in the irrigation scheme, and there was an active drainage network.

Apart from citrus in the summer season, the first crop of corn (corn-I) is considered the second crop after citrus in the area planted in the AID. Corn-I covered an area of 1,818.3 ha (19.15% on average), while the lowest area rate was 16.5 % (1,566.7 ha) in 2021. On the contrary, the highest was 22.2% (2,107.9 ha) in 2020 for corn-I. Additionally, there was second-crop maize/corn (maize/corn-II), which covered 2.47% (234.63 ha on average). The lowest area rate was 1.21% (114.9 ha) in 2022, while the highest value was 3.74% (355.1 ha) in 2023. Corn-I cultivation occupies an average of 5.75% of the total planted area in the AID, equivalent to 545.96 hectares. Throughout 2020-2023, the range of cotton-I planting rates fluctuated between a minimum of 4% (379.8 hectares) in 2023 and a maximum of 7.24% (687.4 hectares) in 2022. In the same context, the average cultivation of cotton-II constitutes 5.4% (512.7 hectares) of the entire AID area during the water years spanning from 2020 to 2023. The minimum recorded value for the cotton-II plantation rate occurred at 3.8% (360.8 hectares) in 2020, whereas the peak value was 8.3% (788.1 hectares) in 2022. According to the data presented, soybean-I's average cultivation area was 1.35% (128.2 hectares), notably lower than soybean-II's, which accounted for 6.6% (624.3 hectares) of the

AID land area from 2020 to 2023. Throughout the study period, there has been a consistent decline in the cultivation areas of soybean-I, as depicted in Figure 4.8. In the soybean-I area, the lowest recorded ratio was 0.7% (66.5 hectares) in 2022, while the highest ratio reached 2.5% (237.4 hectares) in 2020. The decline in soybean cultivation areas can be attributed to a combination of interrelated factors discouraging farmers from investing in soybean farming. The high cost of soybean seeds, persistently low market prices, and fluctuating fertilizer costs over the past two years (2022 and 2023) have significantly increased production expenses, making soybean cultivation less economically viable. Limited access to financial resources, such as agricultural credit and subsidies, has further constrained farmers' ability to manage these rising costs. Additionally, climatic uncertainties, including unpredictable rainfall and extreme weather events, have further reduced the appeal of soybean cultivation. Furthermore, competition from more profitable or less resource-intensive crops, declining export demand, and growing competition in global soybean markets have intensified the shift away from soybean production. These multifaceted issues highlight the complexity of the decline in soybean cultivation areas. Despite these challenges, farmers continued to cultivate second-crop soybeans, with planting rates varying from a low of 4.5% (427.3 hectares) in 2023 to a high of 9.6% (902.0 hectares) in 2021. On average, the cultivation areas for the first and second peanuts were 7.95% (754.9 hectares) and 3.28% (311.4 hectares), respectively. Over 2020-2023, there has been a slight increase in peanut-II cultivation areas. In contrast, the cultivation areas for the first crop of peanuts have decreased within the total AID land area. The lowest recorded plantation rate for the second and first peanut crops occurred at 2.6% (246.9 hectares) in 2021 and 3.9% (370.3 hectares) in 2022, respectively. The decline in first-crop peanut cultivation areas within the AID can be attributed to various economic, climatic, and market-related factors. Due to their higher economic returns, farmers have increasingly prioritized more profitable crops, such as cotton and corn. Furthermore, escalating input costs, including those for seeds, fertilizers, and irrigation, combined with reduced access to subsidies and financial support, have further diminished the feasibility of peanut farming in the region. Conversely, the highest value for peanut-II was observed at 5.9% (560.2 hectares) in 2023, while for peanut-I, it reached 12.3% (1,167.9 hectares) in 202. The classified maps for the summer season revealed that the cultivation of first-crop corn, peanut, and cotton (corn-I, peanut-I, cotton-I) along with second-crop cotton and soybean (cotton-II, soybean-II) accounted for an average of slightly more than two-fifths (44.83%) of the total area in the AID during the study period. In general, this change in cultivation areas in AID is influenced by farmer preferences, changes in input prices, market conditions, etc.

The application of ANN for crop classification in the stressed area was ineffective due to the inability of NDVI values during the crop growth stage to represent the crop canopy adequately. Many parcels were partially covered by bare soil, and some areas experienced limited crop growth due to salinity and other environmental factors. This issue, caused by inadequate crop coverage, hindered the ANN's ability to distinguish and classify crop types accurately. Consequently, ground truth data from the stressed area were utilized to accurately identify and represent the parcel locations, as shown in Figure 4.3b-Figure 4.6b.

Throughout the research period, most citrus and sapling cultivation has been focused on the vicinity of the two coastal lagoons of the LSP, constituting approximately two-thirds of the combined citrus and sapling area. Between 2020 and 2023, the regions adjacent to the coastal lagoons of the LSP were utilized as pastureland. Analysis of RS data revealed that NDVI values for pastureland exceeded 0.26 compared to bare soil, which typically registers NDVI values ranging from 0.18 to 0.22 in AID. This discrepancy can be attributed to sparse grass in these areas, facilitated by the elevated groundwater levels, as shown in Figure 3.9. The cultivation area for wheat crops declined significantly along the coastal regions of the LSP, notably in both 2022 and 2023, as illustrated in Table 4.3. For instance, the area dedicated to wheat cultivation was 279 hectares in 2020 but decreased to 137.1 hectares by 2023. In the stressed region of the Lower Seyhan Plain (LSP), the cultivation areas for soybean-I, soybean-II, peanut-I, peanut-II, and corn-II were notably smaller than those allocated for cotton-I and cotton-II, as shown in Table 4.4. This disparity arose due to the ability of the first and second cotton crops to tolerate elevated salinity levels and groundwater conditions in the LSP. The number of parcels containing vegetable gardens and fruit orchards near the coastal lagoons of the Lower Seyhan Plain (LSP) is significantly lower compared to those within the AID, primarily due to differences in soil quality and groundwater conditions (Cetin et al., 2000). Coastal areas are often characterized by saline or sodic soils, elevated groundwater salinity, and waterlogging, negatively impacting crop productivity (Akça et al., 2020). Furthermore, these regions typically could need advanced irrigation and drainage infrastructure. The higher humidity levels near the lagoons also contribute to unfavorable growing conditions by increasing the prevalence of pests and diseases. Economic factors, such as the preference for salt-tolerant crops, less resource-intensive land use, and land use policies aimed at conserving coastal ecosystems, further exacerbate the disparity. Addressing these environmental and infrastructural challenges is essential to enhance agricultural productivity and optimize land use near the LSP's coastal lagoons.

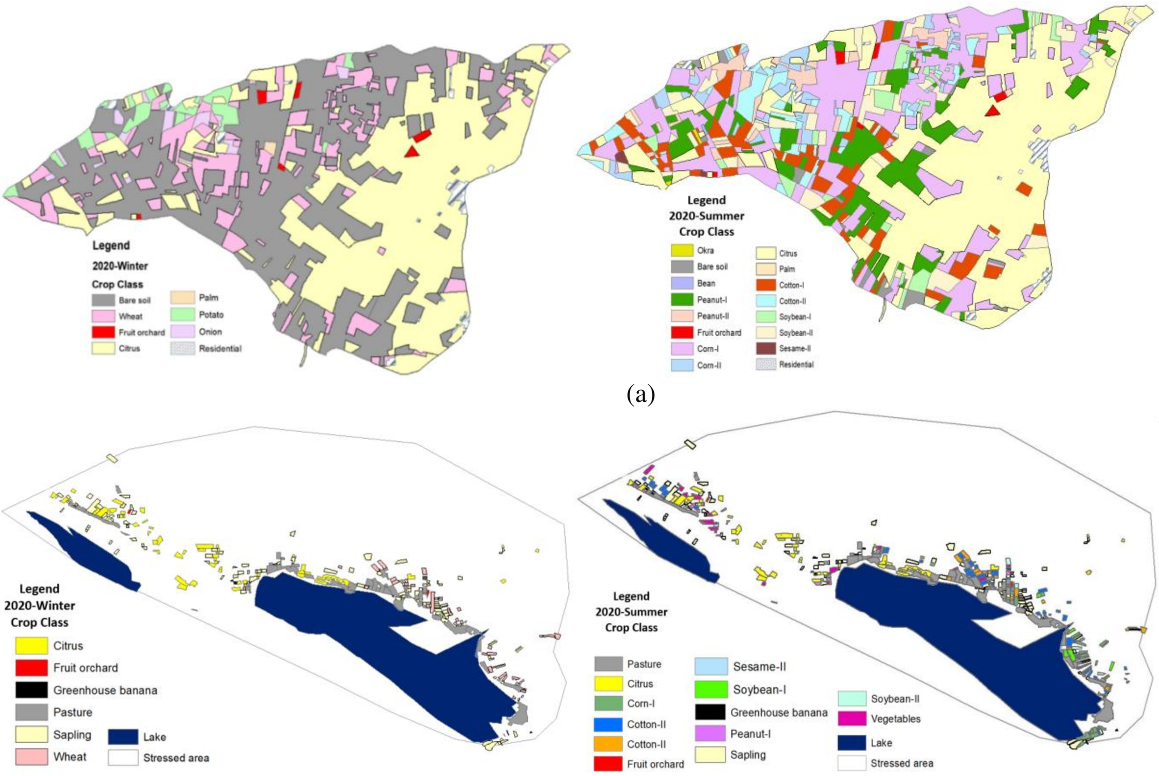

(a)

(b)

Figure 4.3. Crop distribution patterns during the winter and summer of 2020 in (a) AID) and (b) the stressed regions of the LSP in Türkiye

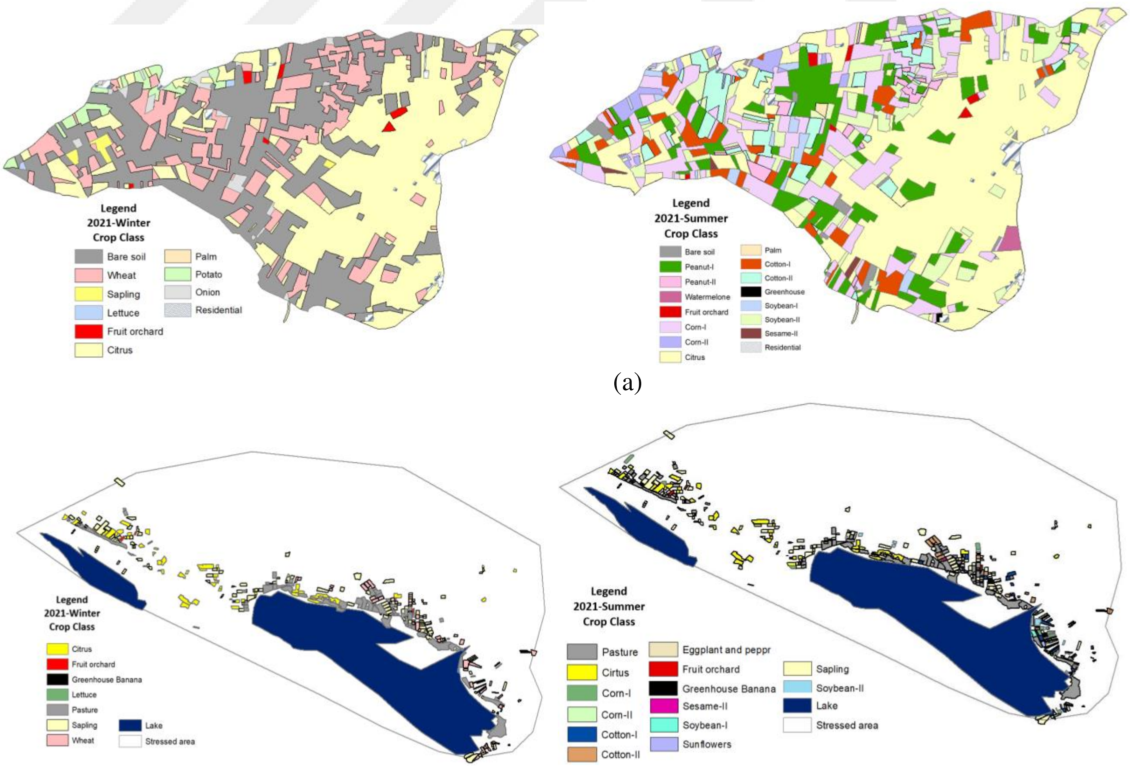

(a)

(b)

Figure 4.4. Crop distribution patterns during the winter and summer of 2021 in (a) AID and (b) the stressed regions of the LSP in Türkiye

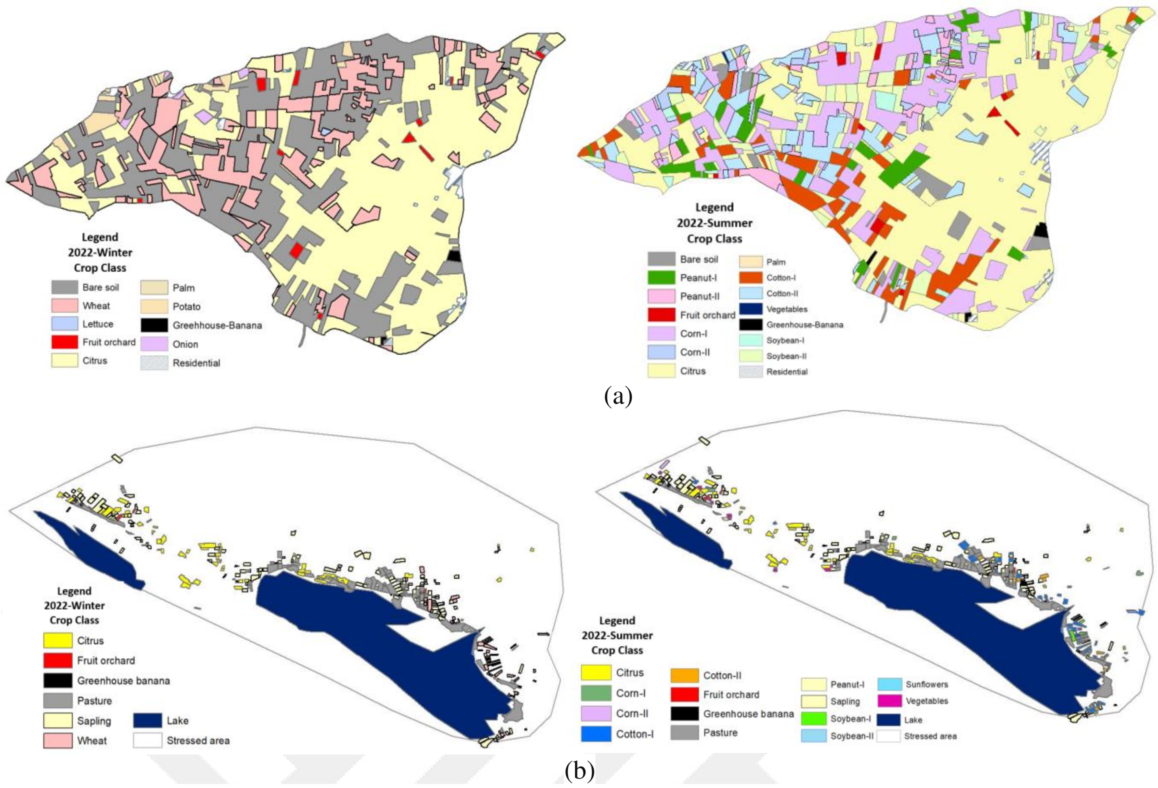

Figure 4.5. Crop distribution patterns during the winter and summer of 2022 in (a) AID and (b) the stressed regions of the LSP in Türkiye

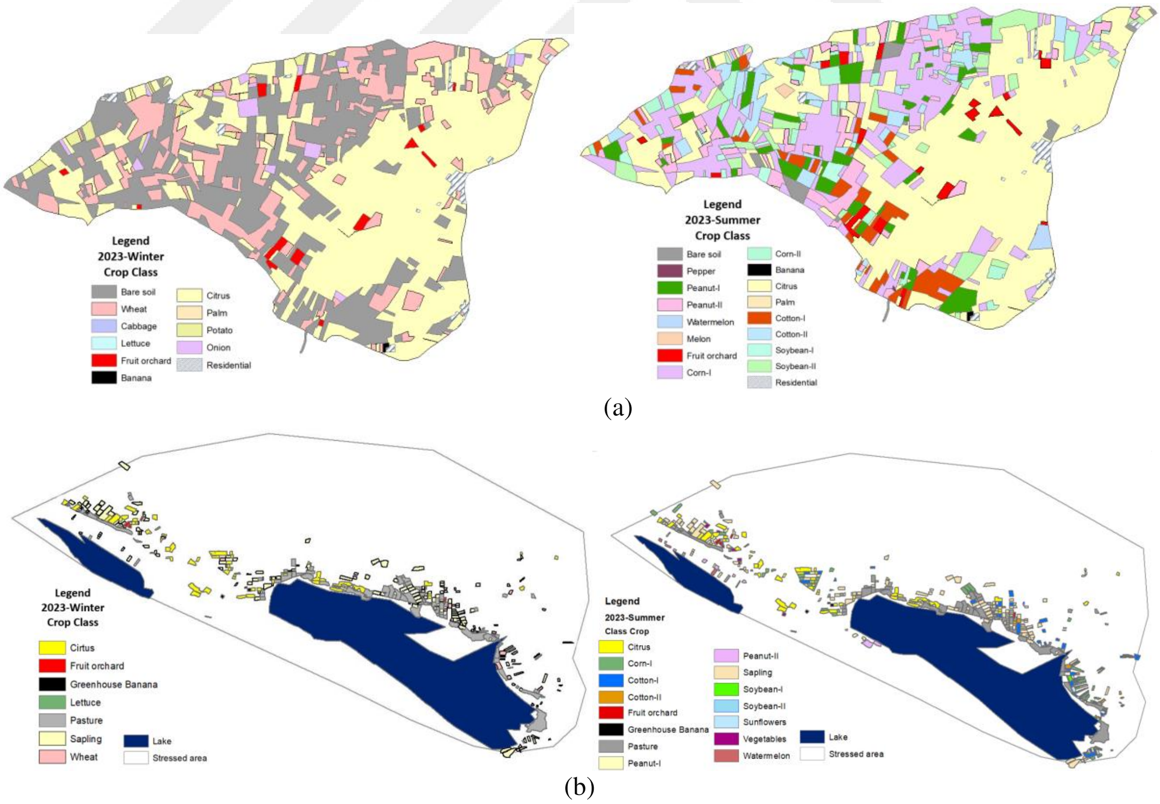

Figure 4.6. Crop distribution patterns during the winter and summer of 2023 in (a) AID and (b) the stressed regions of the LSP in Türkiye

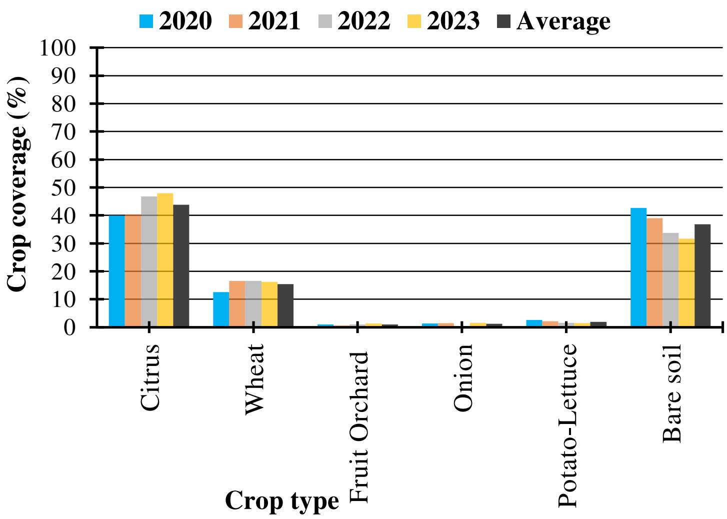

Figure 4.7. The proportions of land area occupied by cultivated plants in the AID during the winter season, categorized by water years

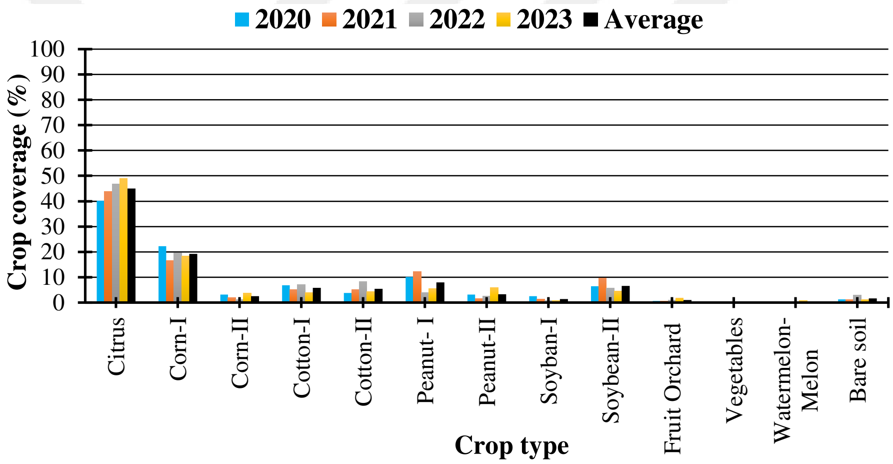

Figure 4.8. The proportions of land area occupied by cultivated plants in the AID during the summer season, categorized by water years

Table 4.3. The land area (ha) cultivated plants in the stressed area during the winter season for the years 2020-2023

	2020	2021	2022	2023
Citrus	540.1	540.1	540.1	560.0
Wheat	279.0	343.7	213.5	137.1
Fruit Orchard	11.8	20.4	21.2	25.4
Potato-Lettuce	0.8	0.0	0.0	17.3
Pasture	1021.2	1043.1	1006.2	1041.8
Sapling	710.7	813.1	934.1	931.8
Greenhouse Banana	6.7	6.7	6.7	10.3

Table 4.4. The land area (ha) cultivated plants in the stressed area during the summer season for the years 2020-2023

	2020	**2021**	**2022**	**2023**
Citrus	540.1	540.1	540.1	560.0
Corn-I	181.7	112.0	62.4	308.2
Corn-II	0.0	0.8	16.9	13.2
Cotton-I	317.6	188.3	296.9	294.1
Cotton-II	135.7	167.7	115.6	64.9
Peanut- I	40.6	99.9	21.1	28.8
Peanut-II	0.0	0.0	0.0	68.3
Soybean-I	95.8	24.9	47.0	19.1
Soybean-II	59.7	55.0	23.0	3.2
Fruit Orchard	11.8	20.4	21.2	25.4
Vegetables	136.9	55.7	0.0	24.8
Watermelon-Melon	0.0	0.0	0.0	20.1
Pasture	1021.2	1043.1	1006.2	1041.8
Sapling	710.7	813.1	934.1	931.8
Greenhouse Banana	6.7	6.7	6.7	10.3
Sunflowers	0.0	15.5	17.0	26.6
Sesame-II	6.2	5.8	0.0	0.0

It is noteworthy that the ground truth data of crop visits agreed with the crop-classified maps generated through the ANN approach during testing, particularly in terms of overall accuracy, as delineated by Alsenjar et al. (2023a), Alsenjar et al. (2023b), Cetin et al. (2023a) and Cetin et al. (2023b), using the AID of the LSP as an exemplar in 2021. They reported that certain crops, such as lettuce, potato, sesame-II, palm, and watermelon, achieved a 100% estimation accuracy, while onion and wheat surpassed 90%. Conversely, other crops, including citrus, the first and second crops of cotton, soybean, peanut, and corn, attained accuracies exceeding 77%, except for fruits. This discrepancy may be attributed to the similarity in shape between fruit orchards and citrus or their coverage features. The results of the classified crop maps by Alsenjar et al. (2023a), Cetin et al. (2023a), and Cetin et al. (2023b) align closely with the estimated crop maps for 2020–2023, particularly when post-processing techniques were applied to test data, as shown in Figure 3.15. Utilizing the ANN approach in ENVI software, these studies suggest that the classification accuracy for distinct crops, such as lettuce and sesame, is exceptionally high due to their unique spectral signatures and growth patterns. However, the consistency in results also emphasizes the role of comprehensive ground truth data and precise calibration processes, as Alsenjar et al. (2023a) highlighted, in reducing misclassification and improving model reliability across various crop types. These findings underline the importance of integrating robust post-processing steps to address classification challenges and enhance the effectiveness of ANN-based mapping techniques. However, visually and morphologically similar crop categories, such as fruits and citrus, pose challenges for classification due to spectral overlaps and structural similarities. These limitations can be addressed by applying advanced post-processing techniques and integrating multi-temporal datasets to enhance classification precision. Furthermore, the consistency of results across multiple years (2020–2023) highlights the robustness and reliability of the proposed approach, showcasing its potential for broader use in precision agriculture and comprehensive crop monitoring applications.

4.3. Estimation of ET_a by the standard METRIC and EEFlux METRIC and comparison with ET_o by the FAO-PM approach

In this study, the $ET_{a\text{-}METRIC}$ estimates, based on the standard METRIC methodology, were obtained utilizing instantaneous climatic data observed locally at L8 and Cotlu stations within the AID, as well as at Gumusyazi and Golkaya stations situated in the stressed region of the LSP. Additionally, 70 Landsat satellite images with a spatial resolution of 30 m×30 m were utilized to span the years 2020-2023. To compute ET_a using the METRIC model, it is necessary to format the climatic data according to the satellite overpass date in Universal Time Coordinated (UTC). To illustrate this procedure, for instance, climate information should be collected for a certain satellite image that passes over the research area on the day before, on the day of, and after a given satellite overpass time. This adjustment is essential to synchronize the local time of in-situ climatic observations with the satellite imagery overpass data presented in UTC. This research implemented this way for the METRIC model and other SEB models to estimate ET_a for 2020-2023. Following a preliminary analysis of the satellite images, they underwent further examination using the METRIC methodology, deriving ET_a values. Consequently, daily areal ET_a values were computed for each date in Table 3.4.

In this study, the land surface energy balance components—including latent heat flux (LE), net radiation (R_n), soil heat flux (G), surface temperature (T_s), and sensible heat flux (H)—were estimated for each dataset corresponding to the satellite overpasses on the specified dates outlined in Table 3.4, following the methodology employed. For instance, Figure 4.9 illustrates the land SEB components across the AID and stressed areas of the LSP captured in the satellite image dated 21.10.2021 (as listed in Table 3.4). Notably, conspicuous local variability exists in the SEB components across the land surface within the study area. This variability can primarily be attributed to the diverse land use types and varying characteristics of soil series present in the two distinct research areas, i.e., AID and stressed areas.

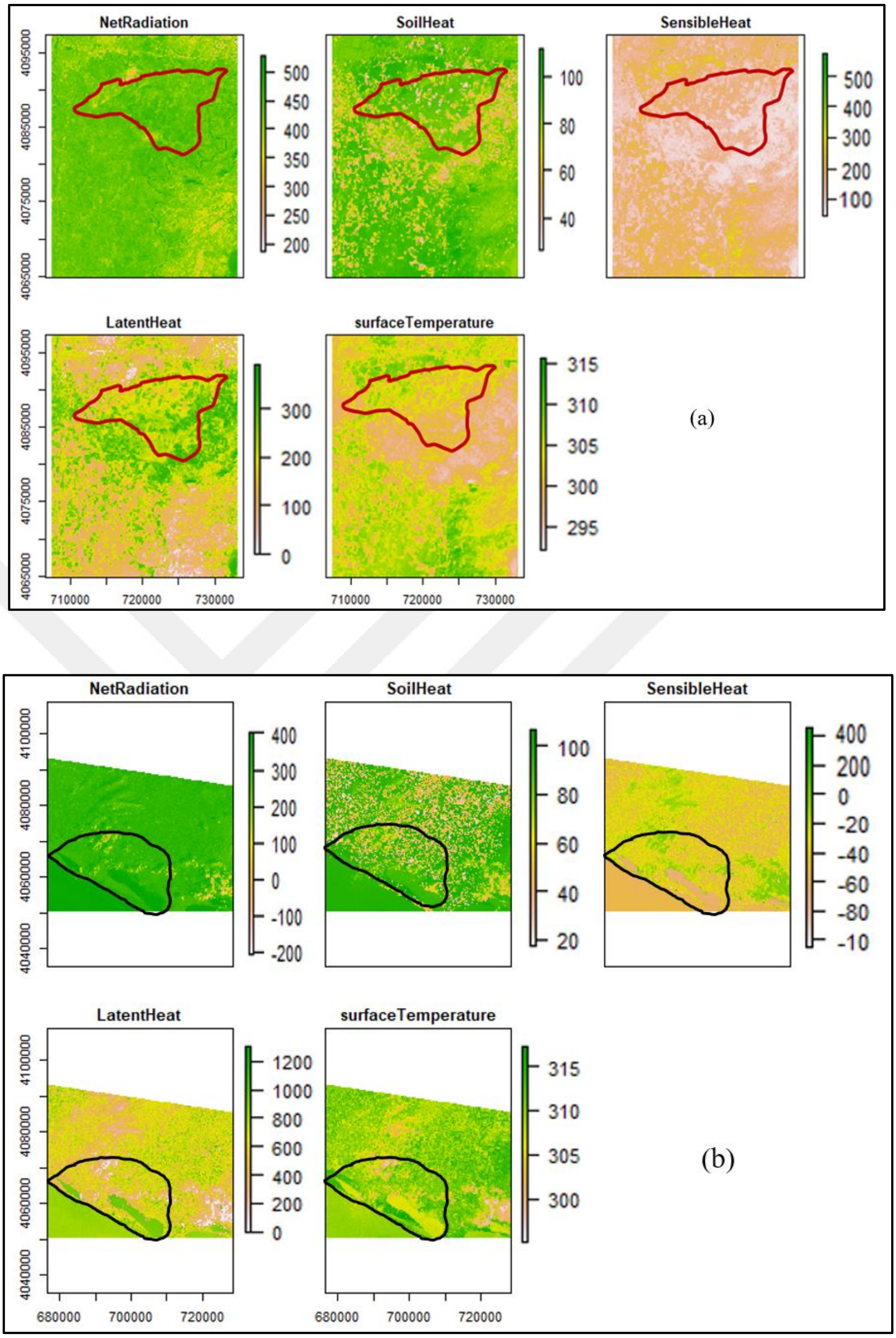

Figure 4.9. Spatial distribution of land surface energy balance (LE, Rn, G, and H, W m^{-2}) components by the METRIC methodology over (a) AID and (b) stressed area on 21.10.2021 (DOY 294)

Numerous satellite images were utilized during the study period for areal ET_a estimations. However, for illustrative purposes, the areal distribution of ET_a (in the unit of mm day^{-1}), calculated utilizing the METRIC methodology, is presented for the area of interest (AoI) polygon based on the satellite image dated DOY 294 (21.10.2021 as shown in Figure 4.10). The AoI polygon was selected as rectangular to make analysis more straightforward, as depicted in Figure 4.10. This polygon encompasses a sizable area, covering approximately 840 km² (25.7 km x 32.7 km), aiming to capture land SEB and compute ET_a over a wider area than the research area. Subsequently, the final ET_a map was generated for each satellite image dataset, as delineated in Table 3.4, by cropping or clipping the AID and the stressed area of the LSP within the polygon. This process was accomplished using the "*clip tool"* of the ArcGIS software. The resultant ET_a map for the AID and stressed area of the LSP on 21.10.2021 (DOY 294) is displayed in Figure 4.11, serving as an example of the methodology employed.

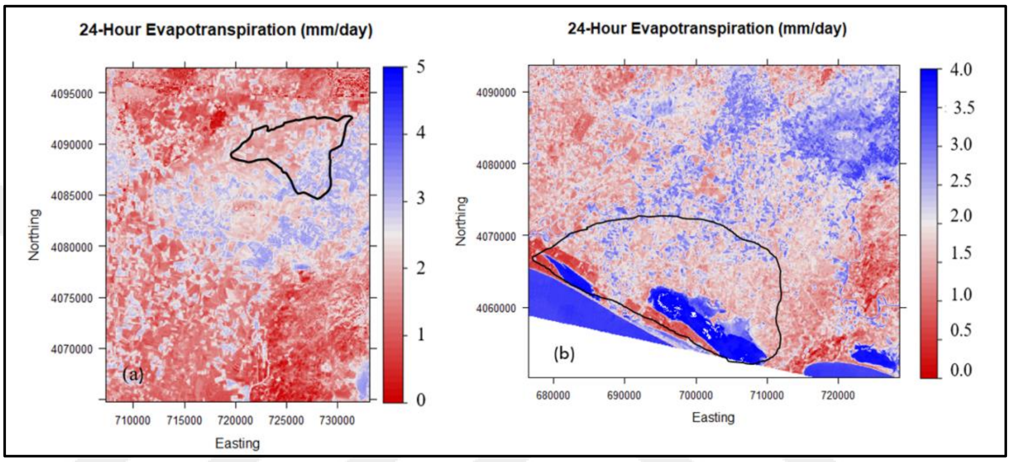

Figure 4.10. Spatial distribution of actual evapotranspiration ($ET_{a\text{-}METRIC}$, in mm day^{-1}) estimated using the METRIC methodology from the satellite image dated 21.10.2021 (DOY 294) for the designated polygon of interest, encompassing (a) the AID area and (b) the stressed area of the LSP

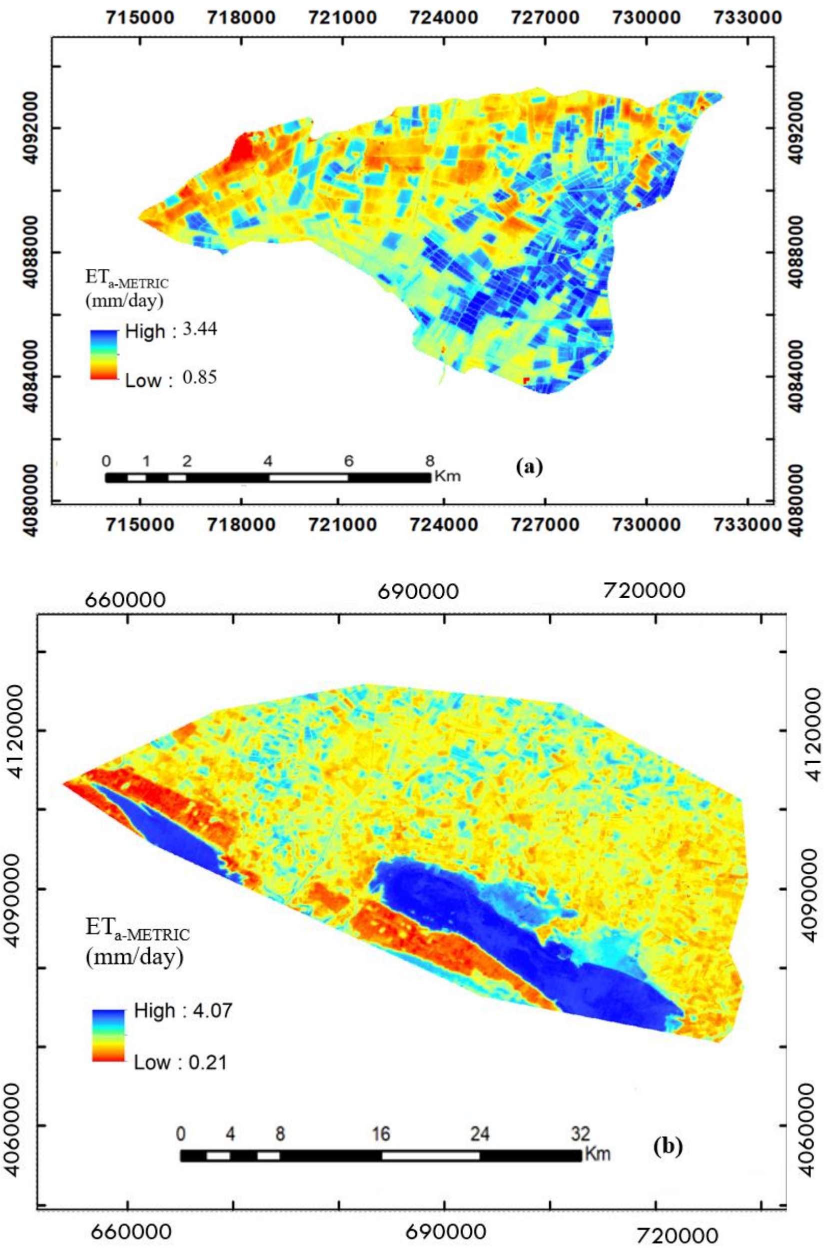

Figure 4.11. Spatial distribution of actual evapotranspiration ($ET_{a\text{-METRIC}}$, mm day^{-1}) estimated using the METRIC methodology from the satellite image dated 21.10.2021 (DOY 294) in the research area, (a) AID, and (b) stressed area

Figure 4.11 shows that ET_a by the METRIC model varies from 0.85 to 3.44 mm day^{-1} in the AID, while it was between 0.21 to 4.07 mm day^{-1} in the stressed regions of the LSP as of October 21, 2021 (DOY 294). Within the research domain, the predominant vegetation consists of citrus plants, constituting approximately half of the total coverage according to the crop pattern map, as shown in Figure 4.4. In citrus cultivation areas, ET_a values range from 2.4 to 3.44 mm day^{-1} within the AID on DOY 294, while in the stressed region, they range from 2.37 to 2.83 mm day^{-1} on the same date. Furthermore, the evaporation rate of coastal lagoons within the LSP peaked at 4.07 mm day^{-1}, marking the highest recorded value in stressed areas. Conversely, ET_a values remain generally lower in fallow lands, particularly during winter, with higher rates observed in vegetated areas.

To express the research results meaningfully, descriptive statistics of the ET_a map obtained using the METRIC model from the satellite image dated 21.10.2021 (DOY 294) are shown in Table 4.5, in the AID and the stressed area of the LSP. The statistical analysis compares the ET_a values between two regions—the NSA (AID) and the SA of the LSP—by examining the distribution of ET_a across these areas as a whole. This approach provides a general overview of the ET_a variations across the study area rather than focusing on a specific crop type. By considering the entire area, the analysis helps to highlight how the mean ET_a value changes when comparing the two regions. This broader perspective aligns, demonstrating regional differences in evapotranspiration rather than focusing on crop-specific variations. This approach is beneficial for understanding overall water use trends and variability in the study area, offering relevant insights for agricultural water management across diverse land uses. The following results provide a detailed comparison of ET_a for the same crop type, focusing specifically on the AID and stressed regions of the LSP, as estimated using the METRIC model. This comparison highlights the differences in ET_a across these areas, offering insights into how varying environmental conditions affect water use for the selected crop. The mean value of ET_a in the AID area was 2.25 mm day^{-1}, while it was 2.09 mm day^{-1} in the stressed area of the LSP. The reduced mean ET_a observed between these areas may be attributed to factors such as salinity, alkalinity, and rising groundwater levels in the stressed area near the Lagoons of the LSP compared to the AID. Additionally, certain crops, including potatoes, onions, fruits, and mixed intercropping varieties, among others, were cultivated in the AID but absent from the stressed area of the LSP. The standard deviation of ET_a was 0.49 mm day^{-1} and 0.84 mm day^{-1} in the AID and the stressed area of the LSP, respectively. These statistics confirmed the notable variation in average ET_a values across different land use types within the research area. The diversity in ET_a values can be attributed to various factors such as the planting dates, physiological characteristics, and growth stages of the different plant species. This variability significantly contributes to the variance and coefficient of variation observed in ET_a maps. For instance, when comparing ground-based data with satellite imagery, it is revealed that areas identified as citrus plantations may have newly planted saplings. Consequently, depending on the agricultural practices in these areas, the soil surface could be bare or partially covered with weeds, leading to considerable fluctuations in ET_a values within supposed citrus parcels, sometimes mirroring bare soil. Moreover, within residential zones, the wide-ranging vegetation density, including weed growth around buildings or densely populated fruit trees, contributes to the variability in ET_a values.

Table 4.5. Some descriptive statistics of actual evapotranspiration by the METRIC model ($ET_{a-METRIC}$, mm day^{-1}) are available on October 21, 2021, within the AID and stressed areas

Statistics	AID (NSA)	Stressed area (SA)
Min	0.54	0.21
Max	3.44	4.07
Mean	2.25	2.09
Standard deviation (S)	0.49	0.84
Coefficient of variation ($CV=ET_{a-mean}/S$) %	21.8	40.2

Satellite images listed in Table 3.4, covering the period from October 1, 2019, to September 30, 2023, were analyzed to calculate ET_a values for each date. These values are presented in Figure 4.12 for the non-stressed area (NSA, i.e., AID) and the stressed area (SA) within the LSP. As estimated using the METRIC model, the variability in ET_a between SA and NSA underscores the substantial impact of stress factors such as salinity, alkalinity, and water availability on plant water consumption. NSA consistently demonstrates higher ET_a values due to favorable growing conditions and adequate irrigation. In contrast, SA exhibits lower and more variable ET_a, especially during peak growing seasons, indicating diverse stress responses. However, fractions (ET_rF) denoted as $K_{c-METRIC}$ were also determined. To obtain ET_a values as a time series, interpolations were made using these fractions between two satellite imagery dates as outlined in the methodology by Allen et al. (2007a). Thus, intermediate ET_a values were estimated for the years 2020-2023. As a result, the ET_a values obtained are shown as a time series in Figure 4.13. Based on the ET_a computations within the AID region, cumulative ET_a values, which are areal as well as unique values for these years, were determined as 1,191.23 mm, 1,254.4 mm, 1,003.0 mm, and 914.07 mm for the years 2020, 2021, 2022, and 2023, respectively, as shown in Figure 4.14. Consequently, the mean annual cumulative ET_a amounted to 1,090.68 mm from 2020 to 2023 within the AID of the LSP. This value serves as a reference point for evaluating the typical water demand in the region, capturing the combined effects of climatic variability, cropping patterns, and irrigation practices over four years. The higher ET_a values observed in 2020 and 2021, compared to 2022 and 2023, highlight temporal variations likely influenced by temperature fluctuations, rainfall, or water availability. The daily mean, lowest, and highest ET_a values by the METRIC model were estimated as 3.00 mm day^{-1}, 0.34 mm day^{-1} on January 16, 2023 (during winter), and 8.86 mm day^{-1} on August 23, 2020 (during summer), respectively, throughout the years 2020-2023. The mean daily $ET_{a-METRIC}$ values were determined to be 3.25 mm, 3.44 mm, 2.75 mm, and 2.50 mm for the years 2020, 2021, 2022, and 2023, respectively, as shown in Figure 4.15. During the summer season (peak irrigation period) from 2020 to 2023, the average daily $ET_{a-METRIC}$ values in July and August were estimated as 5.5 mm, 4.8 mm, 4.4 mm, and 3.7 mm for the years 2020, 2021, 2022, and 2023, respectively. The mean $ET_{a-METRIC}$ rates during the summer season from 2020 to 2023 were notably higher than the average daily $ET_{a-METRIC}$ over the entire year. This increase can be attributed to elevated temperatures and higher humidity levels during the peak irrigation period. The daily ET_a values for the water years 2020 to 2023 exhibit significant seasonal variability. This temporal variability is primarily due to changes in crop patterns, such as the annual selection of different crop types based on farmers' preferences—such as corn, cotton, and soybean—as well as fluctuating market conditions. These crops have varying water consumption rates compared to others. Additionally, minor yearly fluctuations in climatic data contribute to this variability. Together, these factors lead to differences in the mean ET_a values estimated by the METRIC model during the 2020-2023 period.

Figure 4.14 depicts the temporal fluctuations of monthly $ET_{a\text{-METRIC}}$ across the AID. The peak monthly ET_a value of 182.54 mm was observed in August 2020, while the lowest monthly value of 26.91 mm occurred in January 2023. The results in Figure 4.14 indicate that July and August exhibited the highest ET_a values by the METRIC model throughout the study period. Regarding crop varieties and growth stages, elevated ET_a levels were recorded during the mid-season, particularly in July, aligning with the peak of the irrigation season. Conversely, in 2021, notably during the winter months, ET_a estimates surpassed those of the corresponding period in other years. In the same context, lower ET_a rates were noted during the early and late stages of the growing season. As explicitly outlined by Senay et al. (2016), these fluctuations in ET_a could be attributed to various factors such as distinct land use/land cover categories, vegetation growth durations and stages, climatic conditions, and soil moisture availability.

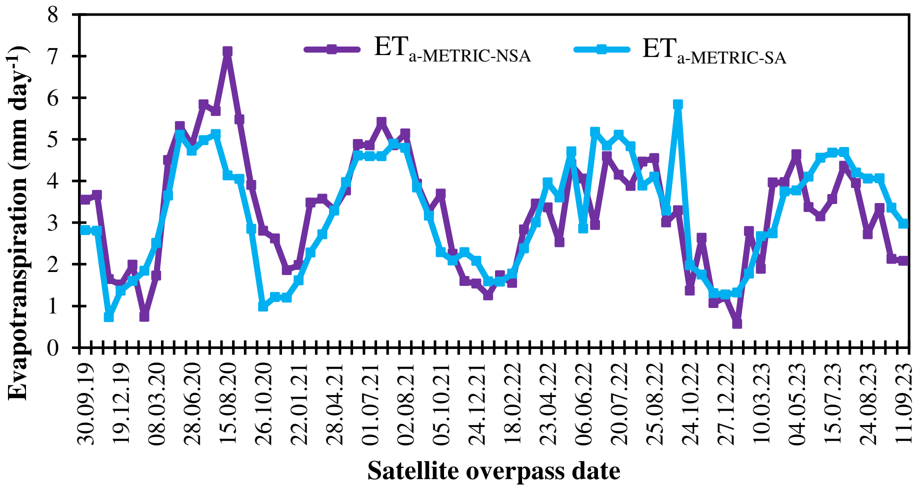

Figure 4.12. The temporal fluctuations in the average daily actual evapotranspiration ($ET_{a\text{-METRIC}}$, mm day^{-1}) values, obtained through the METRIC methodology, during satellite overpasses over the (a) AID and (b) stressed region of the LSP

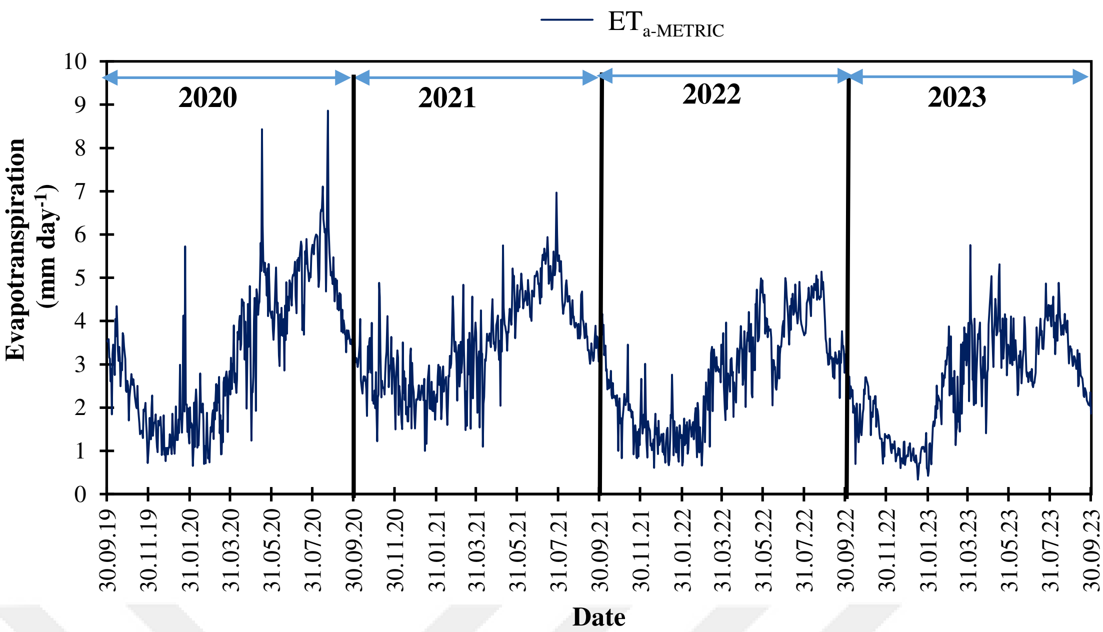

Figure 4.13. The temporal changes in the average daily actual evapotranspiration ($ET_{a\text{-}METRIC}$, mm day^{-1}) values, obtained using the METRIC methodology, from September 30, 2019, to September 30, 2023, across the AID

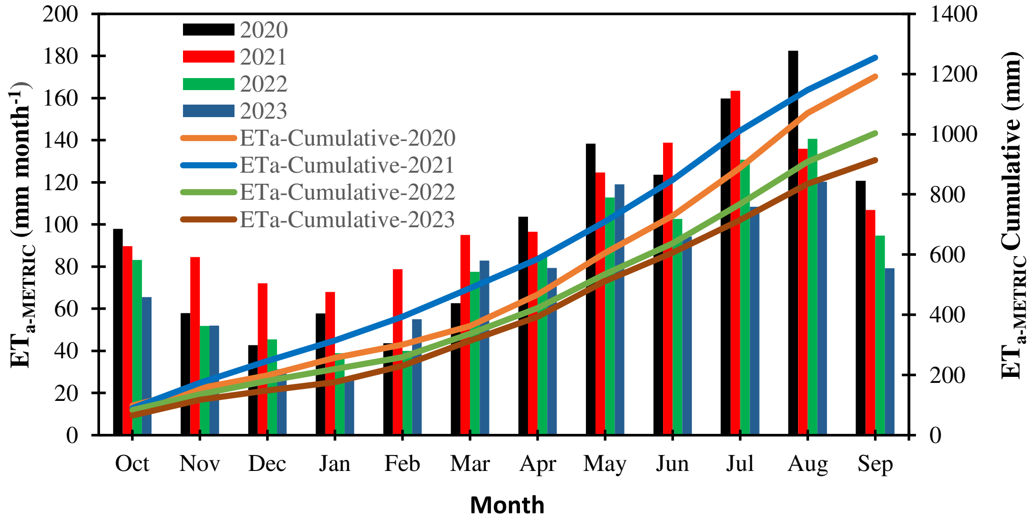

Figure 4.14. Variations in $ET_{a\text{-}METRIC}$ values on a monthly basis across the hydrological years of 2020, 2021, 2022, and 2023 within the AID

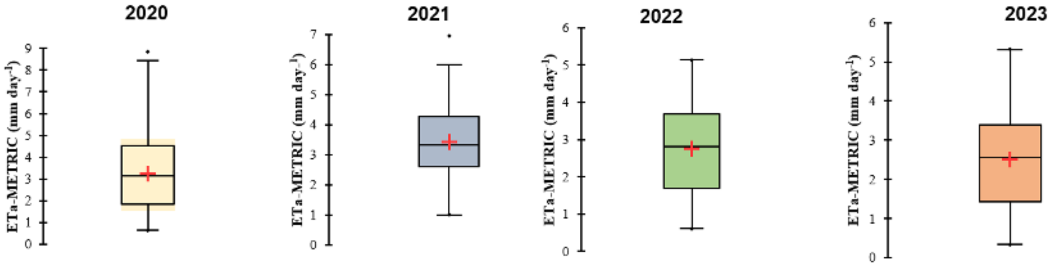

Figure 4.15. ET_a values by the METRIC model over the non-stress area (AID, NS) from 2020 to 202 hydrological year. Horizontal lines in the box plots indicate the median, as well as the 25th and 75th percentiles. Dots on the plot signify outliers (Tukey, 1977; Iglewicz and Hoaglin, 1993), which are data points that lie beyond 1.5 times the interquartile range (IQR) from the first and third quartiles, respectively. The whiskers extending from the plot represent the minimum and maximum values

As outlined in the methodology section, the R-METRIC model and the LandMOD ET Mapper toolbox implemented in MATLAB were employed to compute actual evapotranspiration. Therefore, conducting a comparative analysis of these tools is essential to assess their accuracy, performance, and sensitivity to input data. Additionally, this analysis aims to evaluate how the outputs from each model can be interpreted and utilized and to determine which model offers more practical insights for researchers. These models were employed to estimate ET_a at the pixel, crop, and study area levels. These methods incorporated an automated pixel selection technique using parameters such as NDVI, LAI, and Ts, thereby minimizing the potential for human error (Olmedo et al., 2016; Bhattarai et al., 2017). For instance, hot pixels are identified when NDVI and LAI values are low while T_s is high, while cold pixels exhibit high NDVI and LAI values with low T_s. These features enhance the accuracy and calibration of these programs, enabling them to compute ET_a precisely during satellite overpasses. Moreover, the R-METRIC typically relies on a single weather station, aggregating mean values for each climatic parameter from a network of weather stations within the study area or subdividing the area into smaller segments and estimating ET_a for each sub-area before merging the results into one ET_a map. However, this study did not employ the latter approach because it was insignificant. Instead, LandMOD ET mapper toolbox-MATLAB incorporated multiple weather stations through interpolation methods for climatic parameters such as solar radiation, mean temperature, wind speed, and relative humidity. The LandMOD ET Mapper toolbox in MATLAB is compatible with data from all Landsat satellites (Landsat 7, 8, and 9) as well as MODIS data. On the other hand, the R-METRIC model, included in the water package of the R programming language, is specifically tailored for Landsat 7 and 8 data. Therefore, these tools are essential for estimating ET_a using the METRIC model. The ET_a estimates obtained from the R-METRIC program and LandMOD ET mapper toolbox-MATLAB yielded similar results within the study area. However, it is worth noting that the process of running LandMOD ET mapper toolbox-MATLAB is time-consuming, particularly during the preparation of input data, especially when interpolating climatic data using techniques like Inverse Distance Weighting (IDW) Interpolation in cases where multiple weather stations service the study area. The LandMOD ET Mapper toolbox for MATLAB offers the convenience of estimating ET_a using both the METRIC and SEBAL models with a single click, thanks to its user-friendly interface. In contrast, the R-METRIC package, accessible through R, supports ET_a estimation solely for the METRIC model. However, the R-METRIC package provides notable advantages, including detailed control over input parameters, step-by-step processing visibility, and the ability to store additional results such as NDVI, leaf area index (LAI), surface albedo, emissivity, surface roughness (Z_{om}), surface temperature (T_s), as well as radiation (R_n), soil heat (G), sensible heat flux (H), and latent heat (LE). Conversely, the LandMOD ET Mapper toolbox for MATLAB does not offer step-by-step processing visibility, making it less transparent. Nevertheless, the LandMOD ET Mapper toolbox provides combined K_c maps for the METRIC and SEBAL models and maps for R_n, G, H, LE, and ET_a. Overall, the R-METRIC and LandMOD ET Mapper toolbox for MATLAB have their respective strengths and limitations. Therefore, the user should consider the pros and cons of the two methodologies. Despite differences in inputs, outputs, and processing, in this study, both tools are effective enough for estimating ET_a using the METRIC model in the Lower Seyhan Plain and other global regions.

In estimating ET_a, the R program offers two versions of the water package: a simple one primarily suitable for flat terrains and an advanced version incorporating a DEM to account for slope and other corrections in high-terrain areas. Despite the advanced version's longer processing time due to increased user control over input parameters and coefficients, Alsenjar et al. (2023b) and Cetin et al. (2023b) emphasized that both versions give similar results when applied to flat terrains within the study area for the years 2020-2023. Additionally, comparisons were made between the advanced version of the water package in R and the LandMOD ET mapper toolbox implemented in MATLAB, focusing on specific dates like September 9, 2021 (DOY 190), and October 21, 2021 (DOY 294) as shown in Table 3.4. These comparisons revealed nearly identical results. One notable advantage of the LandMOD ET mapper toolbox in MATLAB over the R-METRIC model is its ability to import various types of Landsat data, including data from Landsat 9 and other sources like unmanned aerial vehicles (UAVs). Conversely, the R-METRIC model is limited to reading data solely from Landsat 7 and 8 satellite images, thus lacking compatibility with Landsat 9 data launched on September 27, 2021. This limitation is an essential consideration within the context of the research. Furthermore, the LandMOD ET mapper toolbox within the MATLAB program offers the capability to estimate ET_a by running both the SEBAL and METRIC models into a single function. This toolbox also supports using Landsat and MODIS data for ET_a estimation. In contrast, the water package in the R program is limited to computing ET_a solely using the METRIC model.

The EEFlux application was employed to assess ET_a utilizing the METRIC model. It leveraged CFSV2 gridded weather data with 70 Landsat satellite datasets at a spatial resolution of 30 m across the study area from 2020 to 2023. This methodology evaluated the precision of ET_a estimations derived from the EEFlux METRIC against those obtained through the conventional METRIC approach and the FAO-PM method for calculating ET_o. For instance, Figure 4.16 illustrates the spatial distribution of ET_a as determined by EEFlux-METRIC on July 30, 2020 (DOY 212). On this specific day, the ET_a values estimated using the EEFlux model were 4.32 mm day^{-1} in the Akarsu Irrigation District (AID) and 4.52 mm day^{-1} in the stressed region of the Lower Seyhan Plain (LSP). Conversely, $ET_{a\text{-METRIC}}$ values for the AID were higher at 5.67 mm day^{-1} compared to the $ET_{a\text{-EEFlux}}$ value of 4.32 mm day^{-1} on DOY 212. Similarly, ET_a values of 5.12 mm day^{-1} by the standard METRIC method in the stressed area exceeded the $ET_{a\text{-EEFlux}}$ value of 4.52 mm day^{-1} on DOY 212. This discrepancy may be attributed to differences in climatic data usage, as the standard METRIC method relied on locally sourced weather data from the study area. In contrast, EEFlux utilized globally sourced CFSV2 gridded weather data. It can be concluded that ET_a values obtained from the EEFlux-METRIC platform were slightly underestimated compared to those determined by the standard METRIC model, which uses local climatic data from the stress region of the LSP in Türkiye on the satellite overpass date. Overall, the EEFlux platform could be a viable alternative for estimating ET_a in the Lower Seyhan Plain of Türkiye when unavailable local climatic data.

Figure 4.17a and Figure 4.17b illustrate the temporal fluctuations in areal mean ET_a values estimated by standard METRIC, EEFlux-METRIC, and ET_o by the FAO-PM approach across the AID and stressed area of the LSP at the satellite image acquisition dates for years 2020-2023. The goal of these figures is to visually depict the temporal variations in ET_a as estimated by the METRIC model and the EEFlux platform compared to the reference evapotranspiration calculated using the FAO-PM method. Additionally, the figures aim to explore the linear relationship between the ET_a estimates from these models and the ET_o values provided by the FAO-PM approach. As presented in Figure 4.17, the ET_o values generally surpassed the combined ET_a values obtained from both the METRIC and EEFlux methods, except for specific dates such as DOY 353, DOY 28, DOY 228, and DOY 244 within the AID and on DOY 271 in the stressed area of the LSP. The difference between these methods can be attributed to the K_c, represented as the ET_rF_i value within the METRIC model, which may exceed 1.0. This discrepancy reflects the influence of various climatic, soil, and vegetation factors, offering a more comprehensive representation of ET_a in the METRIC model than conventional ET_o values derived solely from climatic data, as outlined by Allen et al. (1998). The conventional ET_o values do not account for additional factors such as soil properties, irrigation practices, and salinity, among others. Conversely, ET_a values derived from the METRIC method exceeded those from EEFlux due to spurious scan lines stemming from sensor anomalies in Landsat 7 ETM$^+$, which were retained in the EEFlux cloud product. However, these scan lines were eliminated by the Quantum Geographic Information System (QGIS 3.24.3) software prior to the calculation of ET_a in the METRIC models using Landsat 7 data. These findings agree with the conclusions of Alsenjar and Cetin (2023) regarding the estimation of ET_a using the EEFlux method over the AID for the 2020 water year.

This study employed linear regression analysis to capture and utilize the linear relationship between ET_a values derived from the METRIC model, which utilizes local climatic data from meteorological stations in the study area, and ET_a values obtained from the EEFlux-METRIC platform, which relies on CFSV2 global gridded data. This analysis aimed to evaluate the accuracy of ET_a estimates from the EEFlux-METRIC model compared to those from the standard METRIC model for the study area from 2020 to 2023, as presented in Figure 4.18. Similarly, linear relationships were established to explore the correlation between ET_o and $ET_{a\text{-}METRIC}$ and ET_o and $ET_{a\text{-}EEFlux}$ with each model's respective RMSE, MAE, and d, as outlined in Table 4.6 and Table 4.7. and Figure 4.19. Table 4.6 and Table 4.7. reveal a strong agreement between ET_a values derived from the standard METRIC method when compared with those from EEFlux in both the AID and the stressed area of the LSP. The RMSE between ET_a values from the METRIC model and those from the EEFlux-METRIC platform was 1.19 mm day^{-1} in the AID area and 1.23 mm day^{-1} in the stressed area of the LSP. For the non-stressed area (NSA), i.e., AID, the regression analysis reveals a moderately strong relationship between $ET_{a\text{-}EEFlux}$ and $ET_{a\text{-}METRIC}$, with an R^2 value of 0.61 and a correlation coefficient of 0.78. A similar relationship is observed in the stressed area, with the regression line having a slope close to 1, indicating that EEFlux estimates of ET_a align more closely with METRIC values under water stress conditions. The consistent R^2 and correlation coefficients across both scenarios suggest that the EEFlux model can be a reliable alternative to METRIC for estimating ET_a, regardless of varying stress levels. These results are consistent with those reported by Foolad et al. (2018), who found similar metrics (R^2 = 0.64–0.88, RMSE = 0.55 mm day^{-1}–2.45 mm day^{-1}, slope = 0.51–1.01) in their analysis of the linear relationship between ET_a estimates from the METRIC model and EEFlux based on the GGE platform for agricultural areas. Their study, which covered 58 scenes across the western and central United States, aimed to compare EEFlux results with standard METRIC applications, thereby highlighting the utility of EEFlux products. The proposed equations that link ET_a estimates from the EEFlux model (which utilizes CFSV2 global gridded data) with those from the METRIC approach (which relies on local climatic data) provide a valuable tool for validating and refining ET_a estimations. By establishing a clear relationship between these two remote sensing models, these equations improve the reliability and accuracy of ET_a predictions across various environmental conditions, including both stressed and non-stressed areas. Strong correlations of r = 0.83 for the AID region and r = 0.94 for the stressed area were found between the ET_o values calculated using the FAO Penman-Monteith method and the ET_a values estimated by the METRIC model. The corresponding R^2 values were 0.64 for AID and 0.85 for the stressed area, indicating a strong and reliable relationship between these estimation methods. In both the AID and stressed areas, the RMSE and MAE values for ET_o calculated using the FAO Penman-Monteith method compared to $ET_{a\text{-}METRIC}$ were lower than those for ET_o-FAO-PM compared to $ET_{a\text{-}EEFlux}$ as indicated in Table 4.6, and Table 4.7. Based on the comparison of RMSE and MAE values between different evapotranspiration estimation methods in this study, it is important to mention some issues. Since the RMSE and MAE values show that $ET_{a\text{-}METRIC}$ estimates are closer to the reference ET_o-FAO-PM than $ET_{a\text{-}EEFlux}$, it is recommended that the METRIC model be prioritized for applications with high accuracy. However, $ET_{a\text{-}EEFlux}$, despite exhibiting higher discrepancies and RMSE and MAE values exceeding 1.00 mm day^{-1}, may still provide valuable insights under specific conditions, such as when local climatic data are unavailable at the time of the satellite overpass in the AID and stressed area of the LSP. The equations proposed in this thesis for estimating ET_a using the EEFlux and METRIC models, combined with ET_o from the FAO-PM in the AID and stressed areas, offer an alternative to running the METRIC model. While this approach requires expertise in managing specific input datasets, the EEFlux platform, which relies on global datasets, allows researchers, engineers, and end users to compute ET_a effectively. With a solid understanding of the METRIC model, even users with moderate experience can leverage EEFlux for ET_a estimation.

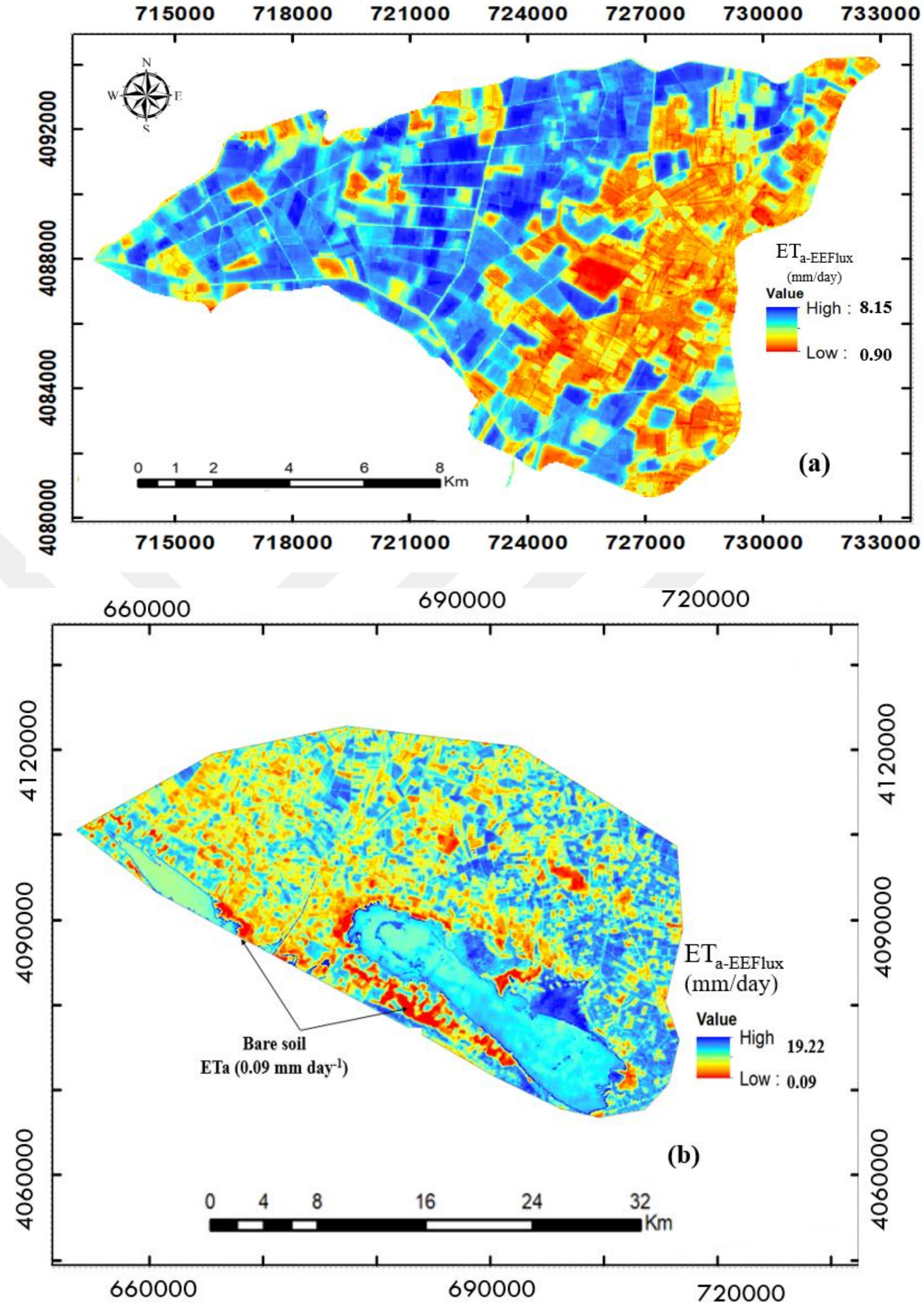

Figure 4.16. Spatial distribution of actual evapotranspiration ($ET_{a\text{-}EEFlux}$, mm day^{-1}) estimated using the EEFlux platform from satellite imagery on 30.07.2020 (DOY 212) for: (a) AID, and (b) stressed area

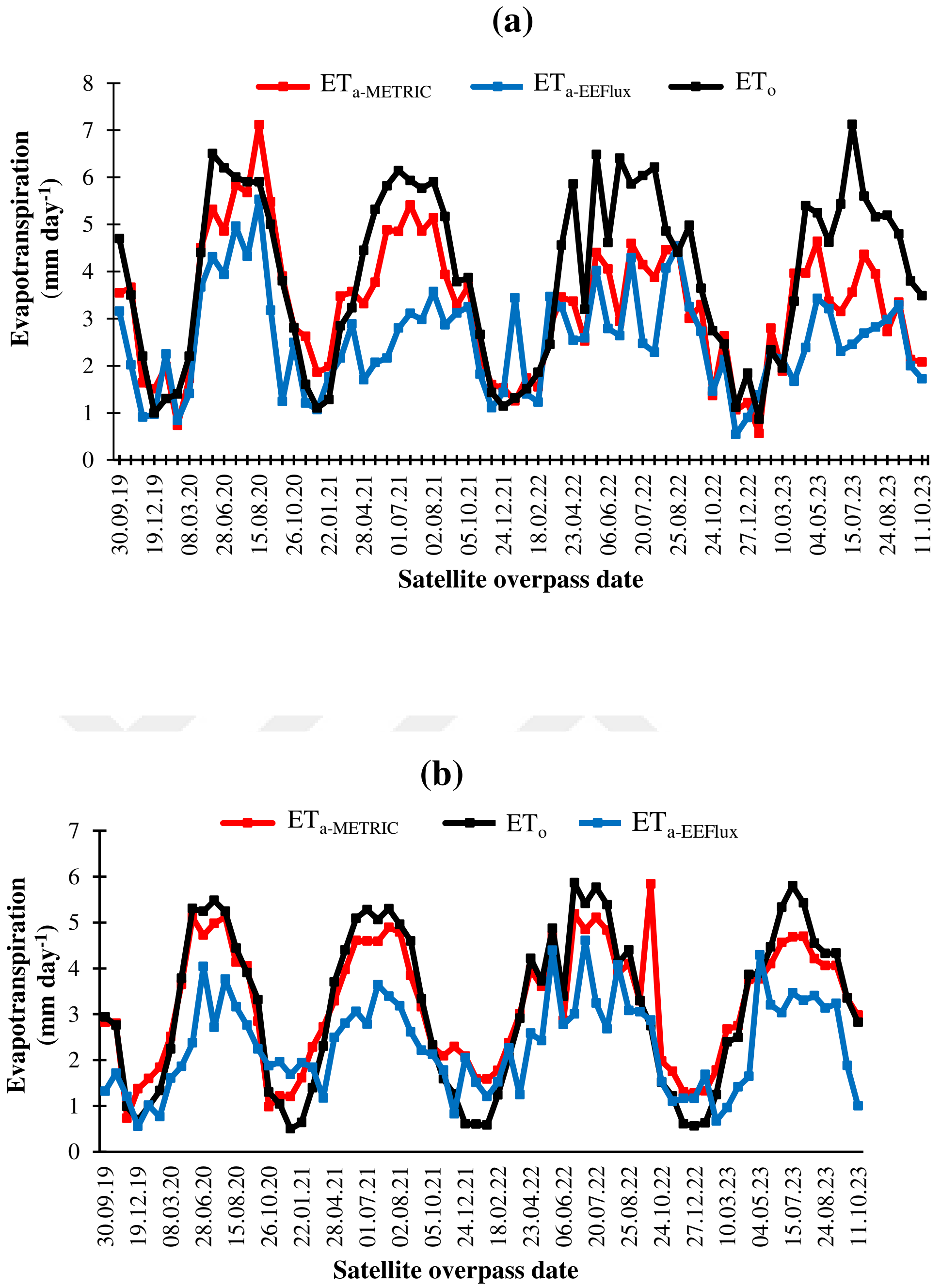

Figure 4.17. Temporal fluctuations in the average daily actual evapotranspiration ($ET_{a\text{-METRIC}}$, mm day^{-1}) values in (a) AID and (b) stressed area of the LSP as determined by the METRIC method, the EEFlux approach, and the ET_o by the FAO-PM method during satellite overpasses

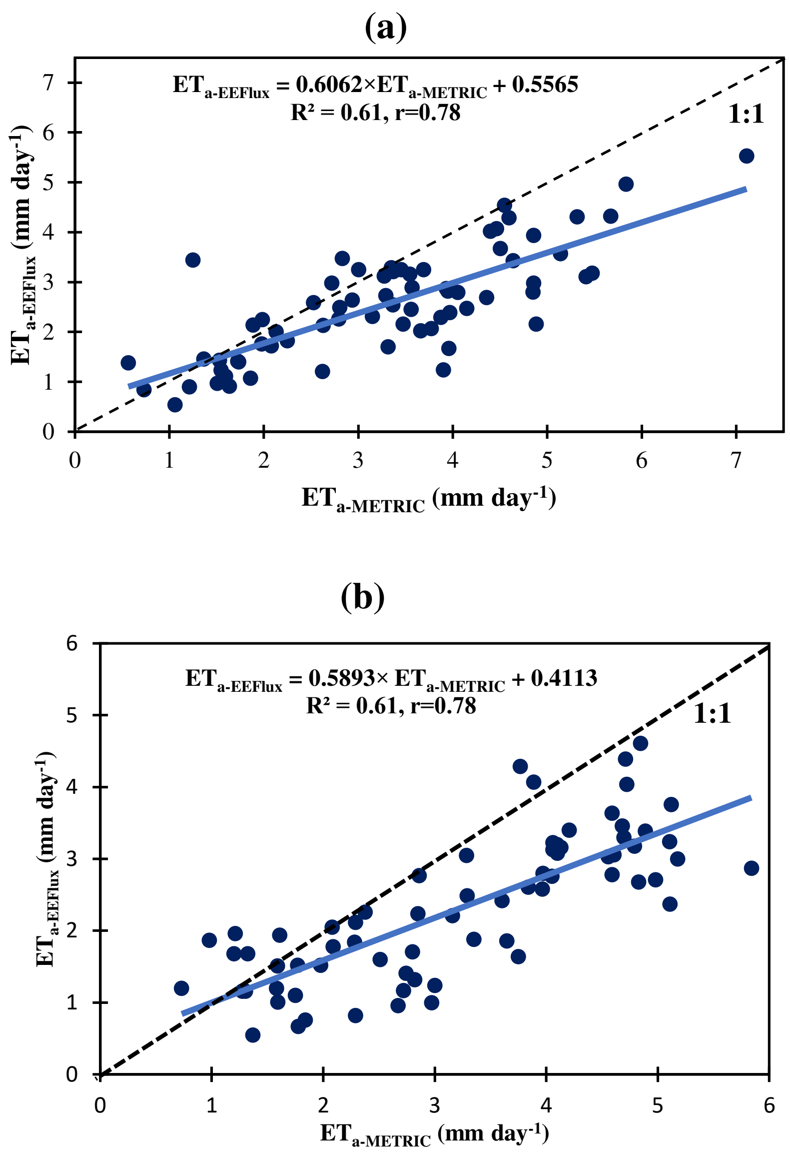

Figure 4.18. Linear relationship between the ET_a (mm day^{-1}) by the standard METRIC approach and $ET_{a\text{-}EEFlux}$ during satellite images overpass dates over the (a) AID and (b) stressed area of the LSP

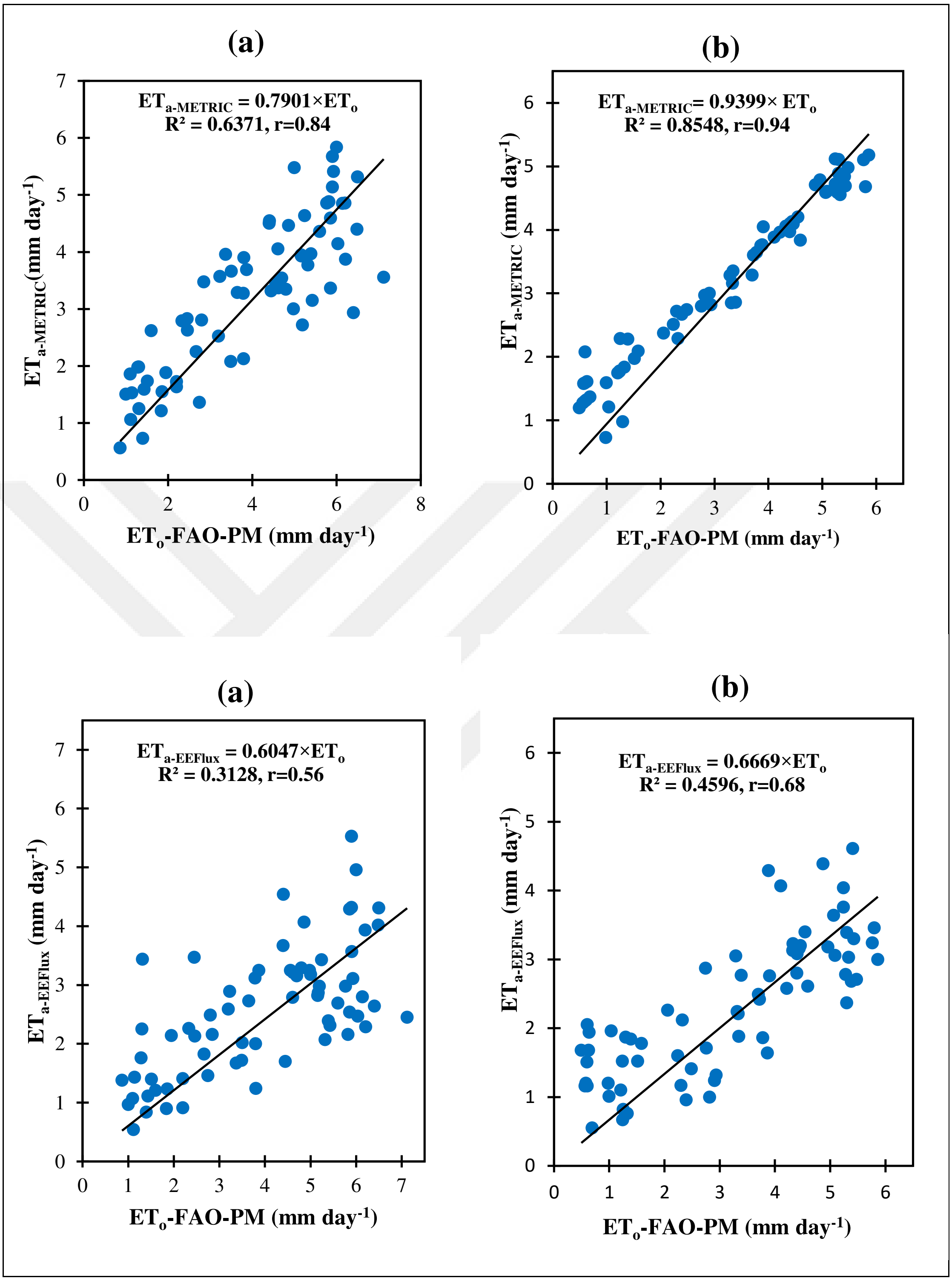

Figure 4.19. Linear relationship between ET_o (FAO-PM method) with ET_a derived from the METRIC model and $ET_{a\text{-EEFlux}}$ platform during satellite images overpass dates over the (a) AID area and (b) stressed area of the LSP

Table 4.6. Comparison of performance metrics of ET_a (mm day^{-1}) derived from the METRIC model, EEFlux, and ET_o (mm day^{-1}) by the FAO Penman-Monteith method across the AID

	Linear Model	$\mathbf{R^2}$	**RMSE (mm day^{-1})**	**MAE (mm day^{-1})**	**d**
ET_o-PM-FAO with $ET_{a\text{-METRIC}}$	$ET_{a\text{-METRIC}} = 0.7901 \times ET_o$	0.64	1.202	0.92	0.85
$ET_{a\text{-METRIC}}$ with $ET_{a\text{-EEFlux}}$	$ET_{a\text{-EEFlux}} = 0.6062 \times ET_{a\text{-METRIC}} + 0.5565$	0.62	1.197	0.897	0.78
ETo-FAO-PM with $ET_{a\text{-EEFlux}}$	$ET_{a\text{-EEFlux}} = 0.6047 \times ET_o$	0.46	1.941	1.576	0.58

Table 4.7. Comparison of performance metrics for ET_a (mm day^{-1}) from the METRIC model, EEFlux, and ET_o (mm day^{-1}) calculated using the FAO Penman-Monteith method in the stressed area of the LSP

	Linear Model	R^2	RMSE **(mm day^{-1})**	MAE **(mm day^{-1})**	d
ET_o-PM-FAO with $ET_{a\text{-METRIC}}$	$ET_{a\text{-METRIC}} = 0.9399 \times ET_o$	0.85	0.648	0.483	0.95
$ET_{a\text{-METRIC}}$ with $ET_{a\text{-EEFlux}}$	$ET_{a\text{-EEFlux}} = 0.5893 \times ET_{a\text{-METRIC}} + 0.4113$	0.61	1.232	1.033	0.73
ET_o-FAO-PM with $ET_{a\text{-EEFlux}}$	$ET_{a\text{-EEFlux}} = 0.6669 \times ET_o$	0.46	1.406	1.117	0.73

4.4. Estimation of ET_a by the standard SEBAL and GeeSEBAL and comparison with ET_o by the FAO- PM approach

In this study, $ET_{a\text{-SEBAL}}$ estimates were derived using the standard SEBAL methodology. Local climatic data from the L8 and Cotlu stations within the study area were utilized along with 70 Landsat satellite images spanning from 2020 to 2023, each with a spatial resolution of 30 m×30 m. However, the SEBAL model and the $K_{c\text{-NDVI}}$ method were not employed to estimate ET_a in the stressed area of the LSP. This decision was based on the similarity in results between the METRIC model and SEBAL, which yielded approximately 80-90% agreement with minor variations. Additionally, the standard crop coefficients (K_c) provided by TAGEM-DSI (2017) apply only to standard crop conditions, meaning full crop development stages without any stress from soil or water salinity issues in the Akarsu Irrigation District (AID). Moreover, NDVI in the stressed area lacks sufficient crop coverage percentage due to incomplete growth stage development compared to the non-stressed area (AID, i.e., NSA). Furthermore, various studies advocate using the METRIC model, a more complex approach than the more straightforward and faster $K_{c\text{-NDVI}}$ method, to estimate ET_a in the stressed area (Zamani and Rahimzadegan, 2018). This preference can be attributed to the METRIC model's dependence on factors such as LAI, albedo, R_n, G, H, and T_s. In contrast, the $K_{c\text{-NDVI}}$ method relies solely on NDVI and reference (standard) K_c under standard conditions. The climatic data was formatted according to the satellite overpass date in Universal Time Coordinated (UTC) to compute ET_a using the SEBAL model for the specified years. Similar to the procedure employed for estimating ET_a with the METRIC model, a preliminary analysis of the satellite images was conducted, followed by a more detailed examination using the SEBAL methodology to obtain ET_a values. Subsequently, daily areal ET_a values were computed for each date in Table 3.4.

Within this study's scope, the land SEB components were mapped for each dataset based on the specified dates detailed in Table 3.4, following the methodology employed. For instance, Figure 4.20 illustrates the distribution of latent heat flux (LE) and ET_a by the SEBAL model through the LandMOD ET mapping toolbox in MATLAB (Bhattarai et al., 2017) across the AID of the LSP, as captured in the satellite image dated July 31, 2023 (as indicated in Table 3.4). Notably, significant local variability exists in both LE and ET_a across the land surface within the AID. This variability primarily arises from the diverse land use types and varying characteristics of soil series present in the AID.

Between 2020 and 2023, 70 satellite images were utilized to estimate ET_a and generate the spatial distribution of ET_a using the SEBAL methodology over the AID. This distribution is illustrated for the designated area of interest (AoI) polygon, based on the satellite image dated, for instance, July 31, 2023 (DOY 212), shown in Figure 4.20. As previously stated, the Area of Interest (AoI) was a rectangular polygon covering approximately 840 km² (25.7 km by 32.7 km). This configuration was chosen to effectively capture the land surface energy balance, compute ET_a using the METRIC and SEBAL models, and assess crop coefficients (K_c) across a broad area. Subsequently, the final ET_a map was generated for each satellite image dataset, as outlined in Table 3.4, by cropping or clipping the AID of the LSP within the polygon. The outcomes of ET_a and K_c maps produced by the SEBAL model for the AID of the LSP on July 31, 2023 (DOY 212), are depicted in Figure 4.21, demonstrating the methodology applied.

Figure 4.21 indicates that ET_a varies within the range of 0.39 to 6.06 mm day^{-1}, while the K_c values range from 0.1 to 1.0 within the AID of the LSP as of July 31, 2023 (DOY 212). Considering the crop types present on this date, the citrus saplings exhibited the lowest ET_a and K_c values as estimated by the SEBAL model. These saplings typically have limited canopy coverage and substantial spaces between them filled with soil, leading to lower actual evapotranspiration and crop coefficient values. Within the AID, the predominant vegetation comprises citrus plants alongside summer crops such as corn, cotton, and soybean, among others. Notably, in areas designated for citrus cultivation, ET_a values range between 3.11 and 4.20 mm day^{-1} within the AID, while K_c values for citrus fall within the range of 0.51 to 0.69.

The first crop, corn (corn-I), exhibited the highest values of ET_a and K_c according to the SEBAL model in the Akarsu Irrigation District (AID) on July 31, 2023, with ET_a reaching 6.06 mm day^{-1} and K_c at 1.0. Additionally, for DOY, 212, i.e., 31.07.2023, the average $ET_{a\text{-}SEBAL}$ across the Akarsu Irrigation District (AID) was computed to be 4.04 mm day^{-1} with a standard deviation of 1.15 mm day^{-1}. The composite crop coefficient (K_c) on the same day was 0.67, with a standard deviation 0.19. Furthermore, the histograms of ET_a and K_c, as derived from the SEBAL model on DOY 212, exhibited identical shapes across the AID. This suggests that the distribution of

ET_a and the crop coefficient K_c followed comparable patterns within the region on that particular day. This indicates that the ET_a and K_c curves exhibit consistent behavior within the same pixel. However, the behavior of different pixels varies due to differences in plant type, soil characteristics, and water availability. As a result, both ET_a values and crop coefficients vary from one pixel to another. These findings confirm the strong relationship between ET_a and K_c. As a result, a spatial distribution K_c map was generated, enabling the identification of K_c for each crop pattern in this study using the SEBAL methodology.

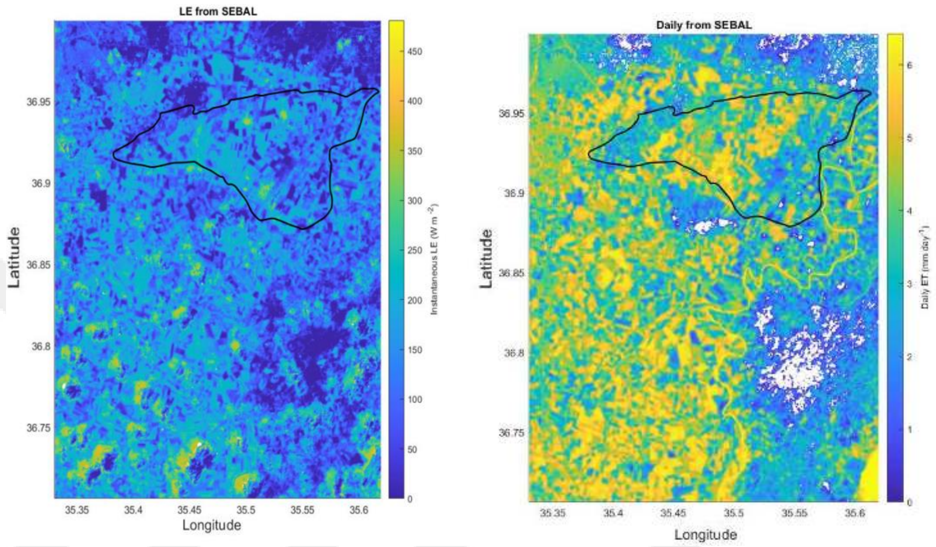

Figure 4.20. Spatial distribution of latent heat (LE-SEBAL, W m^{-2}) and actual evapotranspiration ($ET_{a\text{-}SEBAL}$, mm day^{-1}) using the SEBAL methodology from the satellite image captured on July 31, 2023 (DOY 212), is illustrated within the specified area of interest, covering the Akarsu Irrigation District (AID)

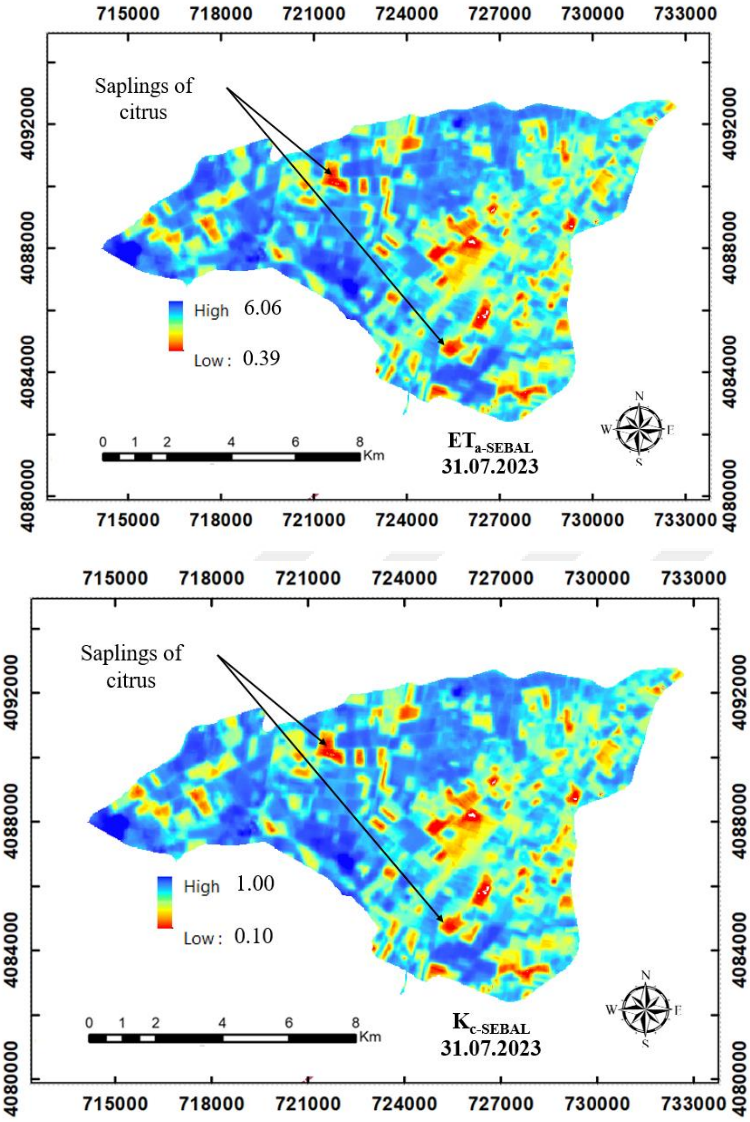

Figure 4.21. Spatial distribution of actual evapotranspiration ($ET_{a\text{-SEBAL}}$, mm day^{-1}) and crop coefficient (K_c) estimated using the SEBAL methodology from the satellite image of July 31, 2023 (DOY 212) in the Akarsu Irrigation District (AID)

Following the methodology outlined by Bastiaanssen et al. (1998a), ET_a using the SEBAL algorithm was computed for each satellite image date spanning from October 1, 2019, to September 30, 2023, as detailed in Table 3.4. Figure 4.22 illustrates the temporal variation of ET_a values estimated by SEBAL and ET_o by the FAO-PM approach on the satellite overpass dates within the Akarsu Irrigation District (AID). Additionally, fractions (EF) referred to as $K_{c\text{-SEBAL}}$ were determined. Figure 4.22 shows that ET_o values calculated using the FAO Penman-Monteith method were generally higher than the ET_a values estimated by the SEBAL model for the AID during the years 2020-2023, except certain summer days when the values were quite similar. This discrepancy can be attributed to rising temperatures and humidity levels in the AID during the same period, which, along with increased water consumption by crops, may have influenced the observed variations. To generate ET_a values as a time series, interpolations were performed using fractions (EF) between two consecutive satellite imagery dates, per Bastiaanssen et al. (1998a) described methodology. Consequently, intermediate ET_a values were estimated for the years 2020-2023. The resulting ET_a values obtained are presented as a time series in Figure 4.23. Based on computations of ET_a by the SEBAL model within the AID region, cumulative ET_a values were determined as 884.8 mm, 986.3 mm, 936.0 mm, and 934.0 mm for the years 2020, 2021, 2022, and 2023, respectively, as depicted in Figure 4.24. Consequently, the mean annual cumulative ET_a amounted to 928.3 mm from 2020 to 2023 within the AID of the LSP. Furthermore, the daily mean, lowest, and highest ET_a values by the SEBAL model were estimated as 2.56 mm day^{-1}, 0.20 mm day^{-1} on December 21, 2022 (during winter), and 7.28 mm day^{-1} on May 17, 2020 (during summer), respectively, throughout the years 2020-2023. The mean daily $ET_{a\text{-SEBAL}}$ values were determined to be 2.42 mm, 2.70 mm, 2.56 mm, and 2.56 mm for the years 2020, 2021, 2022, and 2023, respectively, as shown in Figure 4.25. Notably, the daily ET_a values in the 2020-2023 water years exhibit significant seasonal variability. This variability is primarily influenced by differences in crop growth stages, planting densities, and irrigation practices. Additionally, spatial variability in soil properties, interannual climatic fluctuations, and water availability play a significant role. These factors, combined with farmers' decisions regarding crop selection and market-driven adjustments, contribute to the observed patterns in ET_a and K_c values. In other words, the observed differences in the mean ET_a values estimated by the SEBAL model from 2020 to 2023 can be attributed to shifts in vegetation patterns, variations in meteorological parameters, and other factors such as micro-relief, etc (Alsenjar et al., 2023b; Cetin et al., 2023b; Karahan et al., 2024). The peak monthly ET_a value of 146.8 mm was observed in August 2023, likely due to high temperatures, increased solar radiation, and the active growth stages of most crops during the summer. These factors contribute to higher water demands and evapotranspiration rates. Conversely, the lowest ET_a value of 21.8 mm, observed in December 2022, can be attributed to cooler temperatures, reduced solar radiation, and the slower physiological activity of crops, as many are dormant or in less water-intensive growth stages during the winter. The results in Figure 4.25 indicate that July and August exhibited the highest evapotranspiration values by the SEBAL model throughout the study period. Elevated areal mean ET_a levels were observed during the mid-season, particularly in July, aligning with the peak of the irrigation season. This is consistent with the higher water demands of crops at their most active growth stages. In contrast, lower areal mean ET_a rates were recorded during the early and late stages of the growing season when crop growth was less intensive and water requirements were reduced. These variations highlight the strong relationship between crop growth stages, irrigation practices, and evapotranspiration dynamics, providing valuable insights for efficient water management throughout the growing season.

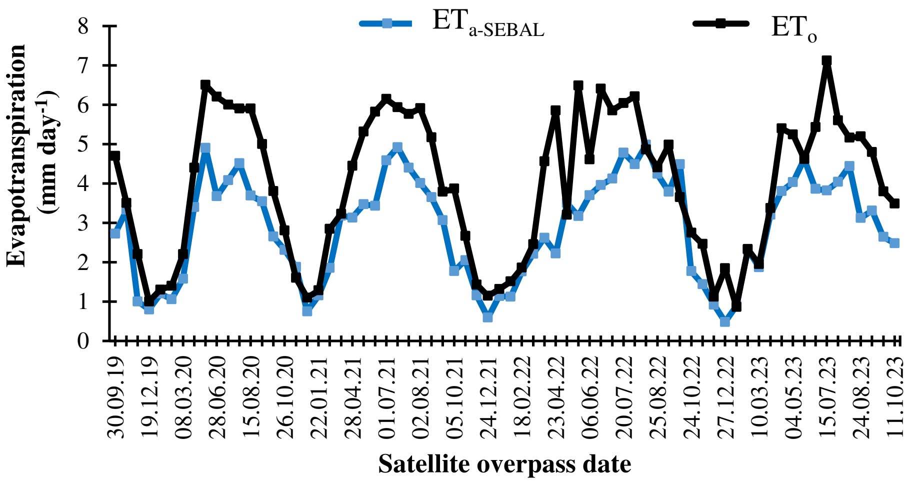

Figure 4.22. Temporal variations in mean daily actual evapotranspiration ($ET_{a\text{-SEBAL}}$, mm day^{-1}) using the SEBAL model and ET_o by the FAO-PM method within the Akarsu Irrigation District (AID) during satellite overpasses

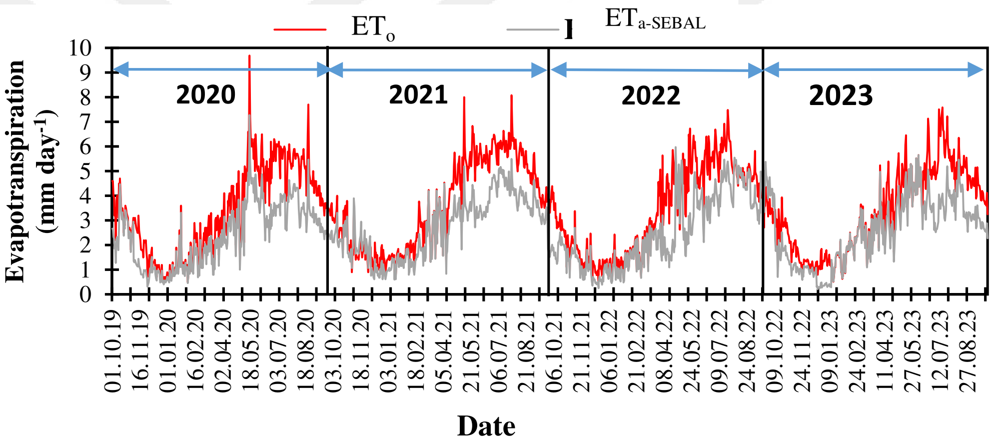

Figure 4.23. Temporal changes in the daily average weighted actual evapotranspiration ($ET_{a\text{-SEBAL}}$, mm day^{-1}) values, using the SEBAL methodology and ET_o by the FAO-PM approach, across the Akarsu Irrigation District (AID) from September 30, 2019, to September 30, 2023

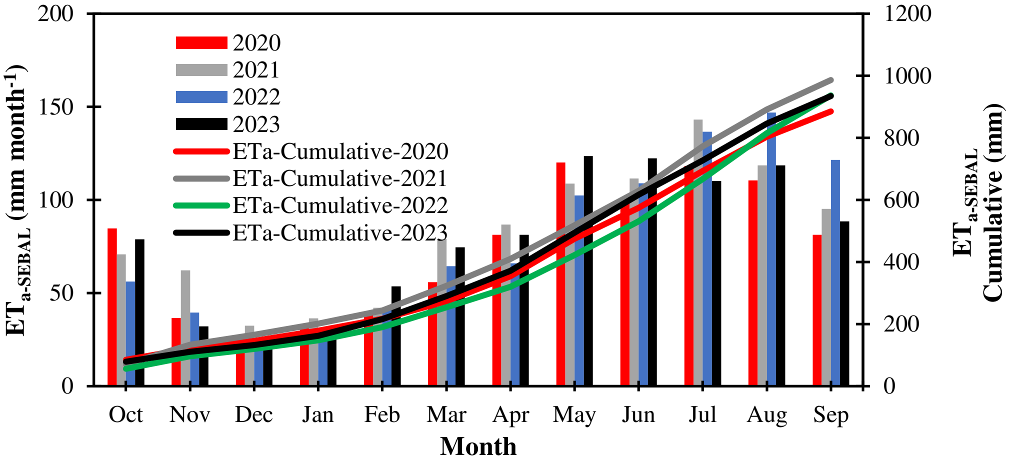

Figure 4.24. Variations in actual evapotranspiration ($ET_{a\text{-SEBAL}}$, mm month^{-1}) values on a monthly basis across the water years of 2020, 2021, 2022, and 2023 within the Akarsu Irrigation District (AID)

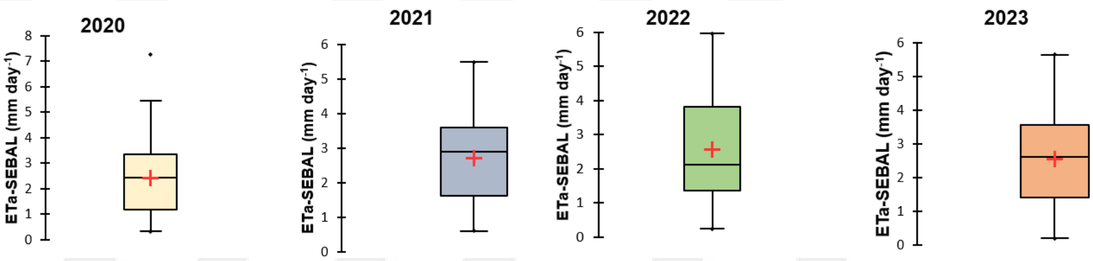

Figure 4.25. Actual evapotranspiration ($ET_{a\text{-SEBAL}}$, mm day^{-1}) values by the SEBAL model over the Akarsu Irrigation District (AID) from 2020 to 2023 hydrological year. Horizontal lines indicate the median, as well as the 25th and 75th percentiles. Dots on the plot signify outliers (Tukey, 1977; Iglewicz and Hoaglin, 1993), which are data points that lie beyond 1.5 times the interquartile range (IQR) from the first and third quartiles, respectively. The whiskers extending from the plot represent the minimum and maximum values

In this work, linear regression analysis was employed to examine and quantify the linear relationship between ET_a estimated using the SEBAL method and ET_o calculated via the FAO-PM algorithm across Akarsu Irrigation District (AID, i.e., NSA) throughout the period from 2020 to 2023, as illustrated in Figure 4.26. Figure 4.27 demonstrates a robust correlation, with r values reaching 0.87, between the ET_a values obtained from the standard SEBAL method and those derived from the FAO Penman-Monteith method within the AID of the LSP during satellite image overpass dates. Additionally, the RMSE and MAE values in AID between $ET_{a\text{-METRIC}}$ and ET_o were determined as 1.403 mm day^{-1} and 1.101 mm day^{-1}, respectively.

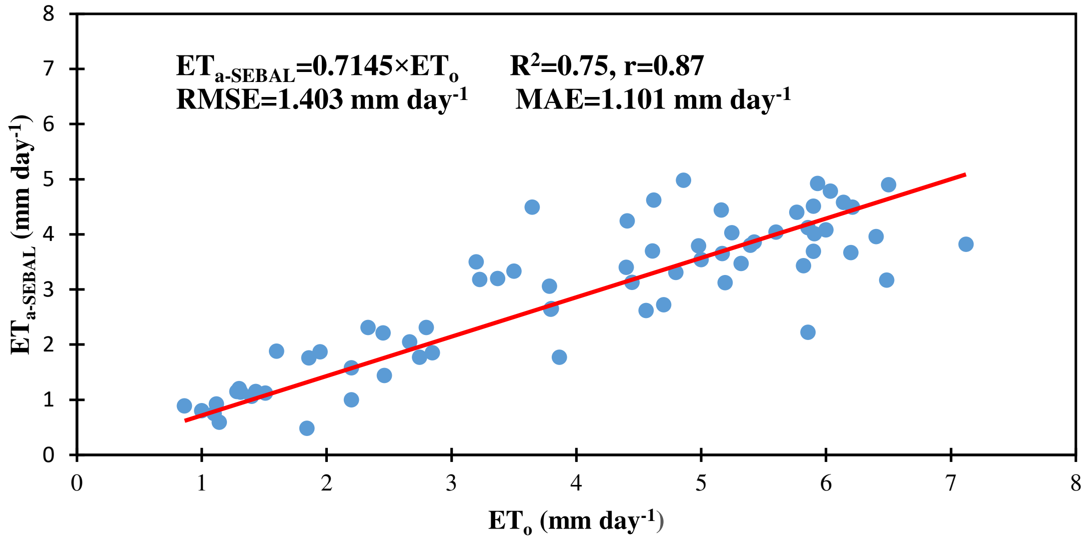

Figure 4.26. Linear relationship between ET_o by the FAO Penman-Monteith method and actual evapotranspiration ($ET_{a\text{-}SEBAL}$, mm day^{-1}) from the SEBAL model during satellite images overpass dates in the Akarsu Irrigation District (AID) for the years 2020-2023

The GeeSEBAL platform produced spatiotemporal ET_a on satellite image dates during the 2020 and 2021 water years, utilizing ERA5 land data combined with 31 Landsat satellite images across the study region. The estimation of ET_a by GeeSEBAL was restricted to two water years (for the years 2020-2021) because the GeeSEBAL platform only generates data until December 31, 2021. Additionally, the GeeSEBAL platform may require further updates to integrate Landsat data with ERA5 beyond this date to estimate ET_a during satellite overpasses of the region of interest. Another limitation could be funding constraints compared to the EEFlux platform, which is directly linked to NASA and supported by a consortium comprising the University of Nebraska-Lincoln, Desert Research Institute, and the University of Idaho, with funding provided by Google. The Akarsu Irrigation District (AID, also called NSA) was selected to compare GeeSEBAL and ET_o due to its normal conditions, characterized by non-saline soils and groundwater levels that are maintained within acceptable limits, with the water table remaining stable throughout the area. In contrast, the GeeSEBAL platform could not estimate ET_a for the stressed areas within the study region during the studied period due to a lack of sufficient ERA5 Land data available through the platform. The ERA5 Land dataset, essential for precise ET_a estimation, was incomplete for the specific conditions of the stressed areas. This limitation hindered the platform's ability to capture the variations in water stress across these regions accurately. As a result, this thesis did not focus on its application in the stressed areas of LSP. Figure 4.27 shows the spatial distribution of ET_a estimated by the GeeSEBAL model for Day of Year (DOY) 228, corresponding to August 15, 2020. On this date, the mean ET_a was 5.32 mm day^{-1}, with values ranging from 2.57 mm day^{-1} to 6.52 mm day^{-1}. Figure 4.28 shows the temporal variation of ET_a by the SEBAL, GeeSEBAL, and ET_o at the time of satellite overpass across the AID for the years 2020-2021. This Figure shows that ET_a values estimated by the GeeSEBAL platform are closer to ET_o and generally higher than those estimated by SEBAL. This discrepancy can be attributed to several factors. First, the GeeSEBAL platform uses ERA5 reanalysis data for ET_a calculations, which typically results in higher values than local climatic data across the AID. Additionally, unlike the SEBAL model, the GeeSEBAL platform did not correct for scan line errors in Landsat 7 imagery. In contrast, these scan lines were removed using QGIS3.24.3 software prior to ET_a calculation in the SEBAL model, mainly when Landsat 7 data was used. These factors could contribute to the GeeSEBAL platform's overestimation of ET_a, bringing its values closer to ET_o than the ET_a estimated by the SEBAL model.

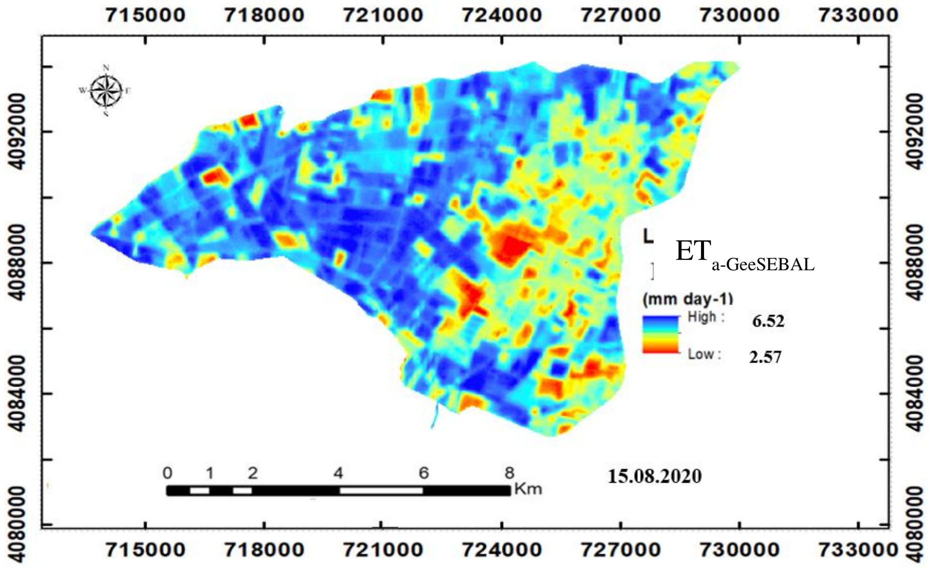

Figure 4.27. Spatial distribution of actual evapotranspiration ($ET_{a\text{-GeeSEBAL}}$, mm day^{-1}) across the Akarsu Irrigation District (AID) on (DOY 228), equivalent to August 15, 2020, as generated by the GeeSEBAL model

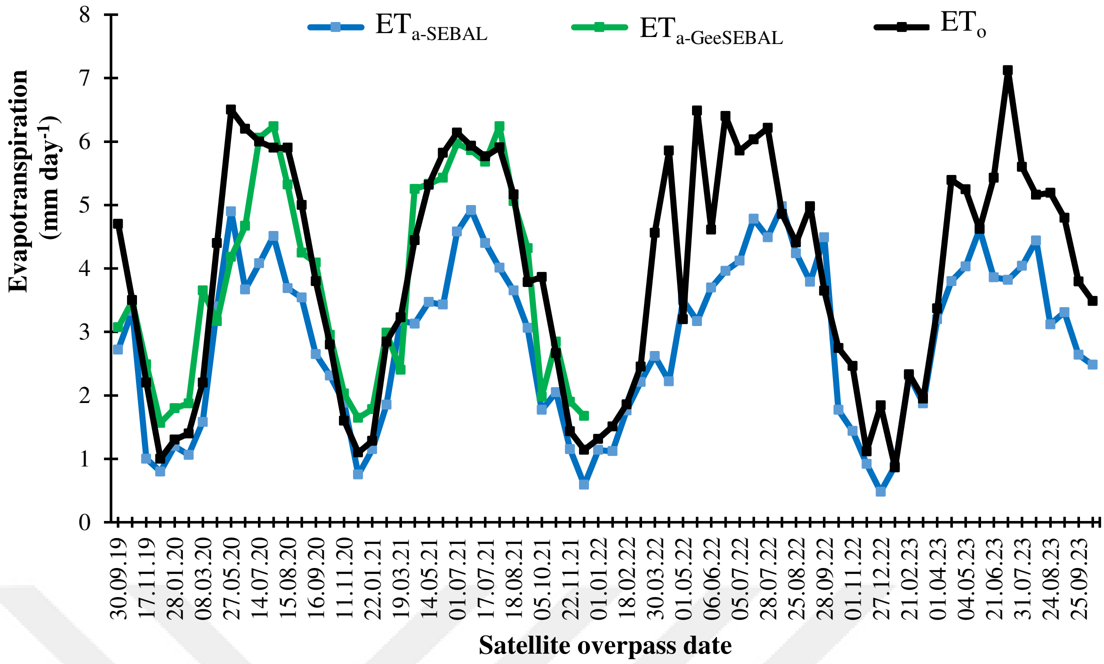

Figure 4.28. Temporal variations in mean daily actual evapotranspiration (ET_a, mm day^{-1}) in the Akarsu Irrigation District (AID), using the SEBAL method, the GeeSEBAL platform, and reference evapotranspiration (ET_o) from the FAO-PM method, during satellite overpasses

In estimating ET_a using SEBAL and GeeSEBAL algorithms within the AID of the LSP for 2020-2023, it is crucial to represent the computed ETa variations across the AID visually. This requires illustrating the variations in ET_a calculated by various models—including SEB, METRIC, EEFlux, SEBAL, and GeeSEBAL—on a unified time scale corresponding to satellite overpass dates. This graphical representation, shown in Figure 4.29, is used to identify and analyze the fluctuations in ET_a across the Akarsu Irrigation District (AID, i.e., NSA). The figure reveals that the ET_a values estimated by the METRIC model are consistently higher than those from other SEB models, including SEBAL, EEFlux, and GeeSEBAL. Additionally, the ET_o values are consistently higher than the ET_a values obtained from the SEB model, which is anticipated. This difference arises because ET_o represents the theoretical potential evapotranspiration under ideal conditions. At the same time, ET_a measures actual evapotranspiration, which can be lower due to crop variety, water availability, and environmental conditions. Notably, during certain days in the winter seasons of 2020 and 2021, the ET_a values estimated by the METRIC model surpassed the reference ET_o values. This suggests that the ET_rF_i values, which correspond to the mean composite crop coefficient (K_c) values, were more than 1.0. During winter, crops such as wheat, citrus, potatoes, onions, and saplings exhibited K_c values exceeding 1.0 on specific dates, including 11.11.2020, 29.12.2020, 23.02.2023, and 01.11.2023, with peak values reaching 1.56 for wheat, 1.72 for citrus, 1.57 for potatoes, and 1.51 for onions and saplings. Similarly, in summer, on 15.08.2020 and 31.08.2020, first and second crops such as cotton, corn, peanuts, and soybeans, as well as citrus, showed elevated K_c values, averaging

1.18, with corn-II recording the highest value of 1.34 on 15.08.2020. Moreover, these values are slightly higher than the reference K_c values for the same crops corresponding to the same day and growth stage, as mentioned by TAGEM-DSI (2017), as illustrated earlier in Table 3.5. These heightened K_c values can be explained by factors like active growth stages, increased transpiration due to environmental conditions, and the physiological water demands during critical growth phases, especially under high temperatures and prolonged daylight during summer. These findings emphasize the significant role of crop physiology and environmental factors in influencing water use efficiency, as reflected by the variations in crop coefficient. The observation suggests that the fraction represented by ET_rF_i (K_c) indicates that the METRIC-derived ET_a collectively accounts for the influence of all climatic variables, soil conditions, and plant types in comparison to the reference K_c values (TAGEM-DSI, 2017) during satellite overpasses.

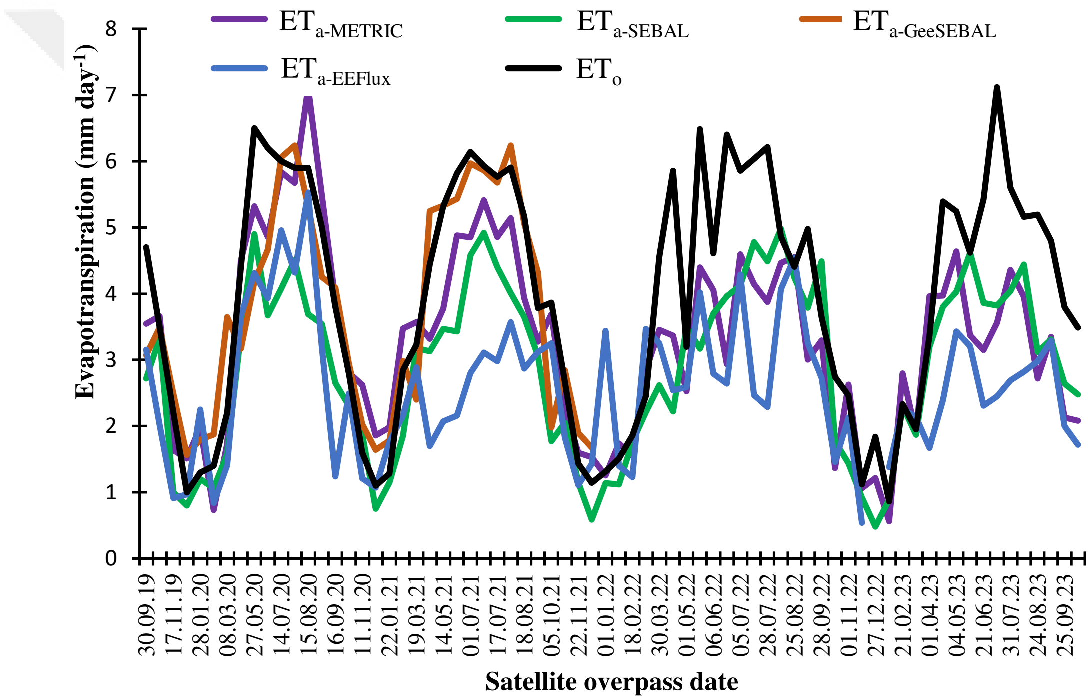

Figure 4.29. Temporal variation of actual evapotranspiration (ET_a, mm day^{-1}) by the SEBAL, METRIC, EEFlux, GeeSEBAL models, and the ET_o by the FAO-PM-56 method over Akarsu Irrigation District (AID) during satellite images overpass dates

4.5. Comparison of ET_a by the SEB models with the ET_c method

4.5.1. Comparison of ET_a by the SEB models with ET_c method over the AID for monthly and yearly time scales

Comparing the monthly and yearly ET_a estimates obtained from the METRIC and SEBAL models with the reference evapotranspiration (ET_o) from the FAO-PM algorithm and crop evapotranspiration (ET_c) derived from the "two-step" procedure (Steduto, 2000; Cetin 2020; Cetin et al., 2023b) across the AID of the LSP for the years 2020-2023 is essential for several reasons. Firstly, this comparison validates the accuracy of the remote sensing models, ensuring they provide reliable estimates of actual water consumption. This is particularly important for assessing their suitability in real applications, such as irrigation management and water resource planning. Secondly, comparing these models allows for a better understanding of the temporal and spatial variations in evapotranspiration, revealing how well the satellite-based models can reflect variations in crop types, vegetation growth, and water availability, often not captured by traditional methods. Furthermore, this comparison helps to identify areas where crops may experience water stress, as remote sensing models can detect deviations caused by environmental factors, such as insufficient rainfall or salinity, that impact crop growth. By comparing ET_a with ET_c, insights can be gained into the severity of stress and potential water shortages, guiding more efficient water use. Additionally, the comparison enables the evaluation of each model's suitability for different crop types and conditions, particularly in diverse agricultural settings where traditional methods may fall short. This information is invaluable for refining irrigation strategies, optimizing water use, and preventing over- or under-irrigation. Regular comparison also supports the calibration and improvement of the models, ensuring they remain accurate and adapted to local environmental conditions. Finally, comparing the remote sensing models with established methods like ET_o and ET_c contributes to long-term water resource management by generating reliable datasets for hydrological modeling and future water use projections, ultimately supporting more sustainable agricultural practices.

The ET_c method calculations are based on crops' spatial distribution to determine each crop type's coverage percentage over the four water years. The corresponding K_c values for each crop type are then applied, as provided in Table 3.5. These K_c values are multiplied by the standard ET_o values derived from the TAGEM-DSI (2017) dataset, following the approach outlined by Allen et al. (1998). The monthly and yearly evapotranspiration for all crops within the AID are then summed for each water year. Figure 4.30 illustrates the monthly temporal variations of ET_a estimated by the METRIC and SEBAL models, alongside ET_o calculated using the FAO-PM-56 method and ET_c for the years 2020 to 2023 across the AID. As shown in Figure 4.30, the monthly ET_o values were higher than those values by the METRIC and SEBAL models during the studied periods except for some months in 2020 and 2021, during which the monthly $ET_{a\text{-METRIC}}$ was higher than ET_o because the METIC model takes into account all factors, including soil, climate, and plant condition (Alsenjar et al.,2023b; Cetin et al., 2023b). The annual ET_o was at 1,136 mm, 1,309 mm, 1,238 mm, and 1,223 mm for the years 2020, 2021, 2022, and 2023, respectively. These values surpassed the annual ET_a estimates obtained from the METRIC model, which were 1,191 mm, 1,255 mm, 1,003 mm, and 914 mm for the corresponding years. ET_a values are anticipated to be lower than ET_o due to various factors, including crop type, growth stage, and actual water availability. Additionally, the FAO-PM model's ET_o calculations rely primarily on climatic data and do not account for soil conditions and crop requirements. In contrast, the METRIC model captures the actual water needs of crops during satellite overpasses in the AID, providing a more accurate assessment of ET_a. Similarly, the annual

ET_a values derived from the SEBAL model were lower, measuring 885 mm, 986 mm, 936 mm, and 934 mm for the years 2020, 2021, 2022, and 2023, respectively. The yearly ET_c values were also calculated as 823 mm, 890 mm, 852 mm, and 829 mm for the same years. The overall annual ET_c value across the study area is lower than the ET_a estimates derived from the METRIC and SEBAL models. This indicates that the reference K_c values used in the ET_c method for different crop growth stages are generally lower than the ET_rF_i fraction in ET_a estimation within the METRIC model and the EF fraction in the SEBAL algorithm. Conversely, the ET_a values obtained from the SEBAL model exhibited closer proximity to the ET_c values than those obtained from the METRIC model. The discrepancy observed can be attributed to the SEBAL model's assumption that the fraction of energy available for evapotranspiration (the EF fraction) remains constant throughout the day. Essentially, SEBAL assumes that the proportion of net radiation used for actual evapotranspiration, as opposed to other processes like sensible heat flux, does not vary during the daily calculation of ET_a. While this assumption simplifies the computation, it may not fully account for the variability in actual field conditions, as noted in previous studies conducted by Bastiaanssen et al. (1998a), Bastiaanssen (2000), Bastiaanssen et al. (2005), Bhattarai et al. (2017), Laipelt et al. (2021), among others. In contrast, the METRIC model accounts for variations in the reference ET fraction (ET_rF_i) or K_c based on daily climatic data obtained during satellite image acquisition. This feature of the METRIC model provides an advantage by enabling the observation of changes in soil, climate, and vegetation instantaneously during satellite overpass, considering alterations in climatic variables. Moreover, Cetin et al. (2023b) affirmed that employing ET_a estimates from the METRIC model alongside in-situ water balance measurements, including basic water balance components of irrigation, drainage, and precipitation during the 2021 water year within the study area (AID), resulted in a change in catchment storage of +67.08 mm, accompanied by a water balance closure error of 3.34%. In simpler terms, utilizing ET_a values from the METRIC model significantly reduced the water budget closure errors compared to ET_c values.

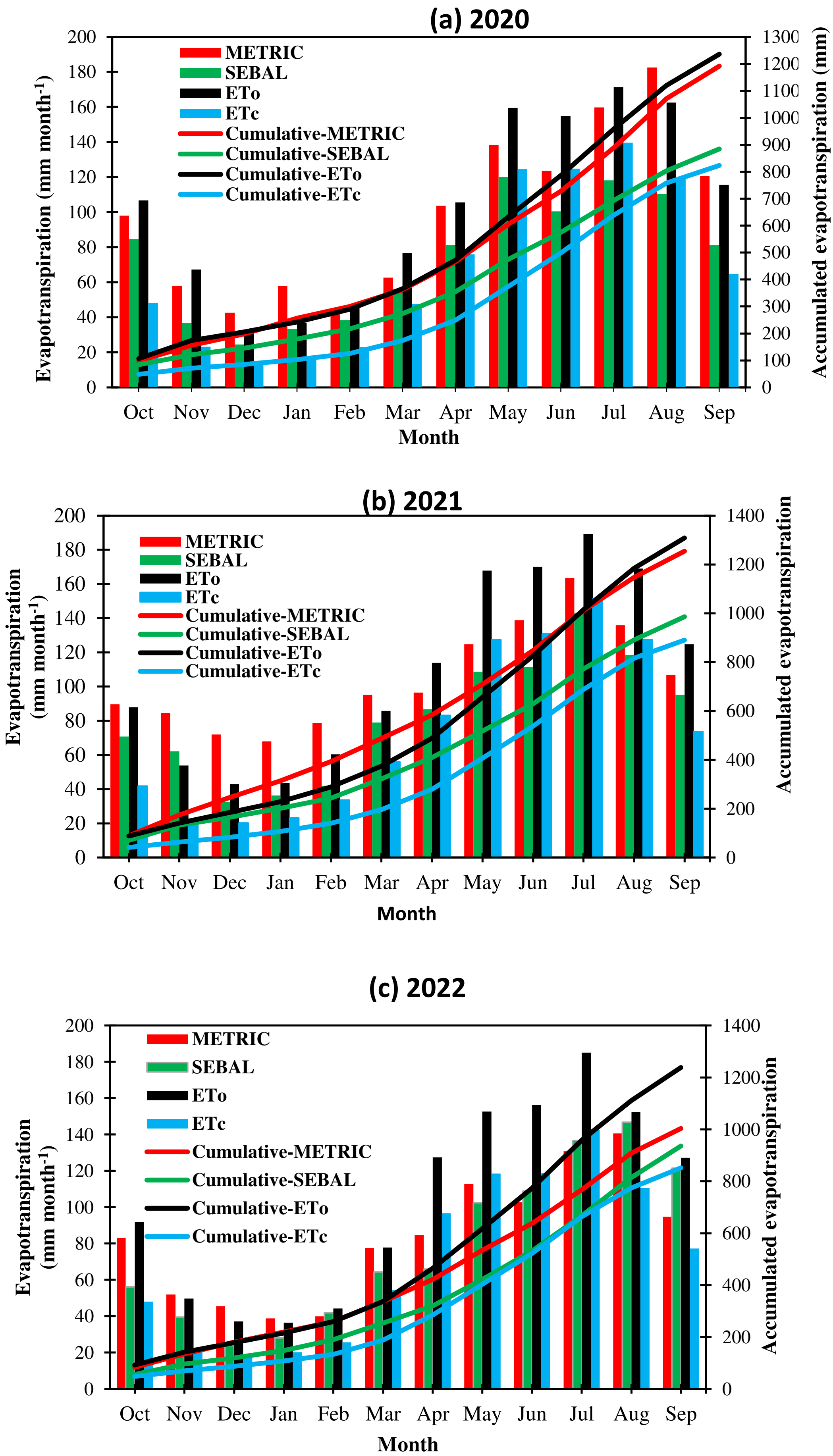
(a) 2020
(b) 2021
(c) 2022
METRIC
SEBAL
ETo
ETc
Cumulative-METRIC
Cumulative-SEBAL
Cumulative-ETo
Cumulative-ETc
Evapotranspiration (mm month-1)
Accumulated evapotranspiration (mm)
Accumulated evapotranspiration
Oct
Nov
Dec
Jan
Feb
Mar
Apr
May
Jun
Jul
Aug
Sep
Month

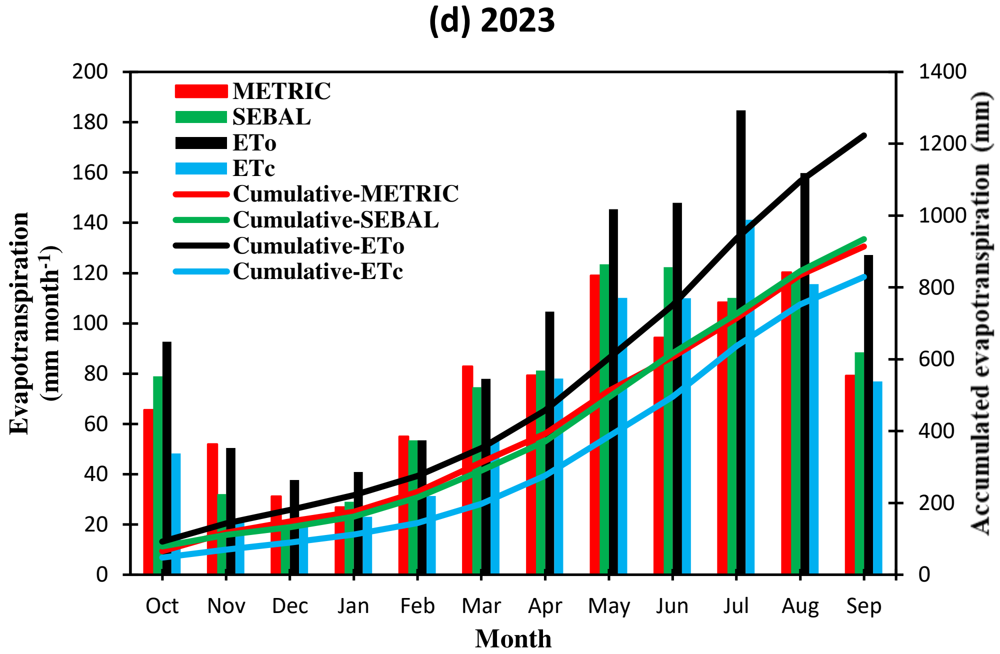

Figure 4.30. Monthly variations in actual evapotranspiration (ET_a, mm month^{-1}) values for 2020–2023 hydrological year as follows as (a) 2020, (b) 2021, (c) 2022 and (d) 2023 in the Akarsu Irrigation District (AID) using the METRIC model, SEBAL algorithm, ET_o by the FAO-PM method, and ET_c method

4.5.2. Comparison of ET_a by the METRIC and SEBAL models with ET_c method for some crops at satellite image acquisition dates

After estimating ET_a using the METRIC model for the entire study area under both standard (AID) and non-standard, stressed conditions (SA) in the LSP, it is crucial to evaluate the ET_a for crops on the specific satellite overpass date and validate the model's accuracy. This is necessary to ensure that the METRIC model accurately represents evapotranspiration across different crop types and environmental conditions. Validation helps to confirm the model's effectiveness in capturing spatial and temporal variations in water use. By comparing the model's outputs with ground-truth data or other established methods, it can assess its precision and reliability, making it a more dependable tool for irrigation management and crop water use assessments. This validation process is essential for improving the model's performance and applicability in real-world agricultural and water resource management contexts. Several comparisons are presented to elucidate the differences between ET_a by the METRIC model and ET_o by the FAO-PM model and the ET_c method, among others. Since citrus crops constitute approximately 50% of the AID for 2020-2023, comparisons were initially focused on evapotranspiration rates by citrus. The ET_a estimation by the METRIC model for the citrus orchard (spanning 15.8 hectares) in the Cotlu village within the AID is significant, as illustrated in Figure 4.31. Under normal conditions, without any stress in citrus in the AID, this value can be extrapolated to estimate ET_a for the entire citrus area without applying the METRIC model to all crops individually. The temporal variation of ET_a for citrus in the Cotlu field and across the entire distributed citrus area on satellite overpass dates, along with ET_o by the FAO-PM model, is illustrated in Figure 4.32. As indicated in Figure 4.32, the ET_a values of citrus in the Cotlu field estimated by the METRIC model closely aligned with the mean ET_a values for all citrus in the AID, exhibiting an R^2 of 0.86, r=0.93, RMSE=0.541 mm day^{-1} and equation ($ET_{a\text{-Citrus-AID}}$= 0.8615×$ET_{a\text{-Citrus-Cotlu}}$ + 0.2662). In this context, the average ET_a estimated by the METRIC model specifically for citrus in the Cotlu field was represented as an independent variable, while the average ET_a for citrus using the METRIC model across the entire study area was represented as a dependent variable during the satellite image acquisition dates from 2020 to 2023. Furthermore, there is a strong correlation between ET_o estimated using the FAO-PM and the METRIC model for citrus in the Cotlu field and across the entire area. The correlation (r) is 0.83 for the Cotlu field and 0.79 for the whole area, with corresponding RMSE values of 1.128 mm day^{-1} and 1.338 mm day^{-1}, respectively.

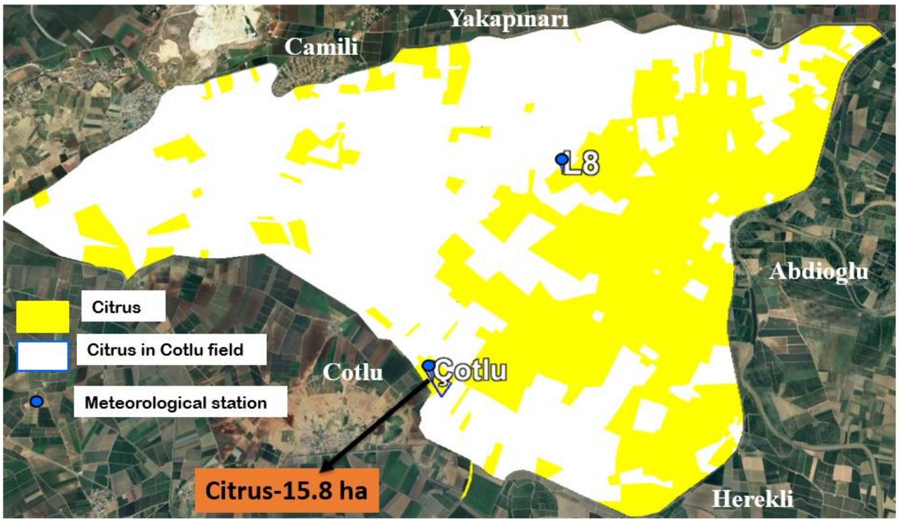

Figure 4.31. The Location of the citrus plantation adjacent to the Cotlu meteorological station and the distribution of citrus fields across the Akarsu Irrigation District (AID) for 2020-2023

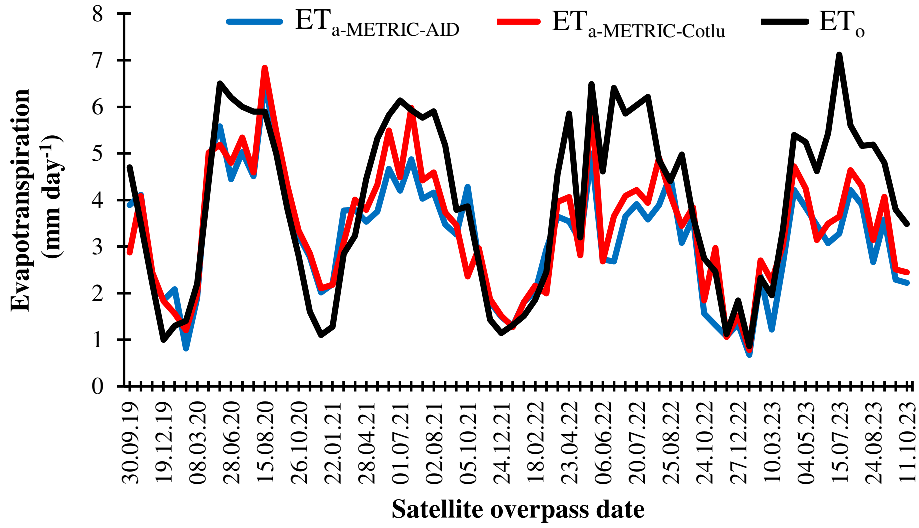

Figure 4.32. Temporal variations of average daily actual evapotranspiration ($ET_{a\text{-METRIC}}$, mm day^{-1}) estimated by the METRIC model for the citrus field near the Cotlu meteorological station and overall ET_a of citrus across the Akarsu Irrigation District (AID), compared with ET_o calculated using the FAO-PM method during satellite overpass dates

Another instance involves estimating ET_a using the METRIC model for mixed crops like watermelon with saplings during the summer of 2022 in the AID. Figure 4.33 illustrates the spatial distribution of watermelons with saplings during the summer of 2022. Figure 4.34 also shows the temporal variation in ET_a values for intercropping saplings with watermelon, as estimated by the METRIC model, alongside the ET_o values calculated using the FAO-PM method over the same period. Notably, ET_a values obtained from the METRIC model were lower than those derived from the FAO-PM approach. Additionally, the K_c values derived from the METRIC model were computed to demonstrate the temporal variations corresponding to the different growth stages of this novel crop type. This uniquely contributes to the study and provides valuable insights for researchers, scientists, and relevant authorities involved in defining K_c for intercropping watermelon with saplings.

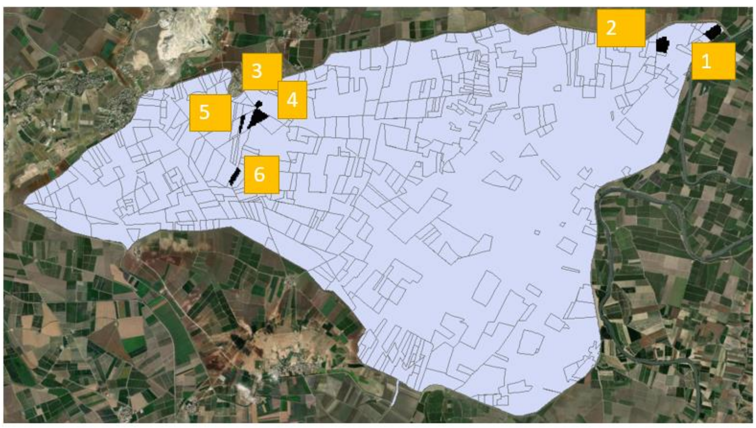

Figure 4.33. Spatial distribution of saplings with watermelon across the Akarsu Irrigation District (AID) during the summer season of 2022

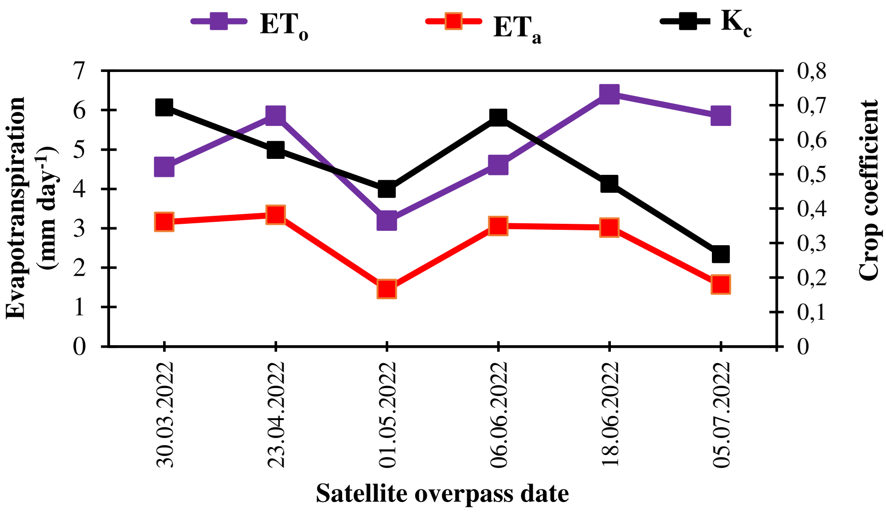

Figure 4.34. Temporal fluctuations of average daily actual evapotranspiration ($ET_{a\text{-}METRIC}$, mm day^{-1}) values for sapling with watermelon obtained through the METRIC model across the entire study area, ET_o by the FAO-PM and $K_{c\text{-}METRIC}$ during satellite overpass dates

A similar comparison was made to evaluate ET_a values estimated by the METRIC model for intercropping watermelon with saplings versus saplings alone during the summer of 2022. Figure 4.35 illustrates the spatial distribution of a) intercropping watermelon with saplings and b) saplings alone. The satellite image dates used to estimate ET_a for intercropping watermelon with saplings were selected based on the growth stages of the watermelon crop (initial, mid, and harvest stages) during the summer of 2022 and the availability of Landsat images. Therefore, the comparison of ET_a was based on four satellite images, as indicated in Figure 4.36. As shown in Figure 4.36, the ET_a and K_c values for intercropping watermelon with saplings were consistently higher than those for saplings alone on the satellite acquisition dates. This difference can be attributed to the watermelon crop occupying the space between the saplings in the intercropping scenario, whereas in the saplings-only scenario, the space between saplings was either bare soil or fallow, leading to lower water consumption. The higher ET_a and K_c values in the intercropped areas can be explained by the watermelon plants covering the bare soil, compared to the bare soil being exposed between saplings in non-intercropped areas. This result underscores that intercropping increases actual evapotranspiration (ET_a) compared to saplings' combined ET_a and bare soil evaporation. This finding highlights the effectiveness of remote sensing (RS)--based ET_a models in accurately estimating evapotranspiration in intercropping or mixed cropping. Such insights are precious for researchers and stakeholders, especially in regions where water is a critical resource and sustainable agricultural water management is essential.

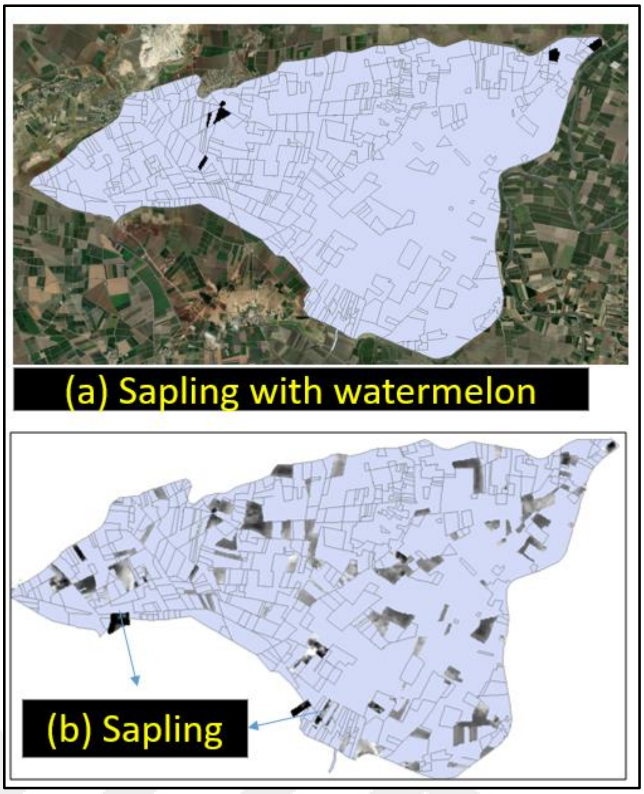

Figure 4.35. Spatial distribution of (a) sapling with watermelon and (b) sapling across the AID in the summer season of 2022

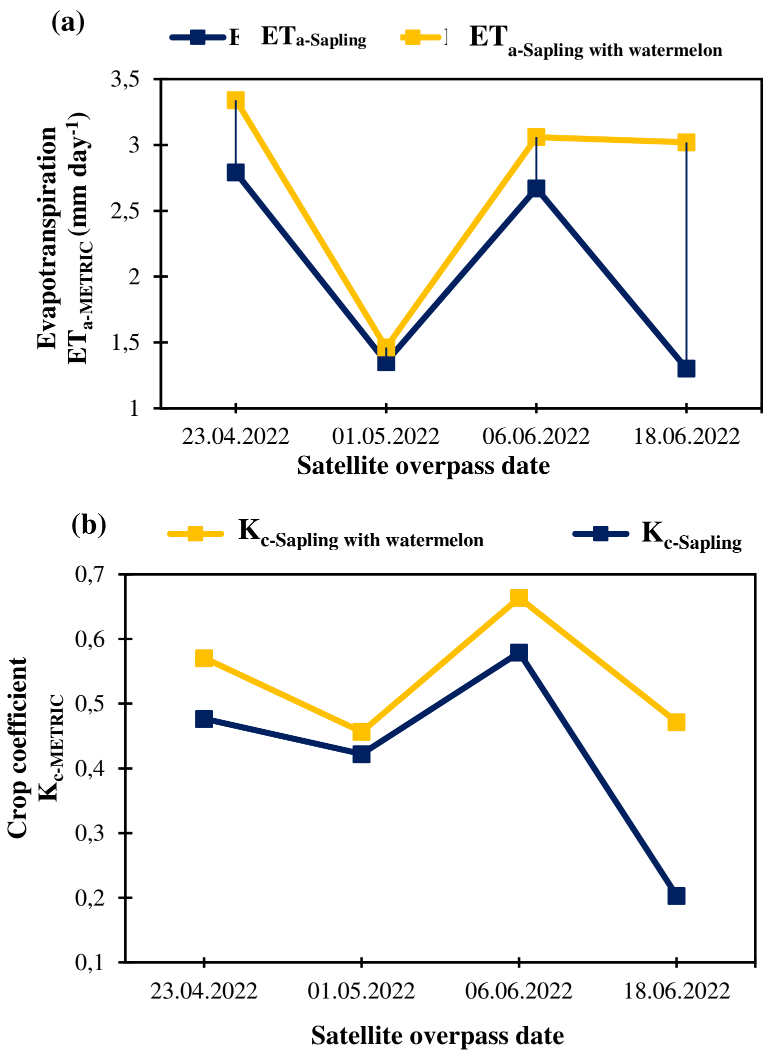

Figure 4.36. Temporal fluctuations of (a) average daily actual evapotranspiration ($ET_{a\text{-}METRIC}$, mm day^{-1}) and (b) K_c values for sapling with watermelon and only sapling, obtained through the METRIC model across the entire AID during satellite overpass dates

In another instance of mixed cropping, saplings were grown alongside a cabbage field spanning 7.71 hectares, and the METRIC model was utilized to estimate ET_a during the winter season of 2023 within the AID. The positioning of the saplings and cabbage field within the AID is illustrated in Figure 4.37. Notably, the ET_o values computed by the FAO-PM method were consistently higher than the ET_a values derived from the METRIC model for the saplings adjacent to the cabbage field, except on DOY 052 (February 21, 2023, as shown in Figure 4.38). This deviation may be attributed to irrigation practices implemented on DOY 052, resulting in higher ET_a values calculated by the METRIC model compared to the ET_o values from the FAO-PM method. It is important to emphasize that the cabbage crop completely covered the interspaces between the saplings, as Figure 4.37 depicts. These results also underscore the importance of ground truth data collected during field visits to identify cropping practices as well as the crop types cultivated across the correct interpreting process, which is crucial for correctly interpreting outcomes derived from remote sensing-based ET_a models like the METRIC model. Furthermore, incorporating in-situ photos during ground truth data collection added significant value to the study by facilitating a more accurate interpretation of the results.

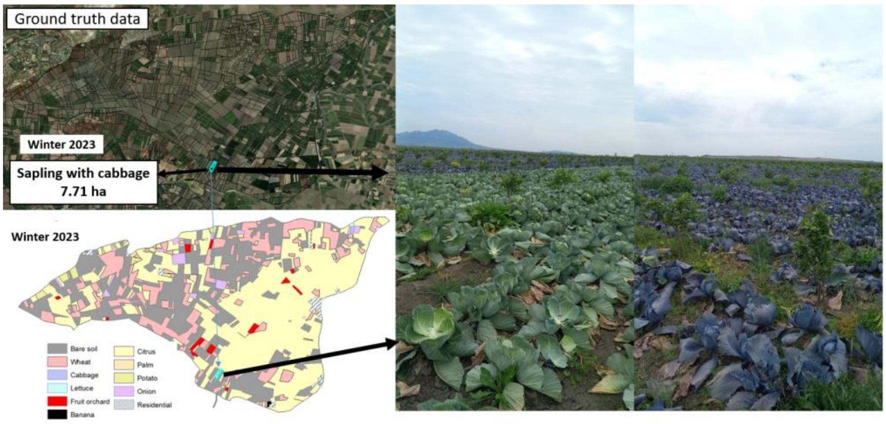

Figure 4.37. Spatial distribution of saplings with cabbage across the AID in the winter season of 2023

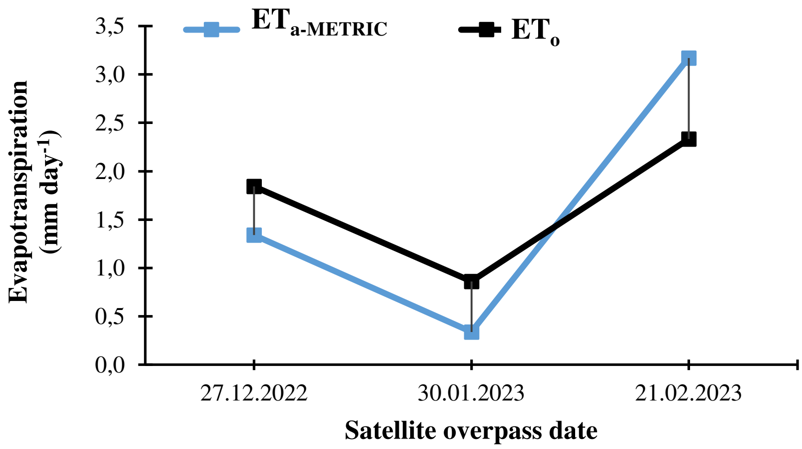

Figure 4.38. Temporal fluctuations of average daily actual evapotranspiration ($ET_{a\text{-METRIC}}$, mm day^{1}) values for sapling with cabbage, obtained through the METRIC model across the entire AID during satellite overpass dates

Numerous studies have employed simple linear regression analyses, demonstrating a relationship between ET_a computed via the METRIC model and various direct measurement methods such as lysimeter (Allen et al., 2007a), eddy covariance method (Liebert et al., 2016), and Bowen energy ratio (Carrasco-Benavides et al., 2014), among others. Allen et al. (2007b) synthesized findings from 19 studies, including validation of METRIC and/or SEBAL results, revealing an average discrepancy of only 4.5%. Additionally, several studies have employed direct methods to calculate ET_a in the Cukurova region where the LSP is located. One such study applied lysimeter measurements to estimate ET_a for soybean-II and compared it with PySEBAL. The R^2 was found to be 0.73, with lysimeter-derived ET_a recorded as 4.4 mm day^{-1} on September 28, 2009 (Sawadogo et al., 2020). Conversely, METRIC-derived ET_a was 4.73 mm day^{-1} in 2021. Furthermore, $ET_{a\text{-METRIC}}$ was estimated for soybean-II within the pixel, as depicted in Figure 4.39, and compared with lysimeter and PySEBAL data on July 16 and August 1, 2009. The black pixel in Figure 4.39 represents the lysimeter field located at the centre of the 0.12-hectare field at the Research Fields of the Agricultural Structures and Irrigation Department, Faculty of Agriculture, University of Cukurova (37°1′N, 35°21′E; 20 m above sea level), Adana, Türkiye. Based on these results, the $ET_{a\text{-METRIC}}$ values were 2.53 mm day^{-1} on DOY 197 (July 16, 2009) and 2.81 mm day^{-1} on DOY 213 (August 1, 2009), whereas lysimeter-derived ET_a was 2.9 and 2.5 mm day^{-1} for the exact dates, respectively. Similarly, Sawadogo et al. (2020) found that the ET_a values calculated by PySEBAL for the same pixel were 2.3 and 3.1 mm day^{-1} for DOY 197 and DOY 213, respectively. The ET_a values obtained from the METRIC model closely matched lysimeter measurements compared to those from PySEBAL for soybean-II in 2009. The SEBAL model assumes that the energy fraction available for evapotranspiration (EF fraction) remains constant throughout the day. While this simplifies the calculations, it may not fully reflect the variability of actual field conditions, as noted in previous studies (Bastiaanssen et al., 1998a; Bastiaanssen, 2000; Bastiaanssen et al., 2005; Bhattarai et al., 2017; Laipelt et al., 2021). In contrast, the METRIC model accounts for variations in the reference ET fraction (ET_rF_i) or K_c by integrating daily climatic data during satellite image acquisition. This capability gives the METRIC model an advantage, enabling it to capture real-time changes in soil, climate, and vegetation during satellite overpass, considering fluctuations in climatic variables.

Based on these results, the METRIC model was closer to the ET_a values measured by the lysimeter than the SEBAL model. Despite their differences in assumptions, both the METRIC and SEBAL models can be applied to estimate ET_a for different crops on a large scale. Researchers and stakeholders can utilize these models in the study area and beyond by following the methodology outlined in this thesis.

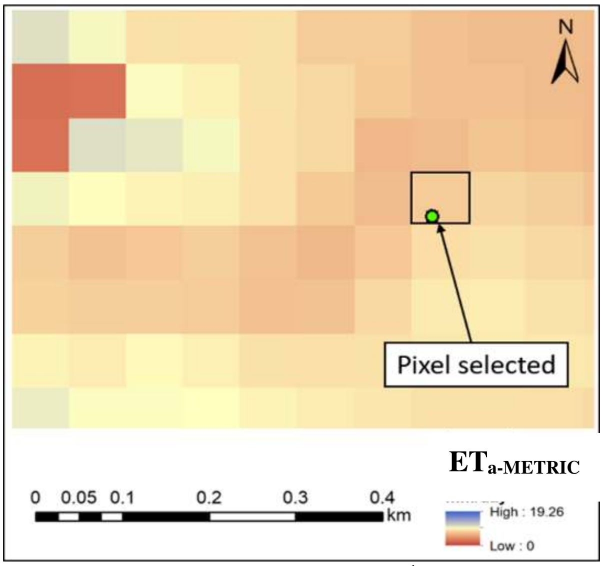

Figure 4.39. Actual evapotranspiration ($ET_{a\text{-}METRIC}$, mm day^{-1}) map by the METRIC model for soybean-II on DOY 197 (16 July 2009) (Alsenjar et al., 2023b; Cetin et al., 2023b)

Some of the thesis results related to estimating ET_a for different crops using the METRIC model for the 2020 and 2021 water years were previously published by Alsenjar et al. (2023b) and Cetin et al. (2023b). Their findings demonstrated a strong alignment between ET_a values derived from the METRIC model and those obtained using the ET_c method and ET_o-FAO-PM for crops such as wheat, lettuce, potato, citrus orchards, and the first and second crops of cotton, peanut, soybean, and corn across the AID region of the LSP during the 2020 and 2021 water years. The research revealed a slight discrepancy in seasonal ET_a obtained from METRIC compared to the ET_c method, which could be attributed to factors such as the utilization of K_c values corresponding to growth stages, variations in growth durations and periods, and inconsistencies in planting/sowing dates of field crops (Alsenjar et al., 2023b; Cetin et al., 2023b). Additionally, one of the key findings highlighted by Cetin et al. (2023b) is that upon overall assessment, particularly of water balance closure errors, the METRIC model was deemed superior to the ET_c approach and yielded more dependable results at the catchment scale. Moreover, the results of this thesis are consistent with previous studies conducted by researchers in the Agricultural Structures and Irrigation Department at Cukurova University, such as Unlu et al. (2010), Unlu et al. (2011), Unlu (2014), and Koc and Kanber (2020). These studies involved calculating ET_c using direct methods, including Bowen ratio, water balance, and lysimeter measurements for crops like citrus, wheat, and soybean-II under irrigated conditions in the Cukurova region during various years (2004, 2005, 2006, 2007, 2008, 2009, 2011, and 2012). The results showed consistency when comparing these direct ET_c measurements with ET_a estimated by the METRIC model and “two-step” procedure (ET_c) for citrus, wheat, and soybean-II, as also confirmed by the findings of Alsenjar et al. (2023a), Alsenjar et al. (2023b) and Cetin et al. (2023b).

Another instance of estimating ET_a using the SEBAL model is outlined by Atasever and Ozkan (2018) in the AID of the LSP, utilizing Landsat 8 images on January 22, 2015; April 28, 2015; and July 01, 2015. The findings demonstrated a strong agreement between $ET_{a\text{-}SEBAL}$ values and ET_o-FAO-PM calculations across the AID on these three days in 2015. In the study by Atasever and Ozkan (2018), statistical analyses, including the t-test and the nonparametric Wilcoxon signed-rank test, were conducted to compare ET_a estimates from the SEBAL model with ET_o values derived using the FAO-PM approach. Their results indicated no significant differences between the ET_a values obtained from the SEBAL approach and those from the FAO-PM model for selected pixels across the AID. However, certain limitations were noted in their study, including the absence of information regarding crop types and the distribution percentages of crop types across the AID. The study by Atasever and Ozkan (2018) did not report mean ET_a values for the AID on the specified dates. These limitations should be considered when comparing the $ET_{a\text{-}SEBAL}$ method with other direct and indirect methods. Conversely, crop type classification and spatial distribution of crops were considered when applying the SEBAL algorithm to the study area, potentially improving the accuracy of SEBAL ET_a estimates and enhancing the value of this research. Shamloo et al. (2021) employed the SEBAL algorithm to compute ET_a for corn crops across the 125,000-hectare Yuregir Plain, as illustrated in Figure 2.4, covering the period from March to September 2018. The estimated ET_a values demonstrated a strong correlation (r=0.95) and low RMSE=1.14 mm day^{-1} compared with the FAO Penman-Monteith method. However, this study has several limitations. Firstly, it focused exclusively on estimating ETa for corn using SEBAL, ignoring other crop types such as cotton, soybean, peanut, and citrus within the Yuregir Plain, including those in the AID. Additionally, the average ET_a calculated by SEBAL pertains only to corn, not the entire area, and the study did not classify the various crop types present within the study area. In other words, the estimation of ET_a by the SEBAL for just one crop did not allow comparing which crop consumes water when compared to others. For this reason, crop type classification could be significant to this study, which was considered in this thesis to add value to this type of research. Also, this study did not provide the meteorological data used, such as the names and locations of the meteorological stations. ET_a was not estimated for the most stressed regions of the Yuregir Plain. In contrast, this thesis addresses all the limitations identified in the study by Shamloo et al. (2021). It makes a significant contribution by focusing on various crop types, especially those located in the stressed areas of the study region in Türkiye.

As previously discussed in this study, the METRIC algorithm was employed to determine ET_a for many crops widely cultivated in the study area. Consequently, it is crucial to analyze the temporal variations of $ET_{a\text{-}METRIC}$ values for specific crops between the AID and the stressed areas of the LSP during satellite overpass dates. To illustrate this comparison, citrus and sapling crops were used as examples to demonstrate the ET_a variations determined by the METRIC model within the study area, as shown in Figure 4.40. Figure 4.40 indicates that the $ET_{a\text{-}METRIC}$ values in the AID were higher than those in the stressed areas of the LSP. Similarly, Figure 4.41 displays the temporal variations of ET_a determined by the METRIC model for wheat, cotton-I, cotton-II, corn-I, soybean-I, and peanut-II, respectively. As shown in Figure 4.41, the $ET_{a\text{-METRIC}}$ values in the AID area are generally higher than those in the stressed area for all crops. The difference in $ET_{a\text{-METRIC}}$ values between the AID and stressed areas can be attributed to the salinity, alkalinity, and poor quality of existing shallow groundwater in the stressed area under non-normal conditions. Additionally, crops in the stressed area do not reach the full growth stage of development compared to the same crops in the AID of the LSP. Several factors, including soil salinity, water availability, and the proximity to saline water bodies, influence the physical conditions near the lagoons, which have brackish water in the LSP. These conditions lead to higher soil salinity levels due to saline water infiltration, negatively affecting salt-sensitive crops and resulting in reduced yields and limited growth potential. Additionally, the salinity of nearby water sources can exacerbate salt stress in crops, making the availability of fresh, high-quality irrigation water crucial for maintaining healthy crop conditions. Lagoons can impact the local climate by increasing humidity, which may alter ET_a rates, heighten crop water stress, and affect the microclimate surrounding the crops. However, near harvest time, the ET_a values in the AID become surprisingly similar to those in the stressed areas for some crops such as cotton-II and corn-I. This convergence occurs because several parcels in the AID were either harvested simultaneously or very close to the harvest time of the crops in the stressed areas. The difference in daily $ET_{a\text{-METRIC}}$ values for soybean-I across the four seasons of the 2020-2023 water years was more pronounced than for other crops in the study area. In the stressed area, the average daily $ET_{a\text{-METRIC}}$ values for soybean-I were 5.32, 4.71, 3.74, and 3.13 mm day^{-1} for 2020, 2021, 2022, and 2023, respectively, approximately 20% lower than those in the AID area (average of 4.23 mm day^{-1}). This difference is directly related to the resulting stress from either soil salinity and/or alkalinity or high groundwater conditions, as well as the higher sensitivity of soybeans to salinity compared to wheat, cotton, and corn. Consequently, the ET_a values for wheat, cotton, and corn in the stressed areas are not significantly higher than those in the AID. These crops are more able to tolerate and absorb salt, and their growth stages appear relatively normal compared to soybeans in the stressed areas.

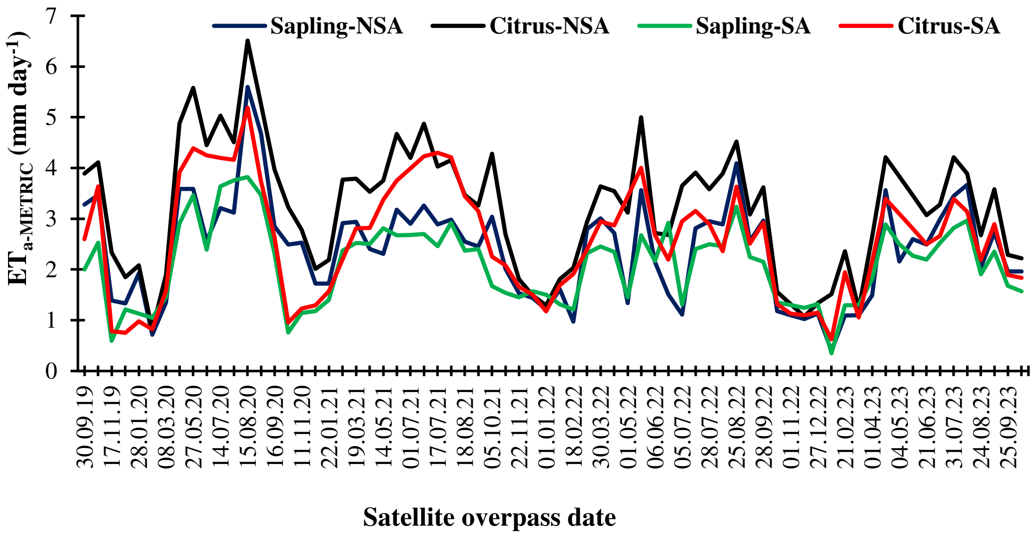

Figure 4.40. Temporal variations in average daily actual evapotranspiration ($ET_{a\text{-METRIC}}$, mm day^{-1}) values for citrus and sapling determined using the METRIC model across satellite overpass dates within the AID and the stressed area of the LSP

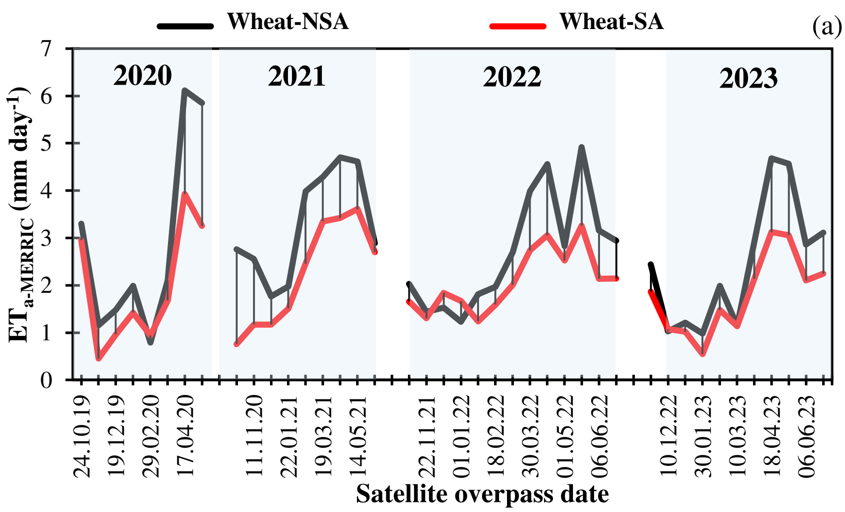

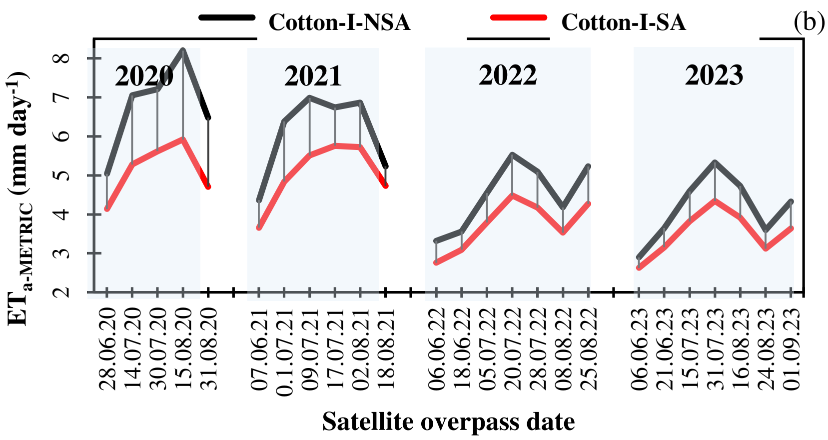

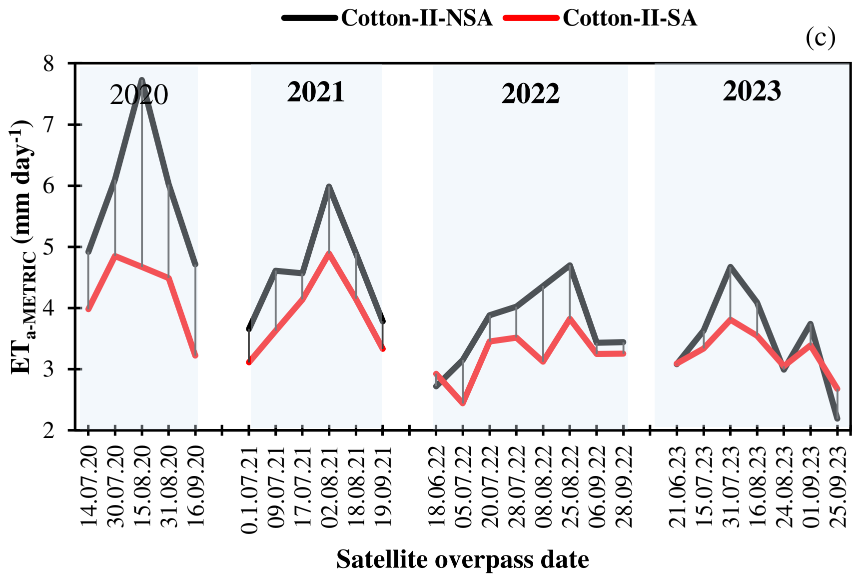
Cotton-II-NSA
Cotton-II-SA
(c)
2020
2021
2022
2023
ETa-METRIC (mm day-1)
8
7
6
5
4
3
2
14.07.20
30.07.20
15.08.20
31.08.20
16.09.20
0.1.07.21
09.07.21
17.07.21
02.08.21
18.08.21
19.09.21
18.06.22
05.07.22
20.07.22
28.07.22
08.08.22
25.08.22
06.09.22
28.09.22
21.06.23
15.07.23
31.07.23
16.08.23
24.08.23
01.09.23
25.09.23
Satellite overpass date

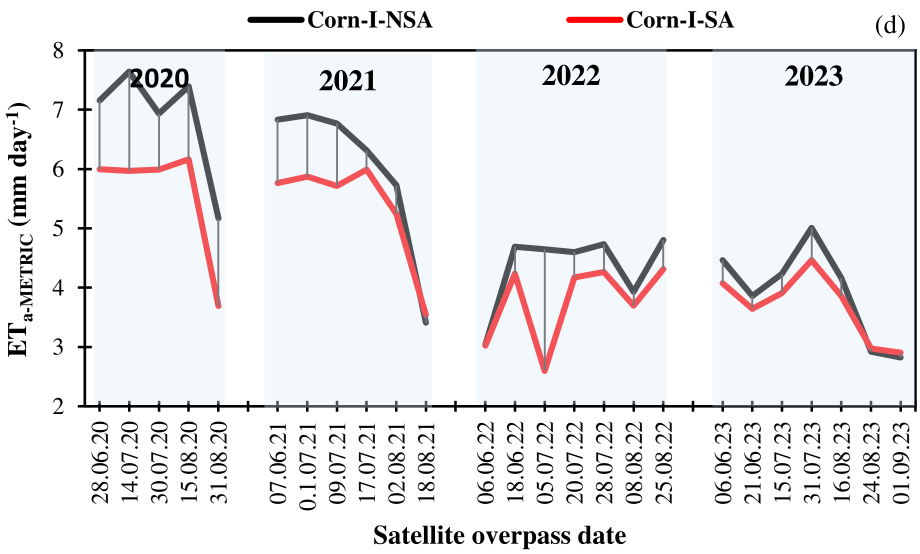
Corn-I-NSA
Corn-I-SA
(d)
2020
2021
2022
2023
ETa-METRIC (mm day-1)
8
7
6
5
4
3
2
28.06.20
14.07.20
30.07.20
15.08.20
31.08.20
07.06.21
0.1.07.21
09.07.21
17.07.21
02.08.21
18.08.21
06.06.22
18.06.22
05.07.22
20.07.22
28.07.22
08.08.22
25.08.22
06.06.23
21.06.23
15.07.23
31.07.23
16.08.23
24.08.23
01.09.23
Satellite overpass date

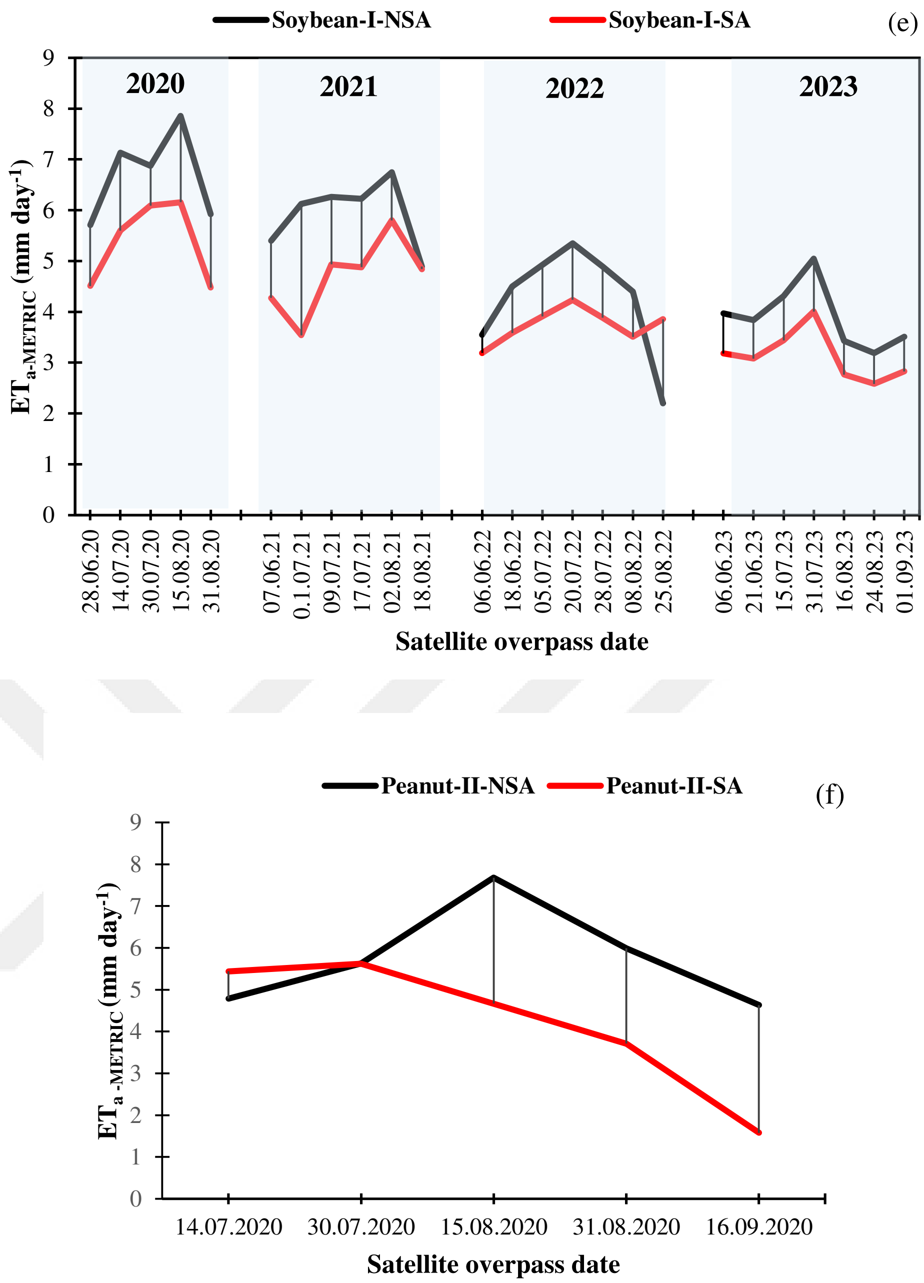

Figure 4.41. Temporal variations in average daily actual evapotranspiration ($ET_{a\text{-METRIC}}$, mm day^{-1}) values for crops: (a) Wheat, (b) Cotton-I, (c) Cotton-II, (d) Corn-I, (e) Soybean-I, and (f) Peanut-II, as estimated using the METRIC model during satellite overpass dates within the AID and the stressed regions of the LSP

One notable advantage of the METRIC model is its ability to compute ET_a with a 30-meter spatial resolution for various crop types as well as pasturelands located near stressed areas in the LSP region of Türkiye at the time of satellite overpass. ET_a estimates for pasturelands add significant value to this study, marking the first attempt to highlight the temporal variations in ET_a values for these areas, as illustrated in Figure 4.42. This analysis is based on the METRIC algorithm, which integrates ground truth data with RS data in the stressed regions of the study area. Pasturelands in these stressed regions are unsuitable for agriculture due to high groundwater levels, i.e., shallow-water-table development and the lack of a drainage system to lower the shallow water table to permissible levels, as depicted in Figure 3.9.

As observed in Figure 4.42, the ET_o values calculated using the FAO-PM method were generally higher than the $ET_{a\text{-}METRIC}$ values for pasturelands, except for specific dates such as October 5, 2021, October 21, 2021, November 22, 2021, and December 24, 2021, etc. This discrepancy could be attributed to precipitation events in the stressed area on those dates, as depicted in Figure 4.42, along with the influence of high groundwater levels. The difference between ET_o values calculated using the FAO-PM method and those obtained from the METRIC model ranged from 3% to 54%. In the same context, the most significant differences were observed from the end of February to the end of September for 2020-2023, with values ranging from 0.06 mm day^{-1} on February 23, 2021, to 2.69 mm day^{-1} on June 18, 2022. Moreover, the pattern of the differences closely resembled a Gaussian distribution, particularly during the summer seasons of 2020 and 2021. In the stressed grassland pasture areas near Tuzla and Akyatan lagoons in the Lower Seyhan Plain, Türkiye, ET_a values derived from the METRIC model were not significantly higher than the ET_o values estimated using the FAO-PM method. This is probably due to soil alkalinity and salinity, which are known to reduce both soil evaporation and grassland evapotranspiration due to excessive stress. These stressors affect plant uptake and the physiological functioning of vegetation, resulting in lower ET_a compared to optimal conditions. Previous studies, including those by Ozcan and Cetin (1996) and Akça et al. (2020), among others, have documented high soil salinity and alkalinity levels in the region. Ozcan and Cetin (1996) identified maximum soil salinity and alkalinity in wetlands from 1956 to 1979, while Akça et al. (2020) analyzed salinity distribution in recently irrigated areas around Akyatan Lagoon. Both studies indicate that salinity impacts water availability and vegetation, affecting evapotranspiration rates in the Seyhan Basin, located in Adana, in the eastern Mediterranean region of Türkiye. Regular monitoring of soil salinity and alkalinity in and around Tuzla and Akyatan lagoons is essential to understanding their long-term effects on evaporation as well as actual evapotranspiration. The current observation that ET_a values are not significantly higher than ET_o values, combined with known soil salinity and alkalinity issues, underscores the need for ongoing assessment. Monitoring will help practitioners elucidate how these stress factors affect water availability and the health of vegetation over time.

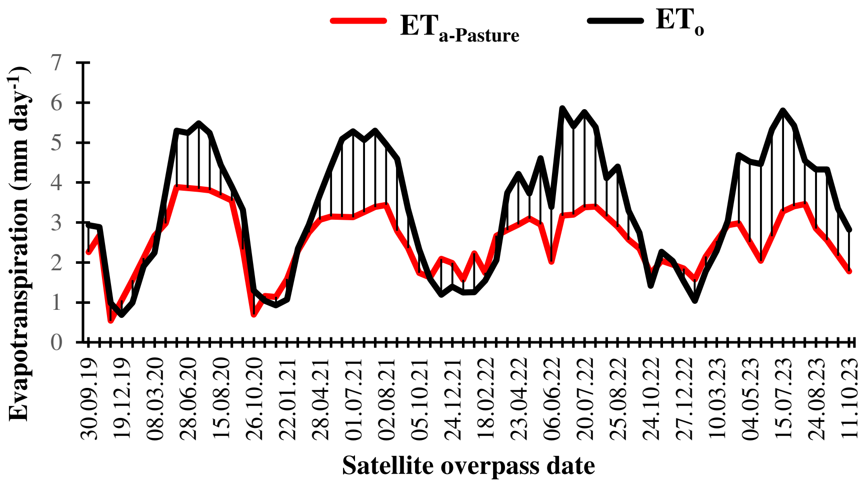

Figure 4.42. Temporal variations in average daily actual evapotranspiration ($ET_{a\text{-METRIC}}$, mm day^{-1}) values for pasture in the stressed region of the LSP, estimated using the METRIC model

4.6. ET_a estimation by the $K_{c\text{-NDVI}}$ model for some crops

The $K_{c\text{-NDVI}}$ method offers an alternative approach to estimating ET_a by leveraging remote sensing data with minimal input requirements. This method establishes a relationship between standard/reference K_c values outlined by TAGEM-DSI (2017) and NDVI values for each specific crop type in the AID, thereby generating new K_c, referred to as $K_{c\text{-NDVI}}$. This approach differs from using standardized K_c values from reference sources alone. The newly generated K_c values are then used with ET_o values, calculated using the FAO-PM method, to derive ET_a. Table 4.8 presents the K_c values derived from the established relationship between K_c values from existing literature TAGEM-DSI (2017) and NDVI values for some crop types. Furthermore, the accuracy of the $K_{c\text{-NDVI}}$ method was validated by comparing these new K_c values with standard K_c values from TAGEM-DSI (2017), as shown in Table 4.9.

To illustrate the methodology, Figure 4.43 presents the temporal fluctuations of reference K_c and NDVI for corn-I during the 2022 water year within the AID, serving as an illustrative example. Additionally, Figure 4.44 demonstrates the relationship between standard K_c values and the newly derived K_c values obtained through the $K_{c\text{-NDVI}}$ method for corn-I within the AID. Subsequently, ET_a estimation using the $K_{c\text{-NDVI}}$ method was conducted for various crops within the AID. Figure 4.45 depicts the variation in ET_a estimates between the $K_{c\text{-NDVI}}$ and ET_c methods, using corn-I as a representative example of this method. The ET_a values closely align with those derived from the ET_c method. This alignment can be attributed to the fact that the adjusted K_c values obtained through the $K_{c\text{-NDVI}}$ method closely resemble the standard values derived from existing literature (TAGEM-DSI, 2017).

Table 4.8. Generated K_c equation between K_c and NDVI (Landsat) for some crops

No.	Crop	$K_{c\text{-NDVI}}$-equation	R^2	r	RMSE	MAE	d
1	**Wheat**	$K_{c\text{-NDV}}$=1.1218 ×NDVI+ 0.3173	0.78	0.88	0.39	0.38	0.48
2	**Cotton-I**	$K_{c\text{-NDVI}}$= 1.6336×NDVI - 0.0348	0.96	0.98	0.33	0.29	0.73
3	**Corn-I**	$K_{c\text{-NDVI}}$= 1.6843×NDVI - 0.1564	0.87	0.93	0.31	0.28	0.67
4	**Soybean-I**	$K_{c\text{-NDVI}}$= 1.2987×NDVI - 0.0164	0.60	0.77	0.24	0.19	0.77
5	**Cotton-II**	$K_{c\text{-NDVI}}$=1.5622×NDVI - 0.0906	0.98	0.99	0.28	0.26	0.68
6	**Corn-II**	$K_{c\text{-NDVI}}$=1.9172×NDVI-0.2922	0.68	0.82	0.29	0.22	0.65
7	**Peanut-II**	$K_{c\text{-NDVI}}$= 1.8894×NDVI - 0.2785	0.89	0.94	0.31	0.26	0.67
8	**Soybean-II**	$K_{c\text{-NDVI}}$= 1.6594×NDVI - 0.193	0.95	0.97	0.25	0.21	0.78

Table 4.9. Validation of the $K_{c\text{-NDVI}}$ to K_c as outlined by the literature review (TAGEM-DSI, 2017)

No.	Crop	Linear equation	R^2	r	RMSE	MAE	d
1	**Wheat**	$K_{c\text{-NDVI}}$=0.7773×K_c + 0.1963	0.78	0.88	0.11	0.08	0.94
2	**Cotton-I**	$K_{c\text{-NDVI}}$=0.9565×K_c + 0.0348	0.96	0.98	0.07	0.065	0.989
3	**Corn-I**	$K_{c\text{-NDVI}}$= 0.879×K_c + 0.0971	0.88	0.94	0.11	0.08	0.97
4	**Soybean-I**	$K_{c\text{-NDVI}}$=0.5952×K_c+ 0.2808	0.60	0.77	0.18	0.15	0.86
5	**Cotton-II**	$K_{c\text{-NDVI}}$= 0.9802×K_c + 0.0174	0.98	0.99	0.04	0.03	1.00
6	**Corn-II**	$K_{c\text{-NDVI}}$= 0.6749×K_c + 0.2469	0.71	0.84	0.18	0.14	0.91
7	**Peanut-II**	$K_{c\text{-NDVI}}$= 0.8878×K_c+ 0.0935	0.89	0.94	0.10	0.07	0.97
8	**Soybean-II**	$K_{c\text{-NDVI}}$ = 0.9485×K_c+ 0.0392	0.95	0.97	0.08	0.06	0.99

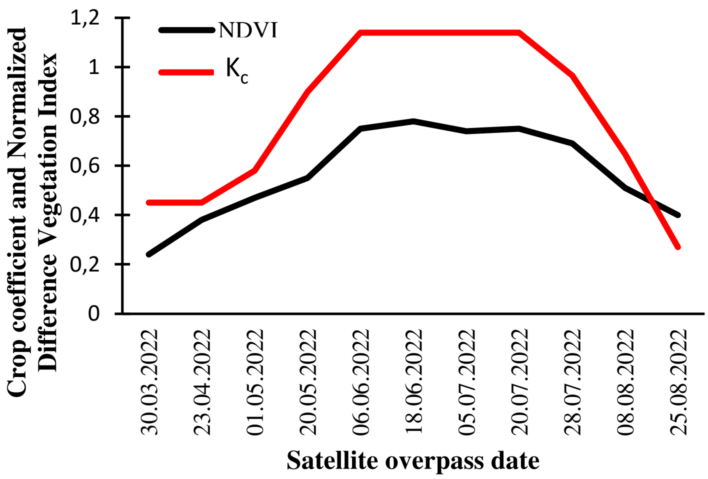

Figure 4.43. Temporal variation of K_c as outlined by the literature review (TAGEM-DSI, 2017) and NDVI for corn-I in the 2022

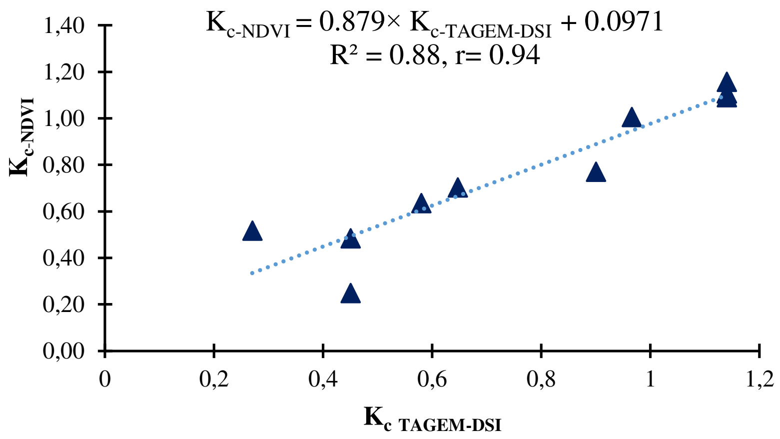

Figure 4.44. Linear relationship between standard K_c by the TAGEM-DSI (2017) and $K_{c\text{-}NDVI}$ for corn-I

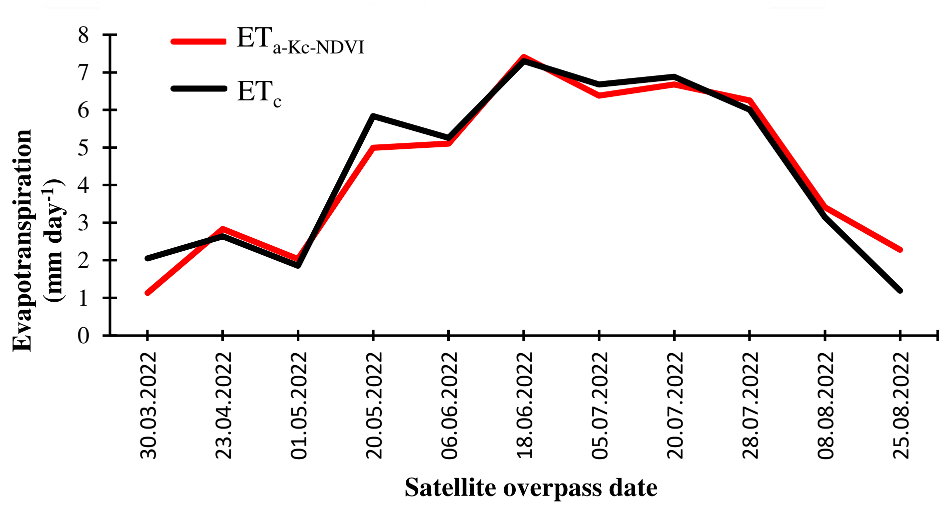

Figure 4.45. Temporal variation of ET_a for corn-I based on the $K_{c\text{-}NDVI}$ method and "two-step" procedure ET_c

This study compared ET_a estimates derived from the $K_{c\text{-}NDVI}$ method (a simple approach) with those obtained from the METRIC model (a complex process) to assess the accuracy of the $K_{c\text{-}NDVI}$ method for wheat crops. This comparison was conducted for the 2020 and 2021 water years. Figure 4.46 shows the daily ET_a as an example on 19.12.2019, which coincides with the day of the year (DOY 353). In turn, wheat ET_a by the METRIC model was 1.48 mm day^{-1}, whereas it was 0.72 mm day^{-1} by the $K_{c\text{-}NDVI}$ method. The difference in ET_a between the two models can be explained by the fact that the METRIC model incorporates multiple variables and parameters, such as LAI, albedo, soil heat flux (G), net radiation (R_n), sensible heat flux (H), and surface temperature, to estimate ET_a. In contrast, the $K_{c\text{-}NDVI}$ approach relies primarily on NDVI as the key parameter to compute ET_a, which is considered acceptable according to the studies conducted by Kamble et al. (2013), El-shirbeny et al. (2015), Reyes-González et al. (2018). However, some discrepancies between surface energy balance (SEB) models, such as METRIC and $K_{c\text{-}NDVI}$, are to be expected.

Finally, the ET_a values by the $K_{c\text{-}NDVI}$ were compared to the METRIC model at the satellite image acquisition dates.

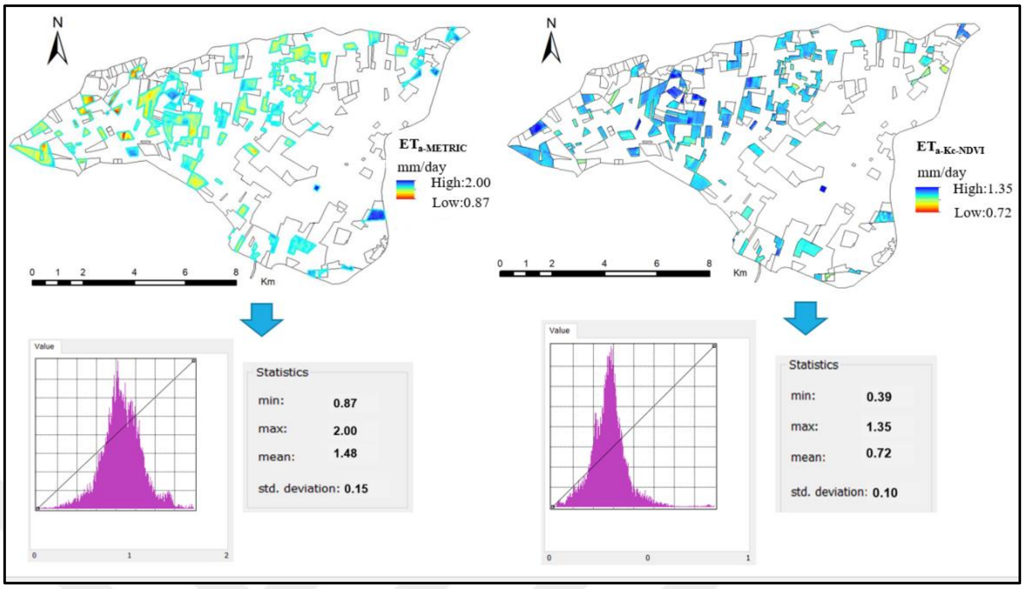

Figure 4.46. Spatial distribution of wheat ET_a by the METRIC model and ET_a by $K_{c\text{-}NDVI}$ method on DOY 353 (December 19, 2019): ET_a in the unit of mm day^{-1}

The variation of $ET_{a\text{-}METRIC}$ and $ET_{a\text{-}Kc\text{-}NDVI}$ of wheat crops in the study area was presented in Figure 4.47 at the time of the satellite overpass. As seen in Figure 4.47, the $ET_{a\text{-}METRIC}$ values were slightly higher than $ET_{a\text{-}Kc\text{-}NDVI}$. The difference in ET_a values between the METRIC model, which utilizes full surface energy data, and the faster $K_{c\text{-}NDVI}$ method for wheat can be interpreted as the K_c (ETrF) value from METRIC being higher than the K_c generated by the $ET_{a\text{-}Kc\text{-}NDVI}$ approach. This suggests that the METRIC model more comprehensively accounts for multiple factors, including climate, soil, and crop characteristics, compared to the $K_{c\text{-}NDVI}$ method, which relies solely on a single parameter, NDVI, derived from remote sensing. These results agree with several literature reviews by Anderson et al. (2012) and Reyes-González et al. (2018), which state that $ET_{a\text{-}METRIC}$ is greater than $ET_{a\text{-} Kc\text{-}NDVI}$. The reason could be interpreted as the K_c in the METRIC model being more representative than the generated K_c in the $K_{c\text{-}NDVI}$ method and standard K_c values documented by Allen et al. (1998). During the winter seasons of 2020 and 2021, as illustrated in Figure 4.47. a, b, the ET_a values from the METRIC model closely aligned with those from the $ET_{a\text{-}Kc\text{-}NDVI}$ method during the mid-growth stage of wheat. However, a notable difference was observed during the early and late growth stages. However, a notable difference was observed during wheat's initial and late (harvesting) growth stage development. The $K_{c\text{-}NDVI}$ method may be well-suited for estimating ET_a with notable precision during the mid-season, especially when compared to the beginning and end of the growing season. This approach can be broadly applied to determine ET_a with significant spatial resolution for various crop types across agricultural fields, spanning small and large irrigation scales within diverse climatic regions worldwide.

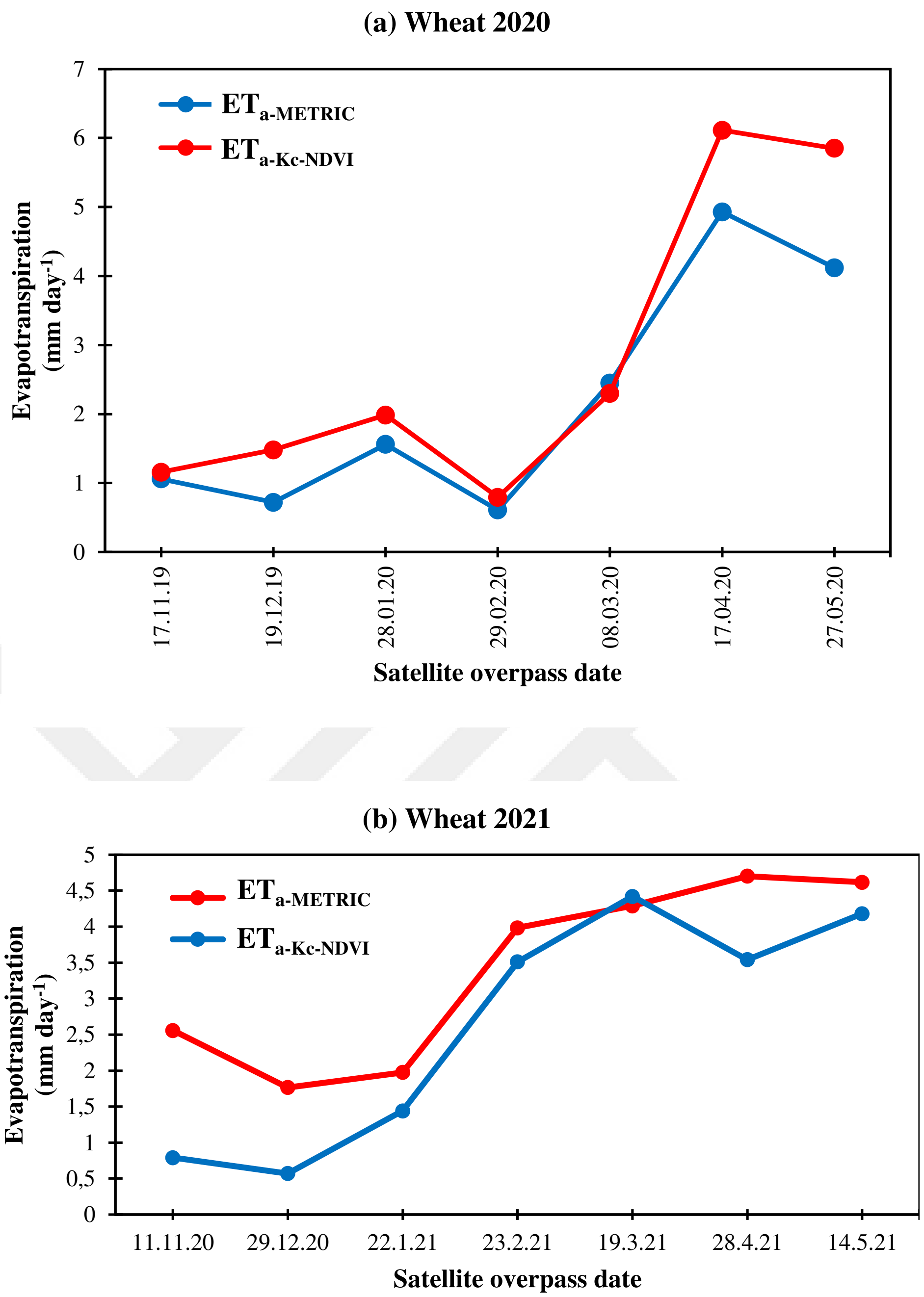

Figure 4.47. Temporal variations of areal mean daily wheat ET_a (mm day^{-1}) values, acquired by the METRIC model and $K_{c\text{-}NDVI}$, at the time of satellite overpass over the AID

The utility and cost-effectiveness of the $K_{c\text{-}NDVI}$ method are highlighted in the context of this study's contribution to agricultural and environmental sustainability. The method provides high-resolution ET_a estimates with minimal ground data requirements, making it an efficient tool for large-scale crop water monitoring. Its simplicity and computational efficiency reduce the need for expensive and labor-intensive field measurements. By offering accurate and timely information on crop water stress and irrigation needs, the $K_{c\text{-}NDVI}$ method supports improved water management practices, contributing to sustainable agriculture and more efficient water resource use, essential for environmental sustainability.

4.7. Temporal variations in daily ET_a using the METRIC, SEBAL, $K_{c\text{-}NDVI}$, and ET_c methods for some crops at satellite image acquisition dates

After estimating ET_a for each pixel and the entire study area using SEB models, it is crucial to emphasize the temporal variations in the areal mean daily ET_a for crops in each model—namely, METRIC, SEBAL, $K_{c\text{-}NDVI}$, and ET_c. The mean daily ET_a for crops in each model-METRIC, SEBAL, $K_{c\text{-}NDVI}$, and ET_c was evaluated for major crop types in the AID for the years 2020-2023. This temporal variation in mean daily ET_a for crops, as determined by these models during satellite overpass, is based on ground truth data and RS data on one basis scale, as shown in Figure 4.48. The ET_a results were categorized into the following nine major crop types: (a) wheat, (b) cotton-I, (c) cotton-II, (d) corn-I, (e) corn-II, (f) soybean-I, (g) soybean-II, (h) peanut-I, (i) peanut-II, and (j) citrus. The METRIC, SEBAL, ET_c, and $K_{c\text{-}NDVI}$ methods were used to compute ET_a for eight crops. However, the analysis was limited to the METRIC, SEBAL, and ET_c models for citrus due to the significantly low correlation between the reference K_c values provided by TAGEM-DSI (2017) and NDVI. This low correlation indicates that the $K_{c\text{-}NDVI}$ method does not adequately capture the relationship between crop coefficients and NDVI for citrus, likely due to the unique physiological and structural characteristics of citrus orchards, such as their evergreen canopy and less pronounced seasonal variation in NDVI compared to annual crops. Limiting the analysis to the METRIC, SEBAL, and ET_c models ensured meaningful and accurate comparisons for citrus crops, providing reliable ET_a estimates that align with the characteristics of these models and the crop under study.

The METRIC model consistently recorded the highest ET_a rates for eight crops in 2020 and 2021, as depicted in Figure 4.48. In contrast, the ET_a values calculated using the ET_c and $K_{c\text{-}NDVI}$ methods were highest for most crops in the most recent two water years, specifically 2022 and 2023. Conversely, for the citrus crop, the ET_a values derived from the METRIC and SEBAL models were higher than those obtained from the ET_c method. This discrepancy indicates that the K_c values used to estimate ET_c for different crop growth stages are generally lower than the ET_rF_i and EF fractions utilized by the METRIC and SEBAL models, respectively, for ET_a estimation. This variation can be attributed to multiple factors that influence the magnitude of ET_rF_i (fraction of reference evapotranspiration) and EF (evaporative fraction) in ET_a estimation. These factors include fluctuations in soil moisture levels, which regulate water availability for evaporation and transpiration, as well as meteorological conditions such as temperature, humidity, wind speed, and solar radiation, which are primary drivers of evapotranspiration. Crop biomass also significantly influences canopy cover, surface resistance, and water use efficiency. Differences in land surface characteristics and vegetation density also contribute to the variability in ET_a estimates (Alsenjar et al., 2023b). By integrating these variables, the models are designed to provide a comprehensive and accurate representation of actual evapotranspiration across diverse environmental and crop-specific scenarios. This multi-factor approach enhances the robustness and reliability of the ET_a estimation process. In contrast, the ET_c method relies on standardized conditions, which may not account for variations in water scarcity, crop diseases, soil salinity, and inappropriate irrigation management practices—factors collectively known as stressors.

The temporal variations of mean daily ET_a computed by the models reveal that the $ET_{a\text{-}METRIC}$ and $ET_{a\text{-}SEBAL}$ patterns follow similarly shaped curves, reflecting consistent trends across the growing season. However, $ET_{a\text{-}METRIC}$ consistently produces slightly higher values compared to $ET_{a\text{-}SEBAL}$, particularly for connected crops such as wheat, first and second-crop cotton, corn, soybean, and peanut within the AID during 2020 and 2021. This indicates that while both models align in their overall patterns, METRIC tends to estimate higher water use, potentially due to differences in how each model handles energy balance components, such as surface temperature and evaporative fraction. This observation underscores the importance of understanding model-specific characteristics when interpreting ET_a results, particularly for crops with high water demand. This contrasts the lower ET_a values recorded by the METRIC model in the 2022 and 2023 water years. The variations in mean daily ET_a observed using the METRIC and SEBAL models across different water years may be attributed to differences in the spatial distribution of crop types, soil properties, and climatic variables as well as the variety of irrigation methods employed by farmers. For example, the locations of wheat fields were not consistent over the four water years, as farmers rotated the wheat fields annually, resulting in changes in soil type. These factors could lead to variations in ET_a rates for the same crop type from one water year to another. Conversely, the $K_{c\text{-}NDVI}$ and ET_c methods exhibited consistently shaped curves for crop ET_a estimates between 2020 and 2023, reflecting a strong alignment in their temporal patterns across various growth stages. This consistency indicates that the $K_{c\text{-}NDVI}$ method effectively captures seasonal changes in crop water use, similar to the ET_c method, despite differences in their methodologies. This observation highlights the reliability of the $K_{c\text{-}NDVI}$ method as a viable alternative for estimating ET_a for different crop types. The difference between the ET_c and $K_{c\text{-}NDVI}$ methods and the RS-ET_a models like METRIC and SEBAL, as previously mentioned, lies in the fact that the ET_c method does not account for the actual status of crops, as the reference K_c values were taken from the reference book by TAGEM-DSI (2017). Additionally, the $K_{c\text{-}NDVI}$ method is only suitable for the middle stage of crop development. Thus, the results -which examine mean ET_a values across different models, crop types, and seasons- provide general insights into the spatial and temporal behaviours of the four models used during satellite overpasses for the years 2020-2023. Overall, the $K_{c\text{-}NDVI}$ method demonstrated better alignment with the ET_c method during the middle growth stages of crops compared to the initial and harvesting stages. Researchers and stakeholders can use the $K_{c\text{-}NDVI}$ method to estimate ET_a based on the relationship between reference K_c and NDVI for specific crops. The $K_{c\text{-}NDVI}$ method offers several advantages for estimating ET_a, particularly in agricultural and water resource management. It demonstrates better alignment with ET_c during the middle growth stages, when water demand is highest, making it reliable for irrigation planning during peak crop growth. By leveraging satellite-derived NDVI data, the method enables large-scale monitoring of ET_a with high spatial resolution, reducing the need for extensive field data collection. Additionally, it is cost-effective, as it minimizes reliance on costly ground-based measurements and is scalable, making it suitable for regional and catchment-level applications, especially in Mediterranean and semi-arid regions. The method integrates seamlessly with existing ET_a estimation frameworks and weather data, providing a practical and efficient alternative to traditional ET_c methods. Researchers could apply the METRIC and SEBAL models to compute ET_a over large-scale irrigation areas for extended time series, especially given the agreement in ET_a values observed across the four consecutive years. These models are particularly valuable for skilled users proficient in handling advanced remote sensing techniques, enabling accurate and consistent ET_a estimation over long periods. This makes them highly suitable for large-scale agricultural monitoring and water management applications.

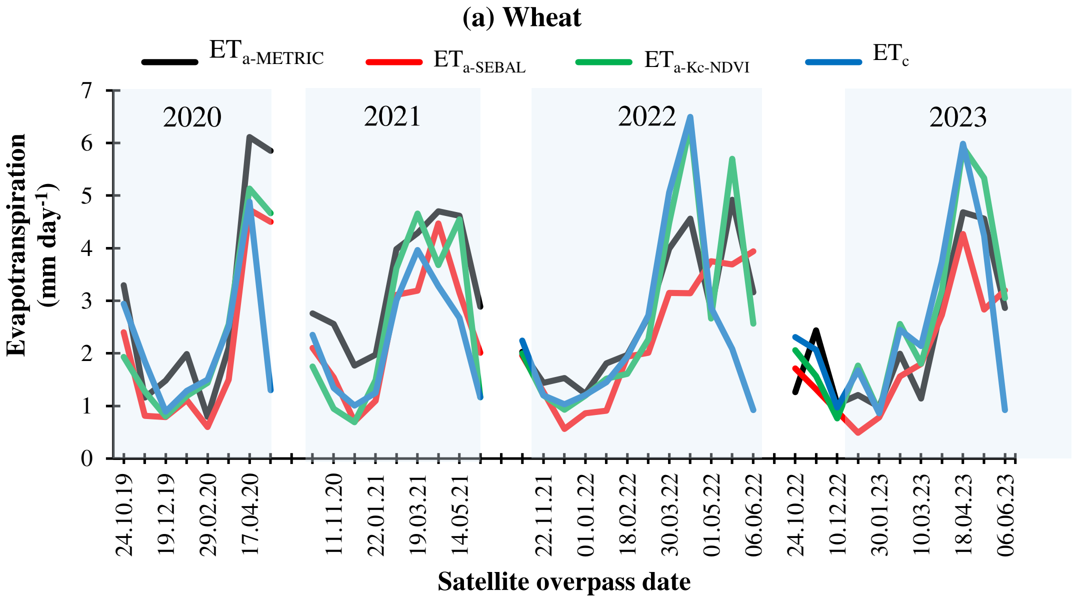

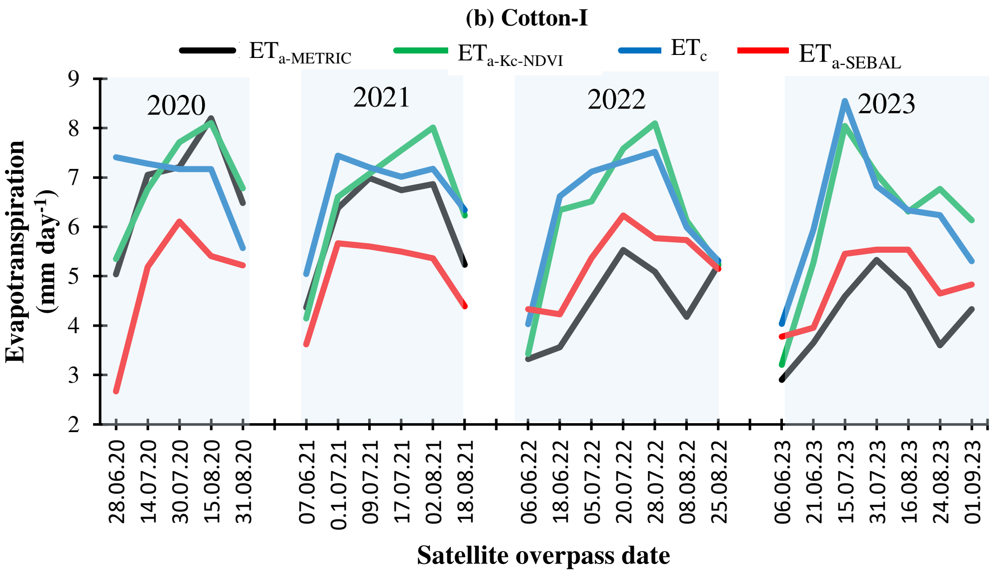
(b) Cotton-I
ET a-METRIC
ET a-Kc-NDVI
ET c
ET a-SEBAL
2020
2021
2022
2023
Evapotranspiration (mm day-1)
Satellite overpass date
28.06.20
14.07.20
30.07.20
15.08.20
31.08.20
07.06.21
0.1.07.21
09.07.21
17.07.21
02.08.21
18.08.21
06.06.22
18.06.22
05.07.22
20.07.22
28.07.22
08.08.22
25.08.22
06.06.23
21.06.23
15.07.23
31.07.23
16.08.23
24.08.23
01.09.23

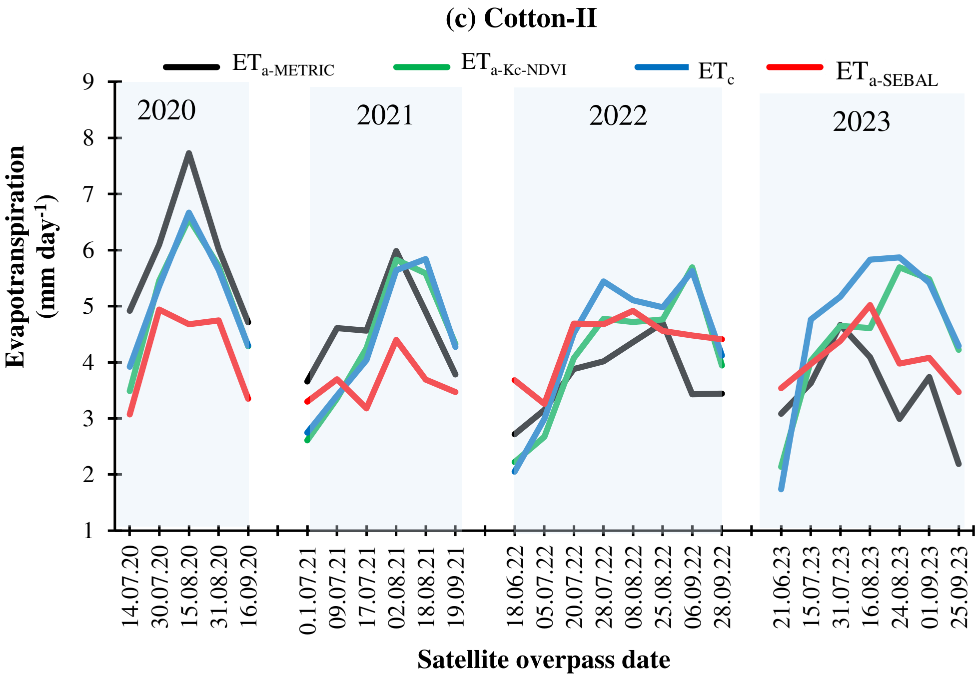
(c) Cotton-II
ET a-METRIC
ET a-Kc-NDVI
ET c
ET a-SEBAL
2020
2021
2022
2023
Evapotranspiration (mm day-1)
Satellite overpass date
14.07.20
30.07.20
15.08.20
31.08.20
16.09.20
0.1.07.21
09.07.21
17.07.21
02.08.21
18.08.21
19.09.21
18.06.22
05.07.22
20.07.22
28.07.22
08.08.22
25.08.22
06.09.22
28.09.22
21.06.23
15.07.23
31.07.23
16.08.23
24.08.23
01.09.23
25.09.23

(d) Corn-I

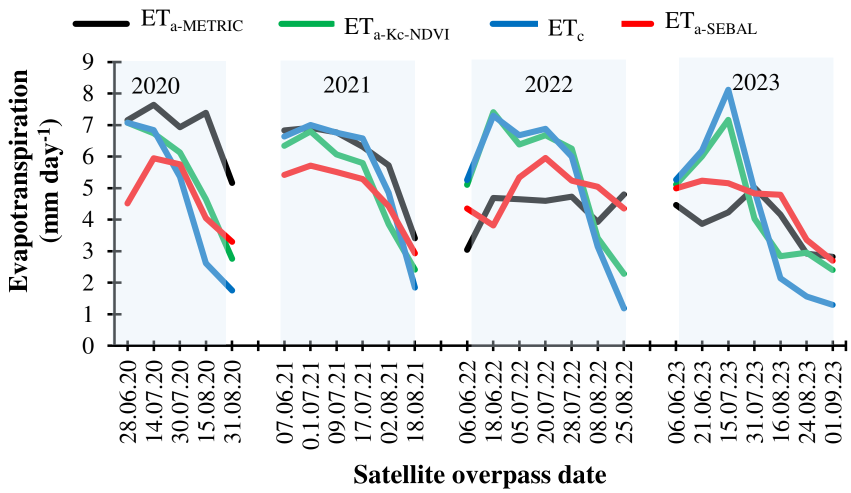

(e) Corn-II

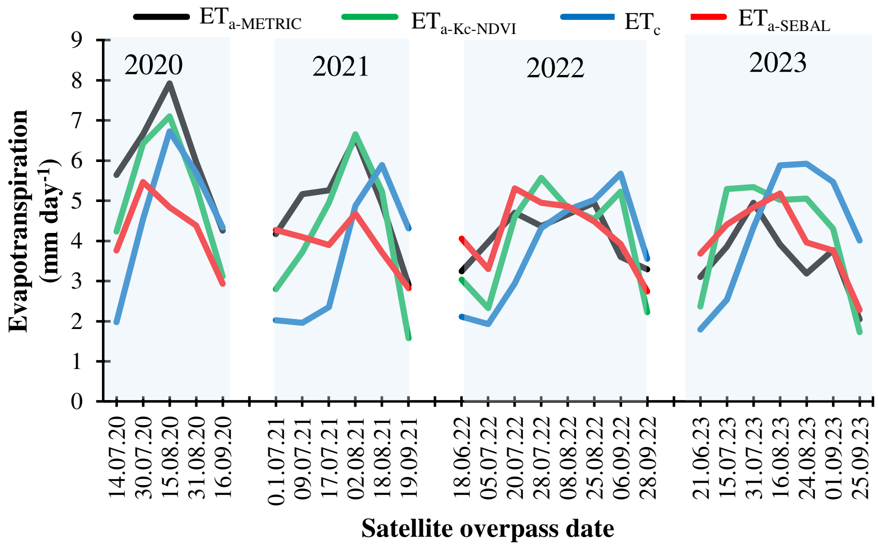

(f) Soybean-I

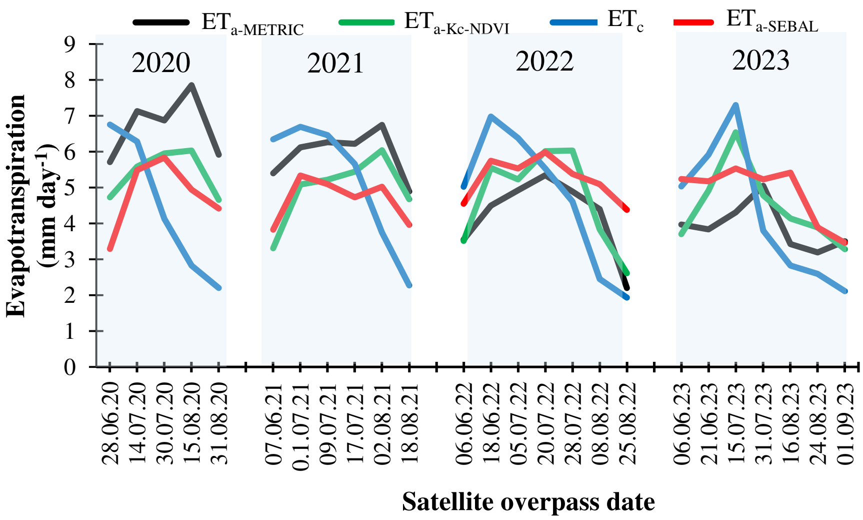

(g) Soybean-II

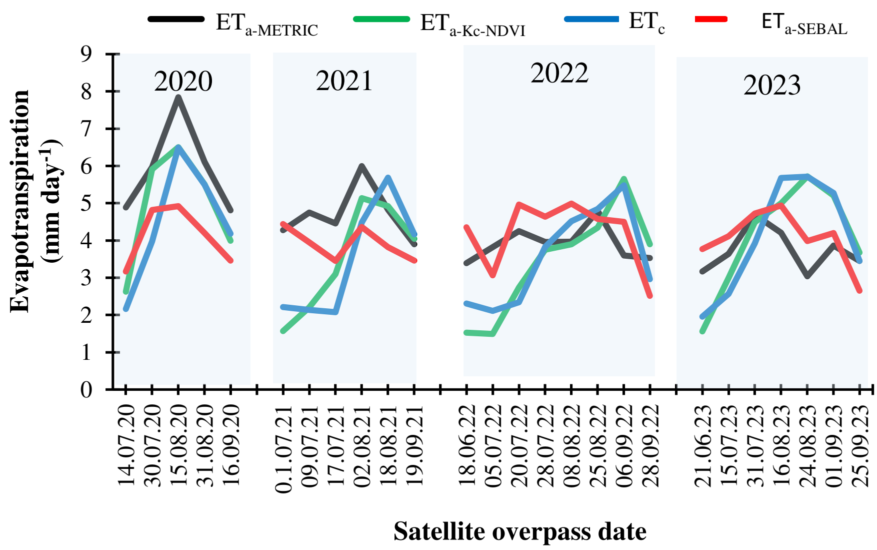

(h) Peanut-I

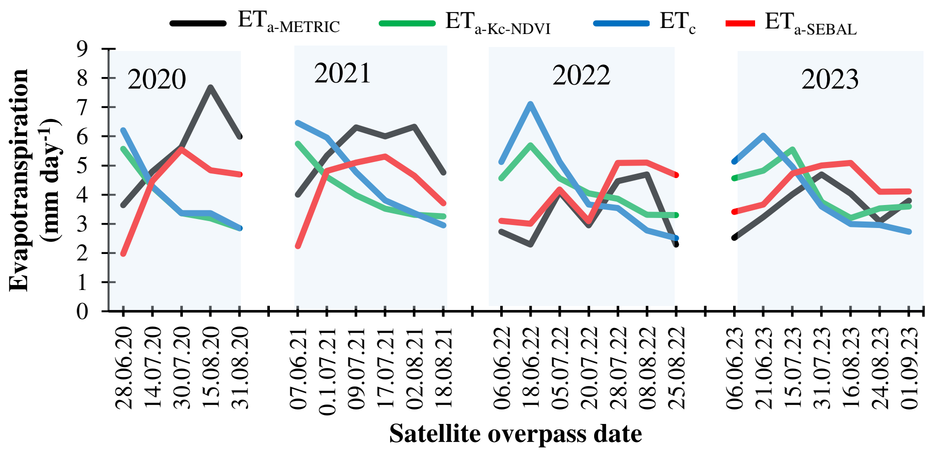

(i) Peanut-II

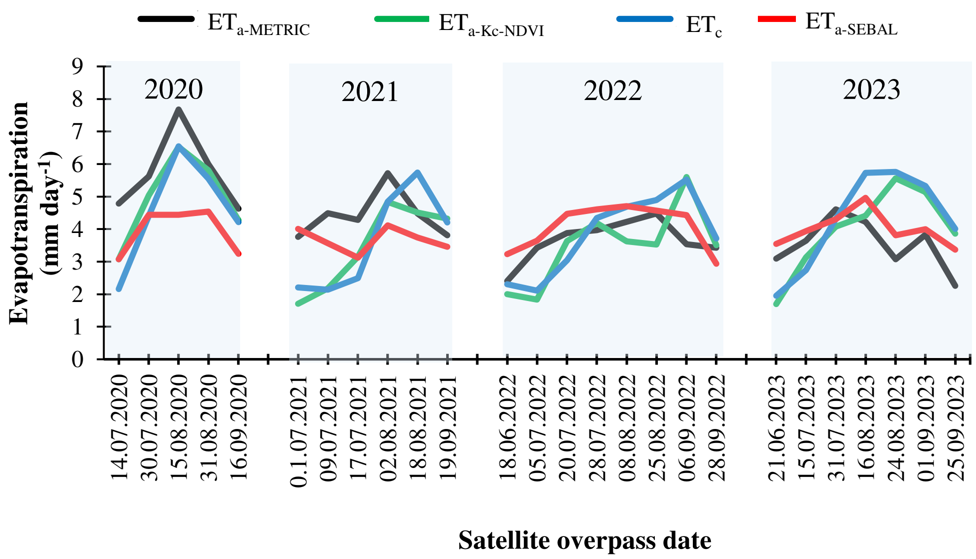

(j) Citrus

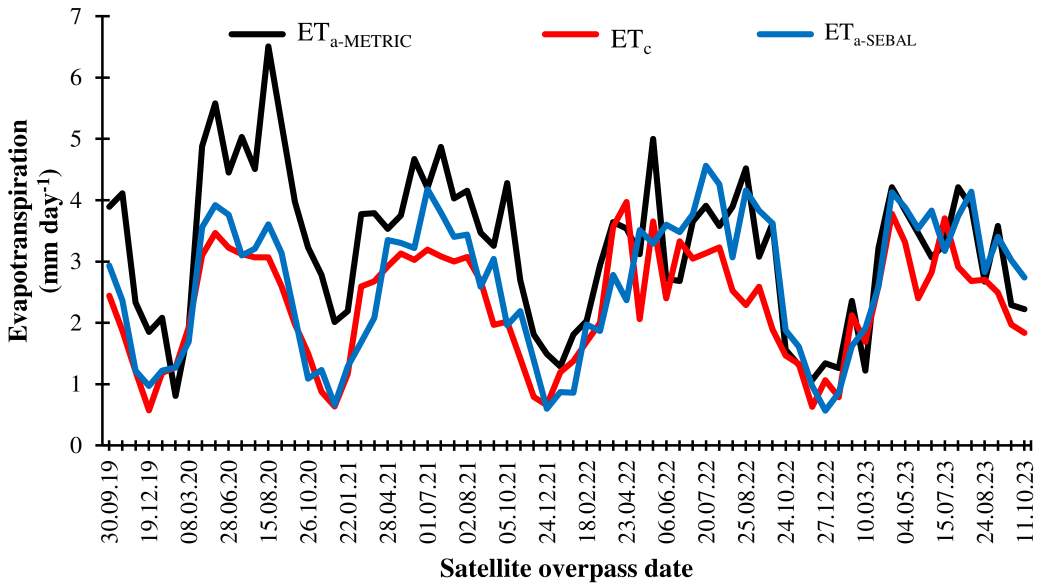

Figure 4.48. Temporal variations in the average daily ET_a values for: (a) Wheat,(b) Cotton-I, (c) Cotton-II, (d) Corn-I, (e) Corn-II, (f) Soybean-I, (g) Soybean-II, (h) Peanut-I, (i) Peanut-II, and (j) Citrus. ET_a estimations were done by the METRIC, SEBAL, $K_{c\text{-}NDVI}$, and ET_c models during satellite overpass dates within the AID of the LSP for the years 2020-2023

Factors such as vegetation type, climatic conditions, satellite overpass times, and soil characteristics can significantly impact the performance of each model. For instance, METRIC tends to outperform SEBAL in areas with high vegetation variability or specific weather conditions due to its incorporation of thermal infrared data. In contrast, SEBAL may be more effective in regions with less complex land cover. The METRIC model performed better in irrigated and controlled environments like AID. SEBAL, however, demonstrated reliable performance for large-scale assessments but required careful validation in heterogeneous landscapes. Regarding vegetation and soil types, the $K_{c\text{-}NDVI}$ approach proved more effective in homogeneous croplands.

4.8. Performance statistics of linear regression model for actual evapotranspiration by the ET_c and SEB models for some crop types

This study estimated daily actual evapotranspiration (ET_a) using several Surface Energy Balance (SEB) models, including METRIC, EEFlux, SEBAL, and GeeSEBAL, as well as a method known as the $K_{c\text{-}NDVI}$ method. These estimates were conducted for the study area, including the Akarsu Irrigation District (AID), during satellite overpass periods in the growing seasons of 2020 and 2023. To assess the accuracy of these SEB models, their ET_a estimates were compared to those obtained through a "two-step" procedure (ET_c) using a simple linear regression model ($ET_{a\text{-}SEB} = a + b \times ET_c$). The performance of the SEB models and the $K_{c\text{-}NDVI}$ method was evaluated by calculating various metrics, including RMSE, MAE, R^2, and the Willmott index of agreement (d). These metrics were used to compare the effectiveness of METRIC, SEBAL, and $K_{c\text{-}NDVI}$ against the ET_c method, which served as the reference. The evaluation was conducted for major crop types in the AID during satellite overpass periods, covering each year from 2020 to 2023. A Student's t-test was used to assess whether significant differences exist between the daily means of ET_c and ET_a as estimated by the SEB models for various crops during satellite overpass periods. Table 4.10. - Table 4.12 present the statistical analysis results conducted to compare ET_c and ET_a values obtained from the METRIC, SEBAL, and $K_{c\text{-}NDVI}$ models for various crops in the non-stressed area (AID). Additionally, these statistics were used to compare the ET_a values estimated by the METRIC model between the non-stressed (NSA) and stressed (SA) areas for specific crops of the LSP.

As noticed from Table 4.10, the METRIC model shows performance improvement when compared with the ET_c method for wheat crops over the years, achieving the best results in 2023 (R^2 = 0.70; Pearson correlation coefficient (r) 0.83; RMSE= 0.88 mm day^{-1}; MAE= 0.69 mm day^{-1}; d= 0.90). In other words, a strong correlation (r=0.83) and lower errors (RMSE= 0.88 mm day^{-1}, MAE= 0.69 mm day) were observed when comparing the METRIC model with the "two-step" approach for wheat crops in 2023. Similarly, the SEBAL model demonstrated improvement, with the best results in 2021 (R^2= 0.76; r=0.87; RMSE= 0.63 mm day^{-1}; MAE=0.51 mm day^{-1}; d= 0.92). The $K_{c\text{-}NDVI}$ method also consistently performed well, particularly in 2023 (R^2= 0.78; r= 0.88; RMSE= 0.81 mm day^{-1}; MAE=0.51 mm day^{-1}; d= 0.94). The METRIC algorithm consistently demonstrated strong performance for citrus crops compared to the ET_c method, particularly in 2021 and 2023. The r values were 0.90 in 2021 and 0.85 in 2023, with RMSE values of 1.23 mm day^{-1} and 0.67 mm day^{-1}, respectively. For citrus plantations, the MAE values between the ET_c method and the METRIC model were 1.16 mm day^{-1} and 0.53 mm day^{-1}, respectively, while the d values were 0.66 and 0.85, respectively. Likewise, the SEBAL model demonstrated enhanced accuracy and reliability over the years, achieving outstanding performance in 2020 with a high correlation (r=0.97) RMSE of 0.35 mm day^{-1}, MAE of 0.28 mm day^{-1}, and a d value of 0.97. It is known that the spatial distribution patterns of citrus remained relatively stable over the four years compared to other crops in the AID of the LSP region in Türkiye. In other words, the citrus orchards mainly were in fixed locations, contributing to the METRIC and SEBAL models showing good accuracy compared to the ET_c method. For cotton-I, in 2021, the METRIC and SEBAL models exhibited the best performance when compared with the ET_c approach (R^2=0.86, 0.95; r=0.93, 0.98; RMSE = 0.71, 1.68 mm day^{-1}; MAE = 0.61, 1.67 mm day^{-1}; d = 0.85, 0.47, respectively), showing significant variability in performance across other years. Conversely, the $K_{c\text{-}NDVI}$ method demonstrated high performance in most years, particularly excelling in 2022 (R^2= 0.94; r = 0.97; RMSE = 0.44 mm day^{-1}; MAE = 0.38 mm day^{-1}; d = 0.97). For corn-I, the METRIC and SEBAL models showed the best performance compared to the ET_c approach in 2021 (R^2=,0.98, 1.00, r = 0.99, 1.00; RMSE = 0.75, 1.13 mm day^{-1}; MAE = 0.50, 1.09 mm day^{-1}; d = 0.94, 0.85, respectively), with performance varying in other years. In contrast, the $K_{c\text{-}NDVI}$ method consistently demonstrated high performance across all years, achieving its peak in 2022 (R^2=0.98, r = 0.99; RMSE = 0.46 mm day^{-1}; MAE = 0.34 mm day^{-1}; d = 0.99).

The correlation coefficients between the estimated ET_a values for soybean-I and peanut-I using the METRIC and SEBAL models and the 'two-step' approach were weakly positive, with coefficients ranging from 0.23 to 0.6. Furthermore, the RMSE and MAE values exceeded 2.00 mm day^{-1} across all years, indicating that both models underperformed compared to the ET_c method for these crops. However, there was a slight improvement by the METRIC model compared to the ET_c method for soybean-I, particularly in 2022 (R^2 = 0.40; r=0.63; RMSE = 1.45 mm day^{-1}; MAE = 1.16 mm day^{-1}; d = 0.68). In contrast, the $K_{c\text{-}NDVI}$ method showed superior performance when compared to the ET_c method for peanut-I, particularly in 2020, with R^2 = 0.99, r = 0.99, RMSE = 0.30 mm day^{-1}, MAE = 0.17 mm day^{-1}, and d = 0.98. It also demonstrated notable improvements for soybean-I, especially in 2022 and 2023, with R^2 values of 0.52 and 0.68, r values of 0.72 and 0.82, RMSE values of 1.21 and 1.14 mm day^{-1}, MAE values of 1.15 and 1.12 mm day^{-1}, and d values of 0.81 and 0.82, respectively. The closer alignment of the $K_{c\text{-}NDVI}$ method with the ET_c method, compared to the METRIC and SEBAL models for peanut-I and soybean-I, can be attributed to the simplicity of its approach. Unlike METRIC and SEBAL, which calculate ET_a using more complex input datasets, the $K_{c\text{-}NDVI}$ method relies on a modified K_c value derived from the relationship between K_c and NDVI. As a result, the ET_a estimates from the $K_{c\text{-}NDVI}$ method closely match those obtained from the ET_c approach. Additionally, the reference K_c values in the ET_c method may not accurately represent the actual conditions of these crops, such as deficit irrigation or varying irrigation timings between different fields, as farmers practice. In contrast, the RS-based ET_a models like METRIC and SEBAL can capture the real-time conditions of crops during satellite overpasses, thereby potentially improving their accuracy.

For cotton-II, the METRIC model demonstrated its best performance with the ET_c method, particularly in 2020 (R^2 = 0.93; r= 0.97; RMSE = 0.77 mm day^{-1}; MAE = 0.72 mm day^{-1}; d = 0.87), with performance varying across other years as indicated in Table 4.10. Similarly, the SEBAL algorithm exhibited high performance with the ET_c method, especially in 2020 and 2022 (R^2 = 0.72 and 0.70; r= 0.85, 0.84; RMSE = 1.15 and 0.79 mm day^{-1}; MAE = 1.02 and 0.61 mm day^{-1}; d = 0.67 and 0.77, respectively), and showed good performance in other years as well, as shown in Table 4.11.

The $K_{c\text{-}NDVI}$ method consistently showed excellent performance across all years compared to the ET_c method, with its peak performance in 2021 (R^2 = 0.98; r=0.99; RMSE = 0.17 mm day^{-1}; MAE = 0.15 mm day^{-1}; d = 0.99). According to the statistical evaluations, the METRIC and SEBAL models consistently showed poor performance compared to the ET_c method for corn-II. In contrast, the $K_{c\text{-}NDVI}$ method performed better in some years, such as 2020 and 2022 (R^2 = 0.40 and 0.53; r=0.63, 0.73; RMSE = 1.44 and 0.97 mm day^{-1}; MAE = 1.21 and 0.82 mm day^{-1}; d = 0.74 and 0.84, respectively) outperforming other years. The statistical metrics showed good performance for the ET_c method when compared with the METRIC model for peanut-II in 2020 and 2022 (R^2 = 0.71 and

0.39; r=0.84, 0.62; RMSE = 1.42 and 0.94 mm day^{-1}; MAE = 1.17 and 0.72 mm day^{-1}; d = 0.73 and 0.67, respectively), outperforming other years. The SEBAL model displayed inconsistent performance when compared to the ET_c method across the years, with its best performance recorded in 2020 (R^2 = 0.65; r = 0.80; RMSE = 1.21 mm day^{-1}; MAE = 1.01 mm day^{-1}; d = 0.68). In contrast, the $K_{c\text{-}NDVI}$ method consistently showed strong alignment with the ET_c method, reaching its peak performance in 2020 (R^2 = 0.97; r = 0.99; RMSE = 0.51 mm day^{-1}; MAE = 0.37 mm day^{-1}; d = 0.97), underscoring its suitability for estimating ET_a for peanut-II. The statistical metrics showed poor performance for the ET_c method when compared with the METRIC and SEBAL models for soybean-II across most years, except 2020 (R^2 = 0.70 and 0.52; r= 0.84, r=0.72; RMSE = 1.68 and 1.13 mm day^{-1}; MAE = 1.46 and 1.09 mm day^{-1}; d = 0.66 and 0.70, respectively). In contrast, the $K_{c\text{-}NDVI}$ method demonstrated generally high performance over the years, as shown in Table 4.12, peaking in 2023 (R^2 = 0.92; r= 0.96; RMSE = 0.41 mm day^{-1}; MAE = 0.34 mm day^{-1}; d = 0.98).

Various evaluation metrics, including R^2, r, RMSE, MAE, and d, were employed to analyze the relationship between the ET_c method and ET_a estimated using the METRIC and SEBAL models, as well as the $K_{c\text{-}NDVI}$ approach for major crops in the AID of the LSP. The results showed that the METRIC and SEBAL models aligned closely with the ET_c method for wheat and citrus. Additionally, the $K_{c\text{-}NDVI}$ method consistently performed well with the "two-step" approach for these crops over four years. This indicates that reliable ET_a estimation for wheat and citrus can be achieved using remote sensing-based models such as METRIC, SEBAL, and $K_{c\text{-}NDVI}$ across large catchment areas. Cotton-I and cotton-II demonstrated reasonably good performance in the METRIC and SEBAL models, with $K_{c\text{-}NDVI}$ also performing well. For corn-I and corn-II, statistical evaluations showed excellent performance of the ET_c method with the METRIC and SEBAL models in 2021, with variability in other years, while the $K_{c\text{-}NDVI}$ method showed consistently high performance. For other crops, including peanut-I, peanut-II, soybean-I, and soybean-II, the evaluation metrics indicated that the METRIC and SEBAL models performed poorly compared to the ET_c method. In contrast, the $K_{c\text{-}NDVI}$ approach yielded better results. The differences in agreement between the RS-based ET_a models and the ET_c method for various crops over the four years can be attributed to variations in irrigation timing, irrigation methods, soil types, and field sowing dates. These variations reflect the complexity of field conditions rather than any inconsistencies in the performance of the models. Generally, tall crops (wheat, cotton, corn, and citrus) showed strong agreement in ET_a estimation using remote sensing-based models when applying the "two-step" procedure. In contrast, short crops (peanut and soybean) exhibited less agreement in ET_a estimation when compared to the ET_c method. This highlights the influence of crop type and management practices on the accuracy of ET_a estimates, with tall crops consistently performing better in remote sensing-based models and short crops showing more variability. Conversely, the $K_{c\text{-}NDVI}$ method effectively estimates ET_a across all crop types, especially during mid-growth.

Table 4.10. Performance statistics of linear regression model for actual evapotranspiration by the ET_c and METRIC models for selected crops over the AID

ET_c with $ET_{a\text{-METRIC}}$						
Crop	**Year**	**Coefficient of Determination R^2**	**Pearson correlation coefficient (r)**	**RMSE (mm day^{-1})**	**MAE (mm day^{-1})**	**d**
Wheat	**2020**	0.32	0.57	1.86	1.27	0.63
	2021	0.80	0.89	1.25	1.14	0.73
	2022	0.46	0.68	1.29	0.85	0.77
	2023	0.70	0.83	0.88	0.69	0.90
Citrus	**2020**	0.73	0.86	1.78	1.61	0.61
	2021	0.81	0.90	1.23	1.16	0.66
	2022	0.49	0.70	0.94	0.74	0.72
	2023	0.72	0.85	0.67	0.53	0.85
Cotton-I	**2020**	0.001	0.032	1.230	0.916	0.056
	2021	0.86	0.93	0.71	0.61	0.85
	2022	0.31	0.56	2.03	1.78	0.33
	2023	0.43	0.66	2.23	2.01	0.34
Corn-I	**2020**	0.44	0.66	2.74	2.13	0.40
	2021	0.98	0.99	0.75	0.50	0.94
	2022	0.01	0.10	2.28	2.11	0.09
	2023	0.39	0.62	2.05	1.72	0.51
Peanut-I	**2020**	0.63	0.80	2.85	2.56	0.00
	2021	0.21	0.46	2.07	1.93	0.00
	2022	0.13	0.36	2.24	1.72	0.00
	2023	0.15	0.38	1.64	1.38	0.00
Soybean-I	**2020**	0.05	0.23	3.11	2.68	0.00
	2021	0.12	0.35	1.71	1.32	0.32
	2022	0.40	0.63	1.45	1.16	0.68
	2023	0.21	0.46	1.63	1.42	0.42
Cotton-II	**2020**	0.93	0.97	0.77	0.72	0.87
	2021	0.55	0.74	0.80	0.74	0.80
	2022	0.55	0.74	1.05	0.85	0.66
	2023	0.14	0.37	1.77	1.63	0.32
Corn-II	**2020**	0.32	0.56	1.97	1.46	0.53
	2021	0.01	0.10	2.20	2.05	0.12
	2022	0.11	0.33	1.27	0.94	0.40
	2023	0.02	0.15	1.77	1.66	0.19
Peanut-II	**2020**	0.71	0.84	1.42	1.17	0.73
	2021	0.18	0.43	1.51	1.37	0.41
	2022	0.39	0.62	0.94	0.72	0.67
	2023	0.07	0.27	1.56	1.39	0.31
Soybean-II	**2020**	0.70	0.84	1.68	1.46	0.66
	2021	0.11	0.33	1.82	1.61	0.27
	2022	0.09	0.30	1.22	0.99	0.29
	2023	0.03	0.19	1.56	1.44	0.21

Table 4.11. Performance statistics of linear regression model for actual evapotranspiration by the ET_c and SEBAL models for selected crops over the AID

ET_c with $ET_{a\text{-}SEBAL}$						
Crop	**Year**	**R^2**	**r**	**RMSE (mm day^{-1})**	**MAE (mm day^{-1})**	**d**
Wheat	**2020**	0.35	0.59	1.37	0.94	0.73
	2021	0.76	0.87	0.63	0.51	0.92
	2022	0.20	0.44	1.61	1.18	0.59
	2023	0.55	0.74	1.18	0.97	0.80
Citrus	**2020**	0.94	0.97	0.35	0.28	0.97
	2021	0.73	0.85	0.58	0.47	0.90
	2022	0.48	0.69	0.97	0.80	0.77
	2023	0.61	0.78	0.77	0.65	0.79
Cotton-I	**2020**	0.06	0.25	2.49	2.00	0.00
	2021	0.95	0.98	1.68	1.67	0.47
	2022	0.37	0.61	1.37	1.09	0.51
	2023	0.53	0.73	1.61	1.34	0.50
Corn-I	**2020**	0.59	0.77	1.55	1.36	0.74
	2021	1.00	1.00	1.13	1.09	0.85
	2022	0.05	0.23	2.06	1.78	0.24
	2023	0.64	0.80	1.77	1.45	0.69
Peanut-I	**2020**	0.85	0.92	2.38	1.99	0.00
	2021	0.16	0.40	1.99	1.54	0.00
	2022	0.49	0.70	2.23	1.96	0.00
	2023	0.24	0.49	1.61	1.45	0.00
Soybean-I	**2020**	0.06	0.24	2.24	2.06	0.00
	2021	0.15	0.39	1.60	1.52	0.36
	2022	0.48	0.69	1.52	1.27	0.54
	2023	0.47	0.69	1.51	1.34	0.62
Cotton-II	**2020**	0.72	0.85	1.15	1.02	0.67
	2021	0.41	0.64	1.15	0.98	0.46
	2022	0.70	0.84	0.79	0.61	0.77
	2023	0.42	0.65	1.27	1.18	0.51
Corn-II	**2020**	0.18	0.42	1.50	1.46	0.55
	2021	0.04	0.21	1.78	1.63	0.00
	2022	0.07	0.26	1.31	1.08	0.39
	2023	0.05	0.23	1.58	1.48	0.33
Peanut-II	**2020**	0.65	0.80	1.21	1.01	0.68
	2021	0.09	0.31	1.34	1.22	0.24
	2022	0.25	0.50	0.95	0.78	0.60
	2023	0.15	0.39	1.15	0.98	0.38
Soybean-II	**2020**	0.52	0.72	1.13	1.09	0.70
	2021	0.00	0.04	1.53	1.35	0.00
	2022	0.18	0.42	1.33	1.08	0.50
	2023	0.22	0.47	1.357	1.285	0.39

Table 4.12. Performance statistics of linear regression model for actual evapotranspiration by the ET_c and $K_{c\text{-}NDVI}$ models for selected crops over the AID

ET_c with $ET_{a\text{-}Kc\text{-}NDVI}$						
Crop	**Year**	**R^2**	**r**	**RMSE (mm day^{-1})**	**MAE (mm day^{-1})**	**d**
Wheat	**2020**	0.45	0.67	1.30	0.64	0.77
	2021	0.87	0.93	0.83	0.65	0.90
	2022	0.58	0.76	1.29	0.72	0.85
	2023	0.78	0.88	0.81	0.51	0.94
Cotton-I	**2020**	0.00	0.04	1.21	1.06	0.00
	2021	0.79	0.89	0.67	0.57	0.89
	2022	0.94	0.97	0.44	0.38	0.97
	2023	0.83	0.91	0.59	0.53	0.95
Corn-I	**2020**	0.93	0.96	1.07	0.78	0.92
	2021	0.93	0.97	0.65	0.59	0.96
	2022	0.98	0.99	0.46	0.34	0.99
	2023	0.95	0.98	0.88	0.77	0.95
Peanut-I	**2020**	0.99	0.99	0.30	0.17	0.98
	2021	0.90	0.95	0.73	0.59	0.89
	2022	0.97	0.99	0.74	0.65	0.90
	2023	0.72	0.85	0.86	0.59	0.87
Soybean-I	**2020**	0.02	0.14	2.20	2.04	0.00
	2021	0.05	0.23	2.02	1.80	0.00
	2022	0.52	0.72	1.21	1.15	0.81
	2023	0.68	0.82	1.14	1.12	0.82
Cotton-II	**2020**	0.98	0.99	0.21	0.14	0.99
	2021	0.98	0.99	0.17	0.15	0.99
	2022	0.96	0.98	0.36	0.31	0.98
	2023	0.87	0.93	0.60	0.46	0.94
Corn II	**2020**	0.40	0.63	1.44	1.21	0.74
	2021	0.14	0.37	1.89	1.72	0.51
	2022	0.53	0.73	0.97	0.82	0.83
	2023	0.01	0.11	1.67	1.49	0.20
Peanut-II	**2020**	0.97	0.99	0.51	0.37	0.96
	2021	0.83	0.91	0.61	0.43	0.94
	2022	0.76	0.87	0.67	0.50	0.91
	2023	0.89	0.94	0.55	0.39	0.95
Soybean-II	**2020**	0.73	0.86	0.90	0.52	0.90
	2021	0.79	0.89	0.64	0.54	0.94
	2022	0.82	0.91	0.58	0.51	0.95
	2023	0.92	0.96	0.41	0.34	0.98

A Student's t-test was conducted at a 95% confidence level to evaluate whether significant differences existed between the means of ET_c and ET_a estimated by the SEB model. Before the Student's t-test, an F-test was performed to determine if the variances of the datasets were equal or unequal. This analysis was carried out for various crops, including wheat, citrus, corn-I, and cotton-I, during the 2021 water year as a case study. These differences may be attributed to the unique characteristics of each crop. For citrus orchards, as shown in Table 4.13, the p-value (0.00028) is much smaller than the significance level of 0.05. Based on the results, it can be concluded that there is a significant difference between the means of ET_c and $ET_{a\text{-}METRIC}$ for citrus, as confirmed by the Student's t-test for unequal variances. In contrast, there is no significant difference between ET_c and $ET_{a\text{-}SEBAL}$ estimates, as the p-value (0.61) is greater than the significance level of 0.05, and the t-statistic (-0.51) is lower than the t-critical value for a two-tailed test (2.05). The Student's t-test results for unequal variances suggest that, although ET_c and $ET_{a\text{-}SEBAL}$ are similar, a significant difference is observed when comparing ET_c with $ET_{a\text{-}METRIC}$ estimates. The results of the Student's t-test equal variances indicate that there is no significant difference in the means of ET_c and the ET_a estimates from METRIC, SEBAL, and $K_{c\text{-}NDVI}$ for wheat crops. The p-values for the comparisons between ET_c and $ET_{a\text{-}METRIC}$ (0.06), ET_c and $ET_{a\text{-}SEBAL}$ (0.78), and ET_c and $ET_{a\text{-}Kc\text{-}NDVI}$ (0.67) are all greater than the significance level of 0.05. Furthermore, the t-statistics are lower than the critical t-values for a two-tailed test, as shown in Table 4.14. These findings suggest that ET_c is comparable to the ET_a estimates from METRIC, SEBAL, and $K_{c\text{-}NDVI}$ for wheat crops. For corn-I, the results of the Student's t-test equal variances, as shown in Table 4.15, indicate that there is no significant evidence to suggest a difference between the means of ET_c and those of $ET_{a\text{-}METRIC}$, $ET_{a\text{-}SEBAL}$, and $ET_{a\text{-}Kc\text{-}NDVI}$. The differences between these datasets are not statistically significant at the 0.05 significance level. For cotton-I, the Student's t-test equal variances results show no significant evidence to suggest a difference between the means of ET_c and those of $ET_{a\text{-}METRIC}$ or $ET_{a\text{-}Kc\text{-}NDVI}$, as shown in Table 4.16. However, significant differences were found between ET_c and $ET_{a\text{-}SEBAL}$ estimates. These results suggest that ET_c, $ET_{a\text{-}METRIC}$ and $ET_{a\text{-}Kc\text{-}NDVI}$ are comparable, but there are notable differences when comparing ET_c with $ET_{a\text{-}SEBAL}$ estimates.

Table 4.13. Student's t-test results comparing the "two-step" approach (ET_c) with the METRIC and SEBAL models for citrus crops in 2021

(ET_c and ET_a in mm day^{-1})	**ET_c**	**$ET_{a\text{-}METRIC}$**	**ET_c**	**$ET_{a\text{-}SEBAL}$**
Mean	2.35	3.62	2.35	2.52
Observations	16			
Pearson correlation coefficient (r)	0.84		0.88	
df	15			
t-stat	-4.73		-0.51	
P(T<=t) two-tail	0.00		0.61	
t critical two-tail	2.03		2.05	

Table 4.14. Student's t-test results comparing the "two-step" approach (ET_c) with the METRIC, SEBAL and $K_{c\text{-}NDVI}$ models for wheat crops in 2021

(ET_c and ET_a in mm day^{-1})	**ET_c**	**$ET_{a\text{-}METRIC}$**	**ET_c**	**$ET_{a\text{-}SEBAL}$**	**ET_c**	**$ET_{a\text{-}Kc\text{-}NDVI}$**
Mean	2.23	3.28	2.23	2.37	2.23	2.70
Observations	9					
Pearson correlation coefficient (r)	0.87		0.86		0.69	
df	8					
t-stat	-2.02		-0.27		-0.43	
P(T<=t) two-tail	0.06		0.78		0.67	
t critical two-tail	2.12		2.12		2.11	

Table 4.15. Student's t-test results comparing the "two-step" approach (ET_c) with the METRIC, SEBAL and $K_{c\text{-}NDVI}$ models for corn-I crops in 2021

(ET_c and ET_a in mm day^{-1})	**ET_c**	**$ET_{a\text{-}METRIC}$**	**ET_c**	**$ET_{a\text{-}SEBAL}$**	**ET_c**	**$ET_{a\text{-}Kc\text{-}NDVI}$**
Mean	5.610	5.99	5.61	4.88	5.61	5.21
Observations	6					
Pearson correlation coefficient (r)	0.99		0.99		0.97	
df	5					
t-stat	-0.39		0.79		0.37	
P(T<=t) two-tail	0.71		0.45		0.72	
t Critical two-tail	2.23		2.22		2.23	

Table 4.16. Student's t-test results comparing the "two-step" approach (ET_c) with the METRIC, SEBAL, and $K_{c\text{-}NDVI}$ models for cotton-I crop in 2021

(ET_c and ET_a in mm day^{-1})	**ET_c**	**$ET_{a\text{-}METRIC}$**	**ET_c**	**$ET_{a\text{-}SEBAL}$**	**ET_c**	**$ET_{a\text{-}Kc\text{-}NDVI}$**
Mean	6.20	5.59	6.20	4.52	6.20	6.10
Observations	6					
Pearson correlation coefficient (r)	0.93		0.98		0.89	
df	5					
t-stat	1.07		3.36		0.15	
P(T<=t) two-tail	0.31		0.007		0.89	
t critical two-tail	2.23		2.23		2.571	

As previously discussed, evaluation metrics were conducted to compare ET_a values estimated by the METRIC model between non-stressed (NSA, denoted as $ET_{a\text{-}METRIC\text{-}NSA}$) and stressed (SA, denoted as $ET_{a\text{-}METRIC\text{-}SA}$) areas for specific crops in the Lower Seyhan Plain (LSP) during satellite overpass periods in the 2020 and 2023 growing seasons. In Türkiye's LSP, the

METRIC model has demonstrated high reliability in estimating ET_a for most crops under varying conditions, including NSA (AID) and SA near the eastern Mediterranean coast. According to Table 4.17, saplings had the lowest RMSE (0.61 mm day^{-1}) and MAE of 0.47 mm day^{-1} among the listed crops, indicating exceptionally precise ET_a estimates using the METRIC model in both NSA and SA. Cotton-I showed the highest coefficient of determination (R^2 = 0.96) and Pearson correlation coefficient (r = 0.98), suggesting very accurate $ET_{a\text{-METRIC}}$ estimates, reflecting highly accurate $ET_{a\text{-METRIC}}$ estimates. However, its RMSE (1.10 mm day^{-1}) and MAE (0.98 mm day^{-1}) were slightly higher than other crops. Wheat, citrus, and corn exhibited strong correlations between ET_a estimates from non-stressed and stressed areas, with low error values, further proving the model's effectiveness for these crops in both AID and stressed areas of the LSP. However, for soybean-II, the METRIC model shows a lower correlation coefficient (r = 0.81) and coefficient of determination (R^2 = 0.65) between non-stressed ($ET_{a\text{-METRIC-NSA}}$) and stressed ($ET_{a\text{-METRIC-SA}}$) areas. Despite this, it has the lowest RMSE (0.72 mm day^{-1}) among soybean varieties, indicating that ET_a estimates for this crop cycle are relatively precise. The variation in model performance can be attributed to crop type, irrigation practices, and local climatic conditions. Based on the metric evaluations, the METRIC model's ability to accurately estimate ET_a is vital for efficient water resource management, especially in regions like the LSP, where water scarcity is a significant concern.

In the LSP of Türkiye, the METRIC model demonstrates high reliability in estimating ET_a for most crops, with wheat, citrus, and corn showing solid performance. Cotton also exhibits high accuracy, albeit with some variability. Soybeans present a challenge for the model, with lower correlation and higher error metrics. These findings emphasize the importance of considering crop-specific factors and local conditions when utilizing ET_a estimates for water management and agricultural planning.

Table 4.17. Performance statistics of linear regression model between $ET_{a\text{-METRIC-NSA}}$ and $ET_{a\text{-METRIC-SA}}$ for some crops

$ET_{a\text{-METRIC-NSA}}$ and $ET_{a\text{-METRIC-SA}}$					
Crop	**R^2**	**r**	**RMSE (mm day^{-1})**	**MAE (mm day^{-1})**	**d**
Wheat	0.84	0.92	1.02	0.82	0.82
Citrus	0.82	0.91	0.82	0.66	0.88
Sapling	0.75	0.87	0.61	0.47	0.88
Corn-I	0.88	0.94	0.85	0.67	0.89
Cotton-I	0.96	0.98	1.10	0.98	0.81
Soybean-I	0.75	0.86	1.16	1.06	0.78
Cotton-II	0.80	0.90	0.97	0.75	0.74
Soybean-II	0.65	0.81	0.72	0.46	0.83

A key finding of this thesis is the application of the METRIC model to estimate the mean daily ET_a for citrus in the Cotlu field ($ET_{a\text{-METRIC-Cotlu}}$), located near the meteorological station in Cotlu village, as well as across all citrus fields ($ET_{a\text{-METRIC-AID}}$) within the AID during satellite overpasses from 2020 to 2023. This approach enabled an evaluation of how accurately ET_a estimates for citrus in the Cotlu field represent ET_a for all citrus crops within the AID. This was done through a linear regression analysis and the evaluation of key metrics such as r, RMSE, MAE, and d. The highest accuracy was observed when comparing $ET_{a\text{-METRIC}}$ for citrus near the Cotlu station with the mean $ET_{a\text{-METRIC}}$ for citrus in the AID under non-stressed conditions, resulting in a high correlation (r = 0.91), low error values (RMSE = 0.54 mm day^{-1}, MAE = 0.40 mm day^{-1}), and excellent agreement (d = 0.95) as outlined in Figure 4.49. The derived equation ($ET_{a\text{-METRIC-AID}} = 0.8615 \times ET_{a\text{-METRIC-Cotlu}} + 0.2662$) can be applied to estimate ET_a for all citrus crops within the AID, provided the ET_a for citrus in the Cotlu field is first determined using the METRIC model. This equation is particularly useful for researchers, agricultural managers, and water resource planners who require ET_a estimates for citrus across the AID without implementing the METRIC model for the entire region. By leveraging the detailed data and meteorological inputs available for the Cotlu field, the equation enables a reliable extrapolation of ET_a values for citrus crops across the AID. However, it is essential to note that the equation was developed based on data from the Cotlu field, which may not fully account for varying agronomic conditions across the Lower Seyhan Plain (LSP), particularly under stressed scenarios.

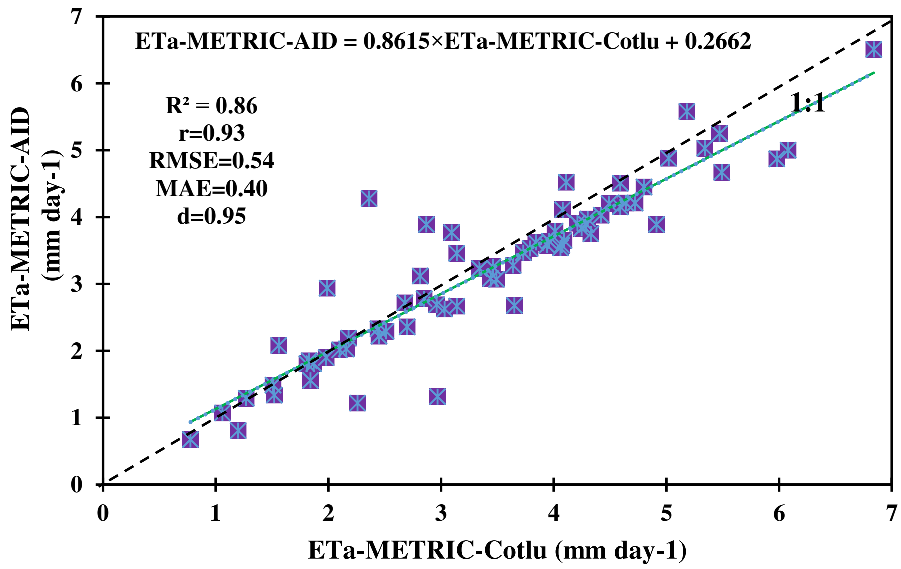

Figure 4.49. A linear relationship between actual evapotranspiration by the METRIC model ($ET_{a\text{-METRIC}}$, mm day^{-1}) for citrus near the Cotlu weather station compared to the mean value of citrus in the AID during the 2020–2023 study period. The dashed black lines represent the 1:1 lines

The findings of this study could have significant implications for local agricultural policies and water management strategies. By providing accurate and high-resolution ET_a estimates, the study can inform decision-makers on water usage efficiency, helping to optimize irrigation practices and allocate water resources more effectively. These insights could contribute to developing more sustainable agricultural policies that promote water conservation and improve crop yield prediction. Additionally, understanding crop water stress and irrigation needs can support the implementation of adaptive strategies in response to climate variability, enhancing overall water management in agricultural regions.

4.9. Evaporation estimation by the METRIC model over lagoons of the LSP

The METRIC model can compute ET_a for agricultural areas as well as evaporation (E_{METRIC}) for lakes and rivers. The METRIC model can estimate evaporation in lagoons, regardless of whether they contain freshwater, saline water, or a mixture of both. Accordingly, this study applied the METRIC model to estimate evaporation and compared its results with those obtained using an empirical method like the Kohler-Nordenson-Fox model (Kohler et al., 1955) based on in-situ climatic parameters collected directly from weather stations near the lagoons. Consequently, the estimation of lake evaporation utilizes the RS-ET_a-based METRIC model, which is applied to the Tuzla and Akyatan lakes along the Mediterranean coast of Türkiye. These lagoons are located in the Cukurova region of Türkiye, at the southeastern edge of the Mediterranean Sea, roughly 30 km south of Adana (Figure 3.1). According to Joyeux and Ward (1998), the Akyatan Lagoon has a surface area of 3 km², an average depth of 0.75 m, and a maximum depth of 3 m. The Tuzla Lagoon covers an area of 11.2 km^2. It is well-known that the lagoons receive freshwater from irrigation canals, drainage systems, rainfall, and non-point underground sources. Additionally, it may be fed by flows from the Seyhan River and the old channels of the Ceyhan River (Davutluoglu et al., 2010; Kuleli, 2010). On the other hand, a study conducted by Çetin and Özcan (1999) clearly showed that the Seyhan and Ceyhan Rivers may feed the shallow water table in the LSP during some months of the year, depending on the hydrological and hydraulic conditions. Furthermore, they pointed out that the lagoon system, i.e., Tuzla and Akyatan lakes, is hydraulically and hydrologically well connected to the shallow water table in the plain. Moreover, the lagoons also receive seawater through a canal connecting it to the Mediterranean Sea. A narrow, 2-kilometre-long canal on the southeastern edge of the lagoons connects them to the sea, allowing for the tidal exchange of water and sediments. This thesis study represents the first attempt to use the METRIC model to capture the spatiotemporal variations of evaporation in saline lakes, adding significant value.

Figure 4.50 illustrates the temporal variations in the mean daily E_{METRIC} rates of Tuzla and Akyatan lakes in the stressed area of the LSP, Türkiye, over several years, estimated using the METRIC model during satellite overpasses. The data spans from September 30, 2019, to October 11, 2023. As shown in Figure 4.50, the E_{METRIC} rates of these lakes fluctuate considerably over time, with higher values typically observed in late spring and early summer and lower values during winter. The peak E_{METRIC} rate was recorded at 7.59 mm day^{-1} on May 27, 2020, while the lowest rate was 1.12 mm day^{-1} on February 17, 2021. Spatially, Figure 4.51 highlights notable differences in E_{METRIC} rates across various lagoons and regions on specific dates, providing insights into the spatial changes in E_{METRIC} rates in the saline lakes of the LSP.

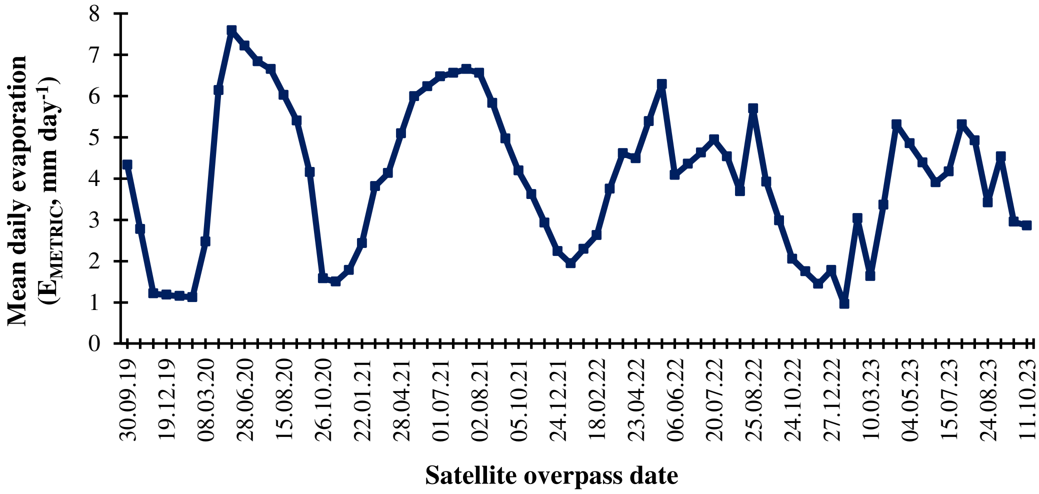

Figure 4.50. Temporal fluctuations of mean daily evaporation (E_{METRIC}, mm day^{-1}) of lagoons derived from the METRIC model during satellite overpass dates

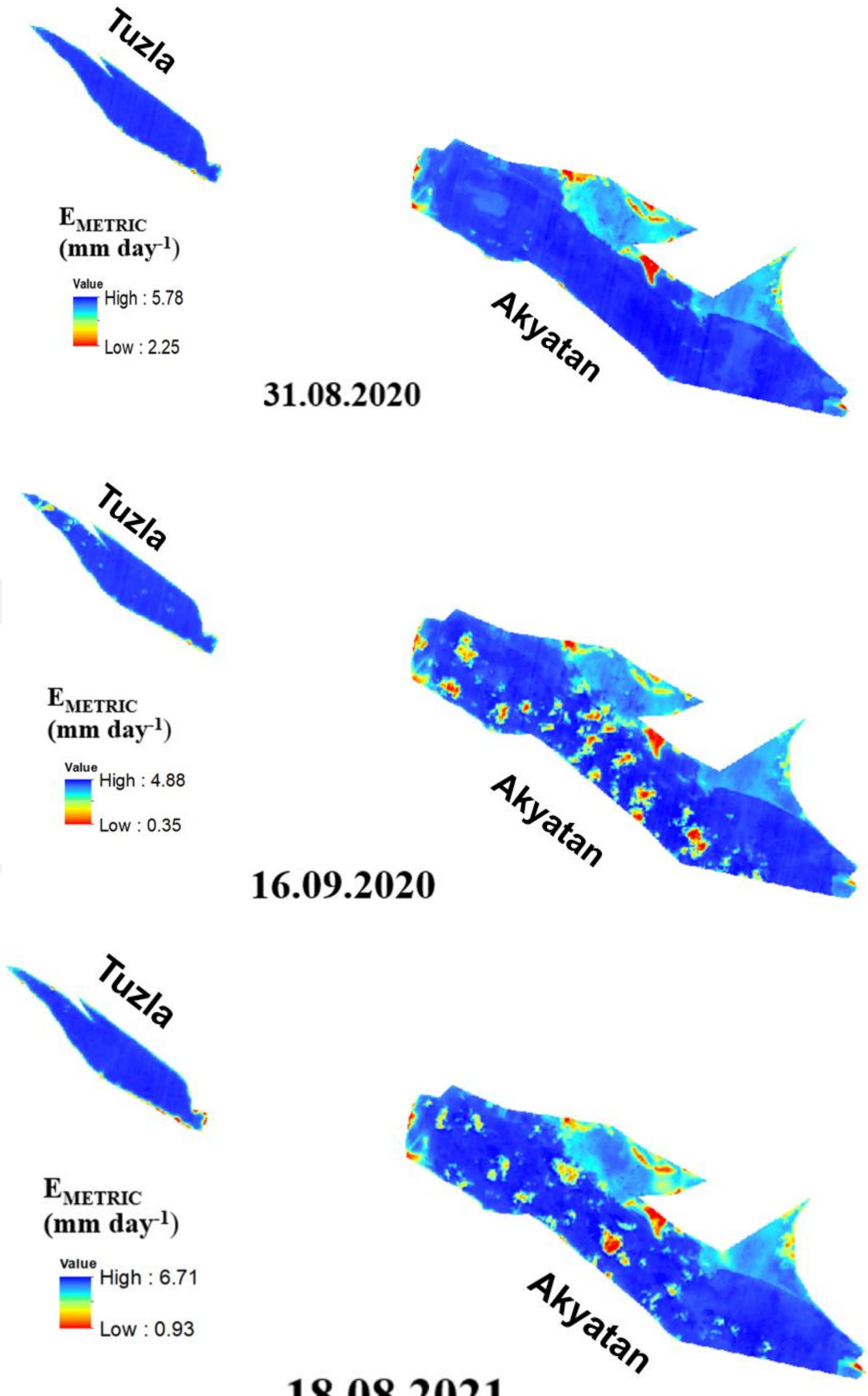
Tuzla
Akyatan
EMETRIC (mm day-1)
Value
High : 5.78
Low : 2.25
31.08.2020
Tuzla
Akyatan
EMETRIC (mm day-1)
Value
High : 4.88
Low : 0.35
16.09.2020
Tuzla
Akyatan
EMETRIC (mm day-1)
Value
High : 6.71
Low : 0.93
18.08.2021

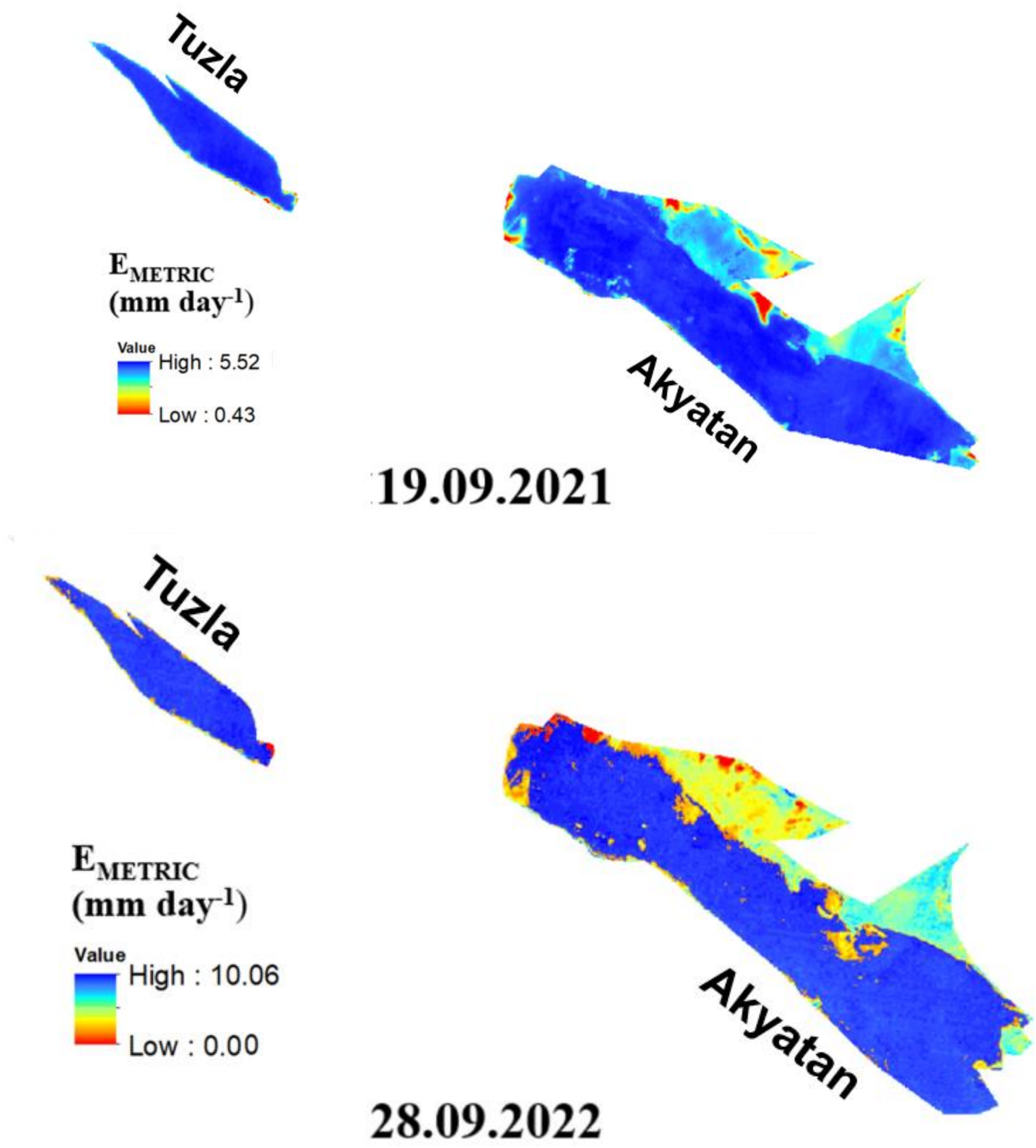

Figure 4.51. Spatial variations in the average daily evaporation (E_{METRIC}, mm day^{-1}) of lagoons near the stressed area of the LSP, as determined by the METRIC model for some dates

In this study, evaporation ($E_{METRIC,}$ stands for 'dependent variable') estimates from the METRIC model were compared to those from the Kohler-Nordenson-Fox (KNF stands for 'independent variable', E_{KNF}) model (Kohler et al., 1955), to evaluate the accuracy of the METRIC model results for lagoons (Tuzla and Akyatan) in the LSP as depicted in Figure 4.52. The results indicated strong performance of the METRIC model, as demonstrated by an RMSE value of 3.98 mm day^{-1}, MAE of 3.51 mm day^{-1}, an R^2 value of 0.49 and a Pearson correlation coefficient (r) of 0.7. This r-value indicates a good correlation between the METRIC algorithm and the KNF model.

Several studies have employed RS-ET_a models, such as METRIC and SEBAL, to estimate evaporation in various global locations. For instance, Zamani Losgedaragha and Rahimzadegan (2018) investigated evaporation from the Amirkabir dam reservoir in a semi-arid climate using SEBAL, METRIC, and SEBS models between 2011 and 2017. They utilized 16 satellite images from Landsat TM5 and OLI as input data, with pan evaporation measurements, considered ground truth data, taken from instruments on the reservoir bank. Their results showed that the METRIC and SEBS models performed relatively well compared to pan evaporation measurements. The METRIC and SEBS models achieved RMSE values of 2.02 mm day^{-1} and 0.62 mm day^{-1}, respectively, with corresponding R^2 values of 0.57 and 0.93. In contrast, the SEBAL model was less reliable for freshwater evaporation, with an R^2 of 0.36 and an RMSE of 5.1 mm day^{-1}. This study represents the first attempt to estimate evaporation from saline lagoons in the Lower Seyhan Plain (LSP) during satellite overpass times, potentially capturing spatiotemporal variations in evaporation. Despite some limitations, such as relatively high error, the proposed equation in Figure 4.52 can be applied to similar saline lagoons in Mediterranean or semi-arid areas. Using the KNF approach, this equation offers a simpler alternative to the more complex METRIC models, which require extensive input data and advanced expertise in remote sensing-based ET_a models. The equation's potential for broader application makes it an effective tool for estimating evaporation from lakes and lagoons, particularly for researchers and water resource managers who may lack access to sophisticated modeling techniques.

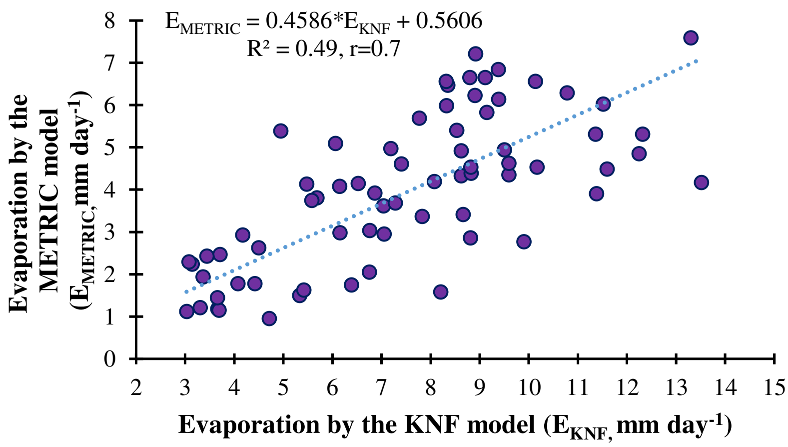

Figure 4.52. Linear relationship between evaporation estimates from the METRIC approach and the KNF model during satellite image overpass dates over lagoons in the stressed region of the LSP

4.10. Assessing the relationship between leaf area index (LAI) and NDVI by the METRIC model for some crop types over the AID

The Leaf Area Index (LAI) is a crucial crop development and growth indicator. The METRIC model, which uses Landsat data, was applied to monitor LAI across different crop types. This approach allows for rapid estimation of LAI for different crops over large areas with a high spatial resolution (30 m x 30 m). Using the R-METRIC model, LAI was computed from the top-of-atmosphere (at-satellite) surface reflectance data (Bastiaanssen, 1998) for various crops within the AID region. For example, during the 2021 water year, LAI was estimated for crops including wheat, first and second types of corn, cotton, soybean, and peanut during satellite overpasses in the AID. Additionally, NDVI values were estimated for the same crops during the 2020-2023 water years. This study explored the relationship between the average Leaf Area Index (LAI) and the average Normalized Difference Vegetation Index (NDVI) for these crops during satellite overpasses across the Akarsu Irrigation District (AID). Figure 4.53 illustrates the spatial distribution of LAI and NDVI over the AID on several days during the summer of 2021. It is evident from Figure 4.53 that LAI values varied consistently with crop type over time.

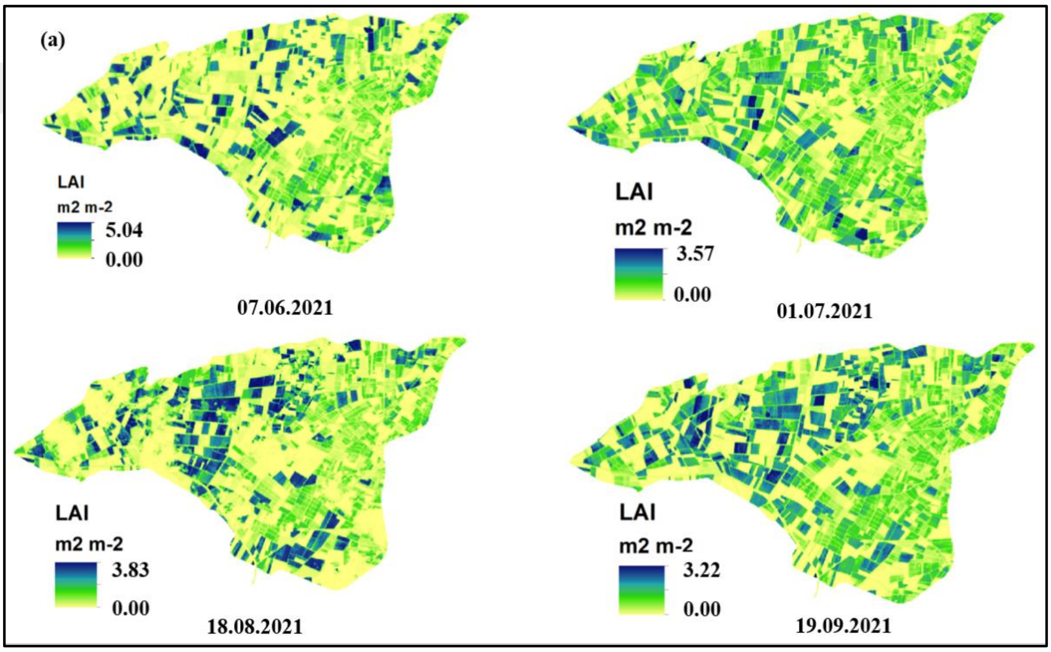

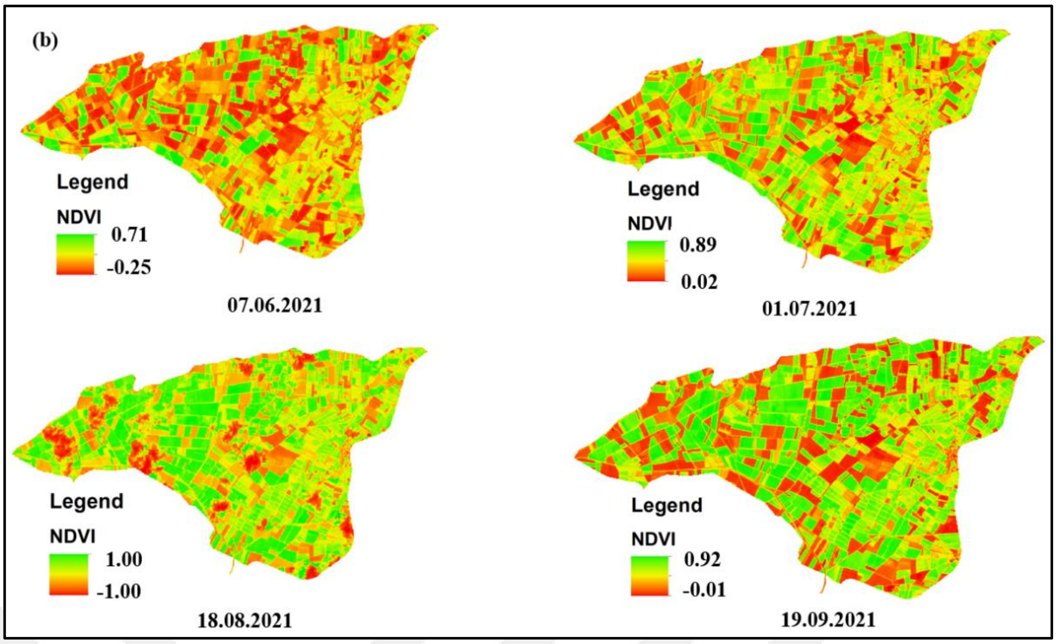

Figure 4.53. Spatial distribution of (a) LAI and (b) NDVI values using the METRIC model over the AID for several days during the summer of 2021. LAI is expressed in units of m² m⁻²

Figure 4.54 illustrates the temporal variation of mean LAI and NDVI for the first and second crop types of corn, cotton, soybean, peanut, and wheat. As observed in Figure the behavior of the first and second crops of cotton, soybean, and peanut appears nearly identical, with differences in mean LAI and NDVI values over time compared to the behavior of the first and second types of corn. The mean LAI and NDVI patterns for wheat crops are similar, showing an initial increase during the early growth stages, peaking in the middle, and then decreasing at harvest. For corn-I, mean LAI values initially rise from 0.49 m^2 m^{-2} to a peak of 3.54 m^2 m^{-2} on DOY 190 (09.07.2021) and then sharply decline to 0.18 m^2 m^{-2} on DOY 230 (18.08.2021). Mean NDVI values for corn-I also increase from 0.42 to a peak of 0.75, followed by a decline to 0.37. Corn-II shows mean LAI values rising from 0.19 m^2 m^{-2} to a peak of 1.84 m^2 m^{-2} and then dropping to 0.10 m^2 m^{-2}. NDVI values for corn-II increase from 0.39 to a peak of 0.74, then gradually decline to 0.22. The observed changes in NDVI values for the second crop type of corn can be attributed to variations in crop growth stages. During the initial stages, the mean NDVI increased, reaching its peak during the mid-growth stages. Subsequently, these values declined, approaching around 0.20 at harvest time, corresponding to bare soil conditions. For cotton-I, mean LAI values steadily rise from 0.20 m^2 m^{-2} to a peak of 3.82 m^2 m^{-2}, then decrease to 2.29 m^2 m^{-2}. Mean NDVI values increase from 0.29 to 0.80, with minor fluctuations. Cotton-II shows mean LAI values increasing from 0.10 m^2 m^{-2} to a peak of 2.90 m^2 m^{-2}, then dropping to 1.95 m^2 m^{-2}. NDVI values for cotton-II trend upward from 0.33 to a peak of 0.79, then slightly decline to 0.68. For soybean-I, mean LAI values rise from 0.93 m^2 m^{-2} to a peak of 3.78 m^2 m^{-2}, then decrease to 1.70 m^2 m^{-2}. NDVI values for soybean-I show a steady increase from 0.42 to 0.80, then slightly decline to 0.71. Similarly, soybean-II mean LAI values gradually increase to 1.37m^2 m^{-2} on day 18.08.2021, then significantly drop to 0.08 m^2 m^{-2}. NDVI values for soybean-

II increase from the lowest value of 0.27 to the highest peak value of 0.76 and stabilize. On the other hand, for peanut-I, mean LAI values increase from 0.16 to a peak of 3.87, then drop to 1.89. The mean NDVI values for peanut-I steadily increased from 0.27 to a peak of 0.82, followed by a slight decline during the crop's senescence stage. This decline is due to reduced leaf chlorophyll content, which lowers photosynthetic activity and gradually decreases vegetation health, typically observed in the later growth and maturation phases. Peanut-II shows mean LAI values increasing from 0.11 m^2 m^{-2} to a peak of 2.02 m^2 m^{-2}, then decreasing to 1.25 m^2 m^{-2}. NDVI values for peanut-II rise from 0.30 to a peak of 0.78, then decline to 0.54. The mean LAI values for wheat increase from 0.12 m^2 m^{-2} to a peak of 2.88 m^2 m^{-2}, then decrease to 0.03 m^2 m^{-2} at the harvest stage. NDVI values for wheat follow a similar pattern, rising from 0.27 to a peak of 0.86 and then decreasing to 0.21.

Figure 4.55 illustrates the relationship between mean LAI and mean NDVI for the first and second crop types of corn, cotton, soybean, peanut, and wheat, based on the R-METRIC model during the satellite overpass of the study area in 2021. The mean LAI positively correlated with the mean NDVI, as indicated by Pearson's correlation coefficient (r), across various crop types throughout the growing season (Figure 4.55). The analysis revealed that the exponential model ($y = ae^{bx}$)) was suitable for describing the relationship between mean NDVI and mean LAI for various crop types over the AID. In this model, LAI from different crops was represented as a dependent variable, while NDVI was defined as an independent variable. Both correlation and regression analyses were conducted, with the correlation analysis revealing a strong relationship between the mean NDVI and the mean LAI, as evidenced by correlation coefficients (r) ranging from 0.85 to 0.99. Furthermore, the regression analysis developed a model to predict LAI from NDVI, reinforcing the strength of their relationship. This relationship was observed across various crops, including the first and second crops of corn, cotton, soybean, peanut, and wheat. This indicates a robust relationship between the two variables, underscoring the effectiveness of NDVI as a predictor of LAI for various crop types. All crops followed a typical pattern of increasing LAI and NDVI values from the early to mid-growing season, peaking when the crops reached full growth and then declining as the plants matured and senesced. These findings are valuable for monitoring crop health and growth stages using satellite data. Understanding the temporal variations in LAI and NDVI can support agricultural management decisions, such as scheduling irrigation, optimizing fertilization, and predicting yield. Additionally, the proposed equations relating mean NDVI to mean LAI can be applied to each crop type in the study area and potentially in the broader Mediterranean region of the world.

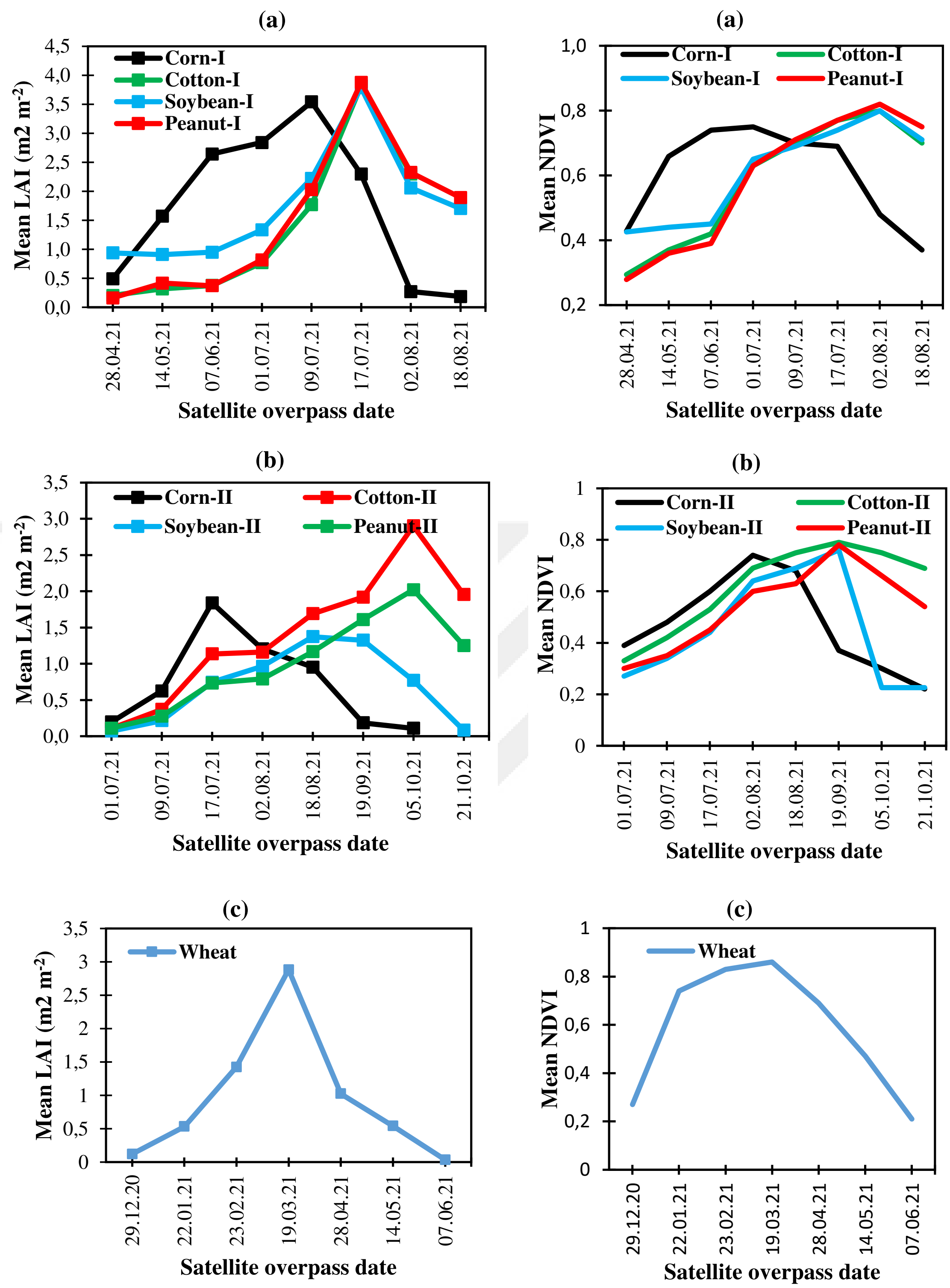

Figure 4.54. Temporal Variations in average Leaf Area Index (LAI) and Normalized Difference Vegetation Index (NDVI) values for various crop types: (a) corn-I, cotton-I, soybean-I, and peanut-I; (b) corn-II, cotton-II, soybean-II, and peanut-II; (c) wheat; across the Akarsu Irrigation District (AID) during satellite overpasses

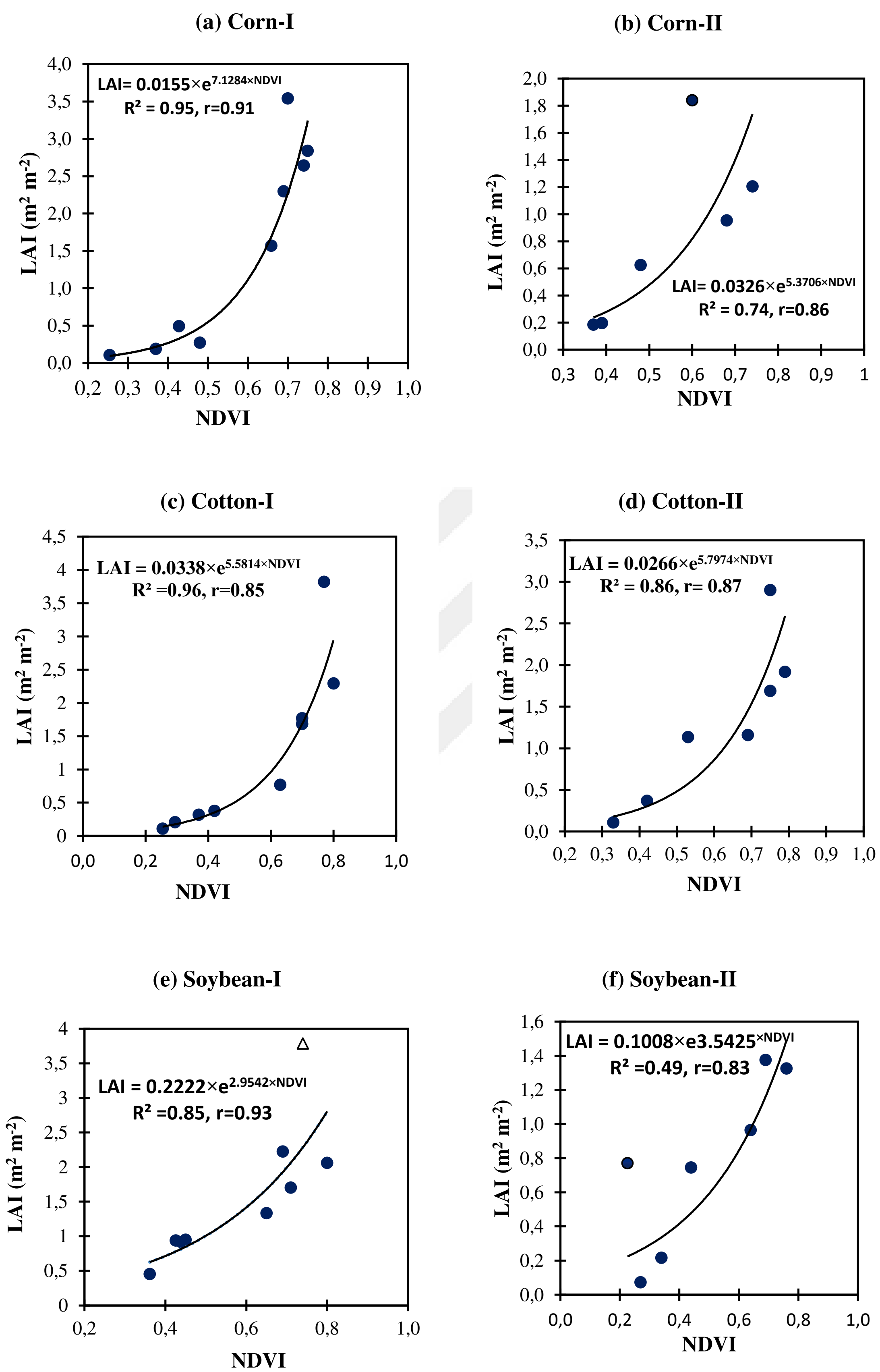
(a) Corn-I
LAI= 0.0155×e7.1284×NDVI
R² = 0.95, r=0.91
LAI (m² m⁻²)
NDVI
(b) Corn-II
LAI= 0.0326×e5.3706×NDVI
R² = 0.74, r=0.86
LAI (m² m⁻²)
NDVI
(c) Cotton-I
LAI = 0.0338×e5.5814×NDVI
R² =0.96, r=0.85
LAI (m² m⁻²)
NDVI
(d) Cotton-II
LAI = 0.0266×e5.7974×NDVI
R² = 0.86, r= 0.87
LAI (m² m⁻²)
NDVI
(e) Soybean-I
LAI = 0.2222×e2.9542×NDVI
R² =0.85, r=0.93
LAI (m² m⁻²)
NDVI
(f) Soybean-II
LAI = 0.1008×e3.5425×NDVI
R² =0.49, r=0.83
LAI (m² m⁻²)
NDVI

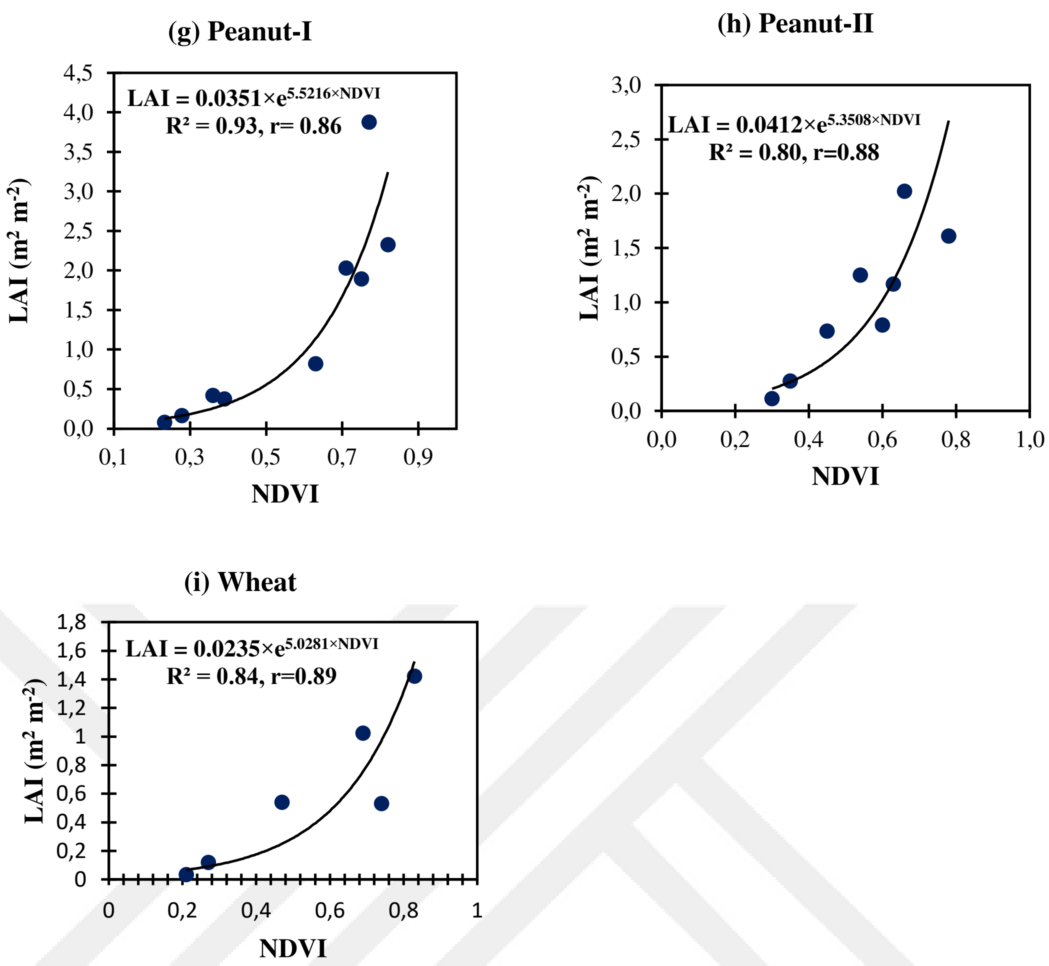

Figure 4.55. Exponential models between average NDVI and average LAI for various crop types: (a) Corn-I, (b) Corn-II, (c) Cotton-I, (d) Cotton-II, (e) Soybean-I, (f) Soybean-II, (g) Peanut-I, (h) Peanut-II, and (i) Wheat, in the Akarsu Irrigation District (AID) during satellite overpasses. Data excluded from calculations, indicated by Δ symbol, were identified as outliers through box plot analysis

The ANOVA test was utilized to assess the statistical significance of the relationship between the Normalized Difference Vegetation Index (NDVI) and the Leaf Area Index (LAI) across various crop types. The results from this analysis, as presented in Table 4.18, revealed a significant correlation between NDVI and LAI, thereby establishing NDVI as a reliable metric for evaluating plant health and canopy characteristics. The analysis yielded an F-statistic of **32.50** for corn-I with a p-value of 0.0007, indicating that the exponential model is highly significant at the 0.05 level. The coefficient of determination (R^2) was 0.823, meaning that the NDVI explained 82.3% of the variance in the LAI. This demonstrates a strong predictive relationship between NDVI and LAI for corn-I. The F-statistic assesses whether the overall exponential model better fits the data than a model with no predictors (null model). Combining a high F-value and a low p-value ($p < 0.05$) strongly rejects the null hypothesis that NDVI does not explain LAI. This outcome emphasizes the reliability of NDVI as a robust indicator for estimating LAI in corn. The additional analyses assessed the relationship between NDVI and LAI for various crops using exponential models, as indicated by their respective F-statistics. For cotton, the study revealed F-Statistics of **18.92** for cotton-I and **15.42** for cotton-II, indicating statistically significant exponential models. Similarly, for soybeans, F-Statistics of **39.63** for soybean-I and **64.47** for soybean-II highlight strong model fits. For peanuts, F-Statistics of **20.19** for peanut-I and **19.73** for peanut-II demonstrate significant relationships between NDVI and LAI. For wheat, the model yielded an F-Statistic of **8.30**, signifying a meaningful association. The F-Statistics highlight the overall explanatory power of the regression models, demonstrating that NDVI is a reliable predictor of LAI across various crops. The substantial R-squared values further validate NDVI's effectiveness in capturing the variance in LAI for these crops. These results emphasize the importance of NDVI as a valuable tool for monitoring crop health, offering critical insights for precision agriculture practices. By integrating NDVI into management strategies, agricultural stakeholders can make data-driven decisions regarding irrigation, pest control, and overall crop management, ultimately improving productivity and sustainability.

Table 4.18. Regression analysis summary (ANOVA; Regression, Residual) for the relationship between NDVI and LAI across various crop types: (a) Corn-I, (b) Corn-II, (c) Cotton-I, (d) Cotton-II, (e) Soybean-I, (f) Soybean-II, (g) Peanut-I, (h) Peanut-II, and (i) Wheat

(a) Corn-I

Regression Statistics	
Multiple R	0.907072
R Square	0.822779
Adjusted R Square	0.797462
Standard Error	0.596825
Observations	9

ANOVA

	df	SS	MS	F	Significance F
Regression	1	11.57603	11.57603	32.49871	0.000735
Residual	7	2.493398	0.3562		
Total	8	14.06943			

	Coefficients	Standard Error	t Stat	P-value	Lower 95%	Upper 95%	Lower 95.0%	Upper 95.0%
Intercept	-2.15275	0.679243	-3.16934	0.015722	-3.75891	-0.5466	-3.75891	-0.5466
X Variable 1	6.570787	1.152615	5.700764	0.000735	3.845285	9.296289	3.845285	9.296289

(b) Corn-II

Regression Statistics	
Multiple R	0.753846
R Square	0.568284
Adjusted R Square	0.460355
Standard Error	0.46833
Observations	6

ANOVA

	df	SS	MS	F	Significance F
Regression	1	1.154867	1.154867	5.265353	0.083430
Residual	4	0.877333	0.219333		

Total	5	2.032200						
	Coefficients	Standard Error	t Stat	P-value	Lower 95%	Upper 95%	Lower 95.0%	Upper 95.0%
Intercept	-0.864440	0.764632	-1.130532	0.321446	-2.987399	1.258518	-2.987399	1.258518
X Variable 1	3.126654	1.362593	2.294636	0.083430	-0.656510	6.909817	-0.656510	6.909817

(c) Cotton-I	
Regression Statistics	
Multiple R	0.854383
R Square	0.72997
Adjusted R Square	0.691394
Standard Error	0.691736
Observations	9

ANOVA					
	df	SS	MS	F	Significance F
Regression	1	9.054632	9.054632	18.92301	0.003355
Residual	7	3.349489	0.478498		
Total	8	12.40412			

	Coefficients	Standard Error	t Stat	P-value	Lower 95%	Upper 95%	Lower 95.0%	Upper 95.0%
Intercept	-1.47277	0.66943	-2.2000	0.0637	-3.05574	0.110195	-3.0557	0.110195
X Variable 1	4.98275	1.14544	4.3501	0.0033	2.2742	7.69129	2.2742	7.69129

(d) Cotton-II	
Regression Statistics	
Multiple R	0.869003
R Square	0.755167
Adjusted R Square	0.7062
Standard Error	0.515658
Observations	7

ANOVA					
	df	SS	MS	F	Significance F
Regression	1	4.100778	4.1007	15.42206	0.011103
Residual	5	1.329517	0.2659		
Total	6	5.430295			

	Coefficients	Standard Error	t Stat	P-value	Lower 95%	Upper 95%	Lower 95.0%	Upper 95.0%
Intercept	-1.43671	0.7301	-1.967	0.1062	-3.3136	0.4402	-3.31367	0.44024
X Variable 1	4.540	1.156	3.927	0.0111	1.569	7.513	1.568	7.513

(e) Soybean-I	
Regression Statistics	
Multiple R	0.931944
R Square	0.868519
Adjusted R Square	0.846605
Standard Error	0.064337
Observations	8

ANOVA					
	df	SS	MS	F	Significance F
Regression	1	0.16405	0.164054	39.63391	0.000748

Residual	6	0.02483	0.004139		
Total	7	0.18889			

	Coefficients	Standard Error	t Stat	P-value	Lower 95%	Upper 95%	Lower 95.0%	Upper 95.0%
Intercept	0.2408	0.0564	4.2683	0.0052	0.1027	0.3788	0.1027	0.3788
X Variable 1	0.246005	0.03907	6.2955	0.0007	0.1503	0.3416	0.1503	0.3416

(f) Soybean-II

Regression Statistics	
Multiple R	0.832442
R Square	0.692959
Adjusted R Square	0.631551
Standard Error	0.130664
Observations	7

ANOVA					
	df	SS	MS	F	Significance F
Regression	1	0.19266	0.19266	11.284	0.0201
Residual	5	0.085366	0.017073		
Total	6	0.278028			

	Coefficients	Standard Error	t Stat	P-value	Lower 95%	Upper 95%	Lower 95.0%	Upper 95.0%
Intercept	0.201133	0.09680	2.0776	0.0923	-0.04771	0.4499	-0.0477	0.44998
X Variable 1	0.358022	0.10657	3.3592	0.0201	0.0840	0.6319	0.0840	0.6319

(g) Peanut-I

Regression Statistics	
Multiple R	0.86169
R Square	0.74251
Adjusted R Square	0.70573
Standard Error	0.12568
Observations	9

ANOVA					
	df	SS	MS	F	Significance F
Regression	1	0.318875	0.318875	20.18646	0.002822
Residual	7	0.110575	0.0157		
Total	8	0.42945			

	Coefficients	Standard Error	t Stat	P-value	Lower 95%	Upper 95%	Lower 95.0%	Upper 95.0%
Intercept	0.3422	0.0622	5.5009	0.0009	0.1951	0.4894	0.1951	0.4894
X Variable 1	0.155356	0.034578	4.492934	0.0028	0.073592	0.2371	0.0735	0.2371

(h) Peanut-II

Regression Statistics	
Multiple R	0.875655
R Square	0.766772
Adjusted R Square	0.7279
Standard Error	0.084913
Observations	8

ANOVA					

	df	SS	MS	F	Significance F
Regression	1	0.142227	0.142227	19.72586	0.004369
Residual	6	0.043261	0.00721		
Total	7	0.185488			

	Coefficients	Standard Error	t Stat	P-value	Lower 95%	Upper 95%	Lower 95.0%	Upper 95.0%
Intercept	0.3195	0.057	5.531	0.0014	0.1781	0.4608	0.1781	0.4608
X Variable 1	0.2202	0.049	4.441	0.00436	0.09890	0.3415	0.0989	0.3415

(i) Wheat	
Regression Statistics	
Multiple R	0.790033
R Square	0.624152
Adjusted R Square	0.548983
Standard Error	0.661844
Observations	7

ANOVA					
	df	SS	MS	F	Significance F
Regression	1	3.637133	3.63713	8.30326	0.034526
Residual	5	2.190185	0.43803		
Total	6	5.827317			

	Coefficients	Standard Error	t Stat	P-value	Lower 95%	Upper 95%	Lower 95.0%	Upper 95.0%
Intercept	-0.76731	0.64194	-1.195	0.2856	-2.4175	0.8829	-2.41747	0.882851
X Variable 1	2.929933	1.0168	2.882	0.0343	0.3162	5.5439	0.31618	5.543688

Several literature reviews have evaluated the use of the METRIC algorithm for estimating ET_a, LAI, and Ts. For example, Reyes-González et al. (2019) utilized Landsat data (path 29, row 29) with the METRIC model. They conducted in-situ measurements to estimate ET_a, LAI, and Ts for corn in eastern South Dakota, USA, during the 2016 growing season at the satellite overpass time. ET_a was computed using an atmometer, K_c, LAI was measured using the AccuPAR model Lp-80 PAR/LAI Ceptometer, and Ts was measured with an Extech infrared thermometer model 42530. Their results strongly agreed with METRIC model estimates and in-situ measurements for LAI, Ts, and ET_a, with R^2 values of 0.76, 0.87, and 0.89, respectively. This confirmed that the METRIC model is a valuable tool for estimating ET_a, LAI, and Ts at a field scale with high resolution. Additionally, Alsenjar et al. (2022) and Cetin et al. (2023a) applied the R-METRIC model to compute ET_a, crop water stress index (CWSI), and LAI for wheat, lettuce, and potato crops over the AID in the winter of 2021. The results demonstrated a strong correlation between CWSI and LAI for wheat (r = 0.95) and lettuce (r = 0.99), while a moderate correlation was observed for potatoes (r = 0.44) during the winter season of 2021. This relationship can be used to compute CWSI, LAI, and NDVI for different crop types using RS data when the satellite overpasses the study area, offering an advantage over the IRT procedure and in-situ measurements, which are limited to a point scale. The proposed equations derived from the relationship between mean NDVI and LAI can be widely used to assess vegetation cover and calculate the Leaf Area Index (LAI) without relying on the METRIC model, which typically demands more inputs and specialized expertise. By determining the NDVI and applying these equations, LAI can be readily estimated for various plant types across large-scale irrigation areas, even under varying vegetation cover conditions. This method offers a more straightforward approach for large-scale agricultural assessments, streamlining LAI estimation across different crop types. In general, it can be concluded that the METRIC algorithm is a valuable tool for estimating ET_a and generating by-products such as LAI, NDVI, Ts, etc., which are time-consuming, costly, and labour-intensive to acquire using traditional methods at a field scale in arid and semi-arid regions. High-resolution LAI and NDVI maps are essential for understanding crop conditions under non-water-stressed and water-stressed scenarios.

5. CONCLUSIONS AND RECOMMENDATIONS

Evapotranspiration (ET) is a critical water cycle component, especially following precipitation. Accurate estimation of actual evapotranspiration (ET_a) is vital, especially given the impacts of climate change and the increasing demands of agricultural practices in semi-arid and arid regions, such as Türkiye's Lower Seyhan Plain (LSP). This study aims to compute ET_a using various models—METRIC, EEFlux-METRIC, SEBAL, and GeeSEBAL—along with the $K_{\text{-NDVI}}$ method. These models employ Landsat data combined with both local and global climatic data. The analysis focuses on two specific regions within the LSP: a non-stressed area and a stressed area near saline lagoons, covering 2020 to 2023. In this study, 70 Landsat satellite images, i.e., all potentially available images, were utilized to encompass the study area over the specified periods. Additionally, in-situ meteorological data were collected from local meteorological stations, and field surveys were conducted to identify crop types, serving as ground truth data. Reference evapotranspiration (ET_o) calculated by the FAO-PM method and crop evapotranspiration (ET_c) were used as benchmarks to compare against the estimated ET_a derived from remote sensing (RS) data. In this thesis, the conclusions and recommendations are presented as follows:

5.1. Conclusions to cropping pattern

The field visit data closely matched the crop classification maps generated using the Artificial Neural Network (ANN) approach, particularly regarding overall accuracy across the Lower Seyhan Plain's Akarsu Irrigation District (AID). For instance, during the 2021 water year, crops such as lettuce, potato, sesame-II, palm, and watermelon achieved 100% classification accuracy, while onion and wheat surpassed 90%. Other crops, including citrus, cotton (first and second crops), soybean, peanut, and corn, showed accuracies exceeding 77%, with fruits displaying lower accuracy, likely due to the similarity in shape between fruit orchards and citrus trees or their overlapping coverage features. The classified crop maps for 2020-2023 were consistent with the post-processed outcomes from the ANN model applied through ENVI software. This supervised classification model proved highly reliable, achieving more than 90% accuracy in crop classification across the AID during the study period. Additionally, the incorporation of ground truth data from stressed areas provided critical insights into crop stress levels and rising groundwater, which had not been studied before. This significantly contributed to the research, offering a deeper understanding of the results and adding value to the overall study.

The use of the ANN algorithm for crop classification with high-resolution satellite data, such as Sentinel-2, demonstrated high accuracy, especially in non-stressed regions. This methodology holds excellent potential for broader applications in stressed and non-stressed areas of the Lower Seyhan Plain and other agricultural regions worldwide. Integrating satellite data with field observations has proven to be a robust method for crop classification, making it a promising tool for global agricultural monitoring and management. Additionally, Unmanned Aerial Vehicle (UAV) data could be integrated to provide even higher-resolution imagery, enhancing crop classification and improving the management of stressed areas, leading to better decision-making in water resource management and crop health assessment. Expanding this approach globally could benefit agricultural systems facing environmental challenges and support sustainable farming practices.

5.2. Conclusions on ET_a estimations by the SEB models, $K_{c\text{-}NDVI}$ and the "two-step" approach

The results revealed a strong correlation between actual evapotranspiration (ET_a) estimated using the METRIC model and reference evapotranspiration (ET_o) from the FAO-PM model in both non-stressed areas (NSA), the Akarsu Irrigation District (AID), and stressed areas (SA) of the Lower Seyhan Plain on satellite overpass dates. The results demonstrated a good agreement between the METRIC and SEBAL models with the "two-step" ET_c method for 2020 to 2023 in the non-stressed area. Discrepancies were observed in the annual ET_a estimates between the METRIC and SEBAL models compared to the ET_c method. This variation arises because the ET_c method utilizes reference K_c values representing standard crop conditions, whereas the RS-based ET_a models account for the actual conditions in the field. The EEFlux-METRIC and GeeSEBAL models have limitations related to repairing the scanline errors, especially for Landsat 7, compared to standard models, i.e., METRIC and SEBAL, that can correct these errors before running the models. However, the ET_a values obtained from the EEFlux-METRIC and GeeSEBAL models can be used as reference ET_a, especially in the absence of local climatic data. The equations presented in this thesis for estimating ET_a, which utilizes the EEFlux and METRIC models alongside ET_o from the FAO-PM in the AID and stressed areas, provide a viable alternative to using the METRIC model. Nevertheless, adopting this approach requires specialized knowledge in handling specific input data and proficiency with the EEFlux platform, which depends on global datasets. Future applications should consider these requirements to effectively implement and benefit from the proposed methods.

Statistical evaluations of ET_a revealed a strong agreement between the METRIC, SEBAL, and $K_{c\text{-}NDVI}$ methods with ET_c for various crop types, including first and second crops of cotton, corn, soybean, peanut, as well as wheat, and citrus. However, the $K_{c\text{-}NDVI}$ method showed better alignment with the ET_c method during the middle growth stages of crops compared to the initial and harvesting stages. The proposed $K_{c\text{-}NDVI}$ equations, derived from the relationship between reference K_c and NDVI for certain crops, can be generalized by researchers and stakeholders. This method offers a modified approach for estimating ET_a, compared to the ET_c method, in this region and similar areas within the Mediterranean regions worldwide.

5.3. Evaluation and recommendations for ET_a estimation tools

In the estimation of ET_a, two versions of the water package in R were compared: a basic version and an advanced version. The basic version is suitable for flat terrains, while the advanced version incorporates a Digital Elevation Model (DEM) to account for slope and corrections in high-terrain areas. For the study area, results from both versions were similar when applied to flat terrains for the years 2020-2023. Further comparisons were made between the advanced version of the water package in R and the LandMOD ET mapper toolbox in MATLAB, focusing on specific dates: September 9, 2021 (DOY 190) and October 21, 2021 (DOY 294). These comparisons showed nearly identical results between the two toolboxes. However, the LandMOD ET mapper toolbox in MATLAB offers several advantages over the R-METRIC model, including a) the ability to import various types of Landsat data, including data from Landsat 9 and UAVs, b) the capability to estimate ET_a by running both the SEBAL and METRIC models within a single function, and c) support for using both Landsat and MODIS data for ET_a estimation. In contrast, the R-METRIC model is restricted to using Landsat 7 and 8 data and is specifically designed for estimating ETa using the METRIC model. Moreover, it does not support Landsat 9 data, launched on September 27, 2021. As a result, the model is constrained to estimating ETa at the standard 16-day interval due to its reliance solely on Landsat 7 and 8 data rather than achieving an 8-day interval. In general, these tools provide robust capabilities for ET_a estimation in research and practical applications despite differences in data handling approaches.

In the estimation of ET_a using the METRIC model, two versions of the water package in R were evaluated: a basic version designed for flat terrains and an advanced version incorporating a Digital Elevation Model (DEM) for slope and terrain corrections. For the study area, both versions produced similar results for flat terrains from 2020 to 2023. Additional comparisons between the advanced R package and the LandMOD ET mapper toolbox in MATLAB, conducted for specific dates (September 9, 2021, and October 21, 2021), revealed nearly identical outcomes. However, the LandMOD toolbox offers several advantages over the R-METRIC model, including (a) the ability to import a broader range of Landsat data, including Landsat 9 and UAV data, (b) the functionality to estimate ET_a using both SEBAL and METRIC models within a single function, and (c) support for both Landsat and MODIS data for ET_a estimation. In contrast, the R-METRIC model is restricted to Landsat 7 and 8 data and only supports the METRIC model. This limitation is particularly relevant as Landsat 9, launched on 27 September 2021, is incompatible with the R-METRIC model. Despite these differences, both tools offer strong capabilities for ET_a estimation in both research and practical applications. Researchers and engineers should consider using the LandMOD ET mapper toolbox for projects requiring the integration of diverse Landsat datasets (including Landsat 9 and UAVs) and using both SEBAL and METRIC models. The R-METRIC model remains viable for studies limited to Landsat 7 and 8 data and those focused solely on the METRIC model. Both tools are adequate for ET_a estimation, but the choice of tool should align with the project's specific data requirements and modeling needs.

5.4. Conclusions on ET_a estimation for various crops and evaporation from saline lagoons using the METRIC method at satellite image acquisition dates

The METRIC model's mean ET_a estimates for the citrus orchard in the Cotlu field closely corresponded to those for the entire citrus-growing area within the AID. With strong agreement ($r = 0.93$, $R^2 = 0.86$, RMSE = 0.541 mm day^{-1} during satellite overpasses), the model demonstrates its accuracy and reliability in estimating ET_a for more significant citrus regions. The METRIC model was applied to the citrus field in Cotlu village within the AID, near the Cotlu meteorological station**.** Thus, the proposed equation ($ET_{a\text{-METRIC-AID}} = 0.8615 \times ET_{a\text{-METRIC-Cotlu}} + 0.2662$) provides a practical approach for estimating ET_a for all citrus crops across the AID once the ET_a for citrus in the Cotlu field has been determined through researchers using the METRIC model. This method provides researchers and stakeholders with a reliable tool for calculating ET_a for citrus crops across the Lower Seyhan Plain, even under diverse conditions. By applying the METRIC model to the Cotlu field, this equation allows for accurate ET_a estimation over larger areas, thereby improving water management strategies and supporting better agricultural decision-making in the region.

The METRIC model demonstrated its effectiveness in estimating ET_a for mixed intercropping systems commonly practiced in citrus plantations in the Lower Seyhan Plain (LSP). Intercropping combinations, such as saplings with watermelon or cabbage, exhibited higher ET_a than orchards consisting solely of saplings during the same period. This finding underscores the model’s ability to capture the complexities of intercropping, offering more precise water use assessments. Researchers and stakeholders can leverage the METRIC model to monitor intercropping practices in citrus orchards and other mixed-crop systems, improving water resource management and promoting sustainable agricultural practices.

The comparison of ET_a values from the METRIC and SEBAL (via PySEBAL in Python) models with lysimeter measurements for soybean-II demonstrates that the METRIC model outperforms PySEBAL in accurately estimating ET_a. This highlights the METRIC model as a preferred method for ET_a estimation and its validation against ground-based measurements. Researchers should consider the METRIC model for field-level studies that require validation against lysimeters or other in-situ measurements.

In stressed areas of the Lower Seyhan Plain (LSP), the METRIC model consistently produced lower ET_a values than non-stressed areas for crops such as corn, cotton, soybean, peanut, citrus, and wheat. It is recommended that the METRIC model be included in agricultural monitoring across both stressed and non-stressed areas to optimize irrigation strategies and improve crop health evaluation. This approach allows for timely interventions, ensuring more efficient water resource management.

The METRIC model effectively estimated evaporation from saline lagoons and actual evapotranspiration (ET_a) from nearby pasture and agricultural fields during satellite overpasses, capturing substantial spatiotemporal variations often missed by traditional methods. These findings highlight the model's suitability for areas with complex land use and environmental conditions, where accurate detection of spatial variations in ET_a and evaporation is essential for optimizing water management. The model is highly recommended for researchers studying large-scale water dynamics and stakeholders responsible for planning irrigation systems.

Additionally, the METRIC model can determine the NDVI and LAI for crops. An exponential model between average NDVI and average LAI was established to assess the relationship for certain crops over the AID. The study established exponential models between average NDVI and LAI for specific crops in the AID, which can be applied and generalized in similar agricultural settings. Researchers and practitioners should incorporate these equations into crop monitoring systems, providing a practical method for estimating crop health and water use. This approach can enhance precision agriculture techniques, particularly for optimizing irrigation schedules and improving crop yield forecasting.

Applying RS-based ET_a models and the $K_{c\text{-}NDVI}$ method showed good agreement with ET_o from the FAO-PM and ET_c methods across the study area. For large areas, RS-based ET_a models such as METRIC and SEBAL are practical tools for computing ET_a for different crop types at various growth stages with high spatial resolution in flat terrain areas of semi-arid regions. Maps of ET_a derived from RS-based systems like METRIC, SEBAL, and $K_{c\text{-}NDVI}$ can be used as inputs for daily, monthly, and seasonal models. These models support agricultural water management, reservoir operations, groundwater management, water balance assessments, hydrological modeling, and irrigation planning for large-scale irrigation schemes. Moreover, compared to traditional point-scale methods, estimating LAI and NDVI can be valuable indicators for monitoring crop vegetation and health conditions. Remote sensing techniques do not directly measure ET_a but infer it through surface energy balance calculations or vegetation indices. These methods are highly effective for assessing ET_a over large areas and capturing spatial variations, particularly when using thermally driven surface energy balance techniques. Satellite-based actual evapotranspiration (ET_a) estimations, such as those derived from the METRIC model, can generate crop coefficient (K_c) curves and ET_a for various scenarios. These include new crop types, different geographic areas, new planting schedules, and regions experiencing water stress.

To improve the practical implementation of this study, specific steps can be outlined for applying the recommendations. These include integrating the proposed methods into existing agricultural monitoring systems, such as incorporating satellite-based ET_a models into local irrigation management practices. Training local stakeholders, including farmers and water resource managers, on how to use these models to optimize water use and crop management will further enhance efficiency. The $K_{c\text{-}NDVI}$ approach should be adapted to region-specific crop types, growth stages, and climatic conditions, with local calibration data collected to increase accuracy. Furthermore, establishing regular data collection protocols (e.g., monthly satellite overpasses and updates from weather stations) along with ground-based validation methods, such as lysimeter data, can help agricultural and water managers to ensure the sustainability and reliability of ET_a estimates for decision-making procedures.

Future research should prioritize expanding the integration of UAV data into remote sensing-based ET_a models to improve spatial resolution and enhance ET_a estimates in areas with complex terrain and environmental variability. UAVs offer higher-resolution data, which can significantly refine ET_a estimations, particularly in heterogeneous landscapes where satellite data may be insufficient. Additionally, investigating hybrid approaches combining the advantages of the SEBAL and METRIC models could result in more accurate ET_a assessments under diverse conditions. This would enable a more comprehensive evaluation of ET_a, especially in regions with varying topography and climate variability, ultimately advancing precision water management strategies in agriculture and hydrology.

REFERENCES

Akça, E., Aydin, M., Kapur, S., Kume, T., Nagano, T., Watanabe, T., Çilek, A, and Zorlu, K. (2020). Catena Long-term monitoring of soil salinity in a semi-arid environment of Türkiye. *Catena*, 193(October 2019), 104614. https://doi.org/10.1016/j.catena.2020.104614.

Aksu, H., and Arikan, A. (2017). Satellite-based estimation of actual evapotranspiration in the Buyuk Menders Basin, Türkiye. *Hydrology Research*, 48 (2), 559–570. doi:10.2166/nh.2016.226.

Alghawry, A. (2018). Management of supplemental and deficit irrigatıon for wheat production under the Mediterranean climatic conditions. Ph.D. Thesis. Çukurova University Institute of Natural and Applied Science, Department of Agricultural structures and irrigation, Türkiye.

Allen, R. G., Irmak, A., Trezza, R., Hendrickx, J. M., Bastiaanssen, W. G. M, and Kjaersgaard, J. (2011). Satellite-based ET estimation in agriculture using SEBAL and METRIC. *Hydrol Process*, 25:4011–402.

Allen, R. G., Pereira, L. S., Raes, D., and Smith, M. (1998). Crop evapotranspiration- guidelines for computing crop water requirements. *FAO Irrigation and Drainage Paper 56 Rome, Italy, FAO.*

Allen, R. G., Tasumi, M., and Trezza R. (2007a). Satellite-based energy balance for mapping evapotranspiration with internalized calibration, METRIC (model). J. Irrig. Drain. Eng. 133,380–394.

Allen, R. G., Tasumi, M., Morse, A., Trezza, R., Wright, J. L., Bastiaanssen, W. G. M., Kramber, W., Lorite, I., and Robsion, C. W. (2007b). Satellite-based energy balance for Mapping Evapotranspiration with Internalized Calibration (METRIC)-Applications. *Journal of Irrigation and Drainage Engineering*, 133, pp. 395–406.

Allen, R. G., Trezza, R., Kilic, A., Tasumi, M., Hongjun, L. (2013). Sensitivity of Landsat-scale energy balance to aerodynamic variability in mountains and complex Terrain. JAWRA J Am Water ResourAssoc 49(3):592–604. https://doi.org/10.1111/jawr.1205.

Alsenjar, O., and Cetin, M. (2023). Comparison of actual evapotranspiration by the Google Earth Engine Evapotranspiration Flux (EEflux) to the METRIC model using remote sensing data and in-situ climate observations. *In The 3rd International Conference on Research of Agriculture and Food Technologies* (I-CRAFT-2023), Adana, Türkiye, 4-6 October 2023; pp. 140–145.

Alsenjar, O., Cetin, M., Aksu, H, Golpinar, Akgul, M. A and Golpinar, M. S. (2022). Estimation of crop water stress index on remote sensing and ground-based data on irrigated crops in the Mediterranean Region of Türkiye. Conference: 11. *Ulusal Hidroloji Kongresi*: Gaziantep-Türkiye.

Alsenjar, O., Cetin, M., Aksu, H., Akgul, M. A. and Golpinar M. S. (2023a). Cropping pattern classification using artificial neural networks and evapotranspiration estimation in the

Eastern Mediterranean Region of Türkiye. *Journal of Agricultural Sciences*, 29, 677-689; DOI:10.15832/ankutbd.1174645.

Alsenjar, O., Cetin, M., Aksu, H., Golpinar, M. S., and Akgul, M. A. (2023b). Actual Evapotranspiration estimation using METRIC Model and Landsat Satellite Images over an irrigated field in the Eastern Mediterranean Region of Turkey. *Mediterranean Geoscience Reviews,* 5, 35-49; DOI:10.1007/s42990-023-00099-y.

Alsenjar, O., Cetin, M., and Aksu, H. (2024). Actual evapotranspiration estimation using SEBAL through Google Earth Engine cloud integrated with Landsat satellite images and ERA5 land data In E-Proceedings of the 2nd *International Symposium on Remote Sensing in Meteorology*, METEO IRS, 11-13 June 2024, ITU Press, Istanbul, Türkiye.

Atasever, U., and Ozkan, C. (2018). A New SEBAL Approach Modified with Backtracking Search Algorithm for Actual Evapotranspiration Mapping and On-Site Application. *Journal of the Indian Society of Remote Sensing*, 46(8), 1213–1222. https://doi.org/10.1007/s12524-018-0816-9.

Bastiaanssen, W. G. M. (1995). Regionalization of surface flux densities and moisture indicators in composite terrain: a remote sensing approach under clear skies in Mediterranean climates. Ph.D. Thesis, CIP Data Koninklijke Bibliotheek, Den Haag, The Netherlands.

Bastiaanssen, W. G. M. (1998). Remote Sensing in Water Resources Management: The State of the Art. International Water Managemen Institute, Colombo, Sri Lanka.

Bastiaanssen, W. G. M. (2000). SEBAL-based sensible and latent heat fluxes in the irrigated Gediz Basin, Turkey. *Journal of Hydrology*, 229(1–2), 87–100. https://doi.org/10.1016/S0022-1694(99)00202-4.

Bastiaanssen, W. G. M., Menenti, M., Feddes, R. A., and Holtslag, A. A. M. (1998a). Remote Sensing Surface Energy Balance Algorithm for Land (SEBAL): 1. Formulation.41 J *Hydrol*., 212-213, 198-212.

Bastiaanssen, W. G. M., Noordman, E., Pelgrum, H., Davids, G., Thoreson, B., and Allen, R. G. (2005). SEBAL model with remotely sensed data to improve water-resources management Under actual field conditions. *J. Irrig. Drain. Eng*. 131, 85 –93.

Bastiaanssen, W. G. M., Pelgrum, H., Wang, J., Ma, Y., and Moreno, J. F. (1998b). A remote sensing surface energy balance algorithm for land (SEBAL). Part 2: Validation. Journal of Hydrology, 212, 213–229.

Bhattarai, N., Quackenbush, L. J., Im, J., and Shaw, S. B. (2017). A new optimized algorithm for automating endmember pixel selection in the SEBAL and METRIC models. *Remote Sensing of Environment* 2017, 196, 178-192; DOI:10.1016/j.rse.2017.05.009.

Carr, J. E. (1990). National water summary 1987: Hydrologic events and water supply and use (Vol. 2350). *US Government Printing Office*.

Cetin, M. (2020). Agricultural Water Use. In: N. B. Harmancioglu, D. Altinbilek (eds.), *Water*

Resources of Turkey, Chapter 9, World Water Resources, Vol. 2, https://doi.org/10.1007/978-3-030-11729-0_9, Springer Nature Switzerland AG 2020, ISBN 978-3-030-11728-3, pp. 257-302.

Cetin, M., Aksu, H., Alsenjar, O., Golpinar, M. S. and Akgul, M. A. (2021). Crop water stress index estimation by remote sensing in the Mediterranean Region of Turkey. *In: E-Proceedings of the International Symposium on Remote Sensing in Meteorology*, *METEO IRS 2021* (A. Öztopal, M. Akin and A. Durmaz, eds), ITU Press, Istanbul, Türkiye, pp. 102–108.

Cetin, M., Alsenjar, O., Aksu, H., Golpinar, M. S., and Akgul, M. A. (2023a). Estimation of crop water stress index and leaf area index based on remote sensing data. *Water Supply* (2023) 23 (3): 1390 -1404. https://doi.org/10.2166/ws.2023.051.

Cetin, M., Alsenjar, O., Aksu, H., Golpinar, M. S., and Akgul, M. A. (2023b). Comparing actual evapotranspiration estimations by METRIC to in-situ water balance measurements over an irrigated field in Turkey. *Hydrological Sciences Journal* 2023, 68, 1162-1183; DOI:10.1080/02626667.20230.

Çetin, M., and Kırda, C. (2003). Spatial and temporal changes of soil salinity in a cotton field Irrigated with low-quality water. *J. Hydrol*. 272, 238 –249. https://doi.org/10.1016/ S0022-1694(02)00268-8.

Çetin, M., and Özcan, H. (1999). Aşağı Seyhan Ovasında Sulanan ve Sulanmayan Alanlarda Meydana Gelen Sorunlar ve Çözüm Önerleri: Örnek Bir Çalışma. *TÜBİTAK Turkish Journal of Agriculture and Forestry* 23 (1999), Ek Sayı 1, 207-217, Ankara.

Cetin, M., Diker, K., and Ozcan, H. (2000). Monitoring and Evaluating the Spatial and Temporal Changes in Groundwater Quality, *Proceedings of the 2nd International Conference on GIS for Earth Science Applications* (ICGESA 2000), 11–14 September, Abstract on Page: 55, Full Text in Attached CD, Menemen-Izmir, Türkiye.

Cetin, M., Kaman, H., Kirda, C., and Sesveren, S. (2020). Analysis of Irrigation Performance in Water Resources Planning and Management: A Case Study. *Fresenius Environmental Bulletin (FEB)*, vol 29. 05: 3409-3414.

Cetin, M., Kirda, C., Efe, H., and Topcu, S. (2007). Using geographic information system for investigating soil and groundwater salinity caused by using low-quality irrigation water. (in Turkish with English abstract) Presented orally in the Second Conference on Water Politics organized by Turkish Chamber of Architectures and Engineers, Conference Proceedings Book, 20-22 March 2008, Ankara, Türkiye, pp.471-481.

Colak, Y., Yazar, A., Çolak, I., Akça,.Ha., and Duraktekin, G. (2015). Evaluation of crop water stress index (CWSI) for eggplant under varying irrigation regimes using surface and subsurface drip systems, 4, 372–382. https://doi.org/10.1016/j.aaspro.2015.03.042.

Davutluoglu, O. I., Seckin, G., Kalat, D. G., Yilmaz, T., and Ersu, C. B. (2010). Speciation and implications of heavy metal content in surface sediments of Akyatan lagoon Turkey.

Desalination 260, 189e210.

Dinç, U., Sarı, M., Şenol, S., Kapur, S., Sayın, M., Derici, M. R., Çavuşgil, V., Gök, M., Aydın, M., Ekinci, H., Ağca, N., and Schlicting, E. (1990). Soils of the Çukurova Region (in Turkish). University of Çukurova, No. 26, Adana, Türkiye.

Dinç, U., Şenol, S., Kapur, S., Derici, R., and Sayın, M. (1991a). Formation, distribution and chemical properties of saline and alkaline soils of the Çukurova region, southern Turkey. Catena 18, 173 –183. https://doi.org/10.1016/0341-8162(91)90015-P.

Dinç, U., Şenol, S., Kapur, S., Sarı, M. (1991b). Catenary soil relationships in the Çukurova region, southern Turkey. *Catena* 18, 185 –196. https://doi.org/10.1016/0341-8162(91)90016-Q.

El-shirbeny, M.A., Sciences, S., Ali, A. M., and Sciences, S. (2015). Assessment of wheat crop coefficient using remote sensing techniques, (October), 10–16. https://doi.org/10.13140/RG.2.1.1673.0325.

EOS. (2019). https://eos.com/Sentinel-2/.

Fick, S. E., and Hijmans, R. J. (2017). WorldClim 2: New 1-km spatial resolution climate surfaces for global land areas. Int. J. Climatol. 37, 4302–4315. https://doi.org/https://doi.org/10.1002/joc.5086.

Foolad, F., Blankenau, P., Kilic, A., Ekonomiczno-humanistyczna, A., and Allen, R. G. (2018). Comparison of the automatically calibrated google evapotranspiration comparison of the automatically calibrated google evapotranspiration application - EEFlux and the manually calibrated METRIC Application. January. https://doi.org/10.20944/preprints201807.0040.v1.

Glenn, E. P., Neale, C. M., Hunsaker, D. J., and Nagler, P. L. (2011). Vegetation index-based crop coefficients to estimate evapotranspiration by remote sensing in agricultural and natural ecosystems. *Hydrological Processes*, 25(26), 4050- 4062.

Gonçalves, I. Z., Ruhoff, A., Laipelt, L., Bispo, R. C., Hernandez, F. B. T., Neale, C. M. U., Teixeira, A. H. C., and Marin, F. R. (2022). Remote sensing-based evapotranspiration modeling using geeSEBAL for sugarcane irrigation management in Brazil. *Agricultural Water Management*, 274(October), 107965. https://doi.org/10.1016/j.agwat.2022.107965.

Gowda, P. H., Chavez, J. L., Howell, T. A., Marek, T. H. and New, L. L. (2008). Surface energy balance based evapotranspiration mapping in the Texas high plains. Sensors 8, 5186–5201.

He, R., Jin, Y., Kandelous, M. M., Zaccaria, D., Sanden, B. L., Snyder, R. L., Jiang, J., and Hopmans, J. W. (2017). Evapotranspiration estimate over an almond orchard using Landsat satellite observations. *Remote Sensing*, 9(5), 1–21. https://doi.org/10.3390/rs9050436.

Henrique, R., Ruhoff, A., Laipelt, L., Mello, E. De, Arruda, V. De, Cristina, G. and Neale, U. (2022). Assessing geeSEBAL automated calibration and meteorological reanalysis uncertainties to estimate evapotranspiration in subtropical humid climates, *Agricultural and Forest Meteorology* 314 (2022). https://doi.org/10.1016/j.agrformet.2021.108775.Imagens

Landsat 8 na Região Semiárida do Brasil. Conexões - Ciência e Tecnologia 11 (1), 22–34.

Hoedjes, J. C. B., Chehbouni, A., Jacob, F., Ezzahar, J., and Boulet, G. (2008). Deriving daily evapotranspiration from remotely sensed instantaneous evaporative fraction over the olive orchard in semi-arid Morocco. *J. Hydrol.*, 354, 53–64, https://doi.org/10.1016/j.jhydrol.2008.02.016.

Ibrikci, H., Cetin, M., Karnez, E., Flügel, W. A., Tilkici, B., Bulbul, Y., and Ryan J. (2015). Irrigation-induced nitrate losses assessed in a Mediterranean irrigation district. *Agric Water Manag* 148(3):223–231. https://doi.org/10.1016/j.agwat.2014.10.007.

Iglewicz, B., and Hoaglin, D. C. (1993). How to Detect and Handle Outliers. Springer.

Irfanoglu, F., and Balcik, F. B. (2018). Agricultural crop detection from multi-temporal Sentinel-2 Images: A Case Study of Mardin-Kızıltepe. *Aku J. Sci. Eng*. 21 (2021) 045505 (881-899). https://doi.org/10.35414/akufemubid.890436.

İrvem, A., and Ozbuldu, M. (2022). Evaluation of the performance of CFSR reanalysis data set for estimating reference evapotranspiration (ET_o) in Turkey. *Italian Journal of Agrometeorology* (2): 49-61. doi: 10.36253/ijam1325.

Irvem, A., Ozbuldu, M., and Ciplak, C. (2018). Drought analysis by using stream flow data of the Seyhan Göksu-Himmetli Sub-Basin. *Journal of Agricultural Faculty of Mustafa Kemal University*, 23(2):148-157.

Joyeux, J. C., and Ward, A. B. (1998). Constraints on coastal lagoon fisheries. Advances in Marine Biology 34, 73e199.

Kacar, M. M. (2007). Investigation of cotton water stress index variations under different water and fertilizer systems. Master. Thesis. Çukurova University Institute of Natural and Applied Science, Department of Agricultural structures and Irrigation, Türkiye,

Kamble, B., Irmak, A., and Hubbard, K. G. (2013). Estimating crop coefficients using remote sensing-based vegetation index. *Remote Sens*. 2013, 5, 1588-1602; doi:10.3390/rs5041588.

Karahan, H., Cetin, M., Can, M. E., and Alsenjar, O. (2024). Developing a new ANN model to estimate daily actual evapotranspiration using limited climatic data and remote sensing techniques for sustainable water management. Sustainability (Switzerland), 16(6). https://doi.org/10.3390/su16062481.

Koc, D L., and Kanber, R. (2020). Determination of evapotranspiration for wheat by Using Bowen Ratio Energy Balance Method. KSU *J Agric Nat* 23(2):544-553. DOI: 10.18016/ksutarimdoga.vi.59798.

Kohler, M. A., Nordenson, T. J., and Fox, W. E. (1955). Evaporation from pans and lakes. U.S. Dept. Commerce Res. Paper 38.

Kuleli, T. (2010). Quantitiative analysis of shoreline changes at the Mediterranean Coast in Turkey. Environmental and Monitoring Assessment 167, 387e397.

Kumar, A., Mishra, A. K., Singh, D. K., Kumar, L., Chakraborty, D., Singh, P., Kumar, A., Sarangi, A., and Sarkar, S. K. (2023). Estimating actual evapotranspiration using EEFlux in Eastern Sone High-Level Command, India. Arabian Journal of Geosciences, 16(12), 1–17. https://doi.org/10.1007/s12517-023-11771-w.

Kumar, U., Srivastava, A., Kumari, N., Rashmi, Sahoo, B., Chatterjee, C., and Raghuwanshi, N. S. (2021). Evaluation of Spatio-Temporal Evapotranspiration Using Satellite-Based Approach and Lysimeter in the Agriculture Dominated Catchment. Journal of the Indian Society of Remote Sensing, 49(8), 1939–1950. https://doi.org/10.1007/s12524-021-01367-w.

Laipelt, L., Henrique Bloedow Kayser. R., Santos Fleischmann, A., Ruhoff, A., Bastiaanssen, W. G. M., Erickson, T.A., and Melton, F. (2021). Long-term monitoring of evapotranspiration using the SEBAL algorithm and Google Earth Engine cloud computing. *ISPRS Journal of Photogrammetry and Remote Sensing*, 178, 81–96. https://doi.org/10.1016/j.isprsjprs.2021.05.018.

Laipelt, L., Ruhoff, L. A., Fleischmann, S.A., Kayser, H. R., Kich, D. E., da Rocha, R. H., and Neale M. C. (2020). Assessment of an automated calibration of the SEBAL algorithm to estimate dry-season surface energy partitioning in a forest-savanna transition in Brazil. *Remote Sens*. https://doi.org/10.3390/rs12071108.

Long, D., Singh, V. P., and Li, Z. L. (2011). How sensitive is SEBAL to changes in input variables, domain size, and satellite sensor? J. Geophys. Res. Atmos. 116. https://doi.org/10.1029/2011JD016542.

Madugundu, R., Al-gaadi, K. A., Tola, E., and Hassaballa, A. A. (2017). Performance of the METRIC model in estimating evapotranspiration fluxes over an irrigated field in Saudi Arabia using Landsat-8 images. *Hydrology and Earth System Sciences; Katlenburg-Lindau*, 21 (12). 6135–6151doi:10.5194/hess-21-6135-2017.

Mahlayeye, M., Darvishzadeh, R. and Nelson, A. (2022). Cropping patterns of annual crops: A remote sensing review. *Remote Sens*. 2022, 14, 2404. https://doi.org/10.3390/rs14102404.

Menne, M. J., Durre, I., Vose, R. S., Gleason, B. E., and Houston, T. G. (2012). An Overview of the Global Historical Climatology Network-Daily Database. *J. Atmos*. Ocean. Technol. 29, 897–910. https://doi.org/10.1175/JTECH-D-11-00103.1.

Mkhwanazi, M., and Chávez, J. L. (2012). Mapping evapotranspiration with the remote sensing ET al algorithms METRIC and SEBAL under advective and non-advective conditions: accuracy determination with weighing lysimeter. Hydrology Days. https://doi.org/10.25675/10217/201029.

Nisa, Z., Khan, M. S., Govind, A., Marchetti, M., Lasserre, B., Magliulo, E., and Manco, A. (2021). Actual Evapotranspiration for a Mediterranean Cropping System in Southern Italy. *Agronomy* 2021,11, 345.https://doi.org/10.3390/agronomy11020345.

Olmedo, G. F., Ortega-farias, S., and Fonseca-luengo, D. (2016). Tools and functions to estimate actual evapotranspiration using land water : tools and functions to estimate actual evapotranspiration using land surface energy balance models. *The R Journal* Vol. XX/YY, AAAA 20ZZ, ISSN 2073-4859.https://doi.org/10.32614/RJ-2016-051.

Ozcan, H., and Cetin, M. (1996). Land degradation induced by high groundwater level and soil salinity in the Fourth Stage Project Area of Yüreğir Plain: a case study. In: S Kapur, E Akça, H Eswaran, G Kelling, C Vita-Finzi, AR Mermut, AD Öcal (eds) Proceedings of the 1st international conference on land degradation. International working group on land degradation and desertification (IWGLDD-ISSS), Çukurova University Press, Adana, Türkiye, pp 93 -99.

Ozcan, H., Cetin, M. and Diker, K. (2003). Monitoring and Assessment of Land Use Status by GIS. Environ Monit Assess 87, 33–45 https://doi.org/10.1023/A:1024433812336.

Pakdel, H., Paudyal, D. R., Chadalavada, S., Alam, M. J., and Vazifedoust, M. (2023). A multi-framework of Google Earth Engine and GEV for spatial analysis of extremes in non-stationary conditions in Southeast Queensland, Australia. *ISPRS International Journal of Geo-Information*, 12(9). https://doi.org/10.3390/ijgi12090370.

Patil, V. C., Al-Gaadi, K. A., Madugundu, R., Tola, E., Marey, S., Aldosari, A., Biradar, C. M., Gowda PH. (2015). Assessing agricultural water productivity in desert farming system of Saudi Arabia. IEEE J Sel Top Appl 8:284–297.

Rafn, E. B., Contor, B., and Ames, D. P. (2008). Evaluation of a method for estimating irrigated crop-evapotranspiration remote sensing and simplified surface energy balance approach to remote sensing surface energy balance algorithm for land (SEBAL). *Resources* Association, 49(3), 577–591.

Rahimzadegan, M., and Janani, A. S. (2019). Estimating evapotranspiration of pistachio crop based on SEBAL algorithm using Landsat 8 satellite imagery. *Agricultural Water Management*, 217(March), 383–390. https://doi.org/10.1016/j.agwat.2019.03.018.

Ramos, J., Cratchley, C., Kay, J., Casterad, M., Martinez-Cob, A., and Dominguez, R. (2009). Evaluating satellite evapotranspiration estimates using ground-meteorological data available for the Flumen District into the Ebro Valley of NE Spain. Agric. *Water Manage*. 96, 638 – 652.

Reyes-Gonzalez, A., Hay, C., Kjaersgaard, J., and Neale, C. (2015). Use of remote sensing to generate crop coefficient and estimate actual crop use of remote sensing to generate crop coefficient and estimate actual crop evapotranspiration introduction (July). https://doi.org/10.13031/aim.20152190105.

Reyes-González, A., Kjaersgaard, J., Trooien, T., Hay, C., and Ahiablame, L. (2018). Assessing accuracy of vegetation index method to estimate actual evapotranspiration. *Earth Sciences*. Vol. 7, No. 5, 2018, pp. 227-235. doi: 10.11648/j.earth.20180705.14.

Reyes-González, A., Kjaersgaard, J., Trooien, T., Reta-s, D. G., Juan, I. S., Preciado-rangel, P. and Fortis-hern, M. (2019). Comparison of leaf area index, surface temperature, METRIC model and in situ measurements. Sensors 2019, 19, 1857. Doi: 10.3390/s19081857.

Rouse, J. W., Haas, R. H., Deering D. W., and Sehell, J A. (1974). Monitoring the vernal advancement and retrogradation (green wave effect) of natural vegetation. Final Rep. RSC 1978-4, Remote Sensing Center.

Santos, L. da C., Cruz, G. H. T., Capuchinho, F. F., José, J. V., and dos Reis, E. F. (2019). Assessment of empirical methods for estimation of reference evapotranspiration in the Brazilian Savannah. *Australian Journal of Crop Science*, 13(7), 1094–1104. https://doi.org/10.21475/ajcs.19.13.07.p1569.

Sawadogo, A., Hessels, T., Gundogdu, K. S., Demir, A. O., and Unlu, Mustafa. (2020). Comparative analysis of the pySEBAL model and lysimeter for estimating actual evapotranspiration of the soybean crop in Adana. *International Journal of Engineering and Geosciences* (IJEG), Vol; 5, Issue; 2, pp. 060-065, ISSN 2548-0960, Türkiye, DOI: 10.26833/ijeg.573503.

Seemann, S. W., Li, J., Menzel, W. P., and Gumley, L. E. (2003). Operational retrieval of atmospheric temperature, moisture, and ozone from MODIS infrared radiances. *JApMe*, 42 (8), 1072 –1091. http://dx.doi.org/10.1175/1520-0450(2003) 042<1072:oroatm>2.0.co;2.

Steduto, P. (2000). Plant nutrient management under pressurized irrigation systems in the Mediterranean Region: crop water requirements In: J. Ryan, ed. Plant nutrient management under pressurized irrigation systems in the Mediterranean Region. Proceedings of the International Fertigation Workshop organized by the World Phosphate Institute (IMPHOS), 25–27 April 1999. Aleppo: ICARDA, 400.

Su, Z. (2002). The surface energy balance system (SEBS) for estimation of turbulent heat fluxes. *Hydrology and Earth System Sciences*, 6, 85–100. doi:10.5194/hess-6-85-2002.

Sun, J. F., Wang, J. F., Zhang, R. H., Gillies, R. R., Xue, Y. and Bo, Y. C. (2004). Air temperature retrieval from remote sensing data based on thermodynamics. Theor. Appl. Clirnatol., 80, 37–48 (2005). https://doi.org/10.1007/s00704-004-0079-y.

TAGEM-DSI. (2017). Plant water consumption of irrigated plants in Turkey. Ankara, Türkiye: The Republic of Türkiye, Ministry of Agriculture and Forestry, *General Directorates of Agricultural Research and Policies (TAGEM*) and *State Hydraulic Works* (*DSI*), Published by *TAGEM*. 590. (In Turkish).

Tasumi, M. (2019). Estimating evapotranspiration using METRIC model and Landsat data for a better understandings of regional hydrology in the western Urmia Lake Basin. *Agricultural Water Management*, 226 (2019), 105805. doi:10.1016/j.agwat.2019.105805.

Trezza, R. (2002). Evapotranspiration using a satellite-based surface energy balance with standardized ground control, biological and irrigation engineering. *Utah State University*, pp. 715.

Trezza, R., Allen, R. G., and Tasumi, M. (2013). Estimation of actual evapotranspiration along the

Middle Rio Grande of New Mexico using MODIS and Landsat imagery with the METRIC model. *Remote Sensing*, 5(10), 5397-5423.

Tukey, J. W. (1977). Exploratory Data Analysis. Addison-Wesley.

Unlu, M., Kanber, R., and Kapur, B. (2010). Comparison of soybean evapotranspirations measured by weighing lysimeter and Bowen ratio-energy balancemethods. *African Journal of Biotechnology* 9(30): 4700-4713.

Unlu, M., Kanber, R., Kapur, B., Tekin, S., and Levent Koc, D. (2011). The crop water stress index (CWSI) for drip irrigated cotton in a semi-arid region of Turkey. *African Journal of Biotechnology*, 10(12), 2258–2273.https://doi.org/10.5897/AJB10.1675.

Unlu, M., Kanber, R., Koc, D L., Ozekici, B., and Kekec, U. (2014). Irrigation scheduling of grapefruit trees in a Mediterranean environment throughoutevaluation of plant water status and evapotranspiration. *Turkish Journal of Agriculture and Forestry* 38(6): 908-915. doi.org/10.3906/tar-1403-58.

Venancio, L. P., Eugenio, F. C., Filgueiras, R., Da Cunha, F. F., Santos, R. A. Dos, Ribeiro, W. R., and Mantovan, E. C. (2020). Mapping within-field variability of soybean evapotranspiration and crop coefficient using the Earth Engine Evaporation Flux (EEFlux) application. PLoS ONE, 15(7 July 2020), 1–21. https://doi.org/10.1371/journal.pone.0235620

Veysi, S., Naseri, A., Hamzeh, S. and Bartholomeus, H. (2017). A satellite-based crop water stress index for irrigation scheduling in sugarcane fields. *Agricultural Water Management*, 189 (July), 70–86. https://doi.org/10.1016/j.agwat.2017.04.016.

Yi, Q. X., Bao, A., Wang, Q., and Zhao, J. (2013). Estimation of leaf water content in cotton by means of hyperspectral indices. *J. Comput. Electron. Agric*. 90, 144–151.

Yılmaz, A. G., and Imteaz, M. A. (2014). Climate change and water resources in Turkey: a review. *International Journal of Water*, 8(3):299-313.

Yilmaz, M. (2018). Object-based classification of summer crops from Sentinel-2 satellite images using random forest algorithm. Hacettepe University, Master of Science, Department of Geomatics Engineering July/2018, Ankara, 95 s., YOK Thesis Center, Thesis No: 524623 (https://tez.yok.gov.tr/UlusalTezMerkezi/tezDetay.jsp?id=_AecABzl2qMBoUtjucjPFQand no=0FGoaty2vbUIt38jiYq1ew).

Zamani, Losgedaragh, S., and Rahimzadegan, M. (2018). Evaluation of SEBS, SEBAL, and METRIC models in estimation of the evaporation from the freshwater lakes (Case study: Amirkabir Dam, Iran). *JHyd* 561, 523 –531.

CURRICULUM VITAE

OMAR ALSENJAR completed his high school education at Hasaka and Damascus schools in Syria. He started to study for his Bachelor's degree in Civil Engineering at Al-Furat University in 2006 and graduated in 2011 with a specialization in water resources engineering. Notably, he was among the top four students in his class and ranked first in the national entrance examination for master's programs. This achievement granted him admission to the prestigious Damascus University, where he earned a Master's in water resources engineering from the Civil Engineering Faculty in 2015. During his master's studies, Alsenjar researched mapping potential sites for pumped storage plants using existing lower reservoirs in Syria. This work gave him practical insights into hydrology, advanced hydraulics, and power generation from small and large water structures. Additionally, he participated in several data collection projects to model renewable energy use in water structure projects. In 2018, Alsenjar began his PhD studies at Szeged University in Hungary, where he gained valuable experience in hydrology, GIS, and remote sensing in water resources. By 2020, he was accepted for PhD studies at the Department of Agricultural Structures and Irrigation at Cukurova University in Adana, Türkiye. His PhD thesis focuses on using remote sensing satellite imagery combined with ground truth data to figure out changes in crop growth stages and estimate actual evapotranspiration (ET_a), including crop water stress index (CWSI) and leaf area index (LAI). Alsenjar is co-author of several high-ranking journal articles in esteemed publications such as the Hydrological Sciences Journal, Sustainability, Mediterranean Geoscience Reviews, Water Supply, and the Journal of Agricultural Sciences at Ankara University. He has also participated in numerous international conferences and workshops across the globe, including in Canada, Hungary, Türkiye, Uzbekistan, Lebanon, and Syria.